Probing the Nature of the Magnetic Interactions in Magnetic Skyrmions

SAMUEL HARRISON MOODY

Probing the Nature of the Magnetic Interactions in Magnetic Skyrmions

Samuel Harrison Moody

A thesis presented for the degree of
Doctor of Philosophy

Department of Physics
Durham University
United Kingdom

February 2023

Contents

Probing the Nature of the Magnetic Interactions in Magnetic Skyrmions

Samuel Harrison Moody

Abstract

Magnetic skyrmions are topologically-protected, solitonic entities which are composed of a vortex-like arrangement of magnetic moments. Recently, they have seen a surge of interest from the condensed matter physics community due to their presence in a number of systems which feature novel and interesting physical phenomena, such as unique transport and frequency responses. These characteristics, together with their countable nature is highly appealing for use within novel spintronic devices. With the ever-growing demand for high processing speeds and data storage, skyrmionic devices have the potential to provide low-power, high density data storage as well as play a key role in a number of next-generation computational devices. Whilst skyrmions do appear in a number of different systems, in this thesis we will focus on skyrmions within bulk-magnets.

In these bulk-systems, skyrmions are stabilised within a small range of temperatures and applied magnetic fields. Commonly, skyrmions are shown to be stabilised by the interplay of the exchange, Dzyaloshinskii-Moriya and Zeeman energies, together with thermal fluctuations or higher-order magnetic anisotropy. Typically, these interactions are only modelled to first order, but there is increasing interest in higher-order and alternative interactions to both generate and manipulate skyrmions.

In this thesis, at Chapter 1 we start with explaining why it is the material specific interactions, and not the particular arrangement of spins, which give rises to the skyrmion stability. We investigate real material parameters and the spin-textures those interactions stabilise using diffraction-based techniques, which we give a brief overview in Chapter 2. In Chapter 3, we design and perform an

experiment for measuring and quantifying the anisotropic exchange interaction, and show that this often overlooked interaction is crucial for the formation of the recently discovered tilted conical phase. In Chapter 4, we look at how to control this tilted conical phase using the magnetoelectric coupling interaction, and show that we are reliably able to manipulate the conical wavevector into different positions via an electric field, and provide mean-field theory to explain the tilt-directions as a function of electric field. Furthermore, we provide micromagnetic simulations of a toy model to show the potential spintronic applications of this manoeuvrability. In Chapter 5, we move away from chiral magnet systems to investigate the spin-textures within a nanoskyrmion-containing material. We find clear phase boundaries between a number of incommensurate magnetic phases, and perform an experiment to accurately resolve their form. We find interesting behaviour with regards to their chirality, which we suggest to arise from local Dzyaloshinskii-Moriya interactions despite the overall centrosymmetric crystal structure. In Chapter 6, we return to chiral magnets and experiment with metastable skyrmions created using a custom fast field cooling method. We then discover a remarkable phenomenon that the skyrmion intensity grows as a function of field, which is contrary to previous literature suggesting that their stability massively decreases. We suggest that both anisotropic interactions and disorder play a role, and perform a thorough directionally dependent study to try to decouple the two arguments. Finally in Chapter 7, we provide the conclusions of this thesis.

Declaration

The work in this thesis is based on research carried out in the Department of Physics, Durham University, UK, with experimental work carried out at the ISIS Neutron and Muon Source (UK), Diamond Light Source (UK), Institute Laue Langevin (FR), Paul Scherrer Institute (CH) and the Deutsches Elektronen-Synchrotron (GE). No part of this thesis has been submitted elsewhere for any other degree or qualification and it is all my own work unless referenced to the contrary in the text.

List of publications

S. Furuta, **S. H. Moody**, K. Kado, W. Koshibae and F. Kagawa. "Energetic perspective on emergent inductance exhibited by magnetic textures in pinned regime". *In Review Communications Physics* Feb. 2023.

R. Brearton, **S. H. Moody**, L. A. Turnbull, J. A. T. Verezhak, P. D. Hatton, G. Balakrishnan, G. van der Laan and T. Hesjedal. "Observation of the Chiral Soliton Lattice above Room Temperature ". *Accepted Advanced Physics Research Feb. 2023.*

M. N. Wilson, M. T. Littlehales, **S. H. Moody**, L. A. Turnbull, B. Huddart, G. Balakrishnan, P. Steadman, R. Fan, and P .D. Hatton. "Demonstration of a thickness-step skyrmion injector in FeGe ". *In Preparation* Dec. 2022.

S. H. Moody, M. T. Littlehales, J. S. White, D. Mayoh, G. Balakrishnan, D. A. Venero and P. D. Hatton. "Electric Field Controlled Mechanism for the Deflection of Skyrmions ". *In Preparation* Dec. 2022.

S. H. Moody, P. Nielsen, M. N. Wilson, D. Alba Venero, A. Štefančič,G. Balakrishnan and P. D. Hatton. "Experimental evidence of a change of exchange anisotropy sign with temperature in Zn-substituted Cu_2OSeO_3". *Phys. Rev. Research* **3**, 043149, 2021.

M. T. Birch, **S. H. Moody**, M. N. Wilson, M. Crisanti, O. Bewley, A. Štefančič,

G. Balakrishnan, R. Fan, P. Steadman, D. Alba Venero, R. Cubitt, and P. D. Hatton. "Anisotropy-induced depinning in the Zn-substituted skyrmion host Cu_2OSeO_3". *Phys. Rev. B.* **102**, 104424, 2020

M. Crisanti, M. T. Birch, M. N. Wilson, **S. H. Moody**, A. Štefančič, B. M. Huddart, S. Cabeza, G. Balakrishnan, P. D. Hatton and R. Cubitt. "Position-dependent stability and lifetime of the skyrmion state in nickel-substituted Cu_2OSeO_3 ". *Phys. Rev. B* **102**, 224407, 2020

M. T. Birch, D. Cortés-Ortuño, L. A. Turnbull, M. N. Wilson, F. Groß, N. Träger, A. Laurenson, N. Bukin, **S. H. Moody**, M. Weigand, G. Schütz, H. Popescu, R. Fan, P. Steadman, J. A. T. Verezhak, G. Balakrishnan, J. C. Loudon, A. C. Twitchett-Harrison, O. Hovorka, H. Fangohr, F. Y. Ogrin, J. Gräfe and P. D. Hatton. "Real-space imaging of confined magnetic skyrmion tubes ". *Nature Communications* **11**, 1726, 2020

A. Štefančič, **S. H. Moody**, T. J. Hicken, M. T. Birch, G. Balakrishnan, S. A. Barnett, M. Crisanti, J. S. O. Evans, S. J. R. Holt, K. J. A. Franke, P. D. Hatton, B. M. Huddart, M. R. Lees, F. L. Pratt, C. C. Tang, M. N. Wilson, F. Xiao, and T. Lancaster. "Origin of skyrmion lattice phase splitting in Zn-substituted Cu_2OSeO_3". *Phys. Rev. Mater.* **2** 111402(R) 2018

Acknowledgements

I would like to take this opportunity to acknowledge the funding from EPSRC and Durham University, as well as to thank my colleagues, friends, and family, without whom the completion of my PhD would not have been possible, or even attempted. There were many people who were instrumental in this process, and I will endeavour to mention everyone. However, it is inevitable that I may miss some people. To those who feel left out - Thank you, and please accept my sincerest apologies. Let me know, and I'll buy you a pint!

Firstly, I would like to start at the beginning and thank those who inspired me to make the fascinating life choice of studying physics at university: Mr. Lucking and Mr. Williams. Both of you helped me to grasp the concepts of physics, kindled my interest, and allowed it to flourish into a passion that now dominates my life. I cannot express enough gratitude for guiding me towards physics. Without your guidance, I might have ended up studying chemistry! Thank you both.

Throughout my PhD, I have been incredibly fortunate to have had the opportunity to visit and work with amazing people at various facilities across different countries. In particular, I would like to express my sincere gratitude to Paul Steadman, Raymond Fan, and Mark Sussmuth for allowing me to understand diffraction by playing with RASOR, Bob Cubit for graciously giving up local control and allowing me to work on D33, Eugen Weschke for transforming UE46_PGM-1 into a Berghain competitor, Sonia Francoual for generously spending her time remotely controlling P09 on my behalf, and Jonathan White for setting up a highly secure remote access interface for controlling SANS-I and for

providing me with a post-doc opportunity. Beyond that, I would like to thank Kagawa-sensei for the warm welcome to Japan and for the vast scientific and personal experiences I gained at RIKEN. Within my own institution, I extend my gratitude to Jason Anderson and Paul Foley for their endless assistance in sourcing random items needed for test experiments ahead of beamtime, Wayne Dobby for trusting my claim that the physics department was indeed radioactive, Leon Bowen for teaching me how to use the electron microscope, and John Dobson, good luck with the Laue, and I promise that I didn't break it.

As part of my PhD, I was lucky to be involved with a wider community as part of the UK Skyrmion Project. In particular, I would like to thank Geetha and the Warwick team for providing me with samples and involving me in your experiments. The samples were great, and I had a fantastic time at Diamond with you. Thanks to James and Alison for being brilliant role models for what academic life could be. Thanks to Ondrej, David and Sebastian for their simulation work, despite how (necessarily) complicated I insisted it must be. Thanks to Thorsten, not only for his terrible jokes but also for introducing me to my Oxford-based partner in crime. Thanks to Richard for the discussions, the lockdown gaming, and the company during beamtime. I hope you remember to take me out to Suzuka like you promised. Thank you, Marta; you welcomed me into the ILL community with open arms and made each visit less like work and more like catching up with old friends. You allowed me to enjoy the devastating 6 am MacDonald's breakfast-type of experiments and showed me that there is more to life than just neutrons and whirly-boys. I'm looking forward to bumping into all of you at various conferences to reminisce about our shared trauma of that terrible improv-acting class.

Thanks to the Jolly Sailor Support Club for your companionship throughout the short days and long nights of thesis writing, and for the slightly less-glazed over look in your eyes than the average person when I went off on long, arduous rants about magnetic whirlpools. I hope you guys enjoy a copy of this thesis - I'm sure it'll make a great addition to the books waiting to be read on the historic

bookshelf.

To the worlds worst physics supporters, thanks for sticking by my side and encouraging me since I was sixteen. You've never made fun of my nerdy choices, and have always been there for me to talk to about my numerous life and physics-based problems. Thanks for your help with correcting this thesis, including, the, addition, of, many, commas, and for helpfully explaining why I can't just say "It's just a Fourier transform" to explain my pretty pictures.

To the friends who helped me stay sane during the various COVID lockdowns in Durham, including Luke, Murray, Thomas, Zach, Max, Michael, and Joao - thank you. I appreciated your company, your compliments on my cooking, and your willingness to go on adventures with me around Durham.

Matt, thank you for the vast amount of time we spent together, from the late-night macro-writing sessions to the World Cup in Paris. I had a great time, and I learned more from talking with you than I did from my entire degree. Good luck finishing off some of the more sensible experiment ideas.

To Thea, thanks for the support you have given to me throughout the years, both the great and the small, from moving up to Durham in the midst of a global pandemic to letting me have the bigger half of dinner. Thanks for your patience and for helping me stick at it, I would have had half of the fun for twice the battle. Lets see where the next adventure takes us.

Usually, when one thanks their family, they express gratitude for their endless interest and vast quantities of physics-related dinner discussions. However, I would like to thank you for the little things - the dubious t-shirt-buying, adventurous visits to Durham, maddening egg hunts, never-ending Christmas nibbling, fanatical Sunday dinners, bizarre rainy barbecues, and the inevitable television sleeping. Thank you for being the best family I could ever ask for.

Finally, I would like to express my gratitude towards my supervisor, Peter, who has watched over me throughout my entire higher education. We first met during the second week of my undergraduate studies at Durham, where I constantly complained about the complexity of the course compared to my peers who

were busy indulging in typical student activities. This resulted in me missing numerous homework deadlines with excuses like "they're only formative anyway" and "it's just a pointless university hoop to jump through." To our surprise, when the second-year exam marks were released, I was quite good at physics. This led me to choose Peter as my supervisor for my masters' project, where he got me hooked on beamtime experiments and the concept of skyrmions. While we were driving back from Diamond, he offered me the PhD opportunity, which I eagerly jumped at, not only because it was a fantastic opportunity but also because we were travelling a little over the speed limit on the M1. Typically, I take most of what you say with a large pinch of salt, but I must admit I was wrong about one thing - these four years have been the best years of my life. Thank you, Peter.

Chapter 1

Introduction

1.1 What are Skyrmions Anyway?

The concept of a skyrmion was first realised by nuclear physicist Tony Skyrme in 1961 [1, 2]. Dissatisfied with the previous shell-model of nuclear matter [3], he pursued the idea of describing individual nucleons and pions as some kind of twist within an ether-like fluid, rather than independent interacting particles, now known to be composed of quarks [4, 5]. This led to a novel non-linear boson field theory where self-interactions admitted states with the phenomenological properties of fermionic particles [6]. Despite losing popularity to the quark model and quantum chromodynamics for describing high-energy physics, the Skyrme model still remains useful today and has received a revived interest for describing the low-energy regimes of atomic nuclei [7].

Skyrmions have since been used to describe a number of excitations, ranging in size from the original pion-model to massive objects such as neutron stars [8, 9]. They Skyrme model has also been used to great success in solid state field theories [10], including ^{3}He condensates [11, 12, 13, 14], quantum Hall fluids [15, 16], superconductors [17, 18, 19], liquid crystals [20, 21, 22] and magnetism [23, 24, 25]. The popularity of using the Skyrme model to describe these various excitations is rooted in the interesting physics of self-interactions of the system, as well as a so called topological protection, which we shall explore further in the

subsection below.

1.1.1 Topological Protection - What is it good for?

As previously mentioned, skyrmions are localised field-excitations. These excitations are typically thought to be long-lived due to a characteristic topological protection, which acts to maintain their stability in the presence of external disturbances, such as thermal fluctuations or defects in the system. This protection can be visualised by the knots (in this case a knot represents a skyrmion) within the ropes shown in Figure 1.1. Here, three weights: A, B and C, are suspended by three separate ropes. Each rope can be thought of as a one dimensional field, whose energy is predominantly determined by gravity. Weights B and C are in elevated, excited states due to a localised twist raising the systems energy when compared to the ground-state, shown as A. Smooth, continuous deformations of the rope in B allows the system trivially to return to the ground state. In contrast, system C remains in an excited state due to the presence of a topological defect; a skyrmion. Note that this analogy goes further, as we can see it is the self-interactions of the rope which prevent the knot from untying – you can't pull the rope through itself! We can see that the removal of skyrmions from their respective fields costs a great deal of energy, requiring the introduction of a localised discontinuity (a rip in the rope) in the field or raising much of the field above the ground state to untie the system.

The topology of a skyrmion is typically analysed by investigating a quantity known as the winding number, N. This counts the number of times the field direction can be mapped onto a surface about the core of the excitation, and is mathematically defined as [26]:

$$N = \frac{1}{4\pi} \int \int n(\vec{r}) \cdot \left(\frac{\partial n}{\partial x_1} \times \frac{\partial n}{\partial x_2}\right) \, dx_1 dx_2, \tag{1.1}$$

where $n(\vec{r})$ describes the vector field orientation (such as magnetisation) at a position $\vec{r}$. The coordinates x_1, x_2 define the surface surrounding the core of the skyrmion which is integrated over. The triple product containing the vector field,

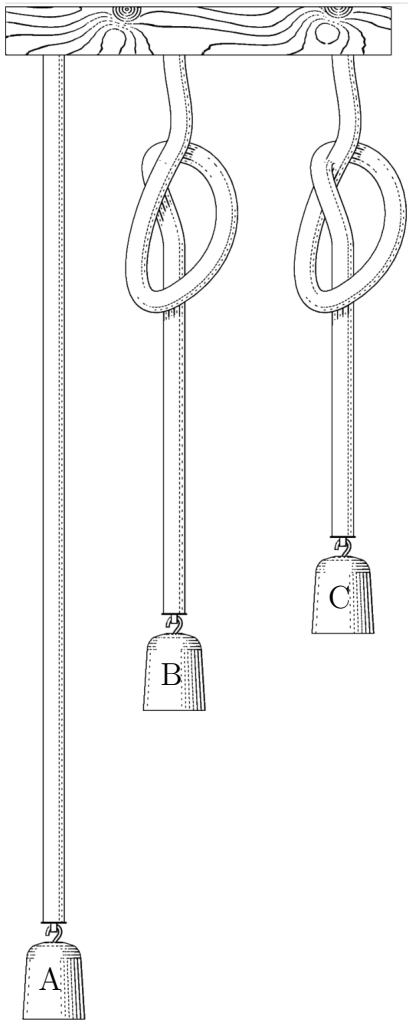

Figure 1.1: Ropes suspending weights under gravity. System A is in the ground-state, B an excited state, and C a topologically protected excited state - a skyrmion.

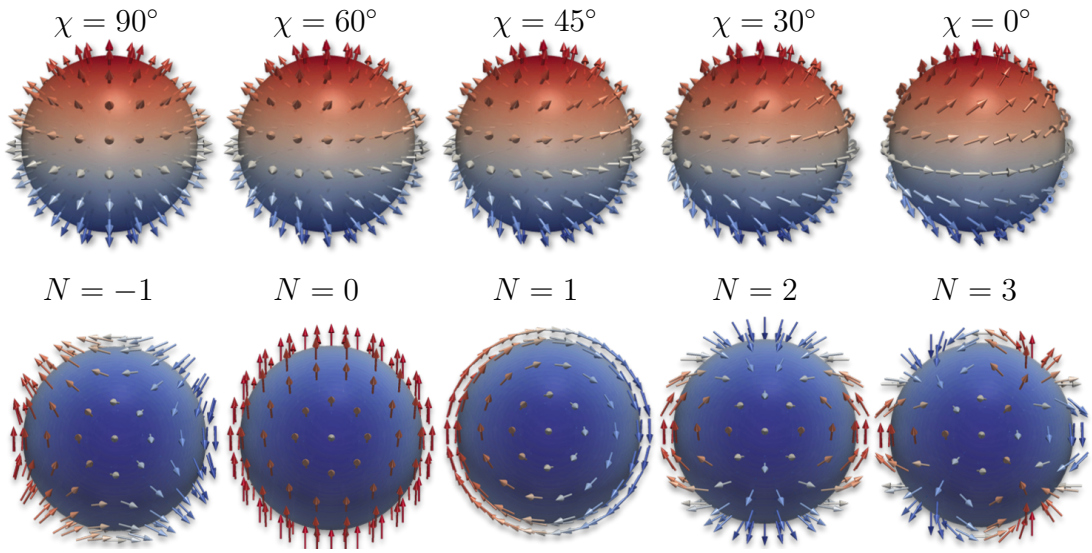

Figure 1.2: Top: Equatorial view (North-up in plane of page) of three dimensional skyrmions all with an equal winding number of one. Each skyrmion varies in terms of a global phase shift χ, changing the static direction of the entire field, without changing the value of the winding number. Bottom: Polar view (North-into plane of page) of three dimensional skyrmions all with an equal phase shift of $\chi = \frac{\pi}{2}$. Each skyrmion varies in terms of a winding number N, displaying an antiskyrmion ($N = -1$), topologically trivial ($N = 0$), and multiple winding numbered skyrmions ($N = 1, 2, 3$).

and the two spatial derivatives mathematically map out the solid angle between neighbouring vectors, and the integrand then counts the number of times the total solid angle across the integrated surface wraps around a unit sphere, hence the division by 4π. Any region of a field with an integer winding number can therefore be identified as a skyrmion.

The winding number can be visualised by looking at three dimensional skyrmions, known as hedgehogs or monopoles [27]. The top row of Figure 1.2 shows $N = 1$ skyrmions, as in each case the total angle spanned by all the vectors completely wraps the unit sphere. This is more easily seen by looking at the rotation of the

field direction as we follow an equatorial path around the sphere. For $N = 1$, an angular path of π-radians from west to east is accompanied by the rotation of the field at the same angular rate and direction as to always lie in the same orientation relative to the surface of the sphere. This means that all the skyrmions in the top row of Figure 1.2 have a positive unit winding number as the spins wrap around the skyrmion in step with the path around the equator. A global phase shift to the vector field, χ, shows one can arbitrarily rotate all the spins without varying the topological property of the skyrmions.

On the other hand, a variety of different winding-numbered entities are shown in the bottom row of Figure 1.2, and visually display vastly different features to the top row. Antiskyrmions ($N = -1$) have a rotation of spins of the same period but wind opposite to the direction of angular rotation. $N = 0$ is a topologically trivial entity and will readily return to its ground state, and $N > 1$ winding numbers have the spins completing multiple, complete rotations per equatorial path. Here, in three dimensions, topological protection again is analogous to a knot. If one imagines shrinking the $N = 0$ and $N = 1$ spheres in the bottom row of Figure 1.2, it is easy to visualise the vectors on the surface of the the $N = 0$ sphere rotating to all align along the same direction, in this case towards the top of the page. For the $N = 1$ skyrmion however, shrinking the sphere causes the spins with opposite moment direction to get closer and closer, massively raising the cost of any energy term which scales as the gradient of the vector field. Furthermore, this energy cost cannot be mitigated, as since the vectors point in all directions, there are no 'spare' directions to twist into.

As we have seen, the topology of the skyrmion plays a role in its stability. However, this stability is only valid when the interactions of the system prevent the deformations. Later, we shall explore why these interactions are so important, but first we will introduce the main focus of this thesis: the magnetic skyrmion.

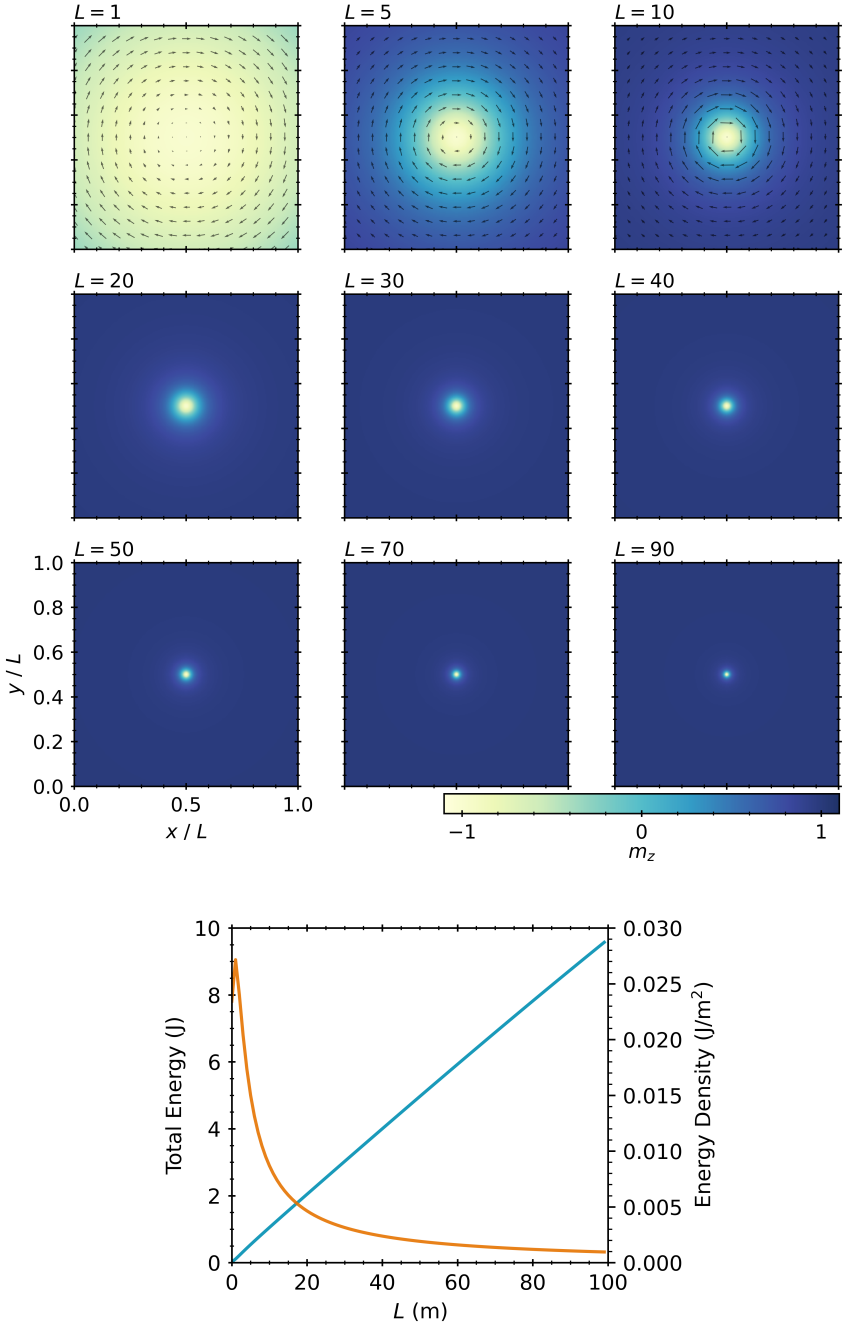

Figure 1.3: Images: Sterographic projections of a 3D skyrmion from a unit sphere onto a plane of size L. Bottom: Total system energy (blue) and energy density (orange) as a function of plane size L when accounting for only the exchange interaction, $A = 1$ J/m.

1.2 Magnetic Skyrmions I

Magnetic skyrmions, rather ungraciously called child skyrmions by mathematicians due to their two-dimensional nature[1] [28, 29, 30], are typically thought to be related to their three-dimensional parents by squashing them into a two dimensional plane in a process known as stereographic projection. This process projects the north pole of a three-dimensional skyrmion (Shown in Figure 1.2) to the origin of a plane, the equator to a unit circle, with the south-pole sent off to an infinite distance.

The stereographic projection of the $\chi = 90$ degrees skyrmion in Figure 1.2 is shown for different system sizes in Figure 1.3. Unfortunately, due to the properties of a stereographic projection, at no point does the field ever become uniform, even in infinite systems. Thus, increasing the system size results in an increased energy cost, shown in the bottom plot of Figure 1.3. Also shown is the inverse quadratic trend in the energy density, showing asymptotic behaviour towards a finite value. Thus integrating the system out to an infinite radius causes the total energy of a single skyrmion to diverge, meaning we should never see them in reality.

The situation is hardly made any better when considering the dimensionality of the magnetic skyrmions. The Mermin-Wagner theorem states that continuous symmetries (such as a ferromagnetic state) cannot be spontaneously broken at finite temperature in systems with sufficiently short-range interactions (such as the exchange) in dimensions $d \leq 2$ [31, 32]. This is because in two-dimensional systems, spontaneous magnons can be created with very low energy[2]. This is

[1] One can imagine a whole family of skyrmions depending on the dimensionality. 'Adult' skyrmions live in 3D space with a 3D field, child skyrmions are in 2D space and a 3D field direction.

[2] This is in fact general across all field-theories. When you break a continuous symmetry (e.g. between a ferromagnetic to paramagnetic state) spontanous, long-wavelength excitations

because in two-dimensions, the dispersion relation of a magnon in an isotropic ferromagnet is quadratic at low energy, with no energy-gap [34]. Thus long-wavelength magnons are readily created for even vanishingly small temperatures. Due to the entropy-increasing nature of long-wavelength fluctuations in finite temperature, they lower the thermodynamic energy of the system, hindering any spontaneous long-range order. However, magnetic ordering can still be obtained in two-dimensions where there is a gap in the spin-wave dispersion curve, arising from presence of other magnetic interactions such as anisotropy and the Dzyaloshinskii-Moriya interaction (DMI) [35].

This lack of stability can be shown using time-dependent micromagnetic simulations. When only using the typical, first order exchange interaction, which is minimised by reducing the magnitude of the spatial derivatives in the magnetisation, we see in Figure 1.4, that the magnetic skyrmion unravels as a function of time (t). In the final frame at $t = 99$ ps, we see that the skyrmion has completely unwound into the field polarised state. Note, the $t = 0$ starting magnetic configuration is the stereographic projection representation discussed earlier.

This shows that whilst an object may be topologically protected, it doesn't necessarily mean that it is stable or even physical in the first place. However, as we shall see, magnetic skyrmions are realised in a number of systems. This is because it is not solely the topological properties of skyrmions which allow their formation, but the various magnetic interactions that admit the skyrmion state to be an energy minimum. In order to understand why these interactions are so crucial for skyrmion formation, we should first briefly review magnetism and magnetic interactions.

are created called Goldstone modes, massless particles which cost no energy to create [33].

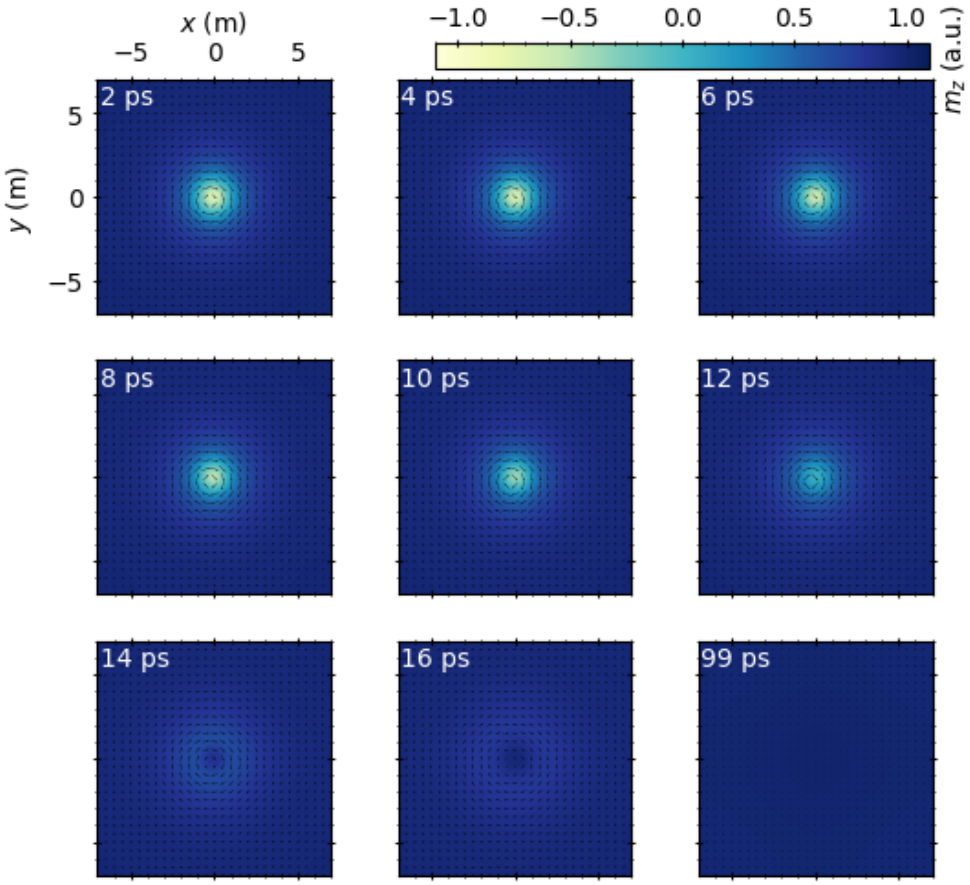

Figure 1.4: Time-dependent micromagnetic simulation of a stereographically projected skyrmion, using normalised micromagnetic parameters of $A = 1$ J/m, $\alpha = 1$ and $M_s = 1$.

1.3 Magnetism and Magnetic Interactions

1.3.1 Isolated Moments

Atoms and ions exhibit an intrinsic magnetic moment, the fundamental object in magnetism. The magnitude, μ, is dominated by the spin and orbital angular momentum of the constituent electrons. One can think of the orbiting motion of an electron around an atomic nucleus to give rise to a finite magnetic moment in a similar way as classical electrodynamics inducing a magnetic field from a current loop. For a hydrogen atom, the electric current, I, from one electron is given by $I = -e/\tau$, where τ is the orbital period equal to $2\pi r_e/v_e$, where r_e, v_e are the radius and velocity of the electron respectively. Using quantum mechanics, we know that the angular momentum of an electron is quantised in units of $\hbar$, such that $m_e v_e r_e = \hbar$. Thus the magnetic moment magnitude of a single electron is [34]:

$$\mu = \pi r_e^2 I = \frac{-e\hbar}{2m_e} = -\mu_{\mathrm{B}}, \tag{1.2}$$

where μ_B is the Bohr magneton, the fundamental unit of magnetism. Similarly, the spin of the electron, with quantum-number S, also contributes to the magnetic moment of the atom, with the spin each electron contributing to the moment with magnitude, $\mu_S = -g\mu_{\mathrm{B}}S$, where $g = 2.0023$ and is the relativistic gyromagnetic ratio of the electron [36]. Since the magnetic moment of an atom is associated with both the angular momentum, **L**, and the spin angular momentum, **S**. To a first approximation, we define the total angular momentum, **J**, to be [34]:

$$\mathbf{J} = \mathbf{L} + \mathbf{S}. \tag{1.3}$$

However, most atoms and ions tend to contain more than a single electron. Due to the shell-filling nature of electrons, most of the angular momentum (both spin and orbital) will be cancelled by a concomitant electron within low-energy electron shells. Therefore, it is only the electrons which lie within unfilled shells which give rise to a non-vanishing total angular momentum. For electrons within a shell with a given orbital angular momentum, L, and spin S, there are $(2L+1)(2S+1)$

possible states for the electrons to fill. Due to the spin-orbit interaction [37, 38], these states are not equal in energy, as a non-zero coupling exists between the spin and orbital angular momentum of each electron. Therefore, the electrons occupy these states within a particular order, which are given to a good approximation using the empirically-derived Hund's rules [34]. Which in order of importance are:

1. Minimise the Coulomb energy: select states which maximise the total value of S to prevent electrons from occupying the same m_l state

2. Maximise the total L: states which 'orbit' in the same direction can avoid each other more efficiently

3. Minimise the spin-orbit energy by using $J = |L \pm S|$ depending on whether the shell is less than or more than half full respectively.

These rules work well for the 4f ions (such as Gd) in the solid state, but tend to do poorer for the 3d (such as Cu) due to crystal field effects, which tend to quench the orbital angular momentum contribution [34].

1.3.2 Interactions

We have seen how it is the electrons within an atom which gives rise to an atomic magnetic moment, but how do these moments interact with one another to potentially produce a magnetically ordered system? We shall explore these interactions, and demonstrate the consequences on the spin-texture using a one dimensional conical Ansatz for the magnetisation[3]:

$$\mathbf{m}(x) = \begin{pmatrix} \cos\theta \\ \sin\theta\cos qx \\ \sin\theta\sin qx \end{pmatrix}, \tag{1.4}$$

[3]This assumption at the magnetisation is used extensively throughout this thesis, so it's good to introduce it here. A real-space representation of this can be found in Chapter 3.

where θ is the conical angle such that when $\theta = 0$, we have a purely ferromagnetic arrangement along the x-direction. For $\theta = \frac{\pi}{2}$, the moments twist round in the yz-plane and are called the helical state. q is the magnitude of the conical wavevector, which lies along x in this 1 dimensional example.

Exchange Interaction

The predominant interaction within magnetic systems is the exchange interaction, and is a quantum mechanical effect. In a two-electron model, with electrons a, b occupying the single electron states $\psi_{a,b}(\mathbf{r}_{a,b})$. The total wavefunction for the system can be written as a product of these two states. One might naively write this as $\Psi_T(\mathbf{r}_a, \mathbf{r}_b) = \psi_a(\mathbf{r}_a)\psi_b(\mathbf{r}_b)$, but quantum mechanics requires these fermions to obey an antisymmetric exchange symmetry: $\Psi_T(\mathbf{r}_a, \mathbf{r}_b) = -\Psi_T(\mathbf{r}_b, \mathbf{r}_a)$. Thus there are two combinations:

$$\Psi_S = \frac{1}{\sqrt{2}}[\psi_a(\mathbf{r_a})\psi_b(\mathbf{r_b}) + \psi_a(\mathbf{r_b})\psi_b(\mathbf{r_a})]\chi_S, \tag{1.5}$$

$$\Psi_T = \frac{1}{\sqrt{2}}[\psi_a(\mathbf{r_a})\psi_b(\mathbf{r_b}) - \psi_a(\mathbf{r_b})\psi_b(\mathbf{r_a})]\chi_T, \tag{1.6}$$

where the spin wavefunction, $\chi_{S,T}$ denote singlet and triplet spin-states respectively, whose symmetry preserves the overall antisymmetric nature of each wavefunction. These two states differ in energy, with the spins preferring to occupy either the triplet or singlet state depending on the nature of the overlap of the single-state wavefunctions. The nature of this overlap determines whether the spins of the electrons prefer to align, or point opposite to one another. This is called a ferromagnetic and antiferromagnetic coupling respectively.

Ultimately, the spins ($\mathbf{S_{a,b}}$) of each electron are coupled via an effective Hamiltonian:

$$\hat{\mathcal{H}} = -2\mathrm{J}\mathbf{S_a} \cdot \mathbf{S_b}, \tag{1.7}$$

where the exchange constant J is obtained via the previously mentioned overlapping of single-electron states. If $J > 0$, the energy of the triplet state is lower, leading to a co-linear arrangement of spins.

The interaction between two electrons on neighbouring magnetic atoms is known as direct exchange, but there also exists other, exchange-like couplings, that are transported via an intermediary. These are called indirect exchange coupling mechanisms, and include super-exchange and double exchange [39, 40]. Accounting for all of these interactions within a system is complex, particularly in systems with complicated unit cells, so it is appropriate to approximate all exchange-like interactions using a symmetry argument. This approximation states that a symmetry-allowed coupling is present in the system, ignores the discrete nature of the lattice, and assumes the moments are *nearly* collinear. The exchange interaction is the leading-symmetry allowed term, as it uses lowest-order, spherical symmetry. The power of this is that it allows us to model the magnetisation as a continuous field, and is called the continuum approximation. Thus, the continuum-form of the exchange interaction energy, E_{exch}, is[4]:

$$E_{exch} = A \int_V (\nabla \cdot \mathbf{m}(\mathbf{r}))^2 \, \mathrm{d}V, \tag{1.8}$$

where A is the continuum form of the exchange coupling. It is important that $A > 0$, thus antiferromagnetism cannot be modelled due to the previously mentioned assumptions. We can see the effects of the exchange interaction on the conical Ansatz by placing Eq. 1.4 into Eq. 1.8. This gives us:

$$E_{exch} = A \int_V (\nabla \cdot \mathbf{m}(\mathbf{r}))^2 \, \mathrm{d}V, \tag{1.9}$$

$$= A \int_V (\frac{\partial \mathbf{m}(\mathbf{r})}{\partial m}) \cdot (\frac{\partial \mathbf{m}(\mathbf{r})}{\partial m}) \, \mathrm{d}V, \tag{1.10}$$

$$= A \int_V q^2 \sin^2\theta [\sin^2 qx + cos^2 qx] \, \mathrm{d}V, \tag{1.11}$$

$$= q^2 AV \sin^2\theta. \tag{1.12}$$

As we can see, the exchange energy can be minimised by setting $q = 0$, corresponding to an infinite-wavelength helical state or by setting $\theta = 0$. Both of these result in a collinear arrangement of spins, as expected. *i.e.* ferromagnetism minimises the exchange free energy.

[4] A derivation can be found here [34]

Dzyaloshinskii-Moriya Interaction

The Dzyaloshinskii-Moriya interaction (DMI) is a higher-order interaction mediated through the spin-orbit coupling, which links an ion within an excited state to another ion in the ground state. The DMI arises in systems with a lack of inversion symmetry, and leads to a canting of the spins within these systems. The energy for both the atomistic form and in the continuum approximation are[5]:

$$\hat{\mathcal{H}}_{DMI} = \mathbf{D} \cdot (\mathbf{S}_a \times \mathbf{S}_b), \tag{1.13}$$

$$E_{DMI} = \int_V D\mathbf{m}(\mathbf{r}) \cdot (\nabla \times \mathbf{m}(\mathbf{r}))\, \mathrm{d}V, \tag{1.14}$$

where $\mathbf{D}$ is the DMI vector, see Chapter 5 for further information. For now, we focus on the continuum form of the DMI which has a constant D, which is typically much weaker than the exchange constant due to being higher order in the spin-orbit coupling. Again, we see the effects of the DMI by inserting the conical Ansatz:

$$E_{DMI} = \int_V D\mathbf{m}(\mathbf{r}) \cdot (\nabla \times \mathbf{m}(\mathbf{r}))\, \mathrm{d}V, \tag{1.15}$$

$$= \int_V D\mathbf{m}(\mathbf{r}) \cdot (-q \sin\theta(0, \cos qx, \sin qx)\, \mathrm{d}V, \tag{1.16}$$

$$= -qD \sin^2\theta. \tag{1.17}$$

Unlike the exchange interaction, the DMI is minimised by maximising q, which is the same as having the tightest helical winding possible. Interestingly, when we account for both the DMI and the exchange interaction, a stand-off between the two interactions occur, with the exchange aiming to minimise q. The total energy of the system, with $V = 1\ \mathrm{m}^3$, is:

$$E_T = q^2 A \sin^2\theta - qD \sin^2\theta. \tag{1.18}$$

Differentiating the energy with respect to q allows us to look for the optimum wavelength:

$$\frac{\partial E_T}{\partial q} = 0 = 2qA \sin^2\theta - D \sin^2\theta = \sin^2\theta(2qA - D), \tag{1.19}$$

[5]Note that the continuum form of the DMI shown here is only valid for crystal symmetries with symmetry class T, O, see here [41] for further forms depending on the crystal symmetry.

where we see that the optimum wavevector is simply a ratio of the DMI and exchange constants: $q = \frac{D}{2A}$. The competition between these two interactions leads to long-wavelength helices, as $D < A$. The periodicity of these spin-textures is not typically an integer of unit-cell spacings, *i.e.* it is incommensurate with the underlying crystal lattice.

Zeeman Interaction

The Zeeman interaction describes the reaction of the magnetisation with an external magnetic field, **H**. This has the continuum-form of:

$$E_{Zee} = -\mu_0 M_S \int_V \mathbf{m}(\mathbf{r}) \cdot \mathbf{H} \, \mathrm{d}V, \tag{1.20}$$

where μ_0 and M_S are the vacuum permeability of free space and the saturation magnetisation respectively. If we apply a magnetic field, H, along the x-direction, we find that increasing the conical angle to be equal to $\frac{\pi}{2}$ minimise the interaction, as the moments before aligned with the magnetic field.

$$E_{Zee} = -\mu_0 M_S \int_V \mathbf{m}(\mathbf{r}) \cdot \mathbf{H} \, \mathrm{d}V, \tag{1.21}$$

$$= -\mu_0 M_S \int_V H \cos\theta \, \mathrm{d}V, \tag{1.22}$$

$$= -\mu_0 M_S V H \cos\theta. \tag{1.23}$$

If we combined all three of these interactions so far, we can derive the field dependence of the conical angle. Using our previous finding that $q = \frac{D}{2A}$, we see the total energy is:

$$E_T = -\frac{D^2}{4A} \sin^2\theta - \mu_0 M_S H \cos\theta. \tag{1.24}$$

Differentiating this with respect to θ is:

$$\frac{\partial E_T}{\partial x} = -\frac{D}{2A} \cos\theta \sin\theta + \mu_0 M_S H \sin\theta, \tag{1.25}$$

which we can solve at the stationary point to find the field dependence of the conical angle:

$$\theta = \arccos(2A\mu_0 M_S H / D^2). \tag{1.26}$$

Finally we see that when we apply a magnetic field along the q-direction of a magnetic helix, in the limit of no anisotropy, the conical state becomes a field polarised state at $H = D/2A\mu_0 M_S$.

Further Interactions

So far, we have seen that the exchange, DMI and Zeeman are the three main interactions that are responsible for transitioning a spin-texture between a helical, conical and ferromagnetic state. However, there are a plethora of other, symmetry-allowed magnetic interactions which also have an influence on the magnetisation. Fortunately, these terms tend to be relativisitic effects that are higher-order in the spin-orbit coupling, meaning that their relative magnitude compared with the exchange is very minor. Here, we introduce two additional terms, which we shall see further in Chapter 3.

Magnetocrystalline Anisotropy (MCA). The spin-orbit interaction and the quenching of orbital angular momentum within crystal systems leads to an energy cost for the moment to align with a particular crystallographic direction. High-energy directions are termed hard axes, whereas low costs are easy axes. The magnetisation would then prefer to lie along the easy-axis, to reduce the energy. In a cubic system, the MCA energy is given by:

$$E_{MCA} = K \int_V m_x^4 + m_y^4 + m_z^4 \, \mathrm{d}V, \tag{1.27}$$

where K is the cubic anisotropy constant, which creates easy $\langle 1\,0\,0 \rangle$ axes and hard $\langle 1\,1\,1 \rangle$ axes if $K < 0$, and vice versa for $K > 0$.

Anisotropic Exchange Interaction (AEI). Similarly to the isotropic exchange interaction, the AEI is minimised by reducing the gradient of the magnetisation. However, here we break the spherical symmetry and enforce cubic symmetry of the system. This has the form:

$$E_{AEI} = \gamma \int_V (\frac{\partial m_x}{\partial x})^2 + (\frac{\partial m_y}{\partial y})^2 + (\frac{\partial m_z}{\partial z})^2 \, \mathrm{d}V. \tag{1.28}$$

In most magnets which host DMI-stabilised helices, these interactions play a minor role in which spin-texture is stabilised. The dominant effect these anisotropic interactions have is controlling the orientation of the zero-field, helical wavevector. This is because the exchange and DMI are both isotropic, so the energy of the helices is identical and only the application of a magnetic field breaks the degeneracy. However, as we shall see later in this Chapter, in the skyrmion-containing material Cu_2OSeO_3, these higher-order interactions become more significant at low temperatures and do lead to novel spin-textures.

RKKY Interaction

For the final interaction, we briefly look at the Ruderman-Kittel-Kasuya-Yosida (RKKY) interaction [42, 43, 44, 45]. In metallic materials, the conduction electrons can act as the mediators which couple the local moments. Due to the non-local nature of the conduction electrons, this interaction is able to couple moments which aren't necessarily adjacent to each other, leading to next-nearest neighbour interactions. The mechanism behind the RKKY interaction lies in the nearby conduction electrons becoming polarised near a local moment, this then screens other conduction electrons, which leads to an oscillatory exchange-like coupling given by [34]:

$$J_{RKKY}(r) \propto \frac{\cos(2k_{\mathrm{F}}r)}{r^3}, \tag{1.29}$$

where r is the separation distance between magnetic ions, and k_{F} is the radius of spherical Fermi surface[6]. Due to the sharpness of the Fermi-surface, the coupling oscillates between ferromagnetic and antiferromagnetic with a wavelength

[6]The approximation that the Fermi-surface is spherical is actually not the best: in materials which feature strong RKKY effects there are large parts of the Fermi-surface that can be mapped onto other regions via a common translation vector. This phenomenon is known as nesting, and leads to spin-density-waves and helices with a wavevector equal to the nesting vector. Nevertheless, the oscillatory nature of the RKKY interaction is the main point of this equation, which this spherical appropriation (which has no common nesting vectors for any part of the surface!) does indeed show.

of $\frac{\pi}{k_F}$. This oscillation has the potential to stabilise magnetic helices within the material.

In the rare-earth metallic magnets, the RKKY interaction is the dominant exchange-mechanism between the large, local 4f moments. The long-range nature of the RKKY interaction causes nearest neighbour and next-nearest neighbour interactions to be significant, with coupling strengths of J_1 and J_2 respectively. For a chain of N magnetic moments in a helical arrangement, that are offset to their nearest neighbours by an angle θ, the total energy is:

$$E = -2N(J_1 \cos\theta + J_1 \cos 2\theta). \tag{1.30}$$

Differentiating this energy leads to:

$$\frac{\partial E}{\partial \theta} = 2N(J_1 \sin\theta + 2J_2 \sin 2\theta = 0, \tag{1.31}$$

$$= (J_1 + 4J_2 \cos\theta)\sin\theta, \tag{1.32}$$

which has solutions for $\theta = 0, \pi$, showing ferromagnetism and antiferromagnetism respectively. However, solving the term in the brackets leads to the optimal angle being: $\theta = \arccos -\frac{J_1}{4J_2}$, which is favoured over the collinear arrangements when $J_2 < 0$ and $|J_1| < 4|J_2|$. This shows us that the RKKY is also a magnetic interaction which can lead to incommensurate magnetic structures, and is in fact responsible for the helical magnetic structures found in Tb, Dy, and Ho [34].

1.3.3 Micromagnetics

At this point, it is worthwhile to briefly mention micromagnetics. We have already used micromagnetic simulations to model a single skyrmion system in Figures 1.3 and 1.4. Specifically, micromagnetics is a tool which aims to predict the sub-micrometer behaviour of magnetic systems. This length-scale is far greater than individual magnetic moments, but within the continuum approximation it is able to resolve the collective behaviour of many magnetic systems, ranging from domain wall motion [46] to skyrmion systems [47].

In this thesis, we use both static and dynamic simulations. In both cases, micromagentics generates a local effective field for each nm-sized cell of magnetisation, $\mathbf{H}_{\mathrm{F}}$, across the whole system. This effective field is defined as [48]:

$$\mathbf{H}_{\mathrm{F}} = -\frac{1}{\mu_0 M_s}\frac{\mathrm{d}^2 E}{\mathrm{d}\mathbf{m}\mathrm{d}V}, \tag{1.33}$$

where $\mathbf{m}$ is the magnetisation of the cell of volume V, and E is the continuum form of energy that is tailored to the specific system by varying the previously mentioned free-energy constants. Once the effective field is calculated, the magnetisation then Larmor-precesses around this effective field, shown in Gilbert form as [48]:

$$\frac{\partial \mathbf{m}}{\partial t} = -|\gamma|\mathbf{m} \times \mathbf{H}_{\mathrm{F}} + \alpha \mathbf{m} \times \frac{\partial \mathbf{m}}{\partial t}, \tag{1.34}$$

where γ and α are the electron gyromagnetic ratio and Gilbert damping respectively. The first term shows that the time dependent behaviour is for the moment to precess about the effective field direction. The second term allows the moment to relax along the effective field direction. For dynamic simulations, these values must be adjusted for each system, whereas for static simulations, we are only interested in the final result of a highly-over-damped simulation, as it allow us to reach to local energy minima as fast as possible.

Thus, micromagnetics is a useful tool to simulate macroscopic magnetic behaviour, and we use it to explain the skyrmion stability in this introduction as well as perform time-dependent simulations in Chapter 5, whose details can be found within.

1.4 Magnetic Skyrmions II

In the previous magnetic skyrmion section, we saw that when only accounting for the dominant exchange interaction[7], the stereographic projection form of a magnetic skyrmion should never be stable due to an infinite energy cost. We

[7] A common approximation for ferromagnets.

can rectify this by accounting for some of the magnetic interactions introduced in the previous section. These magnetic interactions counteract the collapse of the finite-sized skyrmion structure, allowing the skyrmion to be a self-supporting, entity-like object called a soliton.

Solitons were first investigated in the 19th century, when localised and solitary waves would exist within narrow water canals that do not disperse[8]. These canal-solitons were shown to be stabilised by interactions with the shallow canal-floor [49], which included higher-order derivative terms which broke the linearity of the system, supporting the formation of localised states [50].

In magnetic systems, no obvious physical interactions are described by higher-order degrees of spatial derivatives. Thus alternative interactions which admit self-stabilising states are needed in order to generate a skyrmion texture. Pioneering work towards the realisation of magnetic solitons was done in the late 1980s, which found that DMI was a suitable stabilisation mechanism for magnetic skyrmions in chiral magnets [51, 52, 53, 54, 55]. Skyrmions have since been found in a number of systems that host different interactions, which we shall investigate below.

1.4.1 Systems and Materials

Magnetic skyrmions exist within a surprisingly wide range of materials, each of which stabilise its respective skyrmions using different mechanisms. Micron-sized magnetic-bubbles, were first investigated in the 1970s and found that the competition between the in-plane-favouring dipolar interaction and the out-of-plane

[8]Dispersion is a phenomenon that describes the 'spreading out' of waves. Single isolated wave packets are localized in nature, thus a superposition of a large number of harmonic waves are needed to describe the wave packet. Typically, the physical properties such as velocity and dissipation are wavelength dependent, so one would expect the shape of a wave-packet to change with time.

magnetic anisotropy within thin films led to a periodic array of magnetic bubbles [56, 57, 58, 59]. More recently, thin film heterostructures which stack alternating layers of heavy-metal to ferromagnetic layer interfaces have been subject to intense research [60, 61, 62, 63, 64, 65, 66, 67, 68, 69, 70]. The stacking of these layers also breaks inversion symmetry, leading to a so-called interfacial DMI. However, the extent to which this DMI contributes is under debate [71, 72], with the dipolar interaction also playing a significant role. This can be seen by the large variation in skyrmion size as a function of magnetic field [73]. In addition to these interactions, magnetic frustration and four-spin exchange interactions have also been suggested to lead to the formation of magnetic skyrmions [74, 75].

In the rest of this thesis, we depart from the magnetic skyrmions in thin-film systems, and look towards bulk, single-crystalline materials which stabilise skyrmions. At the time of writing this thesis, there are two predominant interactions which lead to the stabilisation of magnetic skyrmions within these systems.

RKKY Skyrmions

We start with the more recently discovered formation mechanism of skyrmions. As we have seen, the long-range nature of the RKKY interaction leads to the formation of magnetic helices in particular magnetic systems. Nanoskyrmions, with size < 3 nm have been found in $Gd_3Ru_4Al_{12}$ [76, 77], Gd_2PdSi_3 [78], $GdRu_2Si_2$ [79], Mn_4Gs_2Sn [80] and $EuAl_4$ [81]. These materials are centrosymmetric so the DMI plays a small role. The exact formation mechanism for the skyrmions within these materials is under debate, and we discuss this more thoroughly in Chapter 5.

Bulk-DMI Skyrmions

Within non-centrosymmetric, chiral bulk magnets, magnetic skyrmions can be stabilised due to a non-vanishing DMI interaction. We show this stabilising effect by performing micromagnetic simulations, which relax the stereographic model

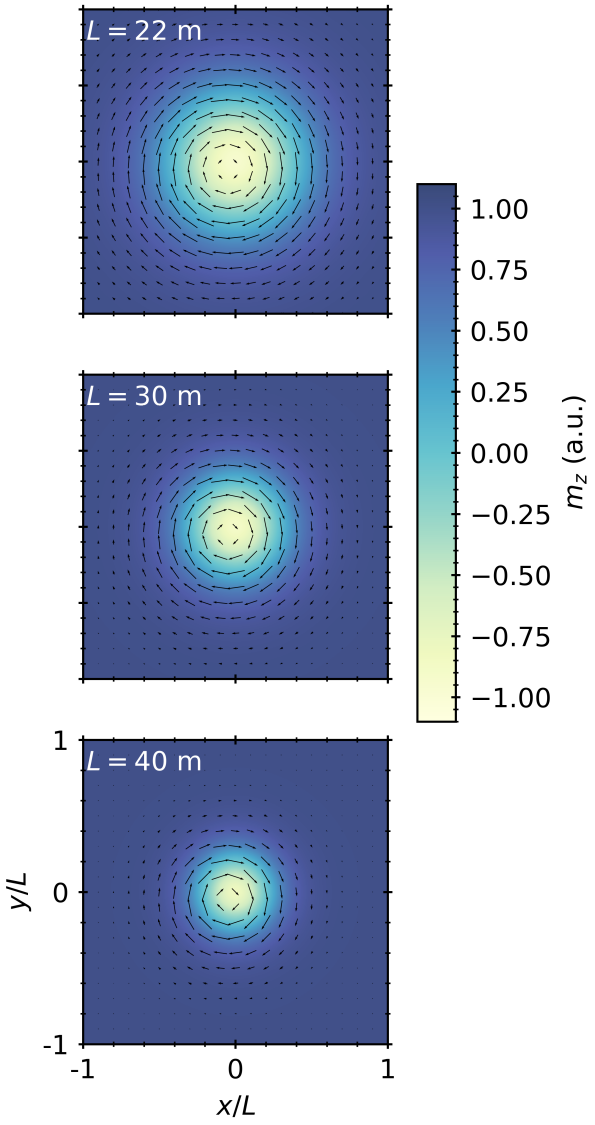

Figure 1.5: Micromagnetic simulations that relax an initial state consisting of the stereographic projection form of a skyrmion, within different system sizes, L. See text for further details.

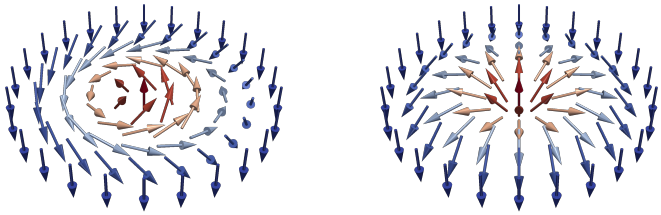

Figure 1.6: Schematic of the spin-texture of a single magnetic skyrmion, with spins point up in the centre and down at the edges. Left and right are Bloch-type and Néel-type skyrmions respectively.

of a skyrmion, shown before in Figure 1.3, with the micromagnetic parameters of $A = 1$ J/m, $D = 0.25$ J/m^2, $H = 10^5$ A/m. As shown in Figure 1.5, we relax the skyrmion within different systems that differ in dimension, but retain the same micromagnetic constants. As shown, the skyrmion is a stable solution and also remains the same size, regardless of the system dimensions. This shows that it is indeed the DMI that provides the skyrmion spin-texture with self-supporting interactions, as the skyrmion remains the same size regardless of the system size, demonstrating its solitonic properties.

As mentioned previously, different crystal symmetries allow different forms of the DMI interaction, leading to different skyrmion states depending on the symmetry of the crystal structure. In these systems, magnetic skyrmions take the form of vortex-like spin structures and we show the two main types in Figure 1.6. These structures are similar to the two dimensional stereographic projections of the $N = 1$ skyrmions with $\chi = 90, 0°$ respectively. The radial profile of these magnetic vortices show a modulation of spin either perpendicular or parallel to the radial direction, leading to nomenclature of Bloch (LHS of Figure 1.6) or Néel-type (RHS) skyrmions respectively in analogy with magnetic domain walls.

Néel-type skyrmions have been found in the $GaV_4S_{8-y}Se_y$ series [82, 83, 84, 85, 86, 87], whose rhombohedrally (C_{3v}) symmetric crystal structure leads to a form of the DMI which favours cycloids whose spins rotate within a plane con-

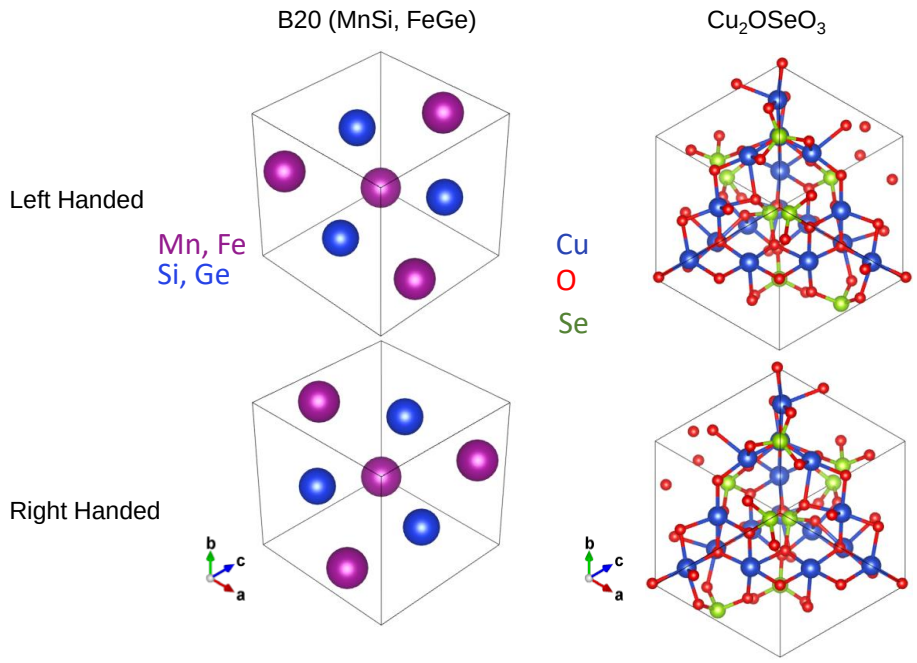

Figure 1.7: LHS: Crystal structure of the B20 helimagnets, such as MnSi and FeGe. RHS: Crystal structure of Cu_2OSeO_3. Both crystals feature a non-centrosymmetric, $P2_13$ structure with two possible chiralities. View is along the [1 1 1] axis for all panels.

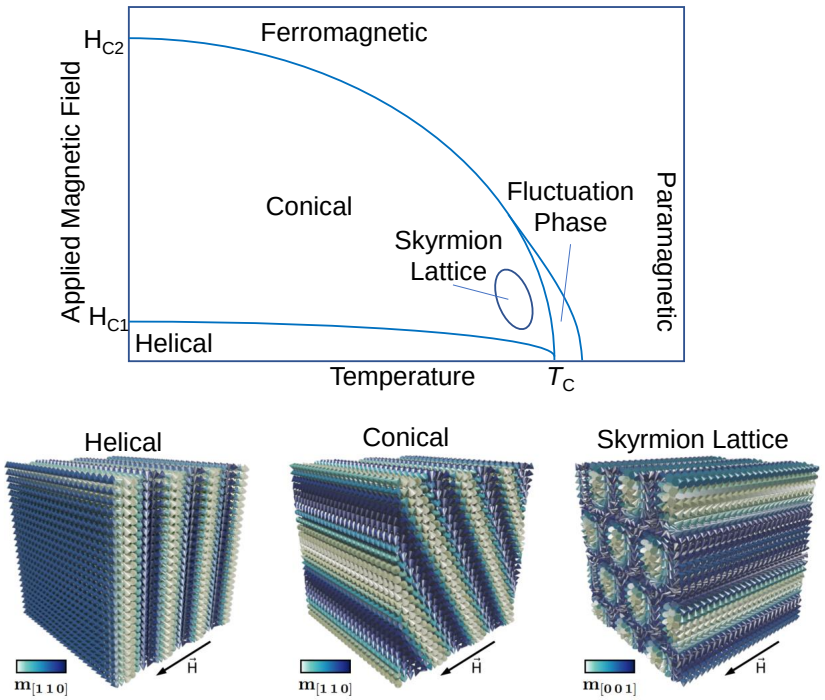

Figure 1.8: Top: Generic phase diagram of the Bloch-type hosting magnetic skyrmion systems. The various forms of the magnetic spin-textures are labelled, and we show a selection of the incommensurate magnetic phases in the bottom row.

taining the magnetic wavevector. On the other hand, Bloch-type skyrmions have been found in the bulk systems; the B20 helimagnets such as MnSi and FeGe, [23, 88]; the $Co_xZn_yMn_z$ series [89]; and the insulator Cu_2OSeO_3[90]. All these materials host a non-centrosymmetric crystalline structure, which we show in Figure 1.7. The lack of inversion symmetry allows for two chiralities of crystal structure, leading to their incommensurate magnetic textures also having different helicities. Furthermore, due to the shared family of magnetic interactions, these materials exhibit a similar magnetic phase diagram. We show this generic magnetic phase diagram in Figure 1.8.

At temperatures a few Kelvin above the Curie temperature, T_C, temperature effects dominate and destroy any magnetic order. As we approach the ordering

temperature, a small region called the fluctuation phase is found. These fluctuations break the typical second-order phase transition between magnetically ordered to disordered state, as they provide a gradual increase to the magnetisation without creating a discontinuity in magnetisation, akin to a Brazovskii-transition [91, 92]. These fluctuations are composed of randomly-oriented chiral helices with a crossover in chirality [93], and a skyrmion-liquid-like fluctuating state [94, 95, 96]. Further decreases in temperature bring the system below T_{C}, at which point degenerate domains of magnetic helices form due to the previously mentioned competition between the DMI and exchange interactions. The helical propagation vector of these domains are determined by the anisotropic interactions, the MCA and AEI. Increasing the magnetic field then breaks the degeneracy of these domains, whose wavevector and constituent moments now cant towards the field direction such that $\mathbf{q}||\mathbf{H}$ and the cone angle $\theta < \frac{\pi}{2}$.

Within a small region of phase space, a previously named anomalous phase occurs [97, 98], which we now know to be constituted of a hexagonal lattice of magnetic skyrmions. Here, the so-called 'skyrmion-pocket' is a highly restricted region close to the ordering temperature. If one minimises a hexagonal-lattice of skyrmions subject to the exchange, DMI and Zeeman energies, we find that the competeting conical phase is always lower in free energy. However, it was shown that we can stabilises a lattice of skyrmions over the conical state by accounting for gaussian thermal fluctuations. Other magnetic interactions, such as cubic anisotropy and longitudinal softness, are also viable skyrmion-stabilising mechanisms [99]. The spin-textures for the helical, conical and skyrmion lattice phase can be seen on the bottom row of Figure 1.8.

In this thesis, we focus on the Bloch-type skyrmion hosting material Cu_2OSeO_3 in Chapters 3,4 and 6; whose complex unit cell gives rise to a number of interesting magnetic interactions which have profound effects on the magnetisation. In Chapter 5, we investigate the newly discovered RKKY-hosting magnetic skyrmion

system, Gd_2PdSi_3. We investigate these materials using diffraction techniques, which we shall explain in the next Chapter. First, we will attempt to justify our research[9], by briefly overviewing the technological applications of magnetic skyrmions.

1.5 Technological Applications

The popularity of magnetic skyrmions was first driven by the potential of using these nano-scale entities within low-energy racetrack memory schemes [100, 101, 102], which are suggested to reduce power consumption as skyrmion motion has been seen with current densities that are 5-6 orders of magnitude lower than driving magnetic domain walls in ferromagnets [103]. We show an example of such a scheme in the top panel of Figure 1.9, which would use the entity-like nature of the magnetic skyrmion to act as the information carriers within the device. For instance, the presence or lack of a skyrmion could be used as a substitute for an electronic bit and represent a 0 or 1. However, the feasibility of using skyrmions for such devices is limited, primarily due to:

- *Size*: Skyrmions are 2 dimensional spin-textures which take up a large footprint of ≈60x60 nm in Cu_2OSeO_3. This is much larger than the atomic-sized memory schemes under active development [104], which consists of just twelve iron atoms. However, the recent discovery of nanoskyrmions in the RKKY systems may provide incentives for further material screening to look towards a more competitive device size.

- *Skyrmion Hall angle*: When driven by an electric current, magnetic skyrmions exhibit a deflection away from the current direction in a manner commonly called the skyrmion Hall effect [105, 106, 107]. This effect arises due to inconsolable damping effects on a material specific basis, such as magnetic damping and anisotropies [108]. However, synthetic antiferromagnets show

[9]The novel and interesting physics alone tends not to persuade scientific funding committees!

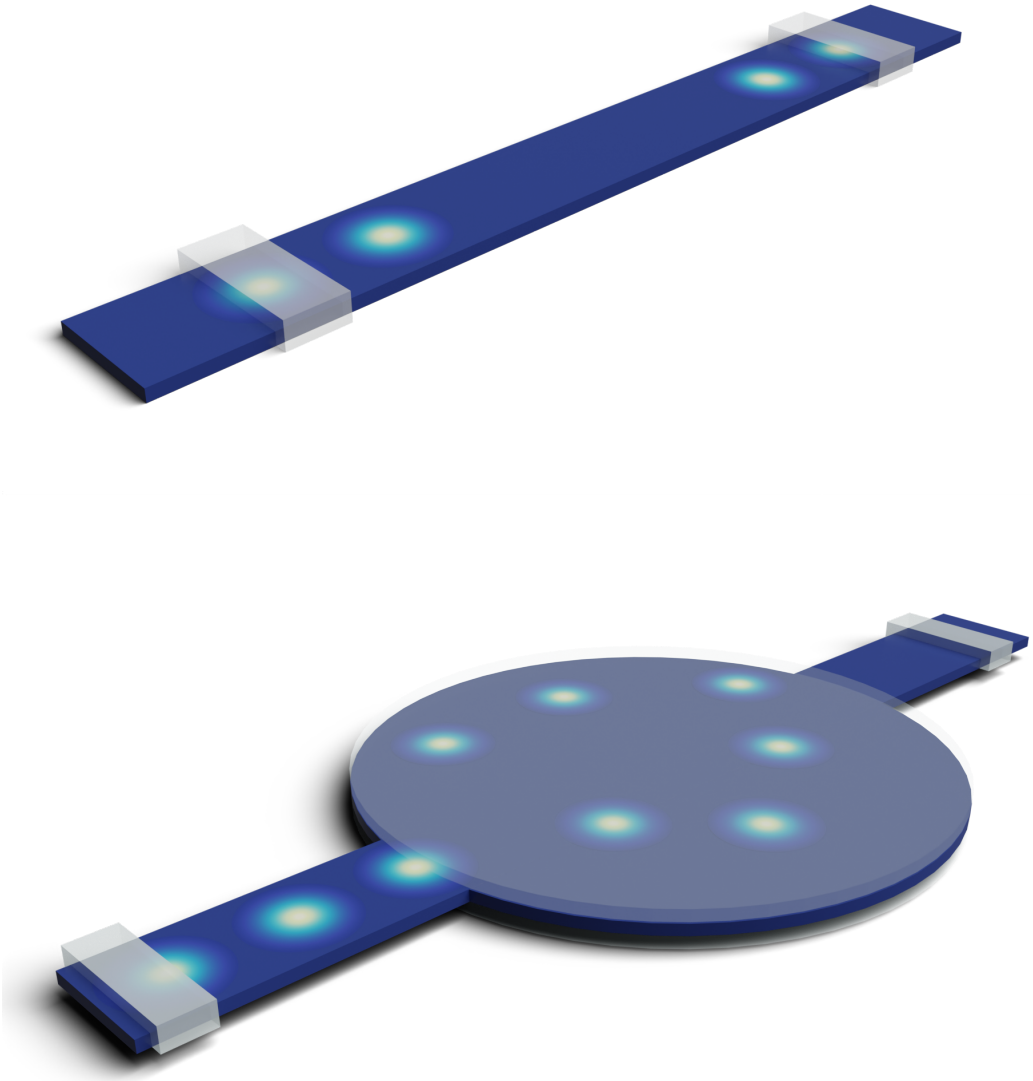

Figure 1.9: Top: Racetrack memory schematic consisting of a magnetic track (blue is field-polarised up, out of plane), with read/write heads (gray boxes), and skyrmions (white is magnetisation into the plane). Below: An advanced skyrmion device featuring a reservoir for magnetic skyrmions to occupy. This scheme would be more suitable for advanced applications such as neuromorphic and stochastic computing, see text for further details.

a promising avenue due to the cancelling Magnus-forces between the two-coupled skyrmions [109, 110].

- *Detection*: The reliable reading and writing of skyrmions is a non-trivial matter. Progress has been made with nucleating skyrmions using an electrical current [111], and detection using electrical resistance and Hall detection [112, 113]

- *Stability*: While zero-field skyrmions have been shown to be stable in some systems [114, 115, 116], typically skyrmions require a non-zero magnetic field. This means any device not using zero-field skyrmions would have to remain connected to a power supply, else all the data would be erased.

- *Pinning*: Pinning effects within multilayer samples have the tendency to massively increase the required current density to become similar to domain wall motion [117], as well as lead to non-linear behaviour [118, 119].

However, the possibility of a catastrophic future-funding-failure can be avoided by looking towards future, next generational spintronic devices. An example of such a device is shown in the bottom of Figure 1.9, which differs from the 1 dimension race track by featuring a large region where skyrmions could accumulate. This 'reservoir' of skyrmions has a number of interesting effects which could be exploited to provide technological benefits. One such is stochastic computing, which utilizes a continuous stream of random values. Complex computations such as image processing can then be efficiently performed by simple, bit-wise operations on these random streams [120, 121]. A reservoir of skyrmions undergoing Brownian motion due to thermal effects has the potential to expel a random stream of skyrmions, or more functionally the random fluctuations in the resistance across the reservoir [122, 123, 124]

Another application is neuromorphic/reservoir computing schemes. These schemes map an input signal into a 'black box', which can be trained to read the input state and map it to the desired output. This requires systems which are

highly complex and non-linear, such as skyrmions [125, 126, 127]. Recently, pattern recognition has been demonstrated, with accuracies akin to the ideal system [128].

Finally, lattices of magnetic skyrmions show collective modes of excitations that lie within the MHz regime [129, 130, 131, 132, 133, 134]. One could potentially use these modes as a microwave signal detector, which are currently difficult to capture using magnetic media due to the typical frequency of a single moment being above the GHz regime.

1.6 Summary

To summarise, we have introduced the concept of magnetic skyrmions starting off from the original three dimensional skyrmion. We have show that whilst magnetic skyrmions are indeed topologically protected, it is the specific magnetic interactions within a material which allow the skyrmion to interact with itself, in a self-stabilising manner. We have briefly reviewed magnetic interactions, and shown the various types of magnetic skyrmion system which these interactions are present in. Since it is clear that the magnetic interactions are essential for skyrmion formation, looking for alternative interactions of skyrmion stability and manipulation would be highly useful in optimising some of the technological applications of magnetic skyrmions, shown in the final section.

Chapter 2

Techniques for Investigating Skyrmions

In this Chapter, we will review the different techniques that have been used in this thesis to study magnetic skyrmions. In the following results Chapters, we will use the experimental techniques of small-angle neutron scattering (SANS)[1] and resonant elastic x-ray scattering (REXS). Both techniques are reciprocal space techniques. They utilise the wave-like nature of incoming particles, and their interactions with matter, to determine properties of the system. This is done by measuring the locations, intensities and widths of the diffracted particles. REXS and SANS are both highly sensitive to magnetic structures, allowing us to accurately probe the complex spin-texture of our samples. We are able to perform these techniques under extreme conditions, such as liquid-helium-cooled low temperatures and high (10 T) magnetic fields, which is currently impossible in many imaging techniques. Furthermore, diffraction gives information about the entire macroscopic magnetic system rather than focussing on the microscopic

[1]SANS was the first technique to observe the characteristic hexagonal diffraction pattern, and identify the origin of such a pattern to be magnetic skyrmions in 2009 [23]. In 2007 [135], and even earlier 1992 [136], SANS studies also saw diffraction, from what we now know to be a skyrmion lattice, but the geometry of the experiment prevented the hexagonal pattern from being fully resolved.

irregularities, allowing us to use mean-field theory to describe our observations.

2.1 Scattering Theory

In this section, we will develop the theory of scattering, starting from a single object and working our way to an entire system. A recommended book for a more thorough explanation is the course book from the Oxford School on Neutron Scattering: *Elementary Scattering Theory* [137].

2.1.1 Scattering from a single object

In an ideal scattering experiment, an incoming particle (such as an x-ray, neutron, electron) with momentum $\hbar\mathbf{k}_i$ is scattered into a new state with final wavevector $\mathbf{k}_F$. Here, we assume the particle loses no energy as it undergoes elastic scattering. This scattering event causes the particle to undergo a momentum transfer, $\mathbf{q}$, which is characterised by:

$$\mathbf{q} = \mathbf{k}_i - \mathbf{k}_f. \tag{2.1}$$

The magnitude of the wavevector, $|\mathbf{k}|$ remains the same in order to conserve energy. The simplest way to model an incoming stream of particles is to describe them mathematically as a complex plane wave:

$$\psi_i = \psi_0 \exp i\mathbf{k}_i \cdot \mathbf{r}, \tag{2.2}$$

where ψ_0 is related to the incident flux, $\Phi_0 = |\psi_0|^2$, i is the elementary imaginary number and $\mathbf{r}$ is the position vector. The real part of this plane wave can be seen in Figure 2.1 a, with positive and negative values on a logarithmic scale. After interacting with an object, the probing particles will radiate outward in a radial manner, described by:

$$\psi_f = \psi_0 \mathrm{f}(k,\theta)\frac{\exp ikr}{r}, \tag{2.3}$$

whose inverse-square law dependence preserves the conservation of energy in two dimensions. The function $\mathrm{f}(k,\theta)$ is system dependent, and contains information about the probability of the incoming particle being scattered in a particular

direction. The scattered wave for the simple $f(k,\theta) = 1$ case is shown in (b). Neutrons and x-rays have a more complicated scattering behaviour, and this behaviour also varies depending on what from these particles are scattering. A selection of $f(k,\theta)$ as a function of $Q = 2k\sin\theta$, where θ is the scattering angle, are shown in (c). For neutrons interacting with a nucleus via the strong nuclear force (blue line), a straightforward relationship $f(k,\theta) = -b$ is found where b is called the scattering length, and is invariant with respect to the wavevector and scattering angle. This scattering length exhibits an erratic variation across different isotopes and elements [138], and the invariant nature stems from the fact that nuclei are orders of magnitude smaller than the wavelength of thermal neutrons [139]. As we shall see, scattering theory is related to Fourier transforms, which map real space into frequency space. Highly localised objects in real space are composed of a great number of different frequencies. Thus, nuclei are well-approximated as Dirac delta functions, whose Fourier transform leads to a continuum of frequencies and hence $f(k,\theta)$ takes a constant value.

This is more complicated again when looking at neutrons scattering from magnetic atoms (green), as well as x-rays from the electron cloud surrounding a nuclei (orange), in Figure 2.1 c. Since both of these particles interact with a spatially extended ensemble of object, their respective Fourier transforms also show a spatial extent, with the frequencies of greater wavelength being less significant than those with a smaller wavelength. Interestingly, the magnetic interaction with a neutron 'falls-off' faster than x-rays interacting with electrons. This comes from the fact that magnetism arises from unfilled electronic shells, which typically occur at a greater distance from the nucleus as we saw in the previous Chapter. On the other hand, x-rays are able to interact with inner-shell electrons, whose more-localised real-space nature has a greater extent in Fourier space. These trends are called form-factors, and have been constructed from a summation of Gaussian functions using the experimentally derived constants for an iron atom [140].

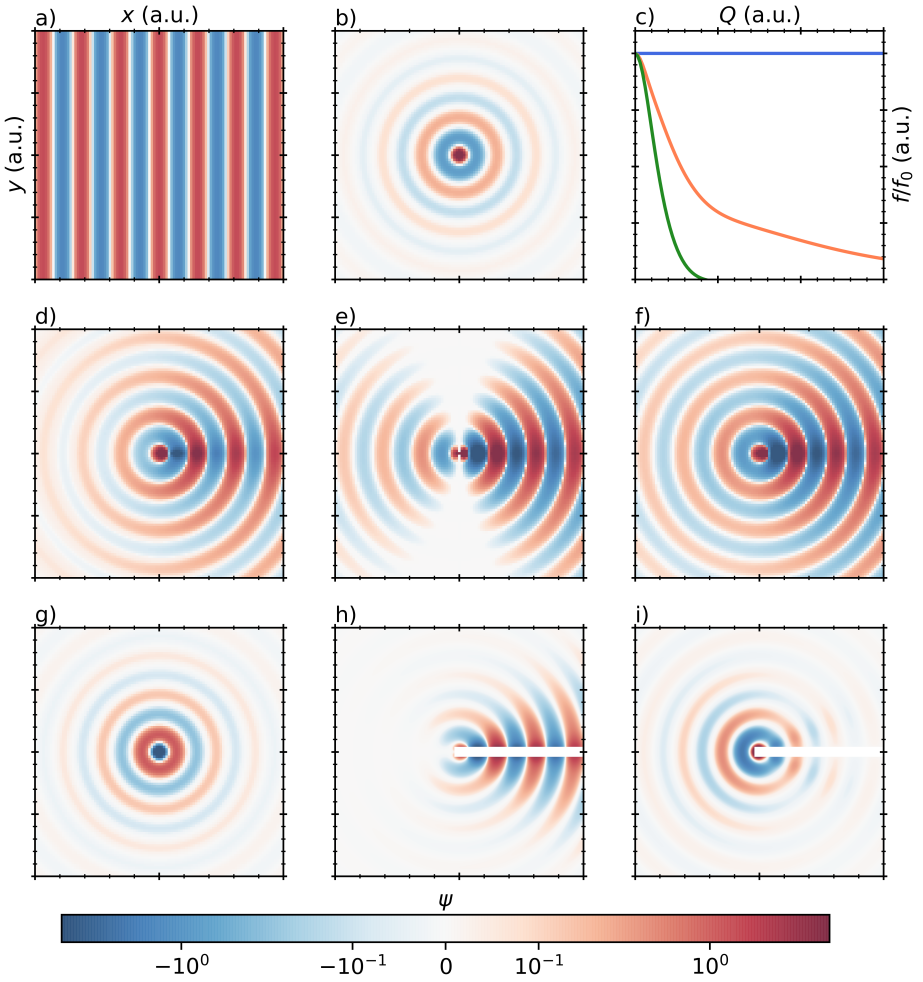

Figure 2.1: Scattering from a single object. a) An incoming plane wave, b) A spherically symmetric radial wave, c) Example form factors for a neutron interacting with a nucleus (blue), with magnetic (green), and an x-ray with charge (orange). d, e, f) Scattered wave of an x-ray from a single atom with polarisation lying out of the page, in the page, and unpolarised respectively. g,h,i) Scattered wave of a neutron from a single atom, and a single moment pointing along the x and y-directions respectively. White line in (g) and (i) are undefined regions due to the division of zero.

The form factors for x-rays, again get even more complicated when accounting for the polarisation of the incoming x-ray. X-rays interact with electrons in a dipole-like manner, meaning that x-rays with their respective electric field are polarised within the scattering plane (in Figure 2.1 this corresponds to the plane of the page) behave differently to those polarised out of the plane. We show this difference in Figure 2.1 d and e, with the unpolarised case shown in (f). A neutron interacting with an atom whose scattering length is positive, $b > 0$, is shown in (g). As shown, the phase reverses when compared to the trivial case in (b), yet both display a lack on angular dependence. The interaction of neutrons with magnetism arises due to a quantum mechanical coupling between the intrinsic spin of a neutron, and the unpaired electrons within the sample. The derivation is highly involved [141], so we skip to the result that neutrons only interact with the component of the moment that lies perpendicular to the scattering vector:

$$\mathbf{M} \perp = \mathbf{M} - (\mathbf{M} \cdot \hat{\mathbf{q}})\hat{\mathbf{q}}. \tag{2.4}$$

The implications of such behaviour, as well as the angular-dependent fall-off, can be seen in Figure 2.1 h and i. These panels show the real part of the scattered wave after interacting with a magnetic atom whose magnetisation lies along the positive x and y directions respectively. Again, further complications arise when accounting for the polarisation of the neutron and spin-flip interactions. Fortunately, the SANS experiments we show in this thesis were performed using unpolarised neutrons – so we'll ignore this complication and turn our attention to what happens when we have an ensemble of scattering objects.

2.1.2 Scattering from an ensemble

We now extend our model from a single scattering site which was located at the origin, to an ensemble of j-objects each with a given location, $\mathbf{R}_j$. Each object makes a small contribution to the scattered wave, $[\delta\phi_f]_j$, given by:

$$[\delta\phi_f]_j = \psi_0 \exp\left(i\mathbf{k}_i \cdot \mathbf{r}\right) \mathrm{f}_j(k,\theta) \frac{\exp\left(i\mathbf{k}_f \cdot (\mathbf{r} - \mathbf{R}_j)\right)}{|\mathbf{r} - \mathbf{R}_j|}, \tag{2.5}$$

where we have now let each object also have an independent form factor, $\mathrm{f}_j(k,\theta)$. Summing over all atoms and using the definition of the scattering vector in Eq. 2.1, we have:

$$\psi_f = \psi_0 \exp\left(i\mathbf{k}_f \cdot \mathbf{r}\right) \sum_{j=1}^{N} \mathrm{f}_j(k,\theta) \frac{\exp i\mathbf{q}\cdot\mathbf{r}}{|\mathbf{r}-\mathbf{R}_j|}. \tag{2.6}$$

The assumption that each scattering element only contributes an infinitesimal change to the scattered wavevector is valid provided we are within the kinematical limit [142]. Also known as the Born approximation, this requires that the scattering power is weak enough such that the particle only interacts once with the entire sample. Events such as multiple scattering, where the neutron interacts twice with the sample, leading to extra peaks within the diffraction pattern, are therefore not accounted for. The intensity of the scattered wave is its modulus, $|\psi|$, which in the far-field limit, $|\mathbf{r}-\mathbf{R}_j| \approx r$, is:

$$|\psi_f|^2 = I = \frac{\Phi}{r^2} |\sum_{j=1}^{N} \mathrm{f}(k,\theta) \exp i\mathbf{q}\cdot\mathbf{r}|^2. \tag{2.7}$$

This equation contains all the information to start investigating an example.

2.1.3 Example: The skyrmion

As shown in the previous Chapter, a hexagonal lattice of skyrmions is found within a number of non-centrosymmetric systems, just below the ordering temperature. This spin-texture is a multilateral composition of unpaired electrons which give rise to an atomic magnetic moment; a whirl-pool like form of these magnetic moments which constitute a single skyrmion; and a hexagonal lattice which the skyrmions occupy. These three ingredients are shown in Figure 2.2 a to c respectively. Their concomitant Fourier transforms are shown below in panels (d) to (f). As previously explained, objects which are highly localised in real-space, such as the electrons on an atom, give a very broad frequency-space signature. Skyrmions are also localised, albeit on a much larger scale, hence the form-factor fall-off is far greater. Note, the circular symmetry of both the skyrmion and the atom is preserved within the Fourier transform. A lattice

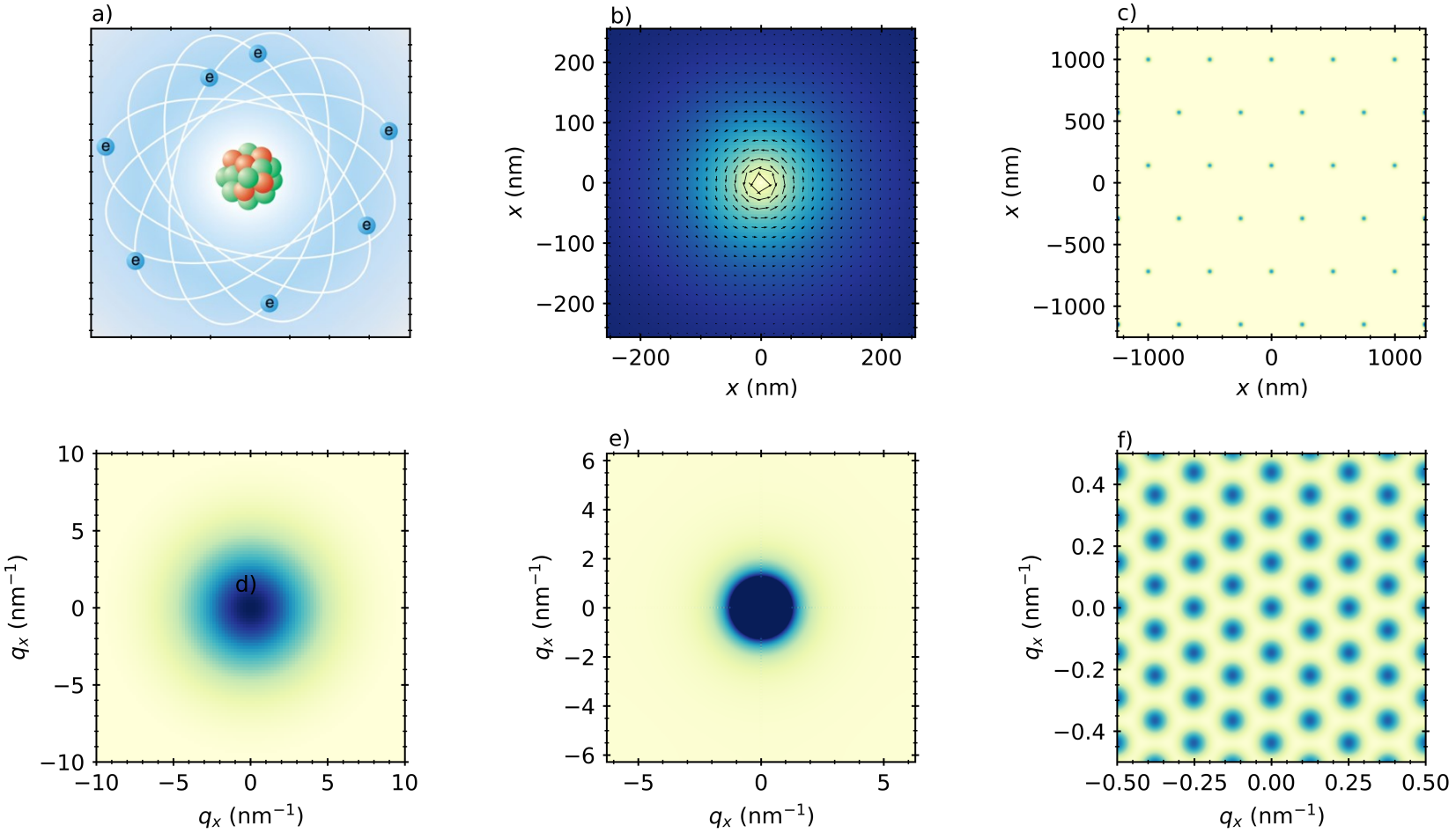

Figure 2.2: a) Diagram of an atom showing lone pairs of electrons which constitute an atomic moment, taken from [143] with permission. b) Real-space image of a magnetic skyrmion, composed of magnetic moments. Lighter colour denotes a moment into the page direction, arbitrary units. c) Hexagonal lattice of Dirac delta functions. d-f) Fourier transform of the above real-space images, note the difference in axis units.

is composed of a repeating array of Dirac-delta functions, and is shown in (c). The Fourier transform of a real-space hexagonal lattice of separation d is again a hexagonal lattice in Fourier space[2]. The spacing of this reciprocal lattice is $4\pi/\sqrt{3}d$, and also undergoes a $\pi/2$ rotation. This rescaling and rotation comes from the fact that the planes which constitute a hexagonal lattice along a principle real-space direction are π-out of phase from each other, thus resulting in destructive interference.

The reason why we have separated the hexagonal lattice of magnetic skyrmions into its constituent parts comes from Eq. 2.7. This equation is multiplication of the Fourier transforms of these three individual components, with the exponent representing the lattice, and $\mathrm{f}(k, \theta)$ representing the form factor of the unpaired electrons which constitute an entire skyrmion. The process of multiplying these three Fourier transforms is identical to a convolution in real-space. That is, for every lattice point in (c), we place a skyrmion, and for every moment of a skyrmion, we place the unpaired electrons. This operation is quite complex, hence why a simple multiplication in reciprocal space is more commonly used. The Fourier transform of such a convolution, is identical to the product of the three component Fourier transforms, which we show in Figure 2.3 a. As can be seen, we again see a hexagonal lattice in reciprocal space. However, the magnitude of the spots rapidly decays with increasing momentum transfer. This is due to the size of the skyrmion, and not the form factor of an individual atomic moment, whose value is approximately uniform across this 'small' region of reciprocal space.

The inverse Fourier transform of the M_z component is shown in (b). Here, we recover a hexagonal lattice of skyrmions. Artifacts remain due to discretisation issues and computational nuances. A skyrmion lattice is typically approximated

[2]Interestingly, the Fourier transform of a hexagonal lattice has an infinite extent in reciprocal space, as the form factor of an individual delta function is infinite, like an atomic scattering length

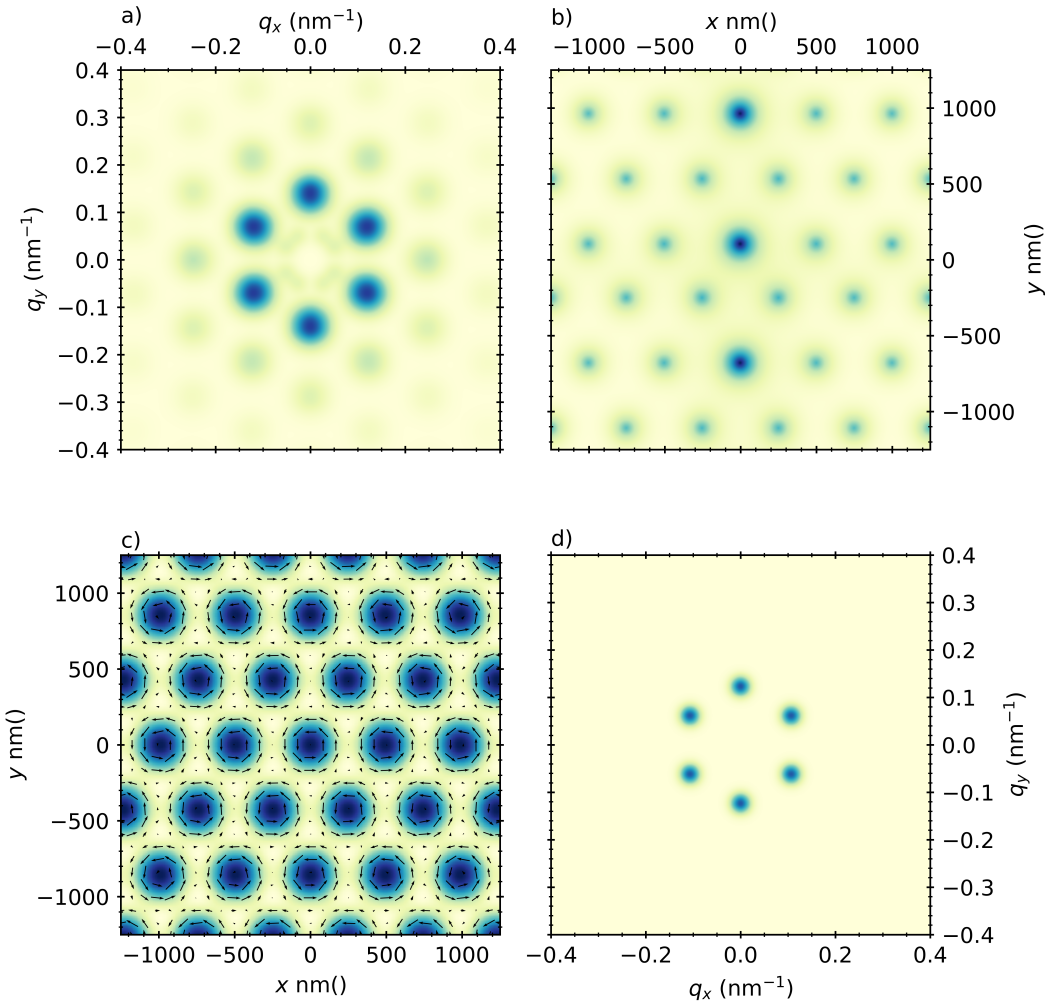

Figure 2.3: a) The product of the three Fourier transforms of the three real-space images shown in Figure 2.2. The finite extent of the Fourier transform of a single skyrmion causes frequencies of shorter wavelength to decay. b) Inverse Fourier transform of (a), showing the M_z component only, with white and blue denoting out-of and into the page respectively. Central skyrmions appear brighter, and sit on a non-ideal lattice due to artefacts within computational Fourier transforms and the irrational nature of a hexagonal lattice fitting on a square grid. c) Real-space, triple-q model of the skyrmions, and its Fourier transform (d).

in the so-called triple-q model. Here, a lattice of skyrmions is created by the superposition of three helical textures that are oriented 60 degrees from one another. This has the mathematical form of [144]:

$$\mathbf{m}(\mathbf{r}) = \sum_{i=1}^{3} \mathbf{m}_{Q_i}(\mathbf{r}), \tag{2.8}$$

where $\mathbf{m}_{Q_i}(\mathbf{r})$ is a helical magnetisation texture, see previous Chapter for a example Ansatz. The triple-q model makes a perfect lattice of skyrmion, and we show this in Figure 2.3 c, along with its Fourier transform in (d). Distinguishing between three, spatially separate domains of helices versus a multi-q model is difficult in diffraction based techniques, and requires the higher-order diffraction peaks to be visible, particularly those not along a helical direction. In most skyrmion materials, the first order peaks dominate, and thus the triple-q model is a good approximate for the equilibrium skyrmion lattice. Finally, we show a selection of other multi-q spin textures in Figure 2.4 to 2.7, which shows that very complex magnetisation textures can be created from a simple superposition of single-q states. It is particularly worth mentioning Figure 2.4 b, which displayed a square lattice of merons and anti-merons. Whilst these objects are vortex-like structures, their wrapping of spins only gives them a winding number of $N = \pm\frac{1}{2}$. We mention this here due to the possibility of a meron-antimeron lattice being present in Gd_2PdSi_3, the material studied in Chapter 5.

Within a diffraction experiment, one probes the absolute value of this Fourier transform of the scattering system. Despite losing the phase information, the measured intensities still contain a wealth of information including the form of the magnetisation, the quality of its ordering, as well as the lattice structure. We will now briefly look at the benefits and limits of using x-rays and neutrons within real experiments.

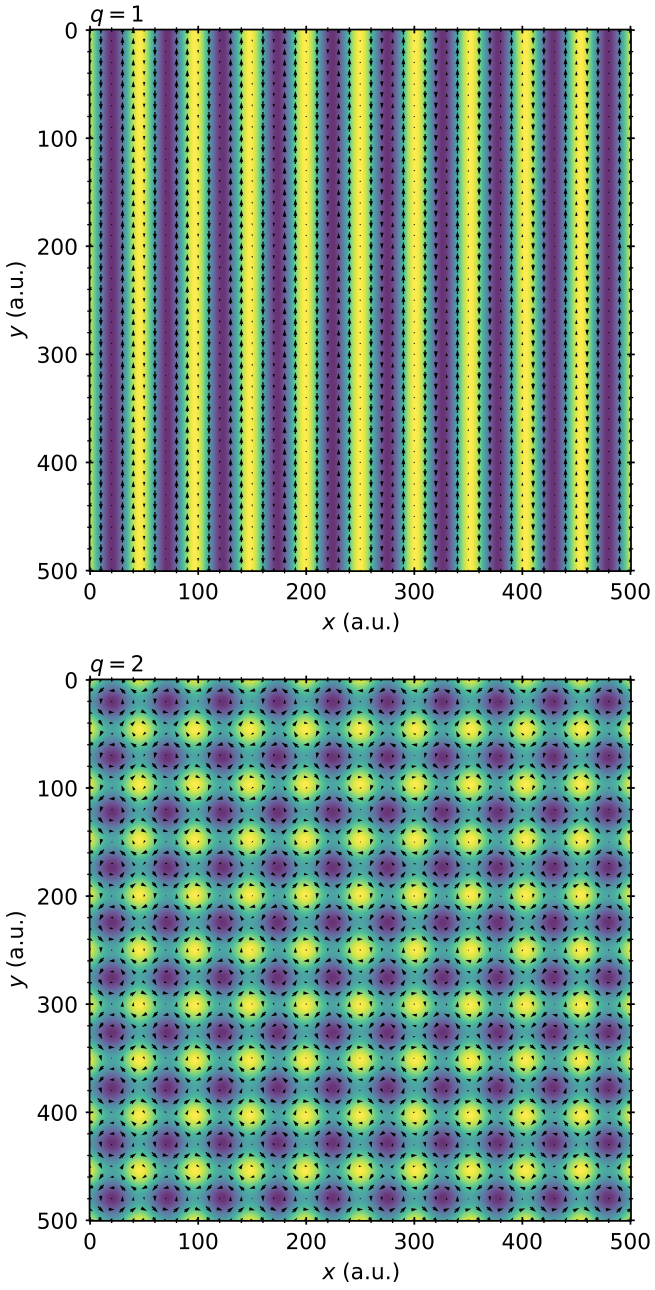

Figure 2.4: Real-space spin-texture of a multi-q state. Top: $q = 1$. Bottom: $q = 2$

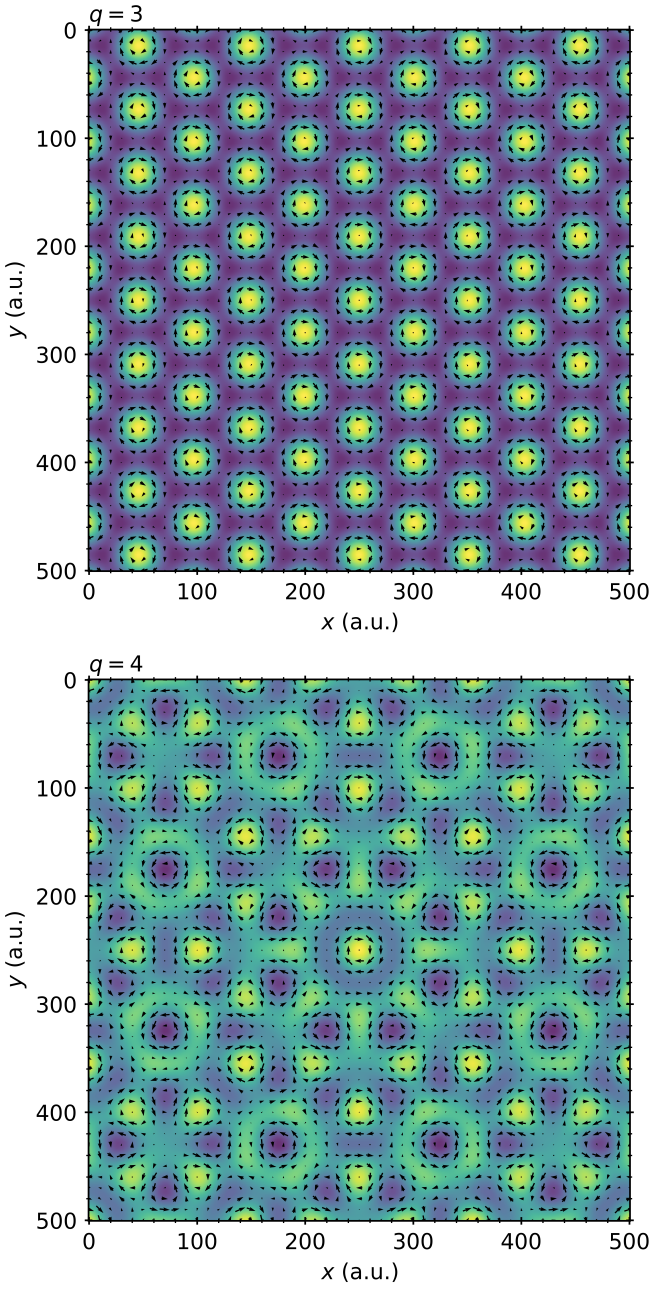

Figure 2.5: Real-space spin-texture of a multi-q state. Top: $q = 3$. Bottom: $q = 4$

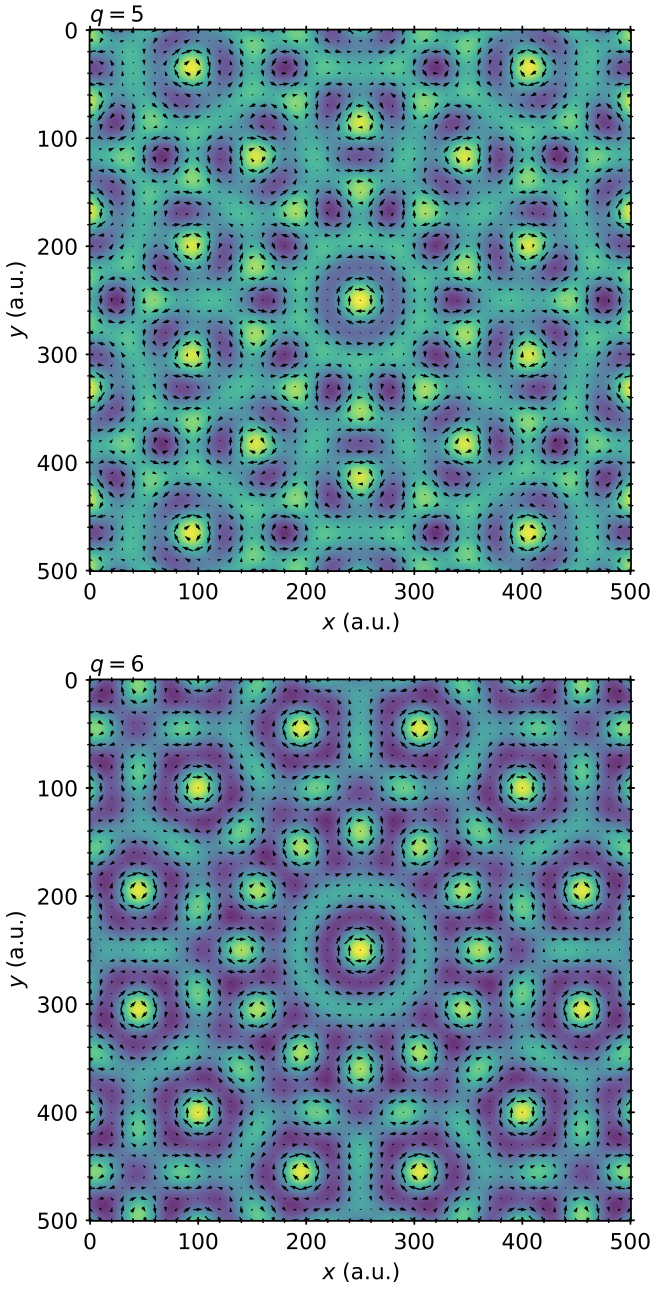

Figure 2.6: Real-space spin-texture of a multi-q state. Top: $q = 5$. Bottom: $q = 6$

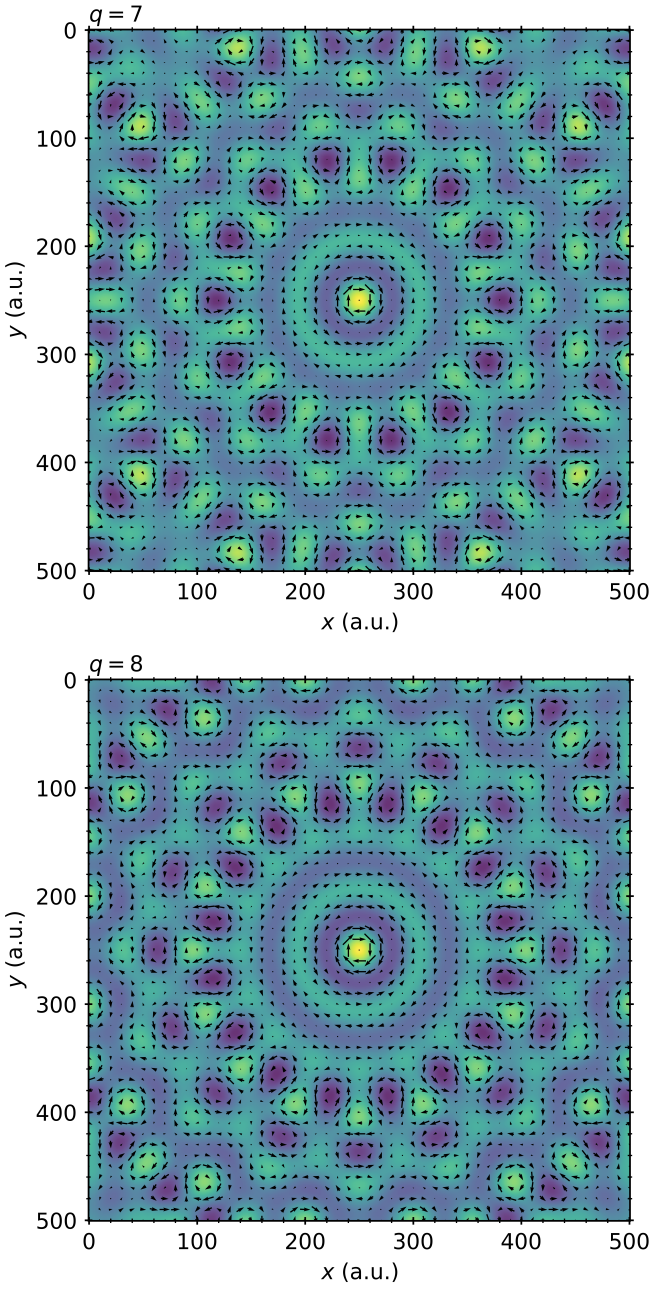

Figure 2.7: Real-space spin-texture of a multi-q state. Top: $q = 7$. Bottom: $q = 8$

2.1.4 X-rays V Neutrons

The first magnetic neutron diffraction experiments were carried out by Shull *et al.*, in 1951, which observed extra superlattice peaks arising from an antiferromagnetic structure upon cooling below the Néel temperature [145]. The intrinsic magnetic moment of the neutron thus provides a direct probe of the magnetisation within the sample, predicted theoretically in 1940 [146]. Neutrons are advantageous due to their highly penetrating nature, which allows the magnetism from the entire crystal structure to be simultaneously investigated.

The first magnetic x-ray diffraction experiment was performed by Bergevin and Brunel in 1972, who used a lab x-ray source to measure an antiferromagnetic superlattice peak in NiO [147]. The weak interaction of x-rays with magnetism compared with charge, coupled with the fact that magnetism only arises from the electrons which are unpaired, meant that count times of a few days per data point were required. Later, highly brilliant and polarised x-ray sources were developed in the form of synchrotron radiation facilities [148]. Later, Hannon et al [149] found that magnetic scattering was massively enhanced at atomic resonances, leading to the term *resonant* elastic x-ray scattering.

The two probes for investigating magnetism are complementary to one-another. For instance:

- X-rays are surface sensitive; neutrons are bulk sensitive.
- X-rays are element specific; whereas neutrons probe the entire sample. This comes with a caveat that one has to measure samples with a resonance in a particular energy range of x-rays. Typically, these fall in the soft x-ray regime, which comes with other challenges such as the absorption by air [150].
- Some elements, such as Cd and Gd, have very large neutron absorption scattering lengths, forcing us to use x-rays to probe the magnetism.

- X-rays cause a significant amount of beam heating, limiting the minimum temperature accessible in an experiment.

In this thesis, we use neutron scattering to look at the entire magnetisation within samples of Cu_2OSeO_3 in Chapters 3, 4 and 6. In Chapter 5, we use resonant elastic x-ray scattering (REXS) to look at the nanoskyrmion material Gd_2PdSi_3, due to the highly neutron-absorbing nature of gadolinium. In that Chapter, we perform a full-linear polarisation analysis (FLPA). Here, we develop a clear overview of the technique below.

2.2 Full-Linear Polarisation Analysis

The specific experimental details the FLPA technique explanation is found in Chapter 5, but here we briefly overview the method and again do another example for a system which only features charge scattering. FLPA is a technique which provides a more insightful probe of a system compared with looking at raw intensities alone. At a high-level, FLPA is a process by which the incoming linear polarisation of an x-ray beam is rotated before interacting with the sample. For each particular incoming polarisation angle, the polarisation of the scattered x-ray is determined. Once the outgoing polarisation is measured for all incoming polarisation angles, a model can be used to determine, and quantify, the nature of the scattering within the material.

In order to start to understand the theory, we must first be able to describe the polarisation of an x-ray. Typically, a linearly polarised x-ray is described in terms of a Jones vector, $\mathbf{V}$, such that the electric-field of the x-ray is described as [151]:

$$\mathbf{E}(t, \mathbf{r}) = \mathcal{R}[\mathbf{V} \exp(-i(\mathbf{k} \cdot \mathbf{r}))], \tag{2.9}$$

where $\mathbf{V} = \binom{V1}{V2}\binom{\hat{\mathbf{e}}_1}{\hat{\mathbf{e}}_2}$, $\hat{\mathbf{e}}_n$ are three orthogonal basis vectors with the wavevector $\mathbf{k}||\hat{\mathbf{e}}_3$. This description of polarised light can be developed further, by taking into account circular polarisation and incoherence. This is done by the Poincaré-Stokes parameters. These three parameters totally describe the polarisation of

an x-ray beam. They are defined as [151]:

$$P_1 = \frac{|V_1|^2 - |V_2|^2}{|V_1|^2 + |V_2|^2}, \tag{2.10}$$

$$P_2 = \frac{|V_1 + V_2|^2 - |V_1 - V_2|^2}{2(|V_1|^2 + |V_2|^2)}, \tag{2.11}$$

$$P_3 = \frac{|V_1 - iV_2|^2 - |V_1 + iV_2|^2}{2(|V_1|^2 + |V_2|^2)}. \tag{2.12}$$

These parameters are then used to describe an ensemble of waves that may somewhat be depolarised by using a coherency matrix [152]:

$$\rho = \frac{I}{2}(\mathbf{1} + \sigma \cdot \mathbf{P}), \tag{2.13}$$

where σ are the three Pauli matrices, $\mathbf{1}$ is the identity matrix, and the intensity is given by the magnitude of the Stokes vector: $I = \sqrt{P_1^2 + P_2^2 + P_3^3}$.

Now we are at a position where we are able to completely describe the polarisation state of an x-ray. We now wish to look at how a scattering element within the sample, say the magnetisation or even charge, can change the state of the incoming polarisation. This is done using a Jones matrix, $\mathbf{M}$, defined as [153]:

$$\mathbf{M} = \begin{pmatrix} < \hat{\mathbf{e}}'_\sigma | M | \hat{\mathbf{e}}_\sigma > & < \hat{\mathbf{e}}'_\sigma | M | \hat{\mathbf{e}}_\pi > \\ < \hat{\mathbf{e}}'_\sigma | M | \hat{\mathbf{e}}_\pi > & < \hat{\mathbf{e}}'_\pi | M | \hat{\mathbf{e}}_\pi > \end{pmatrix}, \tag{2.14}$$

where $\hat{\mathbf{e}}_\pi$ and $\hat{\mathbf{e}}'_\sigma$ denote incoming and outgoing x-rays, polarised within the π and σ-planes respectively. See Figure C.2 for a definitions. M is therefore the matrix operation which scatters one type of polarisation into another. The polarisation of the scattered beam can therefore be determined by:

$$\rho' = \mathbf{M} \cdot \rho \cdot \mathbf{M}^\dagger. \tag{2.15}$$

Thus, if we know the matrix operations for different scattering sources, we are able to determine the outgoing polarisation. Table 2.1, shows three common scattering sources. We show a selection of different scattering matrices in Table. 2.1.

Source	**M**
Charge	$F_0 \begin{pmatrix} 1 & 0 \\ 0 & \cos 2\theta \end{pmatrix}$
Dipole	$-iF_1 \begin{pmatrix} 0 & z_1 \cos\theta + z_3 \sin\theta \\ z_3 \sin\theta - z_1 \sin\theta & -z_2 \cos 2\theta \end{pmatrix}$
Interference	$F_2 \begin{pmatrix} z_2^2 & -z_2(z_1 \sin\theta - z_3 \cos\theta) \\ z_2(z_1 \sin\theta + z_3 \cos\theta) & -\cos^2\theta(z_1^2 \tan^2\theta + z_3^2) \end{pmatrix}$

Table 2.1: Matrix scattering elements for different types of scattering source. z_n are three orthogonal directions of magnetisation, see Figure 2.8, for definitions. Values taken from [154]

By inserting the relevant scattering element into Eq. 2.15, we are able to simulate the polarisation of the scattered x-ray. The methodology for performing an experiment is explained in Chapter 5. We use this equation to simulate some basic systems in Figure 2.9 a to c. In (a), a charge system is modelled for two different scattering angles. For the $\theta = 0$ degree case, we see that the beam doesn't undergo any change in polarisation or magnitude, whereas when $\theta = 45$ degrees, we again see no twisting but a significant reduction of coherence around 90 degree incoming polarisation. This corresponds to the dipole-radiation argument discussed earlier in the Chapter. In (b) and (c), significant twisting can be observed, due to interacting with the magnetism within the sample. Furthermore, the relative phase of the magnetisation can be determined, as chiral textures such as helices produce significant P_3 scattered polarisation, whereas collinear ones do not.

2.3 Summary

To summarise, this Chapter has introduced the basics behind reciprocal space techniques, and the main experimental method used throughout this thesis. We started with how particles scatter from single objects, before moving onto a col-

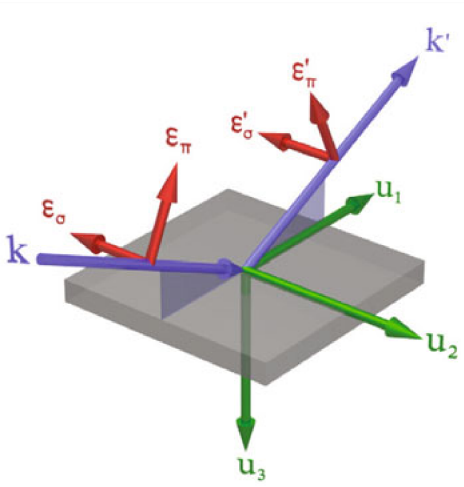

Figure 2.8: Coordinate system and polarisation vectors relative to the incident ($\mathbf{k}$) and scattered ($\mathbf{k}'$) beams. Taken from [155] under CC BY 4.0.

lection of objects in a macroscopic sample. We used an example of a skyrmion lattice to show the importance of convolutions, and were able to simulate a hexagonal lattice of skyrmions using both the convolution theorem and using a triple-q model. We then discussed using neutrons and x-rays as probes of magnetisation, before giving an overview and some simulations of FLPA.

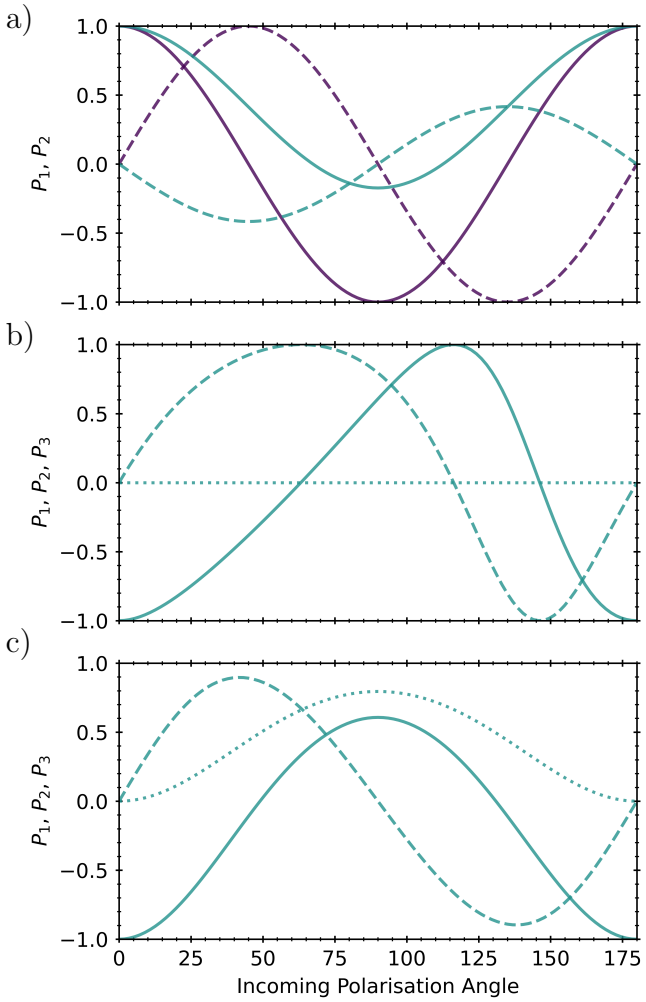

Figure 2.9: a-c) Outgoing x-ray polarisation in terms of Stokes parameters, P_1 (Solid), P_3 (Dashed) and P_3 (Dotted), as a function of incoming polarisation angle. In (a), the model system includes only charge scattering with a scattering angle of 0, 45 degrees for dark and light blue respectively. In (b) and (c), a magnetic system is modelled for incommensurate magnetism that lies within the U_2-U_3 plane. In (b), the moments are in phase, leading to an oblique spin-density wave. In (c), the moments are out of phase, leading to a spiral.

Chapter 3

Exchange Anisotropy Investigations in Cu_2OSeO_3

In the first experimental Chapter of this thesis, we briefly set the scene with an overview of the anisotropic exchange interaction (AEI), and how it differs from the more familiar symmetric exchange interaction. We will then look at how this interaction affects the incommensurate magnetic textures within chiral magnets lacking centrosymmetry. In particular, the helical and conical states within Cu_2OSeO_3. We will explain how to measure the AEI using small-angle neutron scattering (SANS) together with a three-dimensional vector magnet, before showing some experimental results with data collected from the LARMOR SANS beamline at the ISIS Neutron and Muon Source. These results confirm that the AEI is present in Cu_2OSeO_3, and that we found a change of behaviour as a function of temperature, with the AEI going from ferromagnetic to anti-ferromagnetic upon decreasing the temperature from T_C down to 5 K. We finalise the Chapter by explaining how, despite the anisotropies in the material displaying a change of sign, the magnetic helices within the material don't display reorientations, as well as commenting on a possible microscopic mechanism responsible for these low-temperature effects.

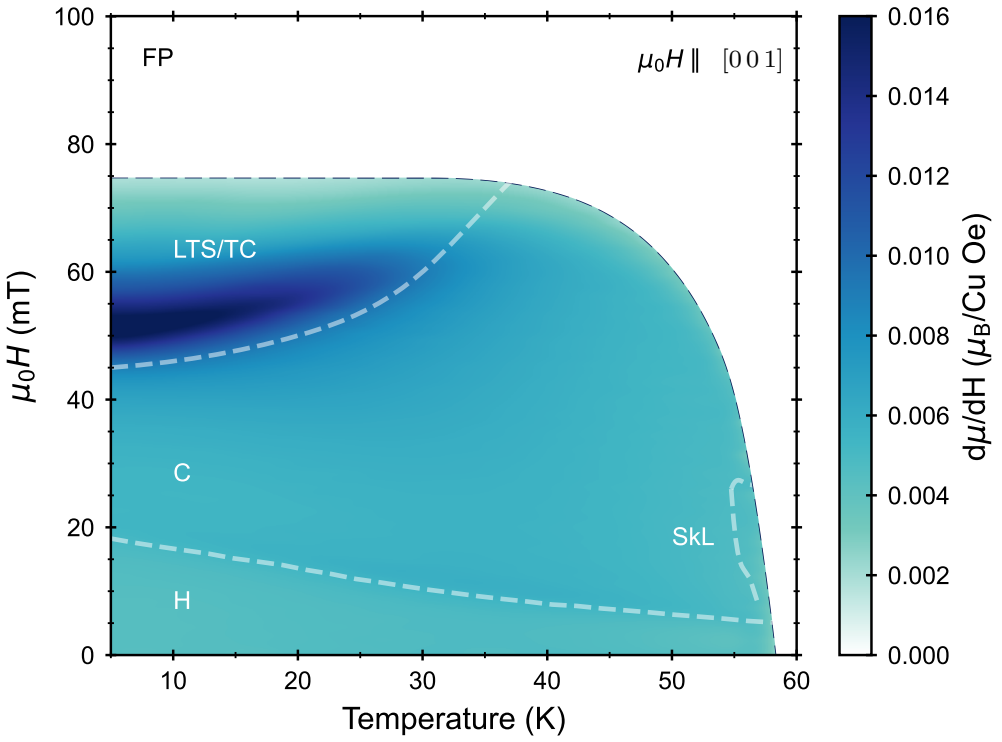

Figure 3.1: Magnetic phase diagram of Cu_2OSeO_3, obtained via magnetometry, for magnetic fields applied along the [0 0 1] crystallographic directions. LTS, TC, C, H, SkL and FP labels refer to the low-temperature skyrmion, tilted conical, conical, helical, skyrmion lattice (A-phase) and field-polarised phases respectively. A large signature can be seen in the LTS/TC region.

3.1 Introduction

3.1.1 Justification: Novel Phases in Cu_2OSeO_3

We introduce this Chapter by justifying why it is worth our time to investigate additional interactions, enriching the picture compared to the three term Hamiltonian introduced in Chapter 1.

In 2018, a novel magnetic state was found in the material, dubbed the tilted conical state [156]. This state is similar to the conical state introduced earlier in this Thesis, but differs since the wavevector of the magnetic texture is not

parallel to the direction of the applied magnetic field. Instead, the wavevector tilts towards a [1 1 1]-type of crystallographic direction. A real space description of this magnetic state is introduced later in this Chapter. In the same year, a separate skyrmion phase was found and shown to be independent from the A-phase skyrmion phase (Near T_C) [157].

The presence of these phases make Cu_2OSeO_3 unique amongst other similar, skyrmion-containing materials. As shown in Figure 3.1, the signatures of these states are found far below the ordering temperature, and only for magnetic fields applied along the [1 0 0]-type directions. This leads to these phases to be known as the anisotropic, low-temperature phases within the material.

We shall see why these novel phases are present in this material and which interactions are responsible in the rest of this Chapter.

3.1.2 What is the Anisotropic Exchange Interaction?

Similarly to the Heisenberg interaction, anisotropic exchange is quantum mechanical in nature and describes the coupling between two nearby magnetic moments [34]. Annoyingly, magnetic nomenclature has lead to a variety of different phenomena being ascribed the name of the anisotropic exchange interaction, including: the dipolar interaction [158], interfacial interactions between two magnetic materials [159, 160, 161] and even the Dzyaloshinskii-Moryia interaction [34]. In this thesis, we follow previous work on non-centrosymmetric bulk samples and use it to describe a directionally dependent exchange interaction [162, 163, 164].

Luckily, this dilemma of different definitions can be consolidated atomistically by using describing the coupling between two adjacent spins, $\mathbf{S_i}$ and $\mathbf{S_j}$ with an exchange tensor $\mathcal{J}_{ij}$ that features components J_{ij}^{ab}, such that the Hamiltonian of the system is the sum over all pairs of spins:

$$\mathcal{H}^{\text{exch}} = -\frac{1}{2}\sum_{i,j} \mathbf{S_i}\mathcal{J}_{ij}\mathbf{S_j}, \tag{3.1}$$

where the exchange tensor in full is,

$$\mathcal{J}_{ij} = \begin{pmatrix} J_{ij}^{xx} & J_{ij}^{xy} & J_{ij}^{xz} \\ J_{ij}^{yx} & J_{ij}^{yy} & J_{ij}^{yz} \\ J_{ij}^{zx} & J_{ij}^{zy} & J_{ij}^{zz} \end{pmatrix}. \tag{3.2}$$

This tensor is typically decomposed into three terms [165], $\mathcal{J}_{ij} = J_{ij}^{I} + \mathcal{J}_{ij}^{A} + \mathcal{J}_{ij}^{S}$, where J_{ij}^{I} is the standard isotropic Heisenberg exchange defined as the average of the diagonal elements, $J_{ij}^{I} = \frac{1}{3}\sum_{\alpha} J_{ij}^{\alpha\alpha}$, and $\mathcal{J}_{ij}^{S} + \mathcal{J}_{ij}^{A}$ are the symmetric and antisymmetric[1] anisotropic exchange tensors respectively. The symmetric, anisotropic exchange tensor is given by:

$$\mathcal{J}_{ij}^{S} = \frac{1}{2}(\mathcal{J}_{ij} + \mathcal{J}_{ij}^{\mathcal{T}}) - J_{ij}^{I}\mathcal{I}, \tag{3.3}$$

$$= \begin{pmatrix} \frac{1}{3}(J_{ij}^{yy} + J_{ij}^{zz} - 2J_{ij}^{xx}) & J_{ij}^{xy} + J_{ij}^{yx} & J_{ij}^{xz} + J_{ij}^{zx} \\ J_{ij}^{yx} + J_{ij}^{xy} & \frac{1}{3}(J_{ij}^{xx} + J_{ij}^{zz} - 2J_{ij}^{yy}) & J_{ij}^{yz} + J_{ij}^{zy} \\ J_{ij}^{xz} + J_{ij}^{zx} & J_{ij}^{zy} + J_{ij}^{yz} & \frac{1}{3}(J_{ij}^{zy} + J_{ij}^{yz} - 2J_{ij}^{zz}) \end{pmatrix}. \tag{3.4}$$

Here, $\mathcal{I}$ is the identity matrix and $A^{\mathcal{T}}$ represents the transpose of matrix A. Whilst this entire matrix may seem daunting at first, it is greatly simplified by enforcing a cubic symmetry to the system. This would cause the diagonal coupling constants[2] $J_{ij}^{xx} = J_{ij}^{yy} = J_{ij}^{zz} = 0$ so that the diagonal elements within $\mathcal{J}_{ij}^{S}$ would vanish, leaving only the off-diagonal components. From this we can see that the coupling between neighbouring spins with collinear moments is zero, as the off-diagonal components are only activated if the spins are canted away from one another. This leaves only the off-diagonal components, which in a non-centrosymmetric crystal are known to be finite due to the non-vanishing DMI interaction. These diagonal moments couple to non-collinear moments, such as those found in some incommensurate magnetic textures, as well as moments which

[1] The antisymmetric exchange tensor, $\mathcal{J}_{ij}^{A}$, is none other than the atomistic Dzyaloshinskii-Moryia interaction (DMI) [166].

[2] These couplings are all equal, so these terms are accounted by the isotropic Heisenberg interaction, J_{ij}^{I}, so this matrix doesn't have to make any corrections.

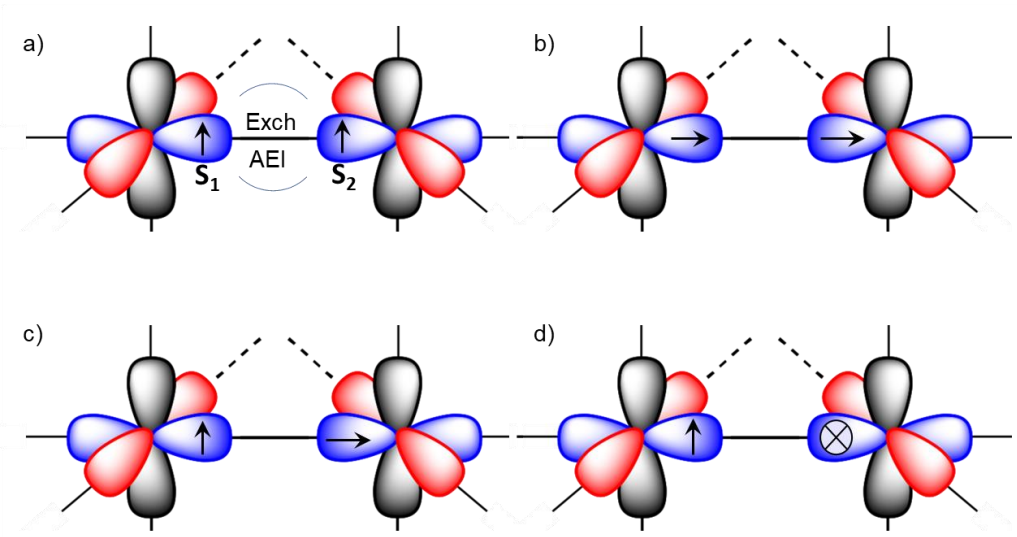

Figure 3.2: Figure shows the directional, and relative angle dependence of the AEI and Heisenberg exchange (exch) for a pair of moments (black arrows) within a simple system consisting of two atoms bonded by a single p-orbital. In (a) and (b), the moment directions are aligned so both the exch and AEI vanish. When the moments lie orthogonal to each other, the exch energy is equal regardless of the relative directions, but the value of AEI between one moment parallel to the bond (c) and both perpendicular to bond (d) is inequivalent due to the inequivalent symmetry.

lie along a non-trivial crystal direction. For non-collinear moments, these off-diagonal elements still favour particular orientations relative to the crystal axes, and are more easily visualised via a symmetry argument as in Figure 3.2.

As can be seen in panel (a) and (b), a parallel arrangement of magnetic moments which lie along a principle axis direction cause the AEI and Heisenberg exchange energy to vanish by definition. However, by looking at the (uniaxial) symmetry of the system, the degeneracy of orthogonal moments is lifted due to the inequivalent scenarios seen in (c) and (d). This energy splitting is due to the AEI, as the Heisenberg exchange only depends on the dot product between the two spins, not their relative orientation with respect to crystal axes. Within a cubic system however, the $\langle 1\,0\,0 \rangle$ directions are equivalent. In this case, the breaking

of degeneracy can be found when considering the $\langle 1\,1\,1\rangle$ and $[1\,0\,0]$ crystal directions, ultimately leading to the AEI being (partly) responsible for controlling the propagation direction of the magnetic helices within non-centrosymmetric magnets, as discussed in the following section.

3.1.3 Exchange Anisotropy in Cubic Helimagnets

The symmetry of the cubic materials place the requirement that the macroscopic physical properties (and therefore the free-energy descriptions) to also exhibit the same symmetry according to the Neumann principle [34]. Since the magnetic textures within the B20 helimagnetic materials are slowly-varying, the continuum approximation is typically used, and to first order the free energy contribution from the exchange interaction is isotropic. We revisit the well-known free-energy expansion first mentioned in Chapter 1:

$$F(\mathbf{r}) = D\mathbf{m}(\mathbf{r}) \cdot (\nabla \times \mathbf{m}(\mathbf{r})) + A(\nabla \mathbf{m})^2 + \mu_0 M_0 \mathbf{m} \cdot \mathbf{H}, \tag{3.5}$$

where A, D are the constants for the previously mentioned exchange and Dzyaloshinskii-Moriya interactions (DMI), and the final term is the Zeeman interaction. This free-energy equation is mostly-isotropic, with the symmetry of the system only being broken by an external magnetic field. In zero field, the energy only depends on the relative angle between the magnetic moments, leading to an infinite number of degenerate configurations as the moment directions with respect to the crystal axes do not influence the final free energy. However, by taking into account higher-order corrections we encounter anisotropic terms. These occur at fourth-order in the spin-orbit coupling and are typically weaker than the terms mentioned in Eq. 3.5, which are lower-order corrections to the free energy (for instance, DMI is first-order). For completeness, we show here the five fourth-order

terms allowed by cubic symmetry:

$$\begin{aligned} F_{anis}(\mathbf{r}) = & \frac{1}{2}\gamma_1[(\frac{\partial m_x}{\partial x})^2 + (\frac{\partial m_y}{\partial y})^2 + (\frac{\partial m_z}{\partial z})^2] \\ & + \gamma_2[(\frac{\partial m_z}{\partial x}\frac{\partial m_z}{\partial x} + \frac{\partial m_x}{\partial y}\frac{\partial m_x}{\partial y} + \frac{\partial m_y}{\partial z}\frac{\partial m_y}{\partial z}) \\ & - (\frac{\partial m_y}{\partial x}\frac{\partial m_y}{\partial x} + \frac{\partial m_z}{\partial y}\frac{\partial m_z}{\partial y} + \frac{\partial m_x}{\partial z}\frac{\partial m_x}{\partial z})] \\ & + 2\gamma_3[\frac{\partial m_x}{\partial x}\frac{\partial m_y}{\partial y} + \frac{\partial m_y}{\partial y}\frac{\partial m_z}{\partial z} + \frac{\partial m_z}{\partial z}\frac{\partial m_x}{\partial x}] \\ & + \frac{1}{2}A_2[\frac{\partial^2}{\partial x^2}\mathbf{m}\cdot\frac{\partial^2}{\partial x^2}\mathbf{m} + \frac{\partial^2}{\partial y^2}\mathbf{m}\cdot\frac{\partial^2}{\partial y^2}\mathbf{m} + \frac{\partial^2}{\partial z^2}\mathbf{m}\cdot\frac{\partial^2}{\partial z^2}\mathbf{m}] \\ & + K(m_x^4 + m_y^4 + m_z^4), \end{aligned} \tag{3.6}$$

where $\gamma_{1,2,3}$ are the three symmetric AEI terms, A_2 is the second-order Heisenberg exchange interaction, and the last term is the fourth-order single-ion magnetocrysalline anisotropy (MCA) with a constant K. In the following, we follow previous studies and set $\gamma_1 = \gamma$ and $\gamma_{2,3}, A_2 = 0$ for simplicity [156]. Note that only the γ_1 term was initally investigated in the original Bak-Jensen model [167]. Due to their relative weakness compared to the isotropic interactions, these anisotropic interactions do not typically play a major role in the formation of the incommensurate magnetic textures present in the chiral helimagnets. However, they do influence the crystallographic direction in which the zero-field magnetic helices propagate. This is most noticeable when comparing MnSi and Cu_2OSeO_3, where the helices in MnSi always follow the $\langle 1\,1\,1\rangle$ directions whereas in Cu_2OSeO_3, the helices are locked along the $\langle 1\,0\,0\rangle$ directions. Interestingly in FeGe, there exists a helical reorientation from the $\langle 1\,0\,0\rangle$ to $\langle 1\,1\,1\rangle$ upon cooling from near room-temperature to below around 230 K [168]. However, revealing the detailed physics behind such a macroscopic reorientation is difficult as both the anisotropic exchange interactions and single-ion anisotropy influence the direction of the magnetic helices.

The orientational dependence of both the AEI and MCA on a number of spin-textures can be seen by inserting a conical state Ansatz into terms 1 and 5 of Eq. 3.6, see Appendix A for the full derivation. Here, we describe the

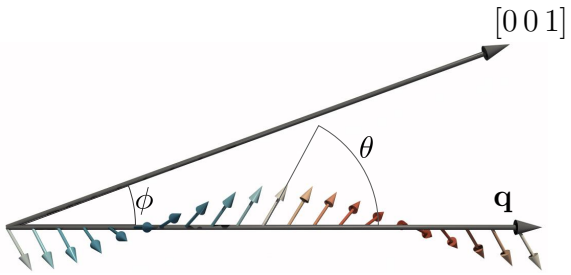

Figure 3.3: Schematic of a magnetic conical state with cone angle, θ, and wavevector ($\vec{q}$) angle ϕ.

magnetisation, $\mathbf{m}(\mathbf{r})$ of a conical state by:

$$\mathbf{m}(\mathbf{r})/M_s = \sin\theta(\cos(\mathbf{q}\cdot\mathbf{r})\hat{\mathbf{e}}_1 + \sin(\mathbf{q}\cdot\mathbf{r})\hat{\mathbf{e}}_2) + \cos\theta\hat{\mathbf{e}}_3, \tag{3.7}$$

where θ is the conical angle, and $\{\hat{\mathbf{e}}_n\}$ define three mutually orthogonal basis vectors, with $\hat{\mathbf{e}}_3 \parallel \mathbf{q}$. In order to simplify this Ansatz, we consider a conical texture with the wavevector restricted to the plane spanned by the three high cubic-symmetry directions ([0 0 1], [1 1 0], [1 1 1]), such that $\mathbf{q} = (\frac{q}{\sqrt{2}}\sin\phi, \frac{q}{\sqrt{2}}\sin\phi, q\cos\phi)$, and the magnetisation can be described by only using two angular coordinates, θ and ϕ. A schematic of this conical state is shown in Figure 3.3.

Here θ is the conical angle which determines how closely the magnetic moments lie along the magnetic wavevector, $\mathbf{q}$, with $\theta = 0, 90°$ for a field-polarised/helical state respectively. Here, we define the direction of the wavevector to be solely determine by a single spherical polar-coordinate ϕ. This definition locks the wavevector to always lie within a plane in space, instead of being free to move in three dimensions, in order to simplify the maths. Fortunately, this simplification matches our experimental observations described in a later section.

In the absence of an external magnetic field, the orientation of the magnetic helicies within non-centrosymmetric cubic helimagnets is determined by both the MCA and the AEI. For these magnets, the leading terms are [167, 156]:

$$F_{MCA} = K(m_x^4 + m_y^4 + m_z^4), \tag{3.8}$$

$$F_{AEI} = \gamma \sum_{i=x,y,x} (\frac{dm_i}{di})^2. \tag{3.9}$$

Inserting the conical Ansatz shown in Eq. 3.7 into these equations and integrating over one conical period, we find the average free energy density per wavelength yields:

$$\begin{aligned} \bar{F}_{MCA}(\theta,\phi) = {} & K \sin^4\theta(\cos^4\phi + \frac{\sin^4\phi}{2}) \\ & + K \sin^2\theta\cos^2\theta(\frac{3\sin^2\phi}{2} + \frac{9\sin^2\phi\cos^2\phi}{2}) \\ & + K \cos^4\theta(\frac{3\cos^4\phi}{16} + \frac{3\cos^2\phi}{8} + \frac{3\sin^4\phi}{8} + \frac{3}{16}), \end{aligned} \tag{3.10}$$

$$\bar{F}_{AEI}(\theta,\phi,q) = \frac{\gamma q^2 \sin^2\theta\sin^2\phi}{4}(3\cos^2\phi + 1). \tag{3.11}$$

The free energy dependence on θ and ϕ is shown in Figure 3.4. Note how the AEI free energy is wavelength dependent, whilst the MCA is not. Here lies the origin of why we are able to separate out the AEI contribution from the MCA, and we shall return to this point later.

As shown in panel (a) and panel (b) of Figure 3.4, both the AEI and MCA influence the direction of the conical wavevector for a variety of different values of θ and ϕ. In (a), the AEI is greatest in magnitude in the helical phase ($\theta = 90$ degrees), and diminishes linearly with increasing conical angle to zero when the moments are all aligned in the field polarised state, regardless of their final crystallographic direction. Furthermore we see two maxima at $\phi = \pm 54.7$ degrees), corresponding to two [1 1 1] directions, and a minima at $\phi = 0°$, the [0 0 1] crystalline direction. Of course, changing the sign of γ reverses these so that the previous maxima are now the minima. This shows us that in the helical state, a positive γ prefers the wavevector to lie along the $\langle 1\,0\,0\rangle$ directions, whereas a negative prefers the $\langle 1\,1\,1\rangle$. Finally, in the field polarised region, the AEI vanishes, similarly to the Heisenberg interaction.

In panel (b), the MCA has also be seen to play a role in the determination of the zero-field magnetic helices, with the wavevectors preferring $\langle 1\,1\,1\rangle$ for $K > 0$

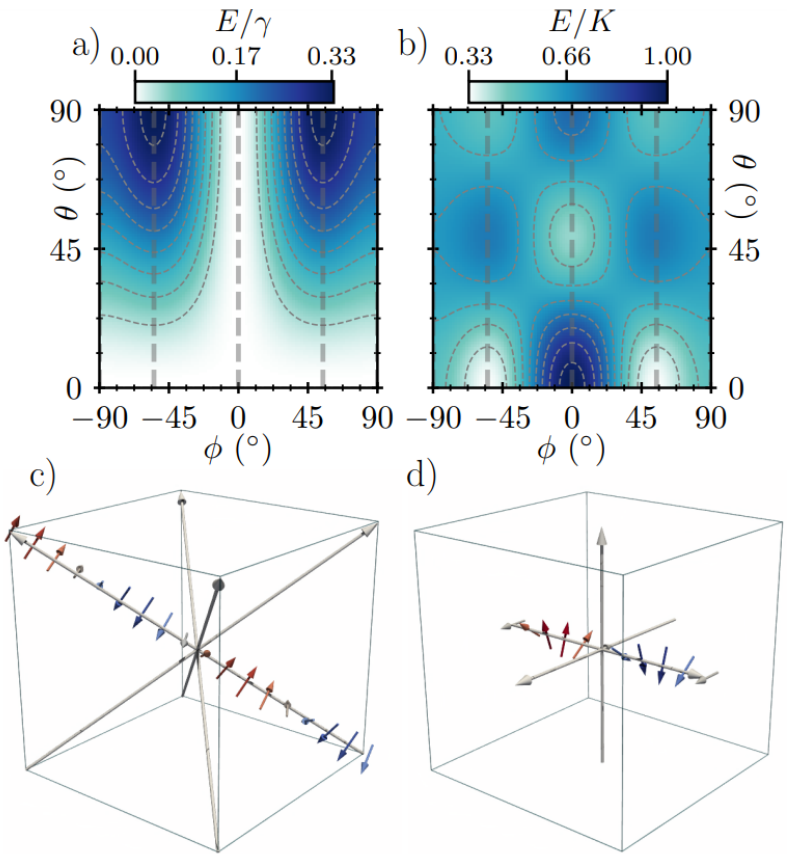

Figure 3.4: Normalised AEI (a) and MCA (b) energy landscapes of a conical state with a cone angle θ and angular direction ϕ, such that $\phi = 0, 90$ is $[0\,0\,1]$, $[1\,1\,0]$. Depending on the signs and strengths of γ and K, the magnetic helices orient along the 4 equivalent $\langle 1\,1\,1 \rangle$ directions (c), or 3 $\langle 1\,0\,0 \rangle$ directions (d).

and $\langle 1\,0\,0 \rangle$ for $K < 0$. However, unlike the AEI, the MCA is most prevalent within the field-polarised state as the anisotropy is not averaged out across a winding texture, as instead the moments simultaneously lie along easy/hard axes respectively. Interestingly, the MCA displayed local minima (for $K < 0$) along the $\langle 1\,1\,1 \rangle$ directions around $\theta = 45$ degrees, which reverses the easy axes from the $\langle 1\,0\,0 \rangle$ at the extremes of $\theta = 0$ and 90° respectively.

These panels show us that, depending on the sign of both the MCA and AEI and their relative strengths, the zero-field magnetic helicies can be stabilised along either the $\langle 1\,1\,1 \rangle$ direction as shown in panel (c) or the $\langle 1\,0\,0 \rangle$ direction, panel (d). Decoupling the relevant anisotropy from the myriad of possible interactions by just looking at the propagation direction of the magnetic helices is therefore impossible, and a more advanced technique than those typically used must be employed to extract the values of the anisotropic free energy contributions.

3.2 Methods and Experimental Details

3.2.1 Technique Overview

As mentioned in the previous section, the effects from a myriad of different anisotropic interactions are hard to decouple. To make matters worse, these terms are typically orders of magnitudes smaller than the conventional exchange interaction. Typically, the in-house techniques of torque magnetometry [169, 170, 171] and ferromagnetic resonance [172, 173, 174] are used for determining the magnetic anisotropy, but both are usually limited to only extracting the uniaxial constant of thin-film magnetic systems, which is far stronger than cubic anisotropy [175, 169]. Due to the symmetry of a thin-film, there is often a large energy difference between magnetisation lying in and out-of the plane of the sample. Separating the various symmetry-allowed single-ion anisotropies is a laborious task [176], and to the best of our knowledge no one has implemented determining the AEI in either technique.

These limitations call for a new method that separates the effects of these two anisotropies. As we shall see, one possibility is using SANS, together with a 3D vector magnet, to probe the orientational-dependence of the incommensurate conical states within chiral bulk-samples. Within these systems, conical states are induced by the application of a moderate magnetic field (See Chapter 1 for the general phase diagram of these systems), with a strength great enough to transition the system out of a helical state locked along a particular orientation, but not so strong as to field-polarise the material. Furthermore, the orientation of these conical states can also be controlled by the direction of the applied magnetic field, giving us the ability to manipulate the wavevector of the spin-texture into any direction as the conical state tends to trivially follow the magnetic field direction[3]. In the following, we provide the mathematical description at the mean-field level of how to measure the AEI by exploiting such control of a magnetic conical state, within a 3D vector magnet.

We start by using the non-constant terms within the free energy expansion derived by Bak and Jensen [167], which is valid for systems of $P2_13$ crystal symmetry that host slowly-varying magnetization densities within the continuum approximation $\mathbf{m}(\mathbf{r})$ [10]:

$$\begin{aligned} F(\mathbf{r}) = & D\mathbf{m}(\mathbf{r}) \cdot (\nabla \times \mathbf{m}(\mathbf{r})) \\ & + \frac{1}{2}A[(\nabla m_x)^2 + (\nabla m_y)^2 + (\nabla m_z)^2] \\ & + \frac{1}{2}\gamma[(\frac{\partial m_x}{\partial x})^2 + (\frac{\partial m_y}{\partial y})^2 + (\frac{\partial m_z}{\partial z})^2] \\ & + K(m_x^4 + m_y^4 + m_z^4) \\ & + \mu_0(\mathbf{m} \cdot \mathbf{H_a}), \end{aligned} \tag{3.12}$$

where D, A are the familiar Dzyaloshinskii-Moriya and exchange stiffness, and K, γ are the 4^{th} order MCA and AEI constants respectively. The final term in Eq. (1) is the Zeeman interaction within an applied field $\mathbf{H_a}$. In the case of

[3] this is not always the case, such as the tilted conical state in Cu_2OSeO_3 [156, 177]

$D = 0$, and $A, \gamma > 0$, the spin-texture reduces to a simple ferromagnet, with the spin direction given by the sign of the MCA constant K.

Similarly to the previous section, inserting the conical Ansatz given in Eq. 3.7 into the free energy expansion, integrating over one conical period, λ, before differentiating with respect to q (See Appendix A for the full derivation) we find a single stable solution:

$$\begin{aligned} \frac{\partial}{\partial q}\overline{F}(q,\phi) &= \sin^2\theta[D + Aq + \frac{1}{2}\gamma q \sin^2\phi(3\cos^2\phi + 1)], \\ q &= \frac{|D|}{A + \frac{1}{2}\gamma \sin^2\phi(3\cos^2\phi + 1)}. \end{aligned} \tag{3.13}$$

As shown by Eq 3.13, the free energies which determine the periodicity of the incommensurate states within non-centrosymmetric magnets at a mean-field level are limited to the DMI and both the isotropic and anisotropic exchange interactions. Due to the the integration and normalisation of the free energy over an entire conical period, the Zeeman and anisotropy energies vanish due to the symmetry of the magnetic Ansatz, and thus changing the magnitude of the applied field has no effect on the conical period. However, the direction of the applied field (H_ϕ) induces a rotation of the conical wavevector angle (ϕ) to follow the field direction, thus subjecting the conical state to the anisotropic effects of the AEI.

An example experimental configuration is shown in Figure 3.5. Here, incoming neutrons are directed along the $[\bar{1}\,1\,0]$ direction of the sample, and are able to diffract off magnetic textures with periodic components that lie within the plane normal to the same direction (cyan circle in Figure 3.5). This geometry places three high-symmetry directions into the scattering plane, namely the $[0\,0\,1]$, $[1\,1\,1]$ and $[1\,1\,0]$. By using a 3D vector field cryomagnet, it is possible to induce a conical state with an arbitrary propagation direction. By aligning the field along different crystallographic directions, we form a conical state with different free energy due to the anisotropic nature of the AEI and MCA. As we will see in the later section, the MCA does not influence the wavelength of the conical state. On the other hand, the free energy contribution of the AEI is proportional to

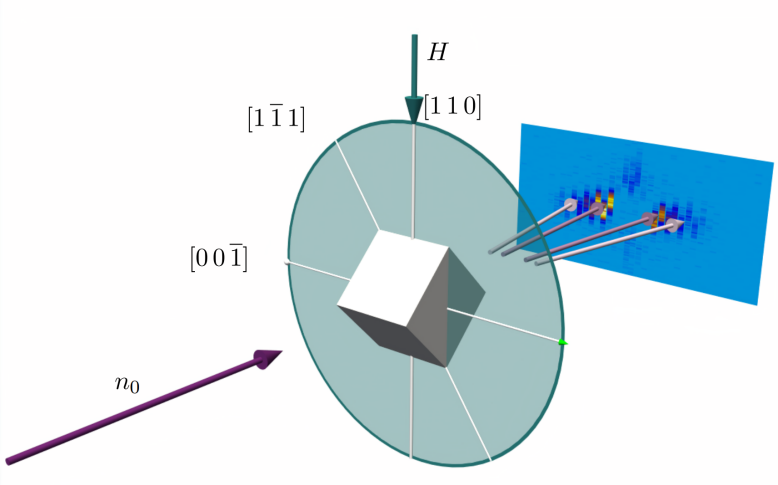

Figure 3.5: SANS scattering geometry with a 3D vector magnet. Incoming neutrons (n_0) parallel to the [1 $\bar{1}$ 0] direction, with the applied magnetic field perpendicular to n_0 within the scattering plane (cyan circle). A polychromatic incoming neutron pulse (dark purple), scatters at different angles depending on the wavelength (lighter purples).

q^2, similarly to the Heisenberg exchange interaction. Thus the wavelength of the conical spin-texture will either shrink or expand in order to minimise the directionally dependent AEI. We perform such an experiment and present the results in the following section.

3.2.2 SANS Experimental Details on the Larmor Beamline

This section presents the experimental results from a 20.5 mg single crystal of $(Cu_{0.98}Zn_{0.02})_2OSeO_3$, that was grown at the University of Warwick utilising the chemical vapour transport technique, see [178] and Chapter 2 for further details. For the SANS experiment, the LARMOR instrument at the ISIS Neutron and Muon Source was used. The sample was aligned with an x-ray Laue camera (Multiwire Laboratories) such that the [1 1 0] direction was vertical in the laboratory frame and the [1 $\bar{1}$ 0] direction was parallel with the incident neutron beam. This orientation allows the magnetic textures whose periodic components lie within

a plane spanned by the all three high cubic-symmetry directions ($\langle 1\,0\,0\rangle$, $\langle 1\,1\,0\rangle$, and $\langle 1\,1\,1\rangle$) to simultaneously satisfy the Bragg condition, as shown in Figure 3.5.

A Zn-substituted sample was chosen for our study due to the reduction of the regular exchange interaction compared to pristine Cu_2OSeO_3, resulting in a greater value of q [178]. Previously, we have shown in our previous work that the Zn ions occupy the Cu-sites in a random distribution, and that the large length scales of the magnetic textures render microscopic pinning effects to be irrelevant [178]. This is shown by the strong similarities of the magnetic behaviour between Zn-substituted and pristine samples [179], and hence we expect our results here will extend to pristine samples. Furthermore, the larger wavevector is more appropriate for LARMOR, which receives a hotter neutron spectrum than other SANS instruments such as ZOOM. Therefore, the diffraction angles are typically smaller and yielding a poorer q-resolution, particularly at low magnitudes of magnetic wavevector. Since we are looking for subtle changes in the magnetic wavevector, the Zn-doped sample is more suitable.

The time-of-flight (TOF) neutron diffraction data were reduced with Mantid [180], which automatically accounts for detector and pixel efficiencies by running a standard sample prior to the experiment, and provides the user with reduced SANS patterns, *i.e.* two-dimensional maps of diffracted neutron intensity at different values of q_x and q_y.

3.2.3 A Note on Hysteresis

Due to the large footprint of the 3D vector magnet at ISIS, the cryostat takes a large amount of time to change and settle to new temperatures. In our sample of Cu_2OSeO_3, it typical to warm the sample above the curie temperature (58 K in our sample) to reset the magnetic state. Changing the temperature from 5 K to 65 K, before returning to a stable 5 K took over two hours to complete, rendering resetting the sample's state many times to be infeasible due to the time-

limitations of a beamline experiment. Therefore, the samples state only reset three times to for the three temperatures studied further in the next section. These resets were done at zero field, warming above 60 K before cooling and stabilising at the desired temperature. The magnetic field was then increased until a pure conical state was observed with no co-existence with helical domains. Then, the magnetic field was rotated without resetting the state each time in a cold sample state. Alternative hysterical studies, using a flash heater mount such as the one used in Chapter 6, would be very worthwhile to investigate the true ground state and look for time-dependent relaxation effects.

3.2.4 Rotating Field Scans

To observe the effects of the anisotropic interactions on the magnetic textures within Zn-doped Cu_2OSeO_3, we performed the required field scans by rotating the direction of the magnetic field whilst maintaining the field at a constant magnitude. Initially, the field was applied vertically in the laboratory frame after zero-field cooling. The field orientation was then rotated 90 degrees in 46 steps about an axis parallel with the neutron beam, such that the $[1\,\bar{1}\,0]$, $[1\,1\,\bar{1}]$, $[0\,0\,\bar{1}]$ directions were parallel with the field at angles of 0, 35.3 and 90 degrees respectively. This procedure was performed at 5, 12 and 50 K at magnetic field magnitudes of 70, 60 and 40 mT respectively. These fields were chosen to avoid phase coexistence between the magnetic conical and helical states, whose phase boundary varies as a function of field, see Chapter 2.

A selection of frames from the field scans are shown in the next section, within Figure 3.6.

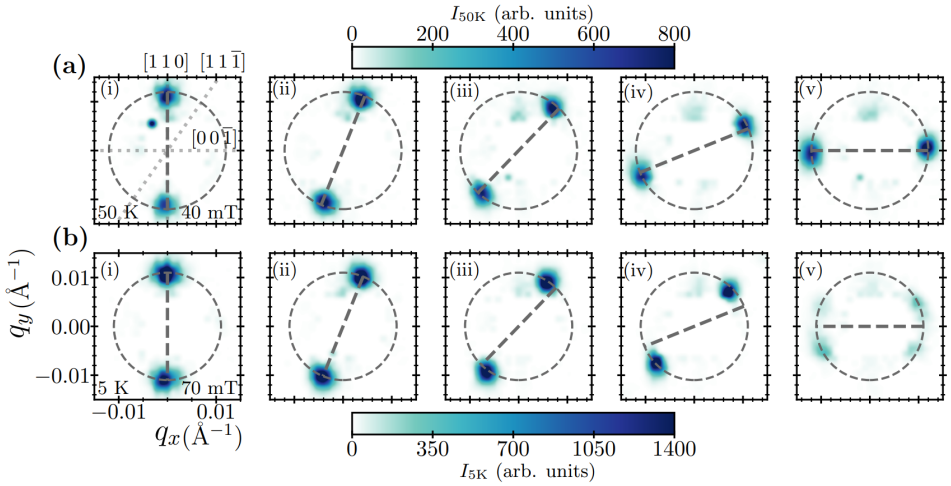

Figure 3.6: Selection of reduced SANS patterns for field rotations at 40 mT, 50 K(a) and 70 mT, 5 K(b). The field angles for each frame are 0, 22, 44, 68 and 90° for frames (i-v) and are shown by the thick dashed lines. The thin-dashed circle gives the location of equidistant $q = 0.011$ Å^{-1}. Crystallographic directions are shown by the dotted lines in a(i).

3.3 Results and Explanation

In the first frame of the 50 K dataset, (a-i), the vertically applied magnetic field induces a magnetic conical state with wavevector along the $[1\,\bar{1}\,0]$ direction, which we detect as a single pair of vertical peaks with $q \approx 0.011$Å^{-1}, with a corresponding real space length of 57 nm, in agreement with previous measurements on doped samples [178, 179]. Upon rotating the field, (a:ii-v), the conical wavevector rotates in an attempt to follow the direction of the magnetic field. This behaviour is expected in the limit in which the AEI and MCA are much smaller than the isotropic Dzyaloshinskii-Moriya and exchange interactions ($\gamma, K << A, D$), allowing the conical wavevector to rotate freely to minimize the Zeeman interaction.

However, this behaviour is not replicated within the data taken at lower temperatures in Figure 3.6b(i-v), which shows that the angle of the conical wavevector (ϕ) consistently lags behind the magnetic field angle (H_ϕ), particularly after the field passes through the $[1\,1\,\bar{1}]$ direction. This offset between the field direction

and q increases in magnitude with further rotation of the magnetic field, up to a maxima just before the field is applied along the $[0\,0\,\bar{1}]$ direction. This magnetic state is characteristic of the tilted conical state seen previously in pristine Cu_2OSeO_3 [156], and shows that while isotropic interactions dominate at temperatures near T_C, the anisotropic interactions be seen to become increasingly important at low temperatures, as they are shown to prevent the free rotation of the magnetic conical state.

To quantify the effects of the anisotropic interactions, the conical peaks collected during the field scans shown in Figure 3.6 and an additional set at 12 K were fitted to two-dimensional gaussian functions defined in polar coordinates, allowing the extraction of the magnetic wavevector angle, ϕ, and magnitude, q. See Chapter 4 for further details about the fitting procedure. The results of this fitting for field angle scans at the three different temperatures are shown in Figure 3.7.

The behaviour of q as a function of field angle is shown in Figure 3.7a. A clear difference between the high temperature and low temperature regimes can be seen. In the 50 K dataset, q initially decreases slightly as the applied field is rotated from the $[1\,1\,0]$ to $[1\,1\,\bar{1}]$ direction and then increases as the field is rotated further, up to a maximum when H is along $[0\,0\,\bar{1}]$. This behaviour is reversed at low temperatures (both at 12 K and 5 K), where the magnitude of the conical wavevector instead increases to a maximum when the field is rotated from $[1\,1\,0]$ to $[1\,1\,\bar{1}]$, before quickly decreasing as the field angle approaches the $[0\,0\,\bar{1}]$ direction. In Figure 3.7b, the effects of the anisotropic interactions can also clearly be seen to be more significant within the low-temperature datasets, where ϕ deviates substantially from linearity after the magnetic field passes through $[1\,1\,\bar{1}]$, as compared to the 50 K dataset where ϕ deviates only slightly from the expected linear trend in the absence of anisotropic interactions.

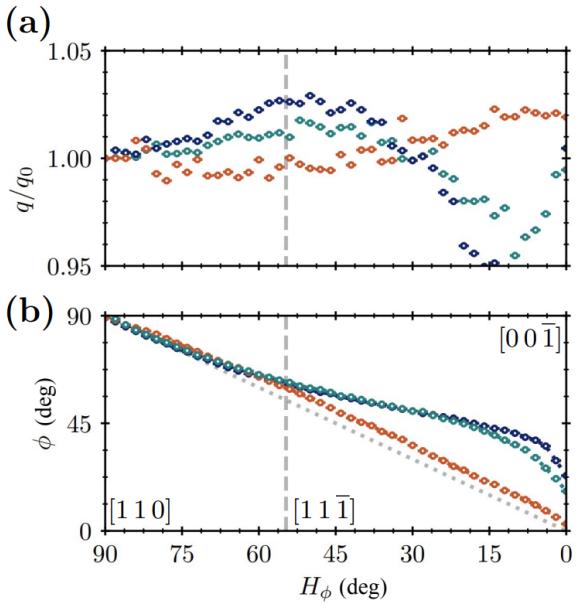

Figure 3.7: a,b) Normalised wavevector magnitude, and wavevector angle, ϕ, of the conical state as a function of applied field angle, H_ϕ. Dark blue, light blue and orange indicate temperatures of 5, 12, and 50 K respectively. Dashed line shows $[1\,1\,\bar{1}]$ direction. Dotted line shows H_ϕ.

In accordance with Eq. 3.13, the implications of this dependence can more easily be seen in Figure 3.8a-c, which shows the experimentally measured values of the conical wavevector q for different conical wavevector angles, ϕ, at 50, 12 and 5 K respectively. At 50 K, the increased wavevector at $[0\,0\,\bar{1}]$ compared to $[1\,1\,\bar{1}]$ is a clear indication of a positive exchange anisotropy constant γ, where energy costs for directions other than the $\langle 1\,0\,0\rangle$, are compensated by a shrinking of the conical wavevector. This behaviour reverses with decreasing temperature, shown in Figure 3.8b and c, where the wavevector maxima are located at the $[1\,1\,\bar{1}]$ and minima towards the $[0\,0\,\bar{1}]$, suggesting a change of sign of γ.

Using the experimentally determined value for the exchange stiffness, $A = 4.4 \times 10^{-13}$ J/m from $T_C = 57$ K [178, 181], and fitting both D and γ in Equation 3.13 to the data in Figure 3.8, we find $\gamma = 2.1(2) \times 10^{-14}$ J/m at 50 K, $-3.4(4) \times 10^{-14}$ at 12 K, and $-6.7(3) \times 10^{-14}$ J/m at 5 K. The low-temperature

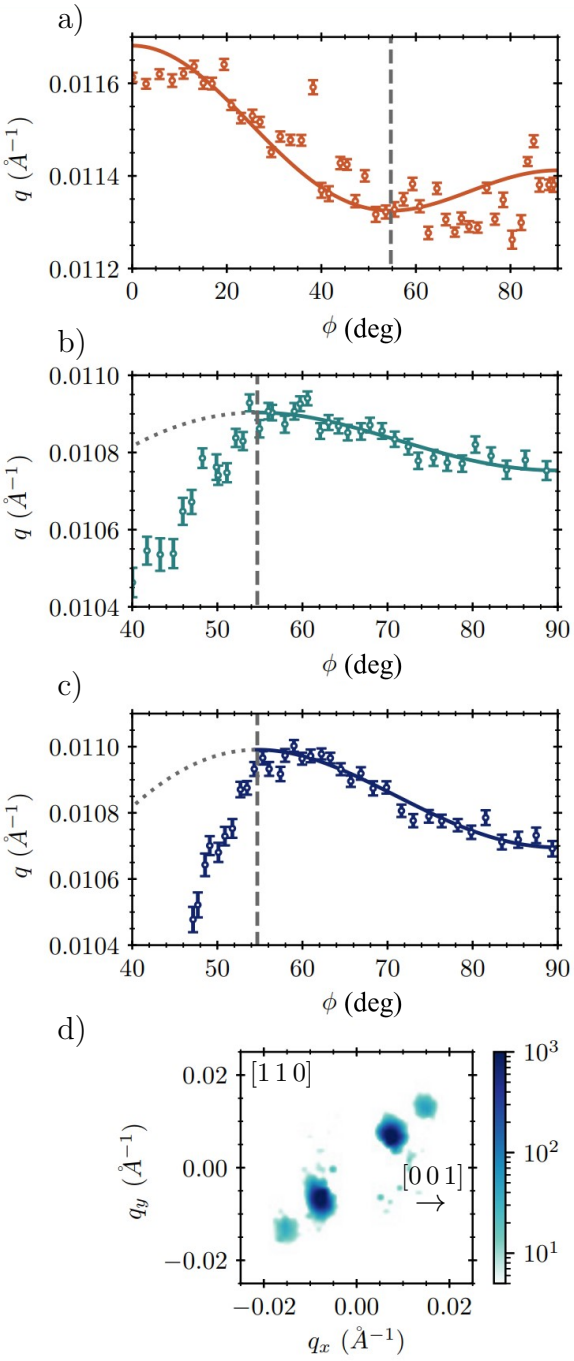

Figure 3.8: Values of the extracted wavevector magnitude (q) against wavevector angle (ϕ) with (a-c) being the 50, 12 and 5 K datasets respectively. Fits to Eq. 3 are shown by the bold lines, with dotted lines showing regions ignored in the fitting procedure due to the appearance of higher-order peaks, shown in (d). Dashed line at $\phi = 54.7$ degrees corresponds to the [1 1 1] direction.

values are consistent with theoretical values of γ required for formation of the tilted conical state [156], in agreement with the TC states observed in this study.

During the refinement of the low temperature datasets, only angles above 55 degrees were used. This is because at low temperatures, the direction of the conical wavevector deviates significantly from the magnetic field direction for $\phi < 55$ degrees, inducing a component of the magnetic field perpendicular to the conical wavevector. Applying transverse fields to a helical state with a pinned $\mathbf{q}$ direction is known to deform the helix [182], introducing higher-order components to the Fourier transform of the magnetic state. The presence of higher order peaks in our SANS pattern shown in Figure 3.8d suggest that similar deformations are occurring in our tilted conical state. For helices, these deformations are known to reduce the value of q as the perpendicular field strength increases, which would be consistent with our observations that a large variation of q occurs when there are prominent higher-order peaks. Fully accounting for these deformations within our model spin-texture remains an avenue intended for future study.

3.4 Discussion

3.4.1 Why do the Helices in Cu_2OSeO_3 always stay along the $\langle 1\,0\,0 \rangle$?

In the previous section, we showed that the AEI is present in Cu_2OSeO_3 and that one can measure it within a bulk sample by investigating the magnitude of wavelength of the conical phase changes as a function of crystallographic direction. Furthermore, we also showed that the AEI constant undergoes a change of sign from positive to negative upon cooling. In the absence of cubic anisotropy, this change of sign of the AEI would induce a helical reorientation from the $\langle 1\,0\,0 \rangle$ to $\langle 1\,1\,1 \rangle$ directions, similar to the helical reorientation in FeGe[4]. For the orientation

[4]However, it is currently not known whether the AEI or MCA is responsible for this

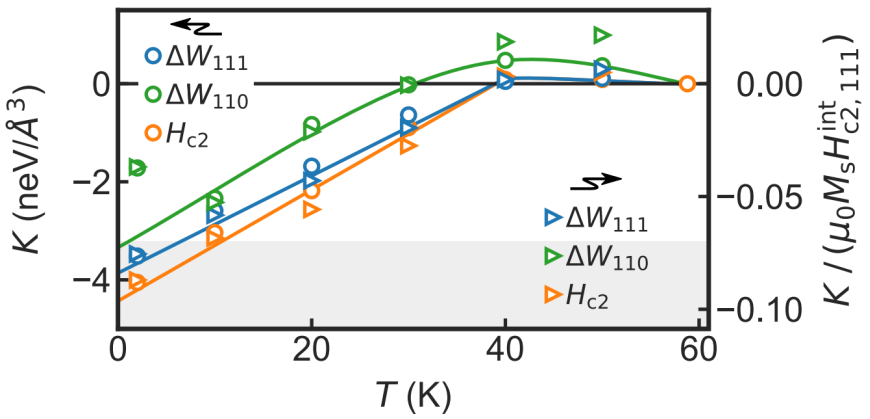

Figure 3.9: Magnetocrystalline anisotropy constant, K, as a function of temperature, as extracted from the magnetic work (green, blue), and the upper critical field H_{c2} (orange). Shown in grey shading is the regime in which an LTS phase becomes favourable, data taken with permission from [183].

of the helical wavevector to remain aligned along the $\langle 1\,0\,0 \rangle$ directions (consistent with experimental observations), we require that K must be negative when γ is also negative, with the condition $|K| > \frac{4}{3}|\gamma|q^2$ found by differentiating Eqs. 3.10 and 3.11. This requires that the magnitude of K increases with decreasing temperatures.

As shown in Figure 3.9, the MCA was found to become increasingly negative upon cooling towards lower temperatures using a variety of experimental techniques. This experimental finding supports our hypothesis that the helicies in Cu_2OSeO_3 lie along the $\langle 1\,0\,0 \rangle$ as the negative MCA dominates over the negative AEI (which would prefer them to align along the $\langle 1\,1\,1 \rangle$). Interestingly, we see that at high temperatures, the value of K is either vanishingly small or even positive, which would prefer a $\langle 1\,1\,1 \rangle$ alignment of helices. Fortunately, our experimental findings reconcile this, as we find a positive γ towards high-temperatures, meaning that near T_C the AEI dominates over the MCA. This delicate hand-over of significance allows the helices to always remain locked along the $\langle 1\,0\,0 \rangle$, despite both interactions undergoing a change of sign. We postulate that at temperatures

where neither interaction is clearly dominating (away from the skyrmion pocket in a region not thoroughly studied), interesting phenomena and novel magnetic states may be waiting to be discovered.

3.4.2 A possible mechanism

The rich behaviour of both the MCA and AEI, together with the recently discovered tilted conical and low temperature skyrmion states arises due to complex unit cell of Cu_2OSeO_3 when compared to the B20 compounds such as MnSi and FeGe, containing 16 Cu^{2+} ions per unit cell.

As shown in Figure 3.10a, these Cu^{2+} ions constitute a network of four corner-sharing tetrahedra, each containing two differing Cu-sites, Cu(1) and Cu(2) in a ratio of 1:3 respectively. These Cu^{2+} ions interact with each other via superexchange, mediated by an intermediate oxygen atom. The symmetries within the crystal structure leads to five inequivalent superexchange constants and Dzyaloshinskii–Moriya (DM) vectors. Both ferromagnetic and antiferromagnetic exchanges are present, whose values have been determined experimentally [184, 185] and from first principles [186]. To summarise previous findings, the strong FM and AFM interactions between the ions within the tetrahedra causes their tetrahedron to behave as an effective spin-1 triplet, coupled weakly to each other as shown in Figure 3.10b. Interestingly, the DM couplings in the ground state of each tetrahedra cancel out by symmetry, showing that the DM interaction within Cu_2OSeO_3 arises due to the effective DM couplings between each tetrahedra and is not of atomistic origin. The effective spins of each tetrahedra have a range of excited states to give a great number of possible effective interactions beyond the five super-exchange and DM couplings between the Cu^{2+} ions.

It was found that the first-excited state within a single tetrahedron appears far above T_C at 275 K [186]. The effective macro-spin of the unit cell, panel (c), is composed of the effective spins from the four tetrahedra, these were found to

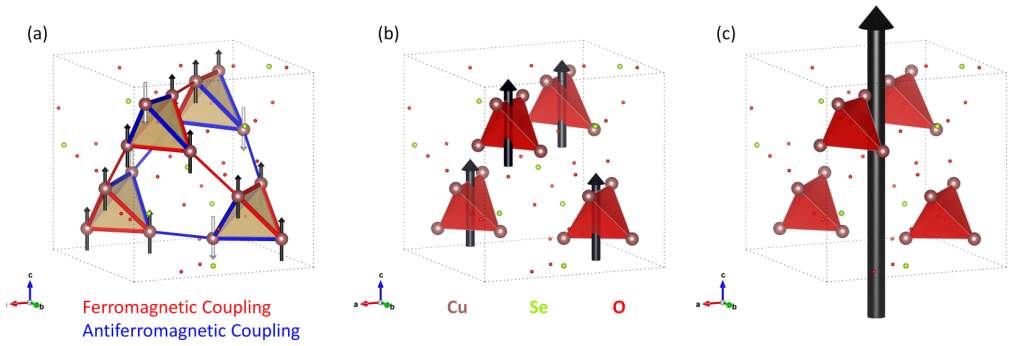

Figure 3.10: a) Unit cell of Cu_2OSeO_3 showing the Cu(1) and Cu(2) sites as white and black arrows respectively. Strong (weak) superexchange couplings, where intermediate oxygen atoms are not connected for clarity, are shown as thick (thin) lines between Cu-spins. Red shows ferromagnetic couplings, blue show antiferromagnetic. b) The strong couplings in each tetrahedra allows each tetrahedron to be modelled as an effective spin, introducing further effective interactions. The long-period magnetic textures are well described using mean-field theory, which ignores the crystal structure and approximates the magnetisation as a density per unit cell, shown in (c).

have excitations in the region of 16 K [186]. We speculate whether the cessation of effective spin-state mixing upon cooling to lower temperatures is responsible for the large change in material parameters away from T_C. We emphasise the point that whilst these individual atomistic interactions are inevitably all temperature dependent, we don't expect any one particular interaction to undergo such a dramatic effect as to change in sign. Instead, we suspect that the highly non-trivial combination of all the subtly-changing magnetic interactions within a unit cell to gives rise to the change in sign of the emergent, mean-field, anisotropic exchange interaction interaction.

3.5 Conclusions

In conclusion, we performed SANS on a single crystal of $(Cu_{0.98}Zn_{0.02})_2OSeO_3$, using a novel 3D vector magnet to decouple the anisotropic interactions within

the material by rotating magnetic field of constant magnitude. We observed a change of behaviour of the magnitude of the conical wavevector, q, as a function of wavevector angle, ϕ, whereby the crystal directions corresponding to a maximum or minimum in q reversed with cooling from 50 K to 12 K. We have explained this using a mean-field, continuum model and find that the AEI constant changes sign between these temperatures, with fitted values consistent with those required for tilted conical state formation. Unlike in the related compound FeGe, helical reorientation does not occur within Cu_2OSeO_3 with the change in sign of the AEI. This is due to an increasingly negative cubic anisotropy, which increases in magnitude faster than the AEI, causing the helical wavevectors to remain along the $\langle 1\,0\,0 \rangle$ directions. We believe our finding that the AEI changes sign at similar temperatures to the occurrence of the low-temperature skyrmions and tilted conical magnetic phases will be highly useful for understanding the formation and stabilisation of these newly discovered magnetic textures within this material.

Chapter 4

Electric Field Controlled Skyrmion Deflection

We introduce this Chapter with how electric-fields can be used to control various magnetic textures via magnetoelectric coupling, which not only opens up another external control parameter, but also provides unique benefits from the viewpoint of novel spintronic devices. We briefly cover the use of E-fields on multilayer skyrmion-systems, before moving onto the effects of E-fields applied to bulk single-crystalline materials and justify the use of bulk materials over heterostructure systems in nano-fabricated device architectures. We explain how a SANS experiment can be performed simultaneously at cryogenic temperatures and within both electric and magnetic fields, before showing recent data collected at the SANS-I beamline at the Paul Scherrer Institute, using a bespoke sample of the magnetoelectric insulator, Cu_2OSeO_3. By fitting the SANS data to two dimensional gaussian functions, we are able to extract a detailed description of how an electric field influences the recently discovered low temperature states within the material. In particular, this SANS experiment provides the first observation that the direction of the skyrmion-coexisting conical states within Cu_2OSeO_3 can be reliably manipulated within a bulk single-crystalline material by varying an applied electric field. We explain these findings using a free energy expansion, which allows us to determine the relevant, material-specific magnetic energies,

which reveals that the interplay of a number of different magnetic anisotropies are critical for attaining this behaviour within nano-fabricated devices. This Chapter provides the detailed requirements for the engineering of future magnetic materials that can directly control individual skyrmion motion within a nanosized racetrack by changing the direction of the localized conical state using our proposed mechanism. In the final section, we show a potential use of such a mechanism within an example nano-device: a skyrmion double transistor. Here, time-dependent micromagnetic simulations are performed in order to show future researchers that the interaction between localised magnetic states is inherently repulsive, which when combined with our proposed deflection mechanism opens up the scope for a large variety of nano-devices.

4.1 Background

4.1.1 A Brief Introduction to Magnetoelectrics

In general, a magnetoelectric (ME) material is one which exhibits a coupling between the magnetic and electric properties of the material. The first theorised (and then subsequently discovered) single-crystalline ME material was Cr_2O_3 [166, 187], whose polarisation was found to have a symmetry-required linear coupling between both an electric and a magnetic field:

$$P_i = \sum_j \epsilon_0 \chi^e_{ij} E_j + \sum_j \alpha_{ij} H_j, \tag{4.1}$$

where χ^e is the electric susceptibility and α_{ij} is a tensor which describes the linear response of the electric polarisation to the applied magnetic field. The tensorial nature of these couplings accounts for a polarisation that lies along a different direction than the applied magnetic/electric field, and is heavily dependent on the crystal symmetry. Since then, a number of different microscopic mechanisms with different effects on their respective coupling tensors have been discovered: single ion anisotropy [188, 189], symmetric-exchange striction [190, 191, 192, 193], heterostructure strain and flexomagnetism [194, 116, 195, 176].

These discoveries paved the way for a new class of materials: multiferroics. These are materials which exhibit a number of spontaneous ferroic properties, typically either magnetisation, polarisation and lattice distortions. An overview of their relevent order parameter and conjugate fields are shown in Figure 4.1. Here, we see that ME coupling links the magnetic and electric order parameters together. The coupling works both ways - not only can the electric polarisation be controlled by an external magnetic field, but the magnetisation can be controlled by an external electric field as well. We can see this by rewriting Eq. 4.1:

$$\mu_0 M_i = \sum_J \mu_0 \chi^m_{ij} H_j + \sum_j \alpha_{ij} E_j, \tag{4.2}$$

where χ^m is the magnetic susceptibility and α_{ij} is the same tensor used in Eq. 4.1. This reciprocity has fueled a huge amount of research into multiferroics, as they open up a large number of possibilities for future devices [196, 197, 198, 199]. One of the major goals is to create electric-field-controlled magnetic data storage. These storage schemes have massive benefits over conventional hard drives, including a decreased power consumption when generating electrical fields opposed to magnetic fields, easier integration into micro-sized memory devices as all the components would solely be electrical, and providing a low-energy-dissipation device by avoiding Joule heating [200].

This goal is also shared by the skyrmionics community, and the effects of an electric field on magnetic skyrmions have been extensively studied within heterostructure systems, as the intrinsic strain induced via a lattice parameter mismatch during the fabrication process leads to an inherent magnetoelectric coupling [206]. Within these systems, it was found that electric fields induce a wide range of effects, including being able to induce skyrmion creation/annihilation in transition-metal multilayers [207, 208, 209, 210, 211], via single-ion anisotropy [212, 213, 214] or by directly influencing the DMI interaction [215, 216, 217]. In some systems, this effect is so strong that even a skyrmion chirality switching can be observed [218, 219, 220]. However, with the recent advances in focussed

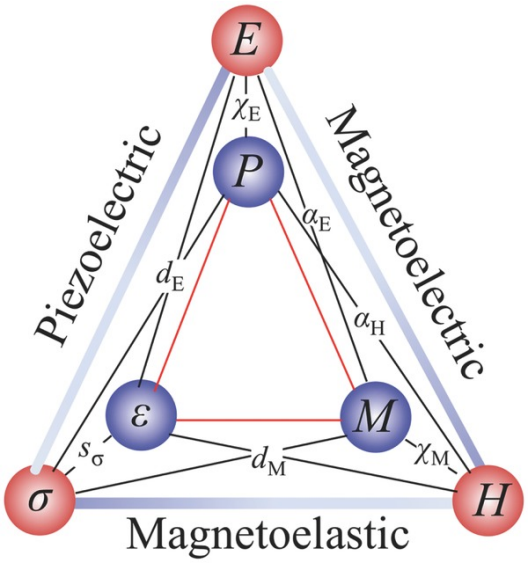

Figure 4.1: A diagram showing different types of multiferroics and their relevant order parameter (blue) and conjugate fields (red). Figure taken with permission from [201].

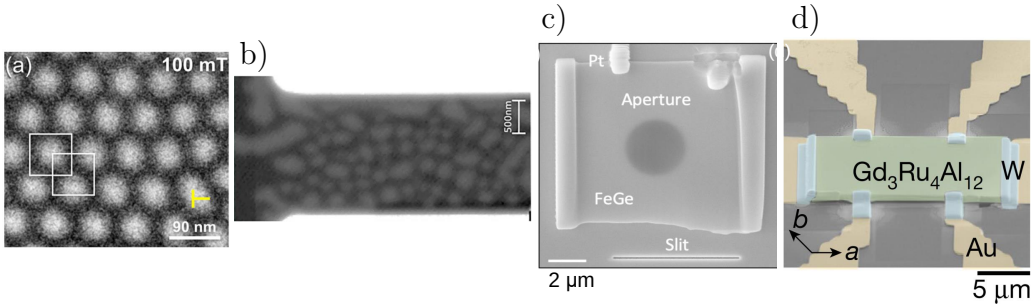

Figure 4.2: Comparison of skyrmions within single crystalline materials in (a), electron holography image of FeGe from [202], with multilayer skyrmions in (b), scanning transmission x-ray microscopy image of CoB/Ir/Pt stacks from [203]. Recent examples of nanofabricated devices used for x-ray holography [204] and for emergent helical induction [205]. All figures reproduced with permission or under the CC BY 4.0.

ion beam (FIB) technology, there is now great interest in fabricating nanosized devices cut from thin lamellae of bulk single-crystal samples, see Figure 4.2 c and d, and [205, 204, 221, 222, 223, 224]. These systems have a number of practical advantages over multilayer systems, as well as featuring different physics. In particular, the lack of inherent pinning sites that are predominant in multilayer systems compared with single-crystalline samples allows for more robust and uniform skyrmion motion, as well as a greater consistency in skyrmion sizes (see Figure 4.2 a) and overall less prone to inconsistencies in multilayer systems [225, 226].

4.1.2 Previous Electric Field Studies on Cu_2OSeO_3

Cu_2OSeO_3 is the only currently known, Bloch-type-skyrmion-hosting, single-crystalline material, which remarkably also possesses the insulating and magnetoelectric properties required for controlling bulk-DMI-stabilised skyrmions within an electric field. Prior to the discovery of skyrmions within the material, a number of novel magnetoelectric effects were under investigation. In particular, the onset of polarisation at the magnetic ordering temperature in the absence of any observable lattice strain was found using neutron scattering and nuclear magnetic resonance techniques, and was unique among magnetoelectric materials at the time [227, 228]. After the subsequent discovery of skyrmions in Cu_2OSeO_3 [90, 229, 230], their magnetoelectric properties and their dynamics were found to be highly directionally dependent on both the crystallographic direction of the applied electric field, as well as the crystallographic plane the skyrmion lattice occupied [231, 232, 233]. A breakdown of the electric polarisation induced by a magnetic skyrmion in Cu_2OSeO_3, depending on the crystallographic direction is shown in Figure 4.3.

This directional dependence of the electric polarisation confirmed that the $d-p$ hybridisation mechanism is the responsible microscopic model for the magnetically induced electric polarisation within the material [234, 235], rejecting an

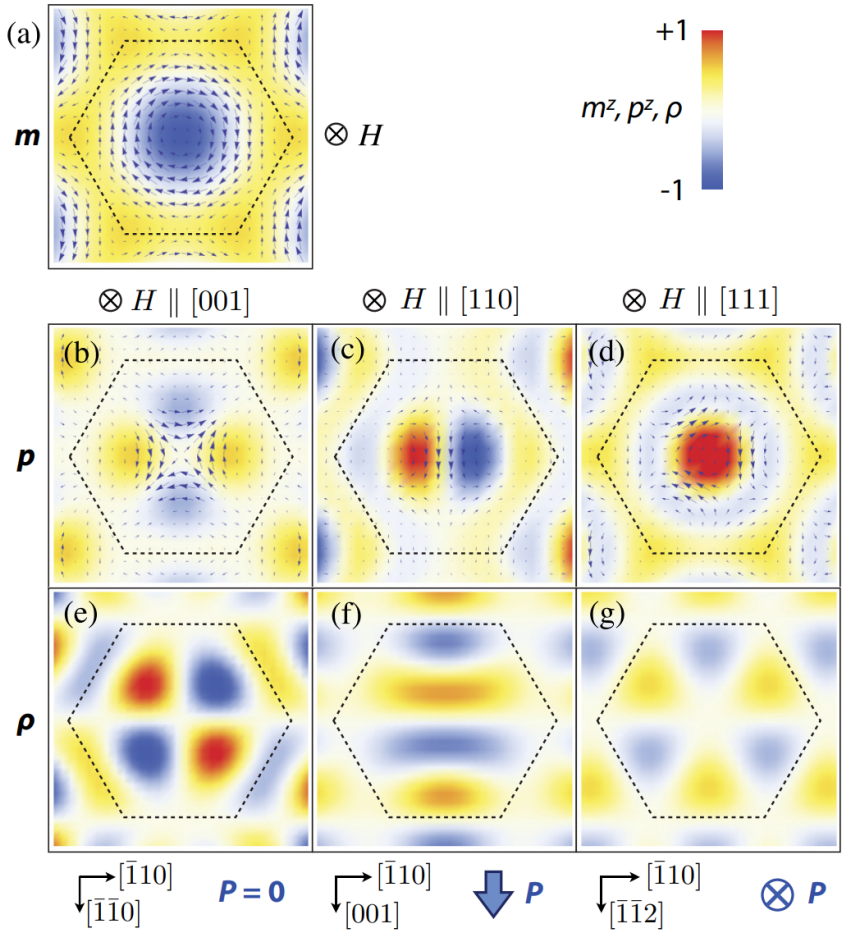

Figure 4.3: Calculated spatial distribution of (a) local magnetisation vector **m**, (b)–(d) local electric polarisation vector **p**, and (e)–(g) local electric charge ρ for the magnetic skyrmion state for different field directions. Taken from with permission [231].

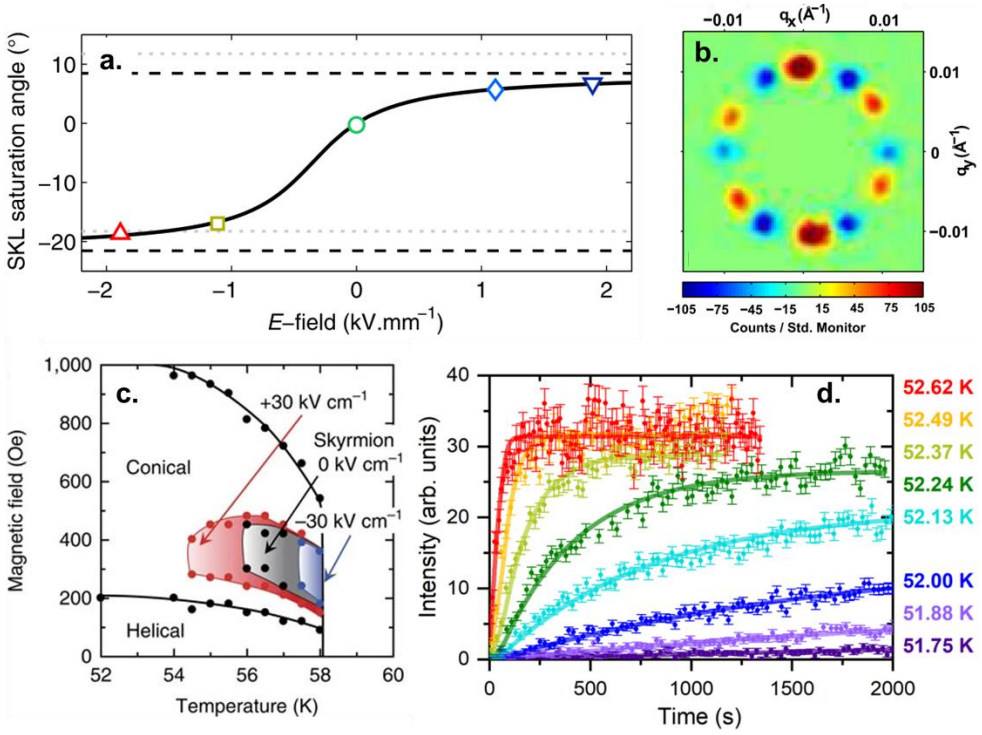

Figure 4.4: (a),(b) Average skyrmion lattice rotation angle as a function of E-field, and subtracted SANS pattern from high/low E-fields respectively, from [238]. (c) Extension/reduction of skyrmion stability in positive/negative E-fields respectively, from [239]. (d) Skyrmion SANS intensity as a function of time after applying an electric field of 1.7 V/μm at μ_0H = 30 mT, from [240]. All figures taken with the required permission.

earlier hypothesis by Jia *et al* [236, 237]. The coupling of this anisotropic polarisation with the magnetic skyrmions allows a number of interesting effects to be observed, which we summarise in Figure 4.4.

As shown in Figure 4.4 a and b, an E-field-induced rotation of the skyrmion lattice occurs when the skyrmions are stabilised by a magnetic field along the [1 1 0] direction. This field direction induces an electric polarisation along the [1 0 0] direction, which in turn couples (in part) to an electric field along the [1 1 1] direction, allowing positive/negative rotations of the skyrmion lattice in positive/negative electric fields respectively [241, 238, 242, 243]. In (c), the application of a magnetic field along the [1 1 1] induces a net polarisation also along

the same direction. The magnetoelastic free energy F_{ME}, is proportional to the the dot-product between the magnetic polarisation and applied electric field, **P** and **E** respectively, such that $F_{ME} \propto \mathbf{E} \cdot \mathbf{P}$. Therefore, in the $\mathbf{E}||\mathbf{H}||[1\,1\,1]$ experimental geometry, we are able to expand/reduce the extent of the skyrmion pocket, depending on the sign of the applied E-field. This variation in free energy changes the regions of phase-space in which the skyrmion lattice is more stable than the competing conical phase [244, 239]. This allows an E-field induced switching-like mechanism between the skyrmion and conical phases, which has been observed in lamellae systems [245, 246], and allows the formation energy barrier to be determined by performing lifetime measurements [240].

As shown in this overview, research on the effect of electric fields has solely focussed on the skyrmion pocket situated just below T_C. However, as we will show in the rest of this Chapter, the effects of an electric field on the recently discovered, anisotropy-stabilised low-temperature magnetic states (See Chapter 3) have not been extensively studied and remain an untapped avenue for research.

4.2 Experimental Setup and Sample Preparation

To perform a SANS experiment within an electric field, a 71 mg sample of Cu_2OSeO_3 was shaped using a polishing wheel into a plate. The final dimensions were $3.5 \times 4 \times 1$ mm^3 with a mass of 51.7 mg. The sample was polished such that there were two parallel $(1\,\bar{1}\,0)$ faces. See Figure 4.5 a and b for the final sample shape and crystal directions. After polishing, the presence of low temperature states within the sample was confirmed using a magnetometer (Quantum Design MPMS 3), as previous studies had used a spherical sample to reduce demagnetisation effects and plate-like samples had not previously been studied [157]. In order to generate the anisotropy-stabilised spin-textures, a field-cycle protocol is required. Here, we determined that rapidly changing the applied magnetic field

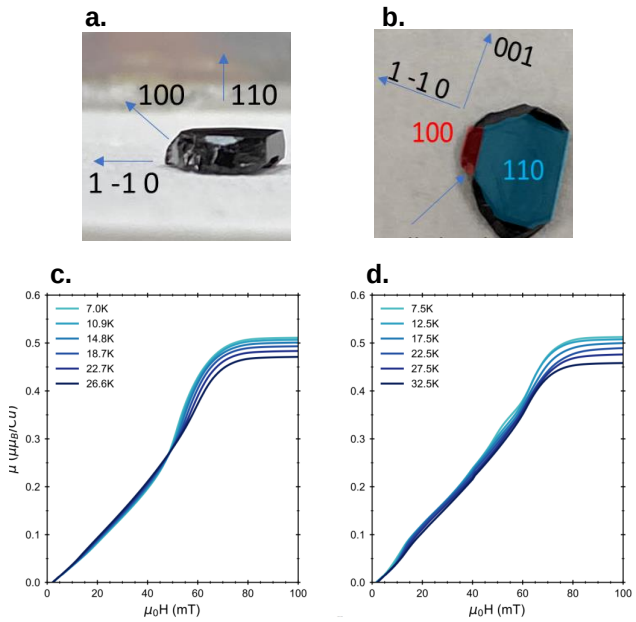

Figure 4.5: a,b) Images of the polished sample of Cu_2OSeO_3 labelled with the crystallographic directions. Magnetic moment versus applied magnetic field μ_0H as a function of temperature a) after zero-field-cooling and b) after forty magnetic field oscillations between 40 at 60 mT.

between 40 and 60 mT was optimal for seeding these low-temperature states, which grew in volume-fraction with the number of cycles (typically we performed 20). The presence of low-temperature states are observed by the clear differences in the magnetisation curves, between the purely zero-field-cooled (ZFC) and ZFC followed by magnetic field cycle protocols. Namely, these differences are the presence of a greater number of inflections, which suggests that a larger number of magnetic phase transitions are present. These confirmed the presence of, and determined the optimum field-cycle range of low temperature magnetic states within the sample, ahead of the SANS experiment.

We primarily prepared the sample to provide a good contact between the electric field plates, in order to ensure a homogeneous electric field across the entire sample as well as to avoid electrical arcing, which ultimately limits the maximum electric field we can apply during an experiment. After preparation and

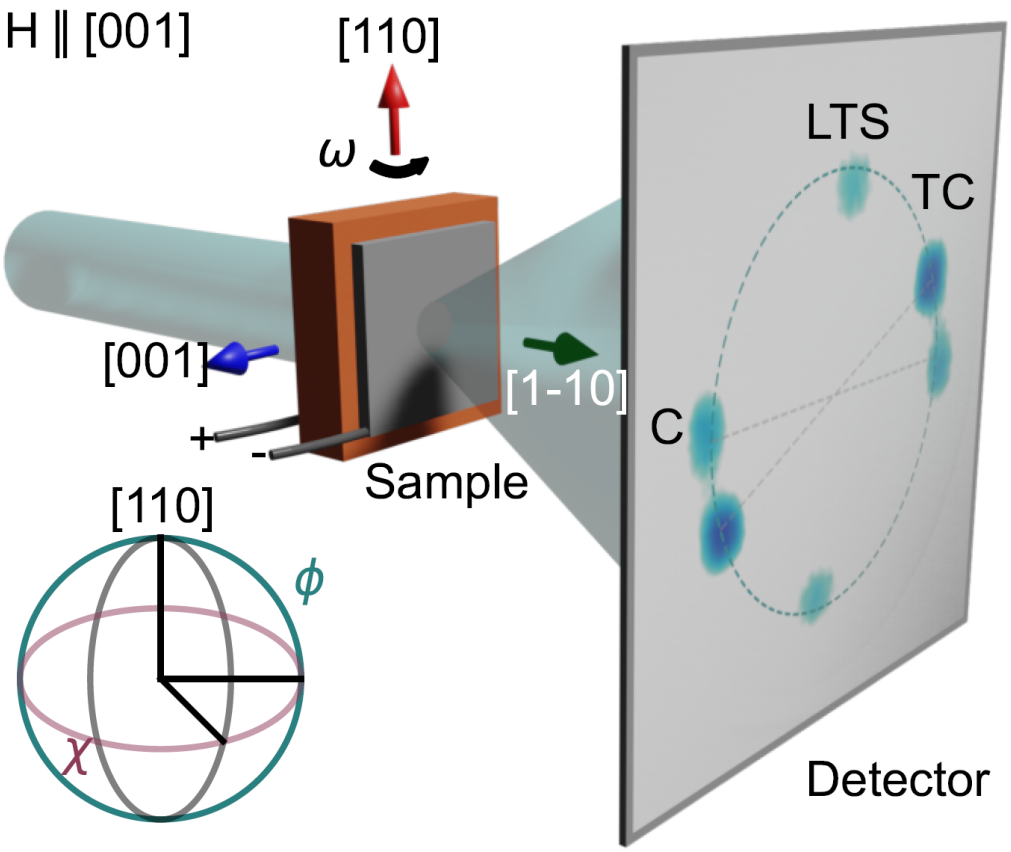

Figure 4.6: Scattering geometry for the E-field SANS experment: incoming neutrons parallel to the [1 1 0] direction with the applied magnetic field perpendicular to the neutron beam, parallel to [0 0 1] (blue arrow). Silver paste contacts on the surfaces apply a uniform electric field along the [1 1 0] (green arrow) direction. This orientation allows the different low-temperature states to be identified by their spatially separated diffraction patterns on the detector.

characterisation, the single crystal was mounted onto a dedicated E-field sample holder (see Bartkowiak *et al.* [247]), with electrodes attached via silver epoxy directly onto the large, flat $(1\,\bar{1}\,0)$ faces. The sample was then placed within a horizontal-field cryomagnet and oriented such that the conditions of $\mathbf{E} \parallel n_0 \parallel [1\,1\,0]$, and $\mathbf{H} \perp n_0 \parallel [0\,0\,1]$, were met simultaneously, as shown in an overview of the experimental setup in Figure 4.6.

As shown on the schematic of the detector, in Figure 4.6, the benefit of us-

ing this experimental geometry is that it has the advantage that all of the low-temperature states can be distinguished as their respective diffraction spots lie within spatially separated regions on the detector. The small-angle neutron scattering measurements were performed at the SANS-I beamline at the Swiss Spallation Neutron Source SINQ, Paul Scherrer Institut, Switzerland, with neutrons of wavelength $\lambda_n = 8$ Å, a wavelength spread $\Delta\lambda_n/\lambda_n = 10\%$, with a collimator and detector distance of 18 m. These conditions allowed us to separately investigate the populations, wavevector and ordering of all three low-temperature magnetic states, and observe the effect of (if any) an electric field applied along the $[1\,\bar{1}\,0]$ crystalline direction.

4.3 *E*-field SANS Results

During a typical SANS experiment which investigates incommensurate magnetism, rocked diffraction patterns (ω-scan in Figure 4.6) are measured by rotating both the sample and cryomagnet together through an angular range such that the diffraction spots completely pass through the diffraction condition, allowing the full intensity of the diffraction spot to be measured, as well as simultaneously providing further information on the ordering and direction of the wavevector of the magnetic texture. In our experiment, we were limited to a 14 degree angular range, and the individual diffraction patterns from an example rocking curve is shown in Figure 4.7.

The finite spatial extent of the spin-textures together with the instrumental resolution broaden the diffraction spots such that we are able to observe the diffracted intensities from all three magnetic phases at a variety of different rocking angles. Each image is a single-frame of a rocking scan, and is composed of raw data (lower left) and the resultant fit from a 2D gaussian function, defined by:

$$I(q,\theta) = \frac{I_{tot}}{2\pi\sigma_r\sigma_\theta}\exp(-\frac{q}{2\Gamma_r^2} - \frac{\theta}{2\Gamma_\theta^2}) + c, \tag{4.3}$$

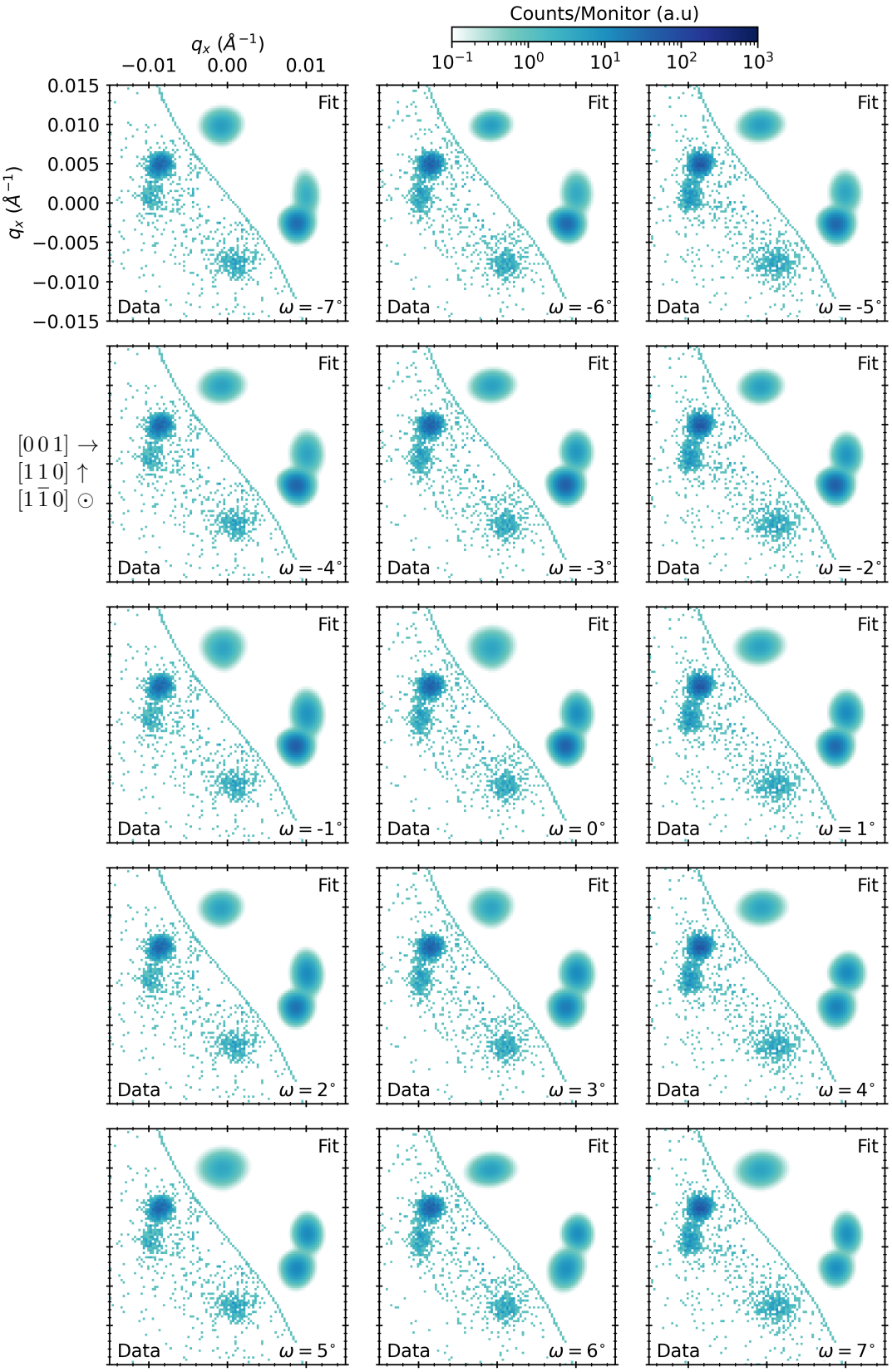

Figure 4.7: Individual frames of the SANS patterns from a single rocking scan taken at 5 K, 40 mT and 0 V. As shown, the gaussian fits are in excellent agreement with the raw data, which are separated by a curved line.

where q is the magnitude of the scattered wavevector, θ is angular coordinate on the detector and σ_i, Γ_i are the standard deviations and FWHMs of the magnitude of q and θ respectively. As can be seen, there is excellent agreement between the raw data and the fitted intensities, allowing us to extract a large amount of additional information (and quantitative errors) other than looking at integrated intensities alone.

Similar rocking scans were repeated eleven times, taken at temperatures ranging from 5 K to 60 K and with magnetic fields ranging between 0 - 250 mT. A consistent, zero-field-cooled procedure was used, starting from 60 to 5 K, before simultaneously ramping to the desired electric field and applying 40 magnetic field oscillations from 40 mT to 60 mT to generate a mixed-state consisting of low temperature skyrmions, tilted conical and regular conical. Background measurements were carried out in the paramagnetic state at $T = 70$ K and within the field-polarised regime at 5 K, 250 mT. The results of these rocking scans are summarised in Figure 4.8.

As shown in the summed rocking scans (creating by taking the sum of all 15 frames during a ω-scan, hence far better counting statistics when comparing to an individual frame in Figure 4.7) in Figure 4.8 a to c, our sample consistently exhibits a coexistence between three different magnetic states (LTS, TC and C) regardless of the magnitude of the applied electric field. The FWHM of the diffracted spots are experimentally limited, suggesting that these phases are long-range ordered and spatially separated by domain walls [248, 249, 250]. To maximise the diffracted intensity from the TC state, a slight canting of the sample was induced to break the degeneracy of the four-possible $\langle 1\,1\,1 \rangle$ TC domain orientations, promoting a single domain whose wavevector aligns closest to the field direction, as expected from previous reports [156]. For the different electric fields, we observe no clear, noticeable differences in the magnitude of the wavevectors or the integrated intensities in the summed images for any of the three coexist-

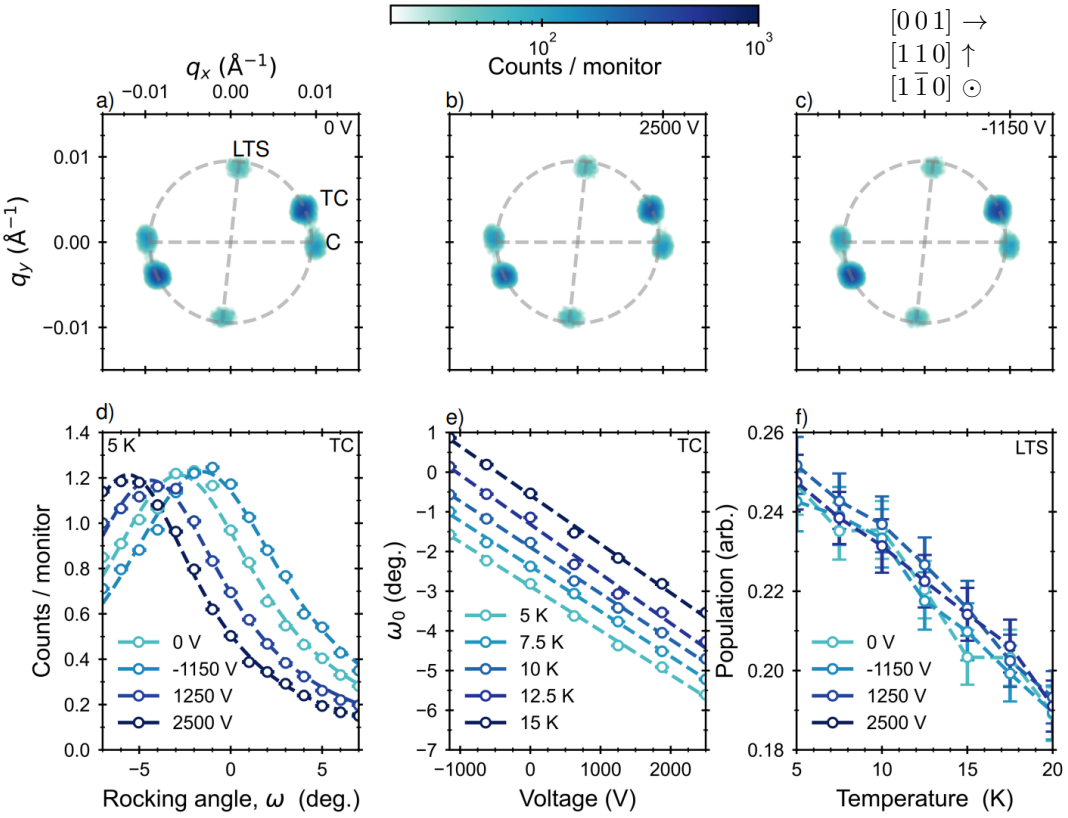

Figure 4.8: a-c) Integrated intensities from rocked SANS patterns in a 40 mT magnetic field at 5 K, after 40 field oscillations within an electric field of 0 V (a), 2500 V (b) and -1150 V (c) respectively. d) Rocking scans of the gaussian-fitted tilted conical intensity taken at a series of electric fields, showing a shift in the peak proportional to the electric field. e) The linear dependence of the peak center of the rocking curve (ω_0) as a function of applied voltage for a selection of temperatures. f) Temperature dependence of the LTS state population within different electric fields.

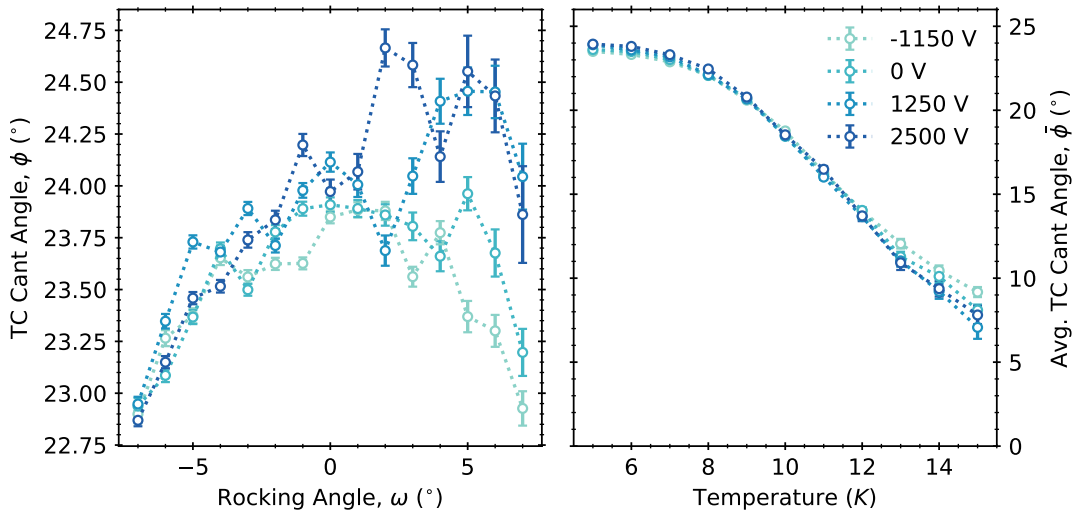

Figure 4.9: a) The tilted conical canting angle, ϕ, obtained by the gaussian fitting procedure, during a rocking scan taken at 5 K, 40 mT and 0 V. The parabolic nature is expected due to the geometry of the experiment, as the projection of the TC conical state away from the optimal diffraction condition reduces the apparent canting angle. b) Temperature and E-field dependence on the total TC canting angle. The canting angles of the tilted cone are very temperature dependent due to material anisotropies varying as a function of temperature. There is little effect from the E-field, whose effect is mostly to deflect the wavevector along an orthogonal angle.

ing magnetic phases, despite being at the limits of the experimentally accessible E-fields with $E = 0$, 2.5 and -1.150 kV/mm respectively.

However, by performing the 2D radial gaussian-fitting procedure to the TC diffracted intensities to each frame in the rocking-curve (this process is highlighted earlier in Figure 4.7), we are able to extract more information than solely investigating the integrated intensities alone. Figure 4.8 shows E-field dependent, gaussian-fitted-intensities across the whole rocking scan for the TC peaks in Figure 4.8 d. We find that the peak of the rocking curve (ω_0) varies as a function of the applied E-field, shifting towards larger (smaller) angles for negative (positive) electric fields respectively. Using the relationship $\zeta_l(\text{nm}) = \frac{1}{2}(q\Gamma)$ to

find the correlation length along the beam-direction, we see the FWHM (Γ) $\approx$ 11 degrees) remain roughly constant leading to a correlation length of approximately 9.5 microns, more than 100 times the size of an individual skyrmion, suggesting that the various phases appear to macroscopically phase segregated rather than microscopically mixed. The correlation lengths along orthogonal directions are experimentally limited due to the large spread of neutron wavelengths.

On the other-hand, the tilted conical angle, ϕ (defined as the angle of the wavevector away from the applied magnetic field), does not vary under different E-fields and the quadratic behaviour found in the ω-dependence shown in Figure 4.9 a is consistent with the experimental geometry. The main parameter which can be used to vary the tilted conical angle is temperature, in agreement with previous studies [156], and we show this for completeness in Figure 4.9 b. The variation of ω_0 and not of ϕ_0 reveals that the propagation direction of the TC spin texture deviates within a finite E-field away from the $E = 0$ alignment, in a direction along the equatorial polar angle, χ (parallel with neutron beam, see inset of Figure 4.6 for angular definitions).

This behaviour is found at a variety of applied E-fields and temperatures, as shown in Figure 4.8 e, with different temperatures offset in ω for clarity. Here, ω_0 varies linearly for both positive and negative applied E-fields, at all temperatures investigated. These experimental results on a bulk single-crystal system unambiguously show that the electric field drives the wavevector of the TC state along a direction perpendicular to the magnetic field. In contrast, no magnetoelectric effects on the LTS are observed. Unlike previous studies of E-field effects on skyrmions in the A-phase, which demonstrated the E-field control of the SkL orientation and phase stability [251, 252, 253, 244, 254, 255, 256, 257], the direction of magnetic modulations of the LTS remain firmly fixed in the plane spanned by the [1 0 0] and [0 1 0] directions, resulting in a zero net electric polarisation due to each skyrmion carrying a cancelling electric quadrupole [90].

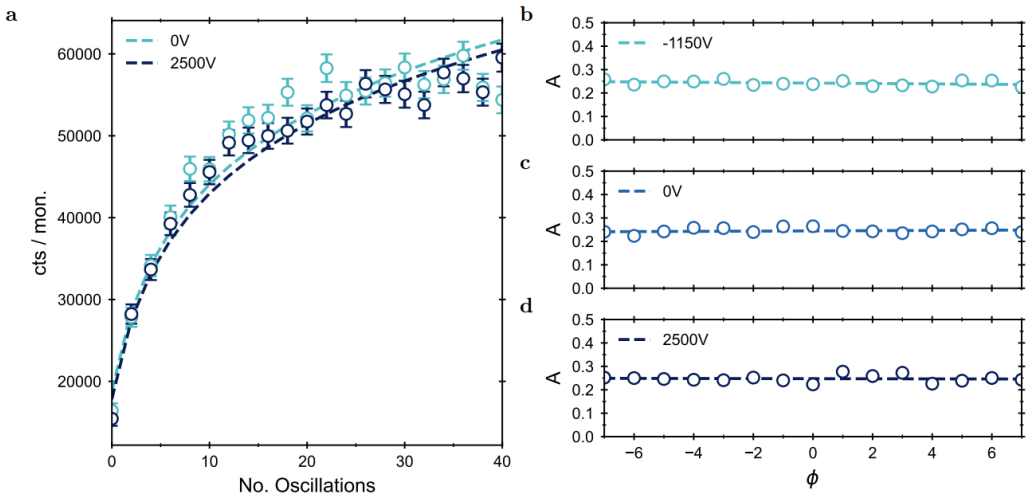

Figure 4.10: LTS fitted-intensity as a function of magnetic field oscillations between 40-60 mT. SANS measurements taken every two oscillations up to 40x oscillations. Repeating the same procedure resulted in an equivalent intensity. (b-d) ϕ_m-rock (orthogonal-to-ω motor of cryostat, not to be confused with tilted conical angle ϕ) of the LTS peaks at electric fields of b) -1150 V, c) 0 V and d) 2500 V. No variance to the ordering can be observed suggesting the low-temperature skyrmions remain in a disordered ring.

This lack of coupling can be seen in the temperature dependence of the LTS intensity, Figure 4.8 f, which shows identical final LTS populations and ordering within statistical limits. An electric field also has negligible affect on the formation-barrier of the low-temperature skyrmions, as can be seen in Figure 4.10 a, which shows identical LTS populations for both zero and high electric field as a function of magnetic field cycling. Finally, the *E*-field also has no effect on the skyrmion ordering, as shown in Figure 4.10 b to d, where the constant value shows the omnipresent ring-like nature of the LTS compared to the hexagonal HTS.

Despite the apparent lack of influence an electric field in this geometry has on the low-temperature skyrmions, the ability to reliably control the orientation of

the TC state using an E-field whilst not altering the stability of the co-existing skyrmions provides possible new functionality paradigms that may find use in skyrmionic devices. In the following section, we will show that this mechanism could be used to control skyrmion motion by dynamically altering the propagation direction of the TC state, such that it acts as a switchable barrier that is able to deflect a skyrmion under motion along different trajectories. In order to develop such a nano-device, it is essential to engineer materials which host the specific anisotropic and magnetoelectric properties. Thus, in the following section we start this process by determining these interactions from a mean-field theory perspective.

4.4 An Explanation: Mean-Field Theory

The E-field-induced reorientations of the tilted conical wavevector within the multiferroic Cu_2OSeO_3 highlights the remarkable anisotropic and magnetoelectric properties of the material. In the proceeding section, we generalise our findings by performing a theoretical investigation to obtain the relevant magnetic interactions as well as their relative strengths, allowing device-suitable magnetic materials to be engineered accordingly. Since the tilted conical state is incommensurate with a periodicity much greater than the chemical unit cell, we can explain our observations using a mean-field theory. According to the cubic crystal symmetry, the continuum form of the electric polarisation, $\mathbf{P}$, is given by [233, 258, 259]:

$$\mathbf{P} = (P_x, P_y, P_z) = \lambda^c_{me}(m_y m_z, m_x m_z, m_x m_y), \tag{4.4}$$

where $\{x, y, z\}$ define a basis following the $\langle 1\,0\,0\rangle$ crystal directions. The material parameter, λ^c_{me}, is the magnetoelectric coupling constant and is related to the strength of the spin-orbit coupling interaction.

As seen in Eq. 4.4, the electric polarisation is determined by the moment directions that constitute a particular spin texture, and we further show this dependence in Figure 4.11 a to d. For a magnetic helix directed along the [1 0 0]

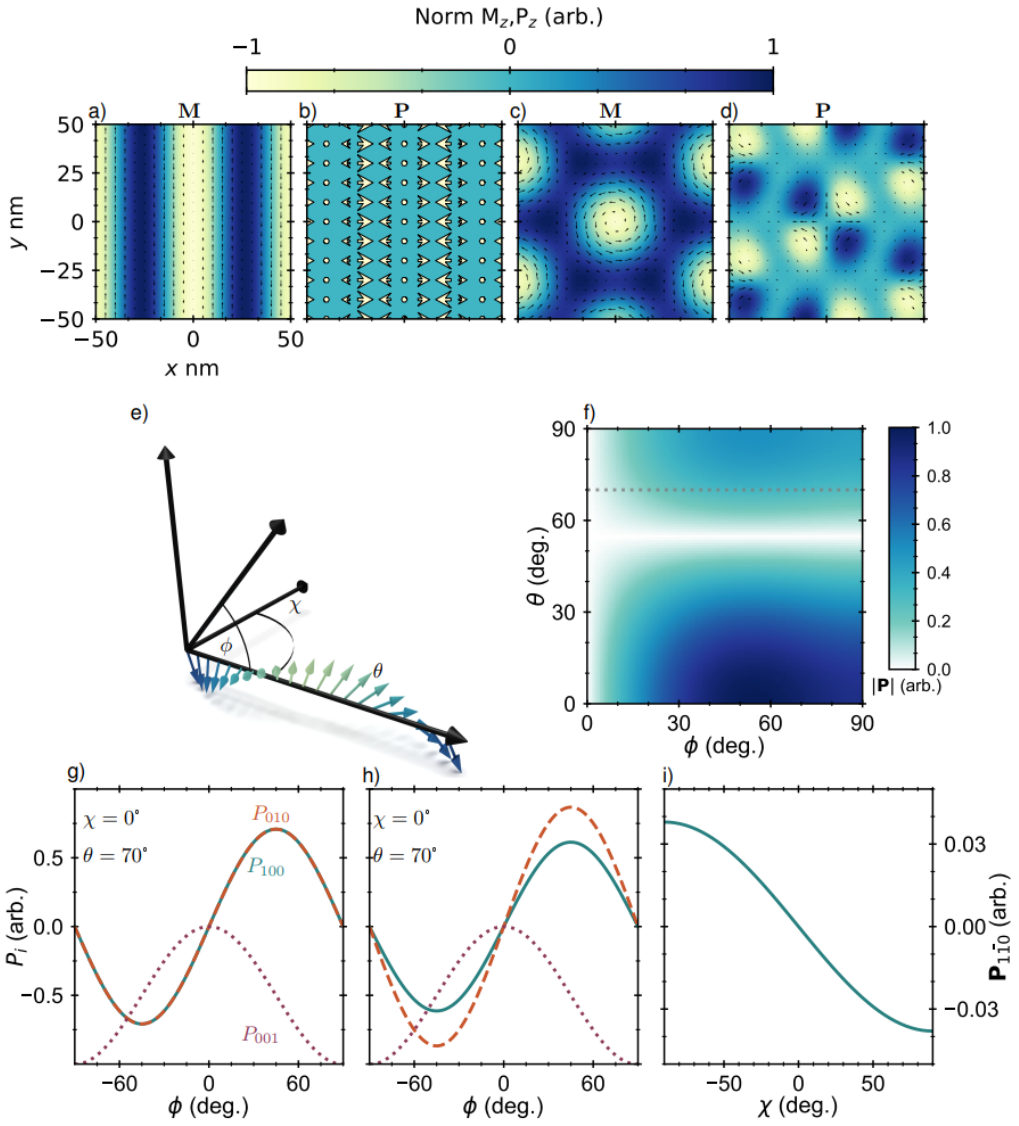

Figure 4.11: a) Magnetization of a helical spin-texture with wavevector along the [1 0 0] (x) direction. b) The electric polarisation induced by the helical state in (a). c) Magnetization of a skyrmion lattice with periodic components confined within the [1 0 0]-[0 1 0] (x-y) plane and concomitant polarisation in (d) which shows a cancelling electric quadrupole when integrated across an entire skyrmion. e) Schematic of a tilted conical state with conical angle θ ($\theta = 90, 0$ degrees for helical/field-aligned state respectively). Polar-angles of ϕ, χ are used to describe the orientation of the TC state. f) Map of total polarisation, $\mid \mathbf{P} \mid$, as a function of θ and ϕ for a particular equatorial angle $\chi = 0$. g-h) The individual components of the **P**-vector as a function of equatorial angle ϕ with $P_{100}, P_{010}, P_{001}$ being blue solid, brown dashed and purple dotted respectively and with $\chi = 0$, 5 degrees for (g) and (h) respectively in agreement with experimental observations. The ϕ dependence follows the path given by the gray dashed line in (a). i) Induced polarisation along the $[1\,\bar{1}\,0]$, $P_{100} - P_{010}$, as a function of equatorial angle χ for a fixed $\phi = 30$ degrees, taken from experimental observations.

direction (a), the resultant polarisation (b) appears with twice the helical frequency and aligns along the propagation vector of the helix. In (c), we show the magnetization of a skyrmion lattice with periodic components confined within the [1 0 0], [0 1 0] plane (in agreement with LTS) and we find that each skyrmion possess an electric quadrupole moment in (d). For both of these spin-textures, integrating across the magnetic unit cell results in net-zero polarisation, and as such little electric field dependence is measured. However, magnetic structures which deviate away from high-symmetry crystal directions may induce a non-vanishing polarisation when integrated across the magnetic unit cell.

One example of such a magnetic state with a non-vanishing polarisation is the tilted conical state. The orientational dependence (ϕ) of the electric-polarisation generated by a tilted conical state for any conical angle (θ, see Figure 4.11 e for angular definitions, and Appendix B for derivation) is shown in Figure 4.11 f. For $\phi = 0$, the wavevector, $\mathbf{q}$, lies along the [0 0 1] direction, and we find there is no induced polarisation for any value of θ. However, even at minor tilt angles (where the state is defined as a tilted cone rather than regular conical state), such as $\phi > 10$ degrees, the tilted conical states induce a significant electric polarisation for a range of conical angles. The vectorial nature of the electric polarisation as a function of ϕ, is shown in Figure 4.11 g and h. This dependence follows the gray-dashed line in Figure 4.11 a, with the conical angle $\theta = 70$ degrees in agreement with the derivation in Appendix B. For the case where the equatorial (χ) angle is zero (Experimentally realized for $E = 0$ V), the polarisation along the [1 0 0] and [0 1 0] crystal directions show an equal, antisymmetric behaviour about $\phi = 0$, in contrast to P_{001}. In this configuration, the polarisation components would then cancel or lie orthogonal to the applied E-field along the $[1\,\bar{1}\,0]$, and the magneto-electric coupling term would not contribute to the overall magnetic free energy.

However, when an equatorial rotation, $\Delta\chi$ is introduced, the degeneracy between P_{100} and P_{010} is broken and a non-vanishing polarisation ($\mathbf{P_{1\bar{1}0}}$) is induced,

see Figure 4.11 h. Here we choose $\chi = 5$ degrees, in agreement with the maximum deflection observed in Figure 4.8. Due to its antisymmetric properties, this polarisation direction changes sign depending on the value of ϕ, akin to reversing the E-field polarity. This change of sign can further be seen in Figure 4.11 i, which shows the value of $\mathbf{P_{1\bar{1}0}}$ as a function of χ for the experimentally determined value of $\phi = 30$ degrees. This deflection of the TC wavevector along the χ direction, when in the presence of the electric field, lowers the free energy of the system via a finite magnetoelectric coupling. However, this deflection causes an increase in anisotropy energy. By expanding the free energy density [156, 177, 167], integrating over a conical period and differentiating with respect to χ (see appendix B), we find the tilted conical deflection along χ direction for small E to be:

$$\frac{\partial \chi}{\partial E} \approx \frac{\lambda^c_{me} \cos\phi f(\theta)}{\gamma q^2 \sin^2\theta \sin^3\phi + K \sin^4\phi g(\theta)}, \tag{4.5}$$

where γ, K are the AEI and MCA constants respectively. $g(\theta)$ and $f(\theta)$ are trigonometric functions of conical angle only. The linear dependence of the χ-deflection with respect to the applied E-field in Eq. A.5, matches the relationship found in experimental data in Figure 4.8 e, showing that the magnetoelectric coupling is less significant than the anisotropic magnetic interactions. The magnitude of the E-field which reorients the TC direction can be reduced by engineering systems with a large coupling constant λ^C_{me}, or by minimising the anisotropic constants. However, reducing the value of K and γ destabilises the TC texture [156, 177], which needs to remain a local minima in the free energy landscape to act as a barrier state within a device setting.

4.5 Demonstration of a Novel Control Mechanism

This Chapter has so far focussed on the experimental observation that the skyrmion-coexisting tilted conical states within Cu_2OSeO_3 can be reoriented via an E-field,

as well as providing an explanation at the mean-field level. In this final section of this Chapter, we turn our attention to the potential impact of our findings.

The current data revolution is being driven by rapid developments within the field of electronics, which has been accelerating since the Nobel-prize-winning development of the bipolar junction transistor [260]. However, the ever-growing demand for higher processing speeds together with more compact data storage has lead to significant environmental concerns due to inevitable increases in energy consumption. One solution is to find alternative, low-energy transistor-mechanisms. As first discussed in Chapter 1, magnetic skyrmions are an active research area with the aim of exploiting possible functional devices. Here, we show that skyrmions are suitable candidates for transistor-like devices, as we are able to control the path of a magnetic skyrmion via the orientation of another localised state. For the purpose of an electric-field-controlled transistor-like device, it is essential that the orientation of this localised state can be controlled by an electric-field, as it is the orientation of this state that influences the trajectory of the skyrmion. We show this via time-dependent micromagnetic simulations, which ultimately prove that by using a specific device-geometry[1], a skyrmion can be deflected into different channels, and be destroyed, in analogy with the three outputs of an electronic double transistor: (-1, 0, 1).

The micromagnetic simulations of the skyrmionic double transistor device were performed with the Ubermag [261] meta-package which uses OOMMF [262]

[1]We note that at the nanoscale the specific magnetic configuration present in our bulk sample during the SANS experiment is significantly different to the spin-configuration investigated micromagnetically here. As always, a direct translation between reciprocal space studies on a bulk system to a real space simulation of a micron-sized device is plagued with caveats. We highlight that whilst there is not a one-to-one spin-mapping between our sample and the simulations, the crux of these simulations are to show that skyrmions can be deflected by co-existing magnetic states, which in our experiment were the E-field-dependent tilted conical phase.

as the micromagnetic system driver. The simulated system was specified with total dimensions $1000 \times 250 \times 5$ nm, using finite difference cells with a volume of 5 nm^3, with a number of cell switched off by setting their magnetization to zero to obtain the desired geometry. We describe the transistor system using the simplest skyrmion-hosting micromagnetic energy functional of a chiral magnet with symmetry class T, which reads:

$$E = \int_V A(\nabla \mathbf{m}) + D\mathbf{m} \cdot (\mathbf{m} \times \mathbf{m}) - \mu_0 M_s \mathbf{m} \cdot \mathbf{H_a} \, \mathrm{d}V, \tag{4.6}$$

where $\mathbf{m}$ is the normalized magnetization, $A = 3.5 \times 10^{-13}$ J m^{-1} is the continuum isotropic exchange constant, $M_s = 1 \times 10^5$ A m^{-1} is the saturation magnetization, $D = 7.4 \times 10^{-5}$ J m^{-2} is the isotropic DMI constant, $\mathbf{H_a}$ is the applied magnetic field which was set with a constant magnitude $\|\mathbf{H_a}\| = 4 \times 10^5$ A m^{-1} applied mostly along the z-direction (out of plane), tilted by 1 degree towards the y-direction to break symmetry. These values are the experimentally determined magnetic parameters of Cu_2OSeO_3[263]. To ensure we had an initial state within an energy minima, the state was relaxed using the `MinDriver()` method. After the state was relaxed, we used the `TimeDriver()` method, which relaxes the system taking into account the magnetization dynamics which are governed by the Landau-Liftshitz-Gilbert (LLG) with spin-transfer torque from the Zhang-Li (ZL) model:

$$\frac{\mathrm{d}\mathbf{m}}{\mathrm{d}t} = -\gamma \mathbf{m} \times \mathbf{H_{eff}} + \alpha(\mathbf{m} \times \frac{\mathrm{d}\mathbf{m}}{\mathrm{d}t}) + \gamma\beta(\epsilon(\mathbf{m} \times \mathbf{m_P} \times \mathbf{m}) - \epsilon'(\mathbf{m} \times \mathbf{m_P}), \tag{4.7}$$

where $\gamma = 2 \times 10^5$ m A^{-1} s^{-1} and $\alpha = 0.5$ are the default values gyromagnetic ratio and damping parameters respectively. In a small number of cells within the barrier region, the gyromagnetic ratio was set to 0 to approximate the effects of pinning required for the localized state [264]. $\beta = 0.5$ is the current density ($j_x = 100$ A m^{-2}) dependent ZL damping parameter, ϵ, ϵ' and $\mathbf{m_P}$ are the spin transfer terms and electron polarisation direction. Time-dependent micromagnetic simulations were done using a step-size of 2×10^{-11} s, with every 100 steps saved for a total of 501 frames.

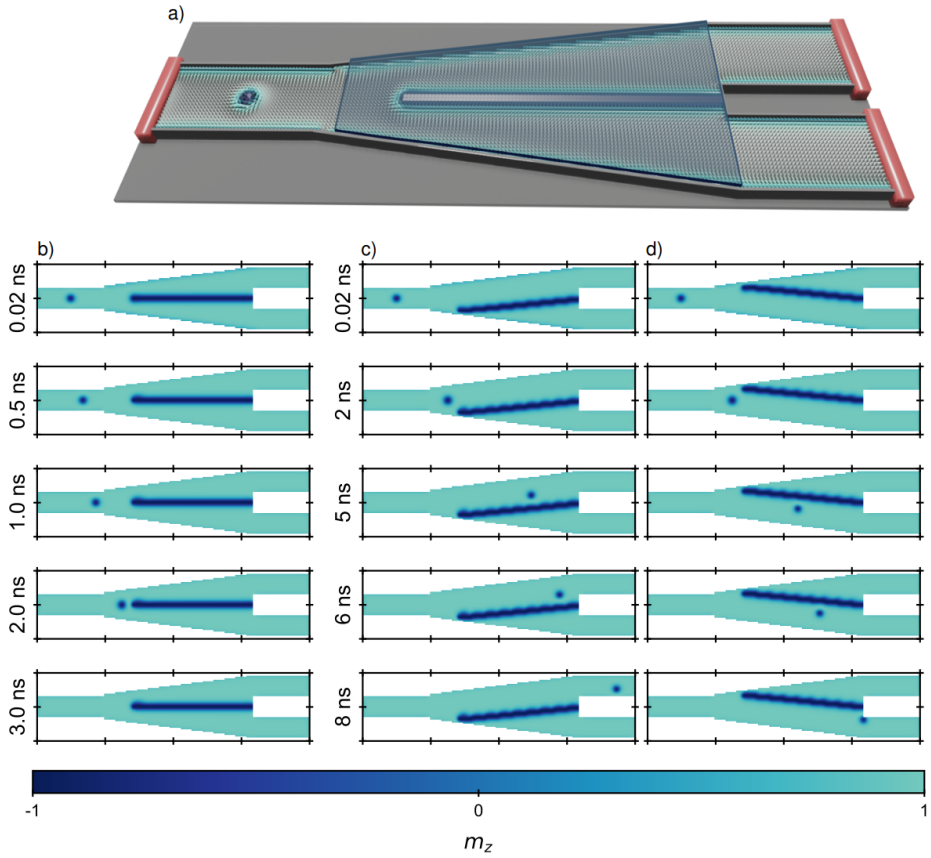

Figure 4.12: a) Example schematic of a skyrmion double transistor with current contacts on either terminal (orange) and the E-field contacts illustrated as the blue plate above the division. b) Skyrmion double transistor with the barrier state aligned in the neutral state illustrated as a function of time. The skyrmion propagates along the track until it is annihilated by the localized barrier texture. c, d) Skyrmion double transistor aligned as one of the two active states such that the localized barrier texture is oriented to mimic the effect of an applied E-field on the TC state. In each case the skyrmion is repelled by the barrier forcing its propagation along one of the two possible paths.

As shown by our simulations in Figure 4.12, an isolated skyrmion is driven downstream towards the two possible exits, guided by edge-twist states [264]. A number of mechanisms have been proposed to induce isolated skyrmion motion, including thermal and magnetic field gradients [265, 266, 108]. However, despite Cu_2OSeO_3 being an insulator, we decided to use the only available micromagnetically implemented method of using a spin-polarised current ($j_x = 100\ \mathrm{A\,m^{-2}}$), which drives the skyrmions via spin transfer torque [267]. In reality, one could use an alternative driving method, engineer a two-layer device consisting of conducting multilayer that is strongly coupled to an insulating region, or add insulating contacts across the device that would allow the creation of a temporary electric field to set the direction of a pinned conical state within a conductive sample via an instantaneous magnetoelectric coupling.

Initially, we relax the system to form an isolated skyrmion, together with a strip of negative magnetization to act as the barrier state in place for the tilted cone, since the 2D projection of a tilted cone with a wavevector component along z is non-physical. We give the barrier state three different starting angles to mimic the effect of using an electric field with $E < 0, E = 0$ and $E > 0$, analogous with our experimental results. For $E = 0$ (Figure 4.12 b) the skyrmion is forcefully driven towards the barrier state, before eventually colliding and annihilating with the barrier state, comparable to the edge-state destruction of skyrmions [268]. However, in Figure 4.12 b and c, the inherent repulsive interaction between the barrier state and the skyrmion causes an alteration in the skyrmion's trajectory. This alteration directs the skyrmion to move towards one of two possible exits. Depending on the angular direction of the barrier state, the skyrmion arrives at the relevant exit gate at different times due to the the skyrmion Hall-angle [226], which arises as a consequence of the skyrmion winding number, by either aiding/hindering the deflection away from the barrier state.

This gives the device three possible output states: skyrmion deflected down,

skyrmion deflected up, and skyrmion annihilated. This output is analogous to an electronic double transistor, which are frequently used in series for the creation of the NOR logic-gate; a universal logic gate that can perform the AND, OR and NOT logic-functions. The practical realization of such a device would allow for all of the operations required by skyrmion computing, as well as providing a useful method to control the number of skyrmions within other proposed skyrmion computing schemes [125, 269, 270, 271]. We have demonstrated that by using an E-field, we can deterministically control the propagation direction of the TC texture. This presents an interesting opportunity for skyrmionic devices by utilizing the fact that well-behaved magnetic states, that are each local minima of the magnetic Hamiltonian (e.g. isolated LTS and localized TC states, shown theoretically to exist [272]), by definition have repulsive interactions [273]. This inherent repulsion between coexisting states allows a novel mechanism to directly manipulate the direction of moving skyrmions within devices settings. For example, individual skyrmions within a racetrack can have their trajectories altered through the interaction with a localized conical state. The skyrmion motion alters according to the orientation of a localized conical state, which is dependent on the magnitude and direction of an applied E-field.

4.6 Conclusions

In conclusion, we have shown that the direction of the skyrmion-coexisting conical states can be controlled by using an applied electric field. We have explained that the microscopic origin for the E-field-induced conical state deflection is well accounted for by using mean-field theory, and shown that this deflection is linear with the magnitude of E. Our findings open up the possibilities of using localised conical states within nanosized skyrmion racetracks as bumper states, which guide the skyrmions towards particular outputs whose outcome can be controlled using an electric field. In particular, we have performed time-dependent micromagnetic simulations of a skyrmion double-transistor device, which is a key element in realizing skyrmion computing and other advanced spintronic devices.

Chapter 5

Resonant X-Ray Scattering from Gd_2PdSi_3

In this Chapter, we investigate the centrosymmetric, intermetallic material Gd_2PdSi_3. Recently it has been reported that a hexagonal lattice of nanosized (2.4 nm) magnetic skyrmions exist within the material. These are not only far smaller than those observed in the B20 materials (MnSi is the smallest at 18 nm), but require a new ordering mechanism due to the lack of a global DMI from the symmetry of the crystal structure. Previous experiments have provided evidence for skyrmions in a region (SkL phase) of greatly increased Hall-resistivity, which the authors attribute due to the topological Hall effect. The skyrmions are flanked in field by two other incommensurate magnetic phase, termed IC-I and IC-II at low and high-fields respectively.

Here, we perform magnetometry measurements and resonant x-ray experiments to investigate the incommensurate magnetic textures within the material. In agreement with previous findings, we find there are three incommensurate textures and that transitions between them can be induced by changing the strength of the magnetic field applied along the crystal c-axis. We further develop our understanding of the material by revealing that a large amount of scattered x-ray intensity arises from charge scattering effects, hindering a thorough interpreta-

tion of the form of the spin-textures when looking at diffracted intensities alone. We overcome this issue by performing a full-linear polarisation analysis (FLPA), which has the capability to separate the contributions of charge and magnetic scattering. Here we find that the IC-I and SkL phases are composed of elliptical helices which are modulated in amplitude, and the charge scattering is a result of stacking faults in the crystalline superstructure, leading to an incoherent, diffuse background. The IC-II phase takes the form of a spin-density-wave. All these phases require that the moment magnitude varies as a function of space, something previously unmentioned in the literature. We therefore suggest a mechanism which uses local DMI, which itself arises due to the crystallographic superstructure, to explain these moment-varying spin textures.

5.1 Introduction

5.1.1 A Brief History of Gd_2PdSi_3

The series of rare earth (R) ternary silicides, R_2PdSi_3, were first synthesised in 1989 and found to mainly order antiferromagnetically with Néel temperatures between 8 and 21 K [274]. Notably, Nd_2PdSi_3 displays anomalous ferromagnetic behaviour, attributed to the hybridisation of the local $4f$ moments with the conduction electrons [275]. Of the series, the Gd member receives the greatest interest due to the large number of interesting physical properties, including: a resistivity minimum at 45 K that is suppressed within a magnetic field [276, 277, 278, 279], slow magnetic relaxation effects that are not due to spin-ice disorder [280], highly anisotropic behaviour despite Gd being an S-state ion [281], first-order-like metamagnetic transitions [281], a negative magnetoresistance [281], a large magnetocalorific effect [281, 282, 283], as well as non-linear Hall [281, 78], and Nernst effects [284].

Of particular interest is the Hall effect, which was shown to be strongly increased within a region of phase space between the two metamagnetic transitions

[281, 78]. However, the physical origin of such an enhanced Hall effect was initially thought to be modification of the Fermi surface across the metamagnetic anomaly, long before Hall contributions arising from magnetic topology were conceived [285]. More recently, it has been suggested that such a large addition arises from nanoskyrmions [78]. However, we note that magnetic-field-induced changes to the Fermi-surface cannot be ruled out, and it is challenging[1] to perform band-structure-mapping techniques within a magnetic field such as angle-resolved-photoelectron-emission-spectroscopy (ARPES). However, field-induced changes to the Fermi-surface were observed using the de Haas-Van Alphen effect in another related nanoskyrmion material, $GdRu_2Si_2$ [286].

For both Gd_2PdSi_3 and Tb_2PdSi_3, ARPES measurements were used to demonstrate Fermi-surface nesting in the absence of an external magnetic field, leading to the momentum-dependent Ruderman-Kittel-Kasuya-Yosida (RKKY) interaction having a maximum coupling strength at a wavevector equal to the propagation vector of the corresponding spin-structures [287]. Furthermore, diffuse neutron scattering was employed to determine the coupling between a number of Gd-atoms within the unit cell, and found that the interactions were spatially extended with a change of sign, consistent with an RKKY mechanism [288]. Despite this experimental evidence, a number of conflicting theoretical mechanisms have been proposed to stabilise the nanoskyrmions within Gd_2PdSi_3. In particular, two first-principles studies investigated the nanoskyrmion formation mechanism in Gd_2PdSi_3. The first study determined the responsible mechanism as being frustration effects between the antiferromagnetic/ferromagnetic couplings between the Gd-4f/Gd-5d orbitals respectively [289]. However, the later study

[1]For ARPES, the band structure is mapped by exploiting the photoelectric effect, whereby using an incoming photon of a particular energy and wavevector, the band structure of the surface of the materials can be precisely mapped by measuring the emission angle and energy of the ejected photo-electron. Performing this within almost any magnetic field deflects the ejected electrons, hindering a thorough characterisation of the band structure.

fully resolved the nested band structure [290], and in agreement with the experimental findings, found the RKKY interaction fully accounted for the ordering of zero-field state.

This picture gets even more confounding when we add to the complexity by considering the crystallographic superstructure of the material, something previously neglected. The crystallographic superstructure is present across all the the members of the R_2PdSi_3 series [291]. As shown in Figure 5.1 a, the primitive unit cell of the material is composed of hexagonal planes of Gd atoms intercalated between a honeycomb mix of Pd/Si atoms in a 1:3 ratio. Typically, a random mix of Pd/Si is considered, yet it has been shown that the primitive cell undergoes a $2 \times 2 \times 8$ times increase due to the stacking of inequivalent layers of Pd/Si. The super-cell is shown in Figure 5.1 b. This increase leads to a great increase in the number of locations in reciprocal space that allow constructive interference, which can be seen in the neutron diffraction pattern showing additional crystallographic peaks occurring at $[h + \frac{1}{2}, h + \frac{1}{2}, \frac{l}{8}]$ [291].

As we have seen, Gd_2PdSi_3 is attracting great research interest and a large number of mysteries about the material still remain. In the rest of the Chapter, we show the results of magnetometry and resonant x-ray scattering experiments which both highlight the existence, and characterise their form, of a number of ordered magnetic phases within the material. Furthermore, we also find a stepwise transition in temperature, which has been under-reported in previous studies. We explain these findings by highlighting something currently unappreciated in the literature, the presence of local DMI in an overall centrosymmetric material.

5.2 Results and Discussion

In order to reveal the nature of these spin-textures, we cut a $2 \times 2 \times 5$ mm^3 single crystal of Gd_2PdSi_3 that was isolated from a large boule grown by the optical floating zone technique at the University of Warwick. X-ray Laue diffraction

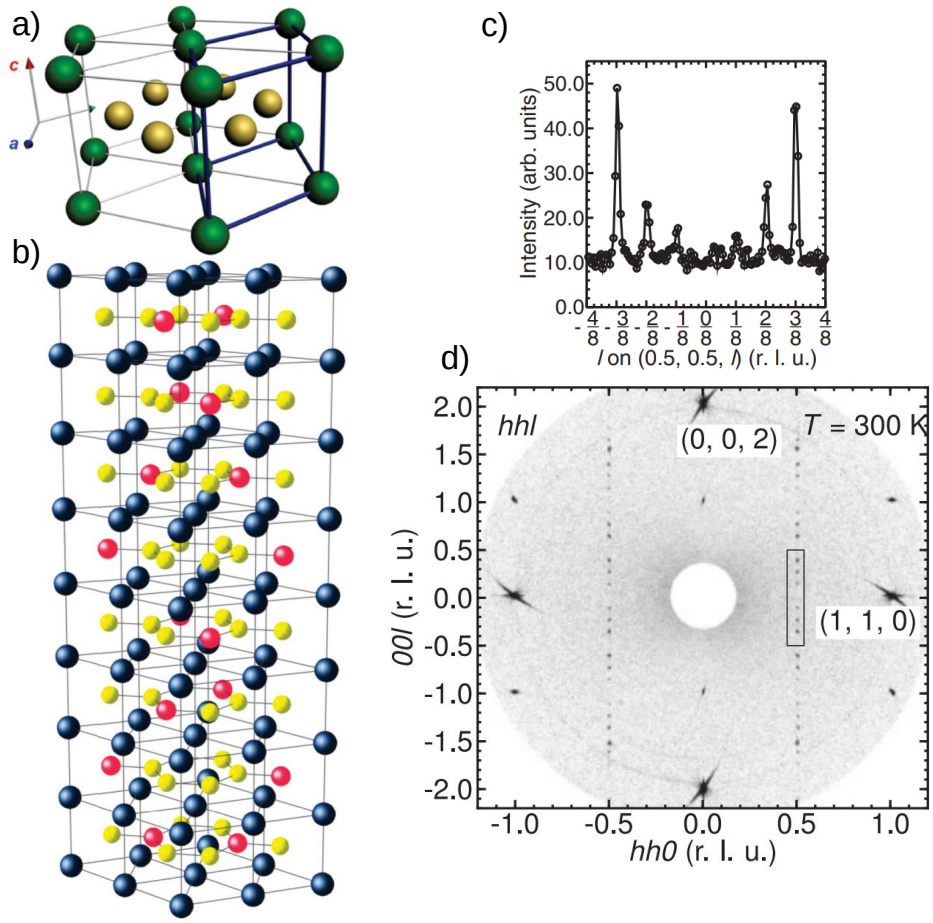

Figure 5.1: All sub-figures are taken from [291]. a) The basic AlB_2 structure. In green are atoms on the $1a$ sites (0, 0, 0), in gold are the atoms occupying the $2d$ sites. The c to a ratio is close to one. b) Sketch of a possible symmetry-degenerate superstructure, with the layer sequence ABCDBADC. c) A line scan across the rectangle shown within the diffracted intensities from reciprocal *hhl* plane of Tm_2PdSi_3 at 300 K in (d).

was used to determine the sample orientation and a high level of crystallinity was observed prior to performing a resonant elastic x-ray scattering (REXS) experiment at the I16 and P09 beamlines of Diamond Light Source and PETRA IV respectively.

5.2.1 Magnetometry

Magnetic susceptibility measurements were performed using a Quantum Design MPMS3 at the I10 support laboratory, Diamond Light Source. Here, a drive field of 1 mT at 10 Hz was used to measure the AC-susceptibility which is useful for identifying magnetic phase transitions. A magnetic phase diagram was created by sweeping the magnetic field, parallel to the c-axis, from 0 to 2 T. These field-scans were measured under a zero field cooling (ZFC) protocol, with each scan finalising by warming the sample above 30 K, and setting the field to zero before driving to the new temperature for the next field scan. The resultant phase diagram is shown in Figure 5.2 a, which displays clear peaks in the magnetic susceptibility, χ', that indicate magnetic phase transitions between the IC-I and A (SkL) phases, the A and IC-II phases, as well as a broad region of increased susceptibility near zero-field between the paramagnetic to IC-I phase boundary.

To investigate the paramagnetic to IC-I phase boundary in more detail, we performed a high resolution DC magnetisation temperature scan using a Quantum Design MPMS2, at Durham University Physics Department, within a near zero magnetic field (1 Oe), and show the results in Figure 5.2 b. Here, a large temperature range is shown for completeness, and shows a large increase in magnetisation at the ordering temperature of 21 K, in agreement with previous studies [78]. Interestingly, we find novel behaviour towards higher temperatures, between 125 and 180 K, which shows a number of inflections suggesting that the material possesses a more complex magnetic behaviour than previously considered in the literature. A detailed analysis of this high-temperature behaviour is beyond the

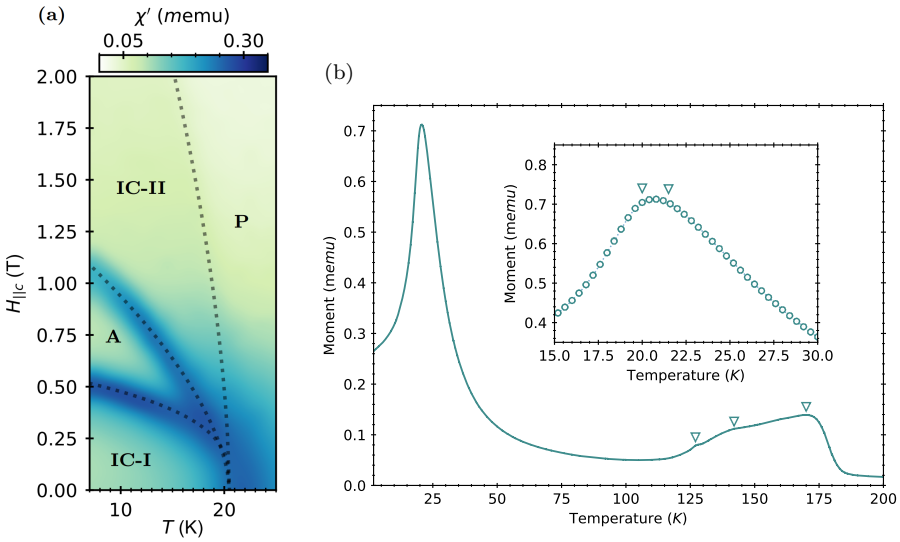

Figure 5.2: a) The real component of AC susceptibility phase diagram of Gd_2PdSi_3 showing the locations of the incommensurate (IC-I/II), previously proposed skyrmion (A) and paramagnetic (P) phases. b) Temperature scan of the magnetisation of Gd_2PdSi_3 within a low-magnetic field of 1 Oe. A number of inflections can be seen and are marked with teal triangles. Inset shows more detail near the critical temperature.

scope of this thesis[2].

As shown by the inset of Figure 5.2 b, the broad peak found in the phase diagram has the possibility of being two successive phase transitions from the paramagnetic to the IC-II, before then transforming into the IC-I state. Here, the difference between a broadened peak and two clear inflections is ambiguous, but previous work using high resolution dilatometric measurements determined that there are two distinct magnetic phases at zero field with different magnetoeleastic coupling constants [292]. In the next section, we perform resonant elastic x-ray scattering, which reveals a deeper level of understanding about these magnetic phase transitions and the form of the incommensurate magnetic phases within the material.

5.2.2 Resonant X-ray Scattering from I16

As shown by the magnetic phase diagram in Figure 5.2 a, cooling Gd_2PdSi_3 below its ordering temperature of 22 K results in a number of different magnetic phases, in which phase transitions between (at least) three distinct magnetic phases can be induced by applying magnetic fields of various strengths along the crystalline *c*-axis. Due to the interference between the crystallographic structure and the incommensurate nature of the magnetic textures, an increased number of locations in reciprocal space can be brought into the diffraction condition. These locations take the form of satellite peaks around a structural Bragg peak, with each satellite isolated by the magnetic wave-vector of the relevant magnetic phase. A diagram of reciprocal space can be found in Figure 5.3 a, which shows a number of crystalline Bragg peaks (orange) within the *ab*-plane, as well as the locations of the magnetic satellites (blue). In (b), we show the scattered wavevector ($\mathbf{k}'$) within the region of reciprocal space that is relevant for our study. We

[2]preliminary analysis suggests that this behaviour could arise from short range ordering with the stacking faults in the layered system, which we shall talk about in more detail in later sections in this Chapter

chose to investigate three satellite peaks surrounding the crystalline (300)-Bragg peak, labelled as $\mathbf{q}_{-1,-2,-3}$ which arise from textures with a magnetic wavevector $\tau_{-1,-2,-3}$ respectively. As highlighted in (b), the scattered x-ray wavevector is nearly collinear with τ_{-2}, with a deflection of less than 7°. This directional similarity, together with the use of polarized x-rays, allows the modulated moment within the basal plane to be broken down into components which are parallel and perpendicular to $\vec{\tau}_{-n}$, as we shall see later in Eq. 5.1.

To obtain magnetic sensitivity, we tuned into the Gd L_2 edge (7.931 keV), with incoming x-rays linearly polarised within the scattering plane (π polarisation in Figure 5.3 c). The polarisation of the outgoing scattered x-rays were determined using a gold (222) analyser crystal[3] to separately measure the outgoing x-rays that were polarised either within the scattering plane, π–σ, or perpendicular to the plane, π–π. In our experiment, the x-ray out-of-plane (σ) direction was collinear with the crystallographic c-axis. The resonant dipole scattering amplitude for each polarisation channel then takes the form [154]:

$$\begin{aligned} f_{\pi\sigma} &= -iF_1(\vec{k}' \cdot \vec{m}_{\perp c}), \\ f_{\pi\pi} &= F_0 \cos 2\theta + iF_1 \vec{m}_{\|c} \sin 2\theta, \end{aligned} \tag{5.1}$$

where θ is the scattering angle, $\vec{k}'$ is the scattered x-ray wavevector and $\vec{m}_{\|c,(\perp)}$ is the magnetisation parallel (perpendicular) to the crystallographic c-axis. The factors F_n determine the strength of the resonance and are highly energy dependent. Resonant charge scattering is determined by the $n = 0$ term, whereas $n = 1$ gives the first-harmonic resonant magnetic scattering. Higher harmonic terms exist but are not relevant for this study. Field scans were taken after a zero-field-cooled (ZFC) protocol, up to the calibrated maximum field of 0.95 T. Temperature control was achieved using a ^{4}He cold finger cryostat. A magnetic field was applied using a water-cooled copper coil electromagnet with iron pole

[3] an analyser crystal is done by trying to find a strongly scattering material, with a Bragg peak which lies close to 90 degrees for your particular x-ray wavelength. The closer the angle is to this extinction angle, the less beam-spillover background ones gets during an experiment.

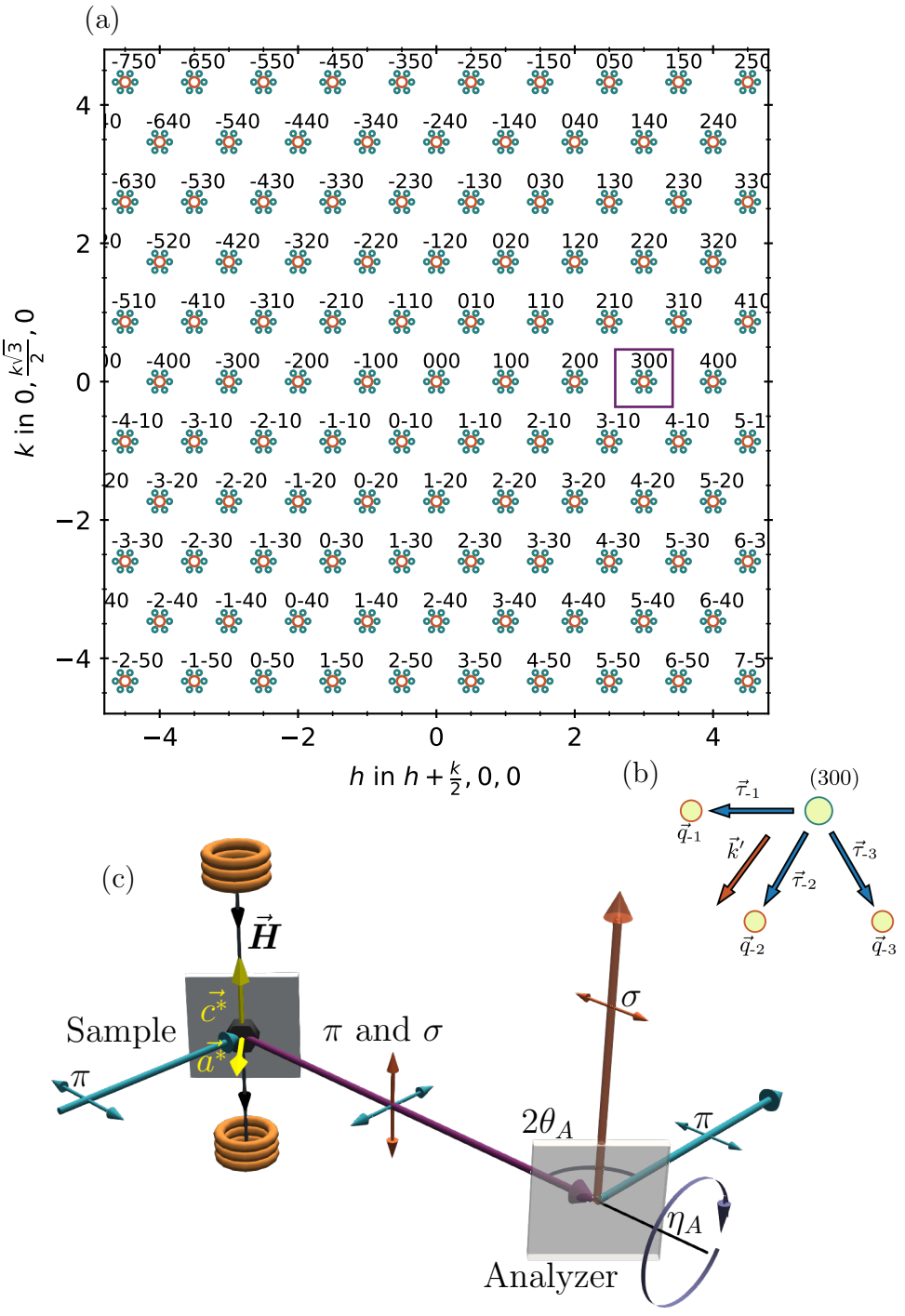

Figure 5.3: a) Diagram of reciprocal space showing the locations of the crystalline Bragg peaks (Orange) and the surrounding magnetic satellites (Teal). b) A zoomed in region of (a) around the (300) Bragg peak, showing the scattering x-ray wavevector being nearly collinear with the magnetic wavevector τ_{-2}. c) Experimental set-up showing the magnetic field ($\vec{H}||c$, the incoming π polarization and the separation of the outgoing x-rays into π–π or π–σ components using an analyzer crystal by rotating the analzer crystal angle η_A from 0 (shown) to 90 degrees respectively.

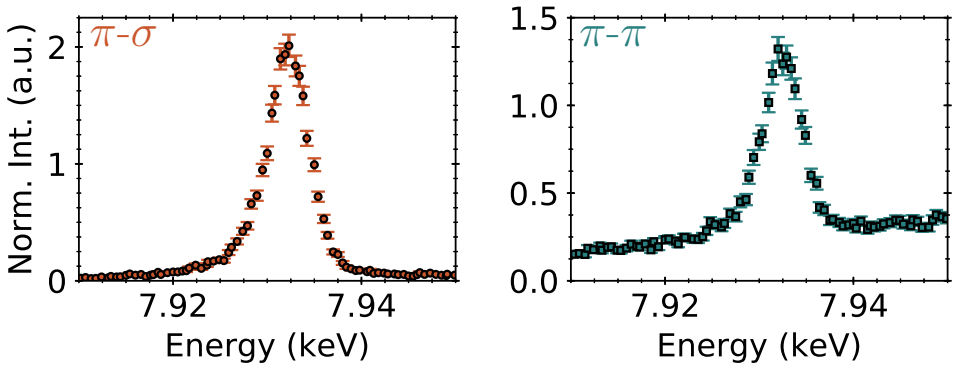

Figure 5.4: a,b) Zero-field scattered intensity at 8 K as a function of x-ray energy across the Gd L_2 edge from the $\vec{q}_3$ satellite in each polarisation channel, π–σ (orange circle) and π–π (teal square) respectively.

pieces.

In this horizontal scattering layout, both the incoming and outgoing x-ray wavevectors are within the crystallographic *ab* plane, and the magnetic field can be applied along the *c* direction. In our setup, as shown by Eq. 5.1, intensity in the spin-flip channel (π–σ) arises from a magnetic modulation parallel to the outgoing x-ray, which is in the *ab* plane, whereas the scattering in the non-spin-flip π–π channel arises from *c*-axis magnetic modulation and/or modulated charge order.

The origin of the scattering can be seen in Figure 5.4 a and b, which shows the zero-field energy scans of the scattered satellite intensity for each outgoing polarisation at a readout temperature of 8 K[4]. In (a), the π–σ channel (sensitive only to magnetic scattering) shows substantial intensity only close to the Gd L_2 edge, and near-zero intensity elsewhere, consistent with the expected large enhancement of the magnetic scattering cross-section on resonance [154]. By contrast, the π–π channel in (b) (sensitive to both charge and magnetic scattering) shows

[4]Note this is the read-out temperature, as discussed later, the readout is substantially lower than the actual temperature.

significant intensity both at resonance and far away from it. This intensity away from resonance cannot arise from magnetic scattering, as the non-resonant magnetic scattering component shown is over two orders of magnitude weaker than the peak at resonance, as expected for purely magnetic x-ray scattering [154], whereas in (b) the averaged off-resonance intensity is much larger at 20% of the resonant peak intensity. We note that it is impossible for this intensity away from resonance to arise from leak-through from the other polarisation channel, as we show this to be near zero in (a). This result shows that a substantial fraction of the incommensurate satellite π–π intensity arises from charge scattering. This charge scattering could have a number of origins, such as the tail-end of a crystalline Bragg peak, diffuse scattering from the presence of structural disorder, or the presence of a low temperature CDW with the same wavevector as the magnetic structures. We will reveal the true the origin in the next section.

The magnetic-field driven behaviour was then subsequently investigated, and we show the polarisation-dependent scattered intensity of each magnetic satellite form the set $\{\vec{q}_{-1,-2,-3}\}$ as shown in Figure 5.5. Here, the intensities were determined by fitting Gaussian functions to rocking-scans across the magnetic satellite peaks, to account for any change in the magnetic wavevector. The intensities from each $\vec{q}_n$ in the π–σ channels (orange curves in Figure 5.5 b to d) arise due to the interaction with an in-plane modulated magnetic moment. For each $\vec{q}_n$, we see an initial increase of intensity with increasing field, up to a maximum near the transition at 0.5 T, followed by a decrease to a non-zero value at the highest measured field of 0.95 T for $\vec{q}_{1,3}$, and near-zero for $\vec{q}_2$. We interpret this reduction to be caused by the magnetic moments uniformly aligning with the magnetic field, reducing the in-plane modulation and thus the scattered intensity at these wavevectors. In addition, we find that the π–σ intensity from $\vec{q}_2$ peak is very small at all fields. This corresponds to a lack of a magnetic modulation along the direction of the magnetic wavevector [154], with the remnant intensity arising due to the small 7 degree angle between the vectors. Our data are

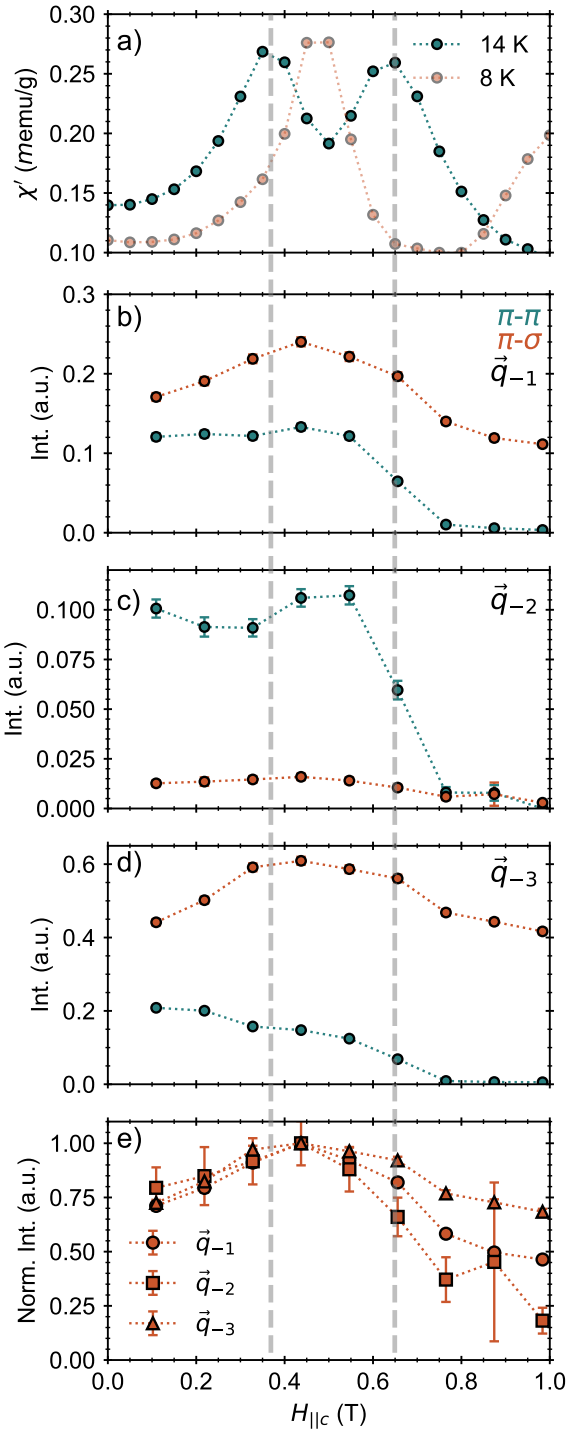

Figure 5.5: a) Real component of the AC-susceptibility of Gd_2PdSi_3 as a function of magnetic field applied along the c-axis at both 8 K (orange) and 14 K (teal). b-d) X-ray intensity separated into the π–π (teal) and π–σ (orange) channels as a function of applied field for each of the incommensurate satellites, $\vec{q}_{-n}$. The temperature for all measurements was nominally 8 K, see discussion in text. (e) Geometrically normalized π–σ intensities for all $\vec{q}_{-n}$ assuming the moment-modulation is perpendicular to $\vec{\tau}_{-n}$.

therefore consistent with in-plane magnetic moment oscillations for all fields lying perpendicular to the direction of the in-plane magnetic wavevector, in agreement with the findings of Kurumaji *et al.* [78].

The intensities within the π–π channels (teal curves on Figure 5.5 c to e) show further interesting features. At low fields, the intensities for the different satellites in the π–π channel are not equal. Previously, residual strain arising from mounting the sample has been suggested to lift the degeneracy of magnetic and charge domains [293, 78]. This results in a higher population of one domain, explaining the increased scattering for $\vec{q}_{-3}$. Upon increasing the field, the intensity from $\vec{q}_{-3}$ drops while the others remain constant, but ultimately results in near-equal intensities for all three peaks at fields above 0.55 T.

Increasing the magnetic field past the phase transition at 0.5 T, we see a decrease of the intensity in the π–π channel, stabilizing at 0.75 T to a near-zero intensity. This field of 0.75 T does not match the magnetic phase transitions observed from AC susceptibility at 8 K (red dataset in Figure 5.5 a) ; in fact, it lies directly between the two transitions at the point where we would expect the magnetic A-phase to be most stable. The origin of this was later found to be a large temperature offset between the thermocouple and sample, and by comparing our REXS data to the 14 K magnetometry we recover the phase-transitions in the correct place. Whilst such a large temperature offset is relatively uncommon, in our experiment we used an unattenuated incoming beam which locally raises the temperature of the sample. By matching the phase-transition signatures from the REXS data in Figure 5.5 b to d to the magnetometry data in (a), we determined a temperature offset of 6 K, with the true temperature being around 14 K.

Information about the relative magnetic domain populations is shown by the geometrically normalized π–σ intensity, $I_n^{\pi\sigma}/(\vec{\tau}_\perp \cdot \vec{k}_{i,n})^2$, which is obtained from the modulus of Eq. 5.1 assuming that the in-plane moment is perpendicular to the

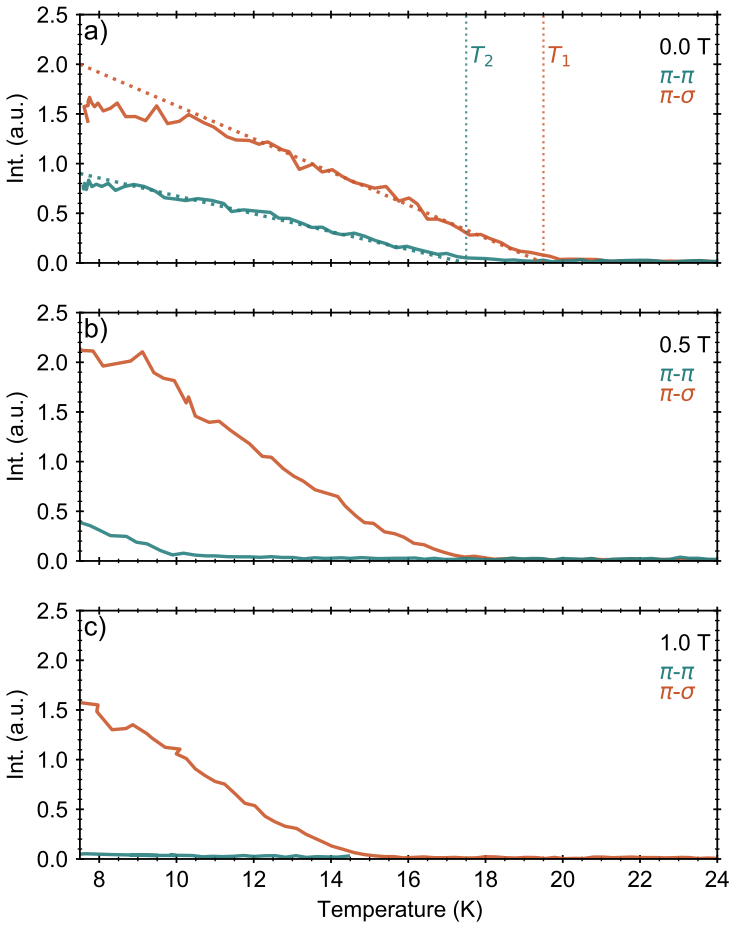

Figure 5.6: a-c) Temperature dependence of the $\vec{q}_3$ satellite with polarisation separated intensity, π–π (teal) and π–σ (orange), within constant magnetic field of 0, 0.5 and 1 T respectively.

magnetic wavevector, in Figure 5.5 e. We find near equal scattering within error for all fields in which the IC-I phase exists, rendering the ability to distinguish the magnetic texture between three single-q textures and one triple-q texture impossible. This observation is at odds with the π-π scattered intensities at low fields, in which $\mathbf{q}_{-3}$ had a larger weighting compared to the other two wavevectors. Here, we assume this is due to crystal strain during the mounting process, possibly giving this low-field spin-texture a greater c-axis component, rather than a greater population. After the magnetic transition, the normalized intensities from the three wavevectors strongly overlap at 0.55 T, and then continually drift apart under an increasing field up to 0.95 T. This shows us that the IC-II phase is most likely composed of separate domains of single-q textures, whilst for the IC-I and A-phase we are unable to categorically rule out either from REXS alone.

We now turn our attention to the temperature-dependent evolution of the magnetic textures in Gd_2PdSi_3. We measured the zero-field temperature dependence of the scattered intensity from $\vec{q}_{-3}$, which we present in Figure 5.6 a. The different polarisation channels show that the onset of the c-axis modulation occurs at an appreciably lower temperature than the planar magnetism (orange/π–σ), suppressed by $\sim$2 K. This step-wise transition reveals the nature of the broad-peak of increased magnetic susceptibility shown in Figure 5.2 b. Specifically, two separate transitions are observed, namely from the paramagnetic to IC-II, then from the IC-II to IC-I respectively. This is in agreement with previous magnetoelastic measurements [292].

At larger magnetic fields, the temperature difference between the c-axis ordering and ab-plane increases from $\sim$2 K at zero field, to $\sim$8 K at 0.5 T, and the c-axis component never appears at 1.0 T. These observations are in agreement with the magnetic phase diagram in Figure 5.2 a, which shows that the IC-II phase becomes more dominant at higher magnetic fields, suppressing the formation of out-of-plane modulated textures such at the SkL phase. Note, in all of

these a significant temperature offset is present, which we again attribute to local beam-heating. In all magnetic fields investigated, we see that the IC-II phase initially forms out of the disordered phase upon decreasing the temperature, before the other spin-texture (if at all). A similar feature has been seen in another nanoskyrmion material, $Gd_3Ru_4Al_{12}$, and was attributed to the evolution of a magnetic helix (which has a *c*-axis modulation) from a 1-dimensional transverse spin density wave (which has no *c*-axis component) [294]. However, the origins for this mechanism and its subsequent discussion has been under-investigated in recent reports on this material. We will provide a possible mechanism for Gd_2PdSi_3 later in this Chapter.

5.2.3 Full-Linear Polarisation Analysis from P09

In order to obtain a more detailed understanding of the incommensurate magnetic textures within Gd_2PdSi_3, we performed a full-linear polarisation analysis experiment at the P09 beamline at the Deutsches Elektronen-Synchrotron (DESY). This beamline features a heavy-load horizontal Psi-diffractometer, a two-axis instrument which is capable of applying up to 14 T within a temperature range between 2.3 to 300 K using the standard variable temperature insert [295], perfect for studying the magnetic textures within Gd_2PdSi_3. Prior to performing the FLPA, we briefly repeated the findings from I16 to calibrate the temperature, energy and identify the field-dependent magnetic phase boundaries. We show these repeated measurements in Appendix C.

During a FLPA experiment, the outgoing x-ray polarization η' is measured for number of incident linear polarization angles η_i, allowing a more detailed investigation of the scattering processes compared with raw intensities alone, see Chapter 2 for a more detailed explanation. In the following section, we investigate the magnetic [3+τ, -τ, 0] reflection, where τ is the magnitude of the wavevector of the incommensurate magnetic texture, at 12 K within magnetic fields of 0, 0.55, and 1.5 T, corresponding to the IC-I, SkL and IC-II phases respectively, as

labelled in the phase diagram in Figure 5.2.

The polarisation of the scattered x-ray is determined by performing angular θ-rocks of a graphite (006) analyser crystal[5], close to the optimum diffraction condition with $2\theta_A \approx 90°$, as shown in Figure 5.7 a. By rotating the angle of the analyser crystal about the scattered wavevector, η_A in Figure. 5.3 c, different projections of the scattered x-ray polarisation are obtained. Fitting the diffracted intensities as a function of η_A (see top of Figure 5.7 b) provides the polarisation density matrix of the scattered x-ray, μ' in terms of the Poincare-Stokes polarisation vector $\mathbf{P'} = (P'_1, P'_2, P'_3)$. Density matrices allow a complete description of the polarisation [155]. The measured values of P_1 and P_2 for the IC-I, SkL and IC-II states for various incoming polarisation angles are shown in Figure 5.7 c as open triangles, squares and circles respectively, offset from each other for clarity. The process of scattering a particular polarisation into another via an optical element with forward scattering power $\mathbf{M}$ is given by $\mu' = \mathbf{M}^{\dagger}\mu_{\mathbf{i}}\mathbf{M}$ [296, 297]. Here, we include both the charge and the magnetic scattering contributions within the refinements, with scattering powers given by:

$$\mathbf{M}_c = F_c \begin{pmatrix} 1 & 0 \\ 0 & \cos 2\theta \end{pmatrix}, \tag{5.2}$$

$$\mathbf{M}_m = -iF_m \begin{pmatrix} 0 & z_1 \cos\theta + z_3 \sin\theta \\ z_3 \sin\theta - z_1 \cos\theta & -z_2 \sin 2\theta \end{pmatrix}, \tag{5.3}$$

where F_c and F_m are the charge and magnetic scattering amplitudes respectively, and the matrix elements describe the transitions between states of different polarisation [154]. The magnetisation directions, z_n, are determined by the scattering geometry [297]. During the refinement, arbitrary magnetic structures can be constructed from a set of irreducible components, $\{\Gamma_n\}$. For our crystal symmetry and the incommensurate magnetic wavevector, only three irreducible components exist, and they can be seen in Figure 5.7 d. These components are analogous to

[5]Similar angle at the Gd-L3 edge to Au (006)

spin-density waves with the magnetic moments that are restricted along a single crystalline direction and vary in magnitude. Specifically, $\Gamma_2 \parallel (1,-1,0)$, $\Gamma_3 \parallel (0,0,1)$, $\Gamma_4 \parallel (1,1,0)$. Since we use a hexagonal coordinate system, Γ_2, Γ_4 are parallel/perpendicular to the magnetic wavevector respectively.

Using MagStREXS[6] [298], we determined the form of the magnetic modulations by fitting a model to the raw data in Figure 5.7 c. The best fit is obtained by considering the outgoing polarisation to arise from two independent, incoherent scattering sources with probability p_i such that $\mu' = p_m\mu'_m + p_c\mu'_c$. This accounts for scattering from separate, incoherent magnetic and charge contributions respectively. The refined parameters are shown in Table 5.1 and the fit by the solid lines in Figure 5.7 c, which are in excellent agreement with the measured data. A fit including coherent magnetic and charge (for example a charge density wave), and those considering magnetic-only contributions poorer still, can be found in the Appendix C.

The presence of an incoherent charge scattering indicates a large amount of crystallographic disorder within the system, which we attribute due to stacking-faults within the superlattice structure [299]. This interpretation is in agreement with our observations of diffuse charge scattering and the crystallographic superstructure with electron diffraction and the x-ray energy scans in the previous sections. The concomitant scattering from both magnetism and diffuse charge explains the inconsistencies to previous interpretations about the form of the spin-textures, which have found circular helices, fan-states and coplanar magnetism when looking at scattered x-ray intensities alone [300, 78].

The elliptic nature of the magnetic states can be seen by the ratio fitted parameters, Γ_3/Γ_4 in Table 5.1, which shows the periodic magnetism lies mostly within the *ab*-plane, with the *c*-axis component at 0 T being diminished by $\approx \frac{1}{\sqrt{2}}$.

[6] We are truly grateful for the help of Pablo Bereciartua, who performed these simulations.

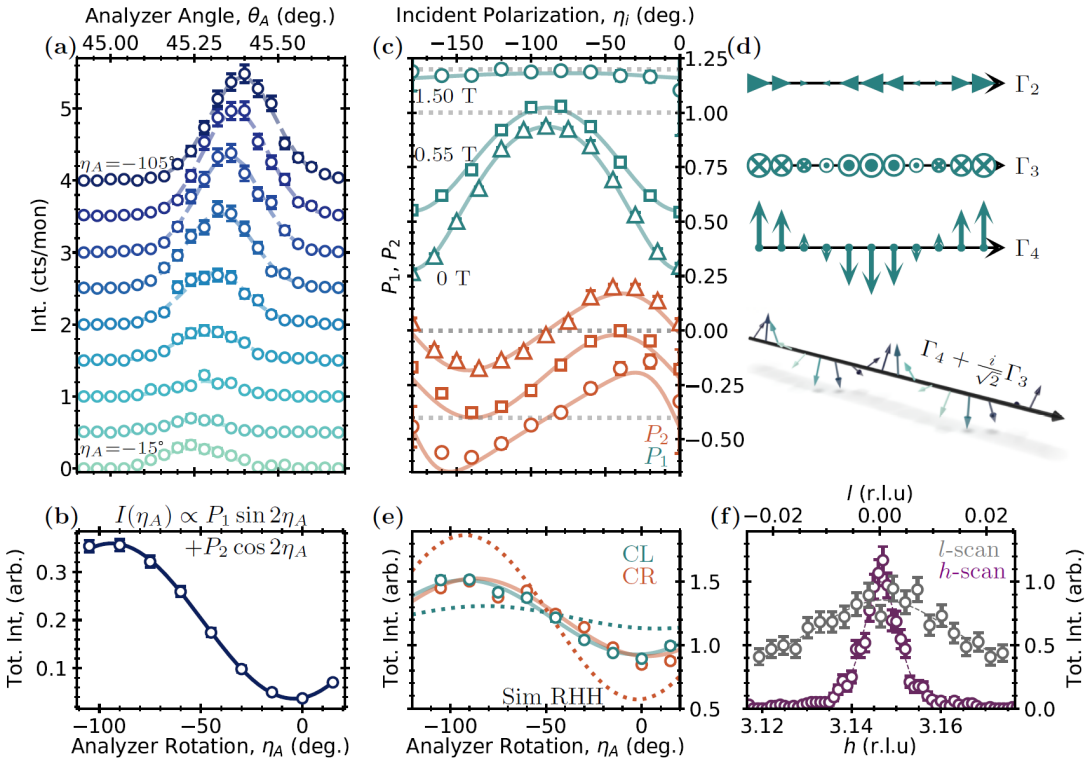

Figure 5.7: a) Rocking scans of θ_A for different analyser crystal orientations. b) Fitted intensities of (a) as a function of analyser rotation, providing P_1, P_2 using equation shown. c) Stokes parameters P_1(blue), P_2(orange) for different incoming polarisations, at 12 K for applied magnetic fields of 0(triangles), 0.55(squares) and 1.5(circles) T. Fits considering two incoherent charge and magnetic sources are shown. d) Real-space diagrams of the irreducible components, Γ_n, and the real-space fitted texture at 0 T. e) Intensity as a function of η_A for circular left and circular right incoming polarisation. Dotted lines show simulation of a right-handed helix (RHH) f) Reciprocal space scans of the magnetic satellite along the l (grey) and h (purple) directions.

Field (T)	Γ_2	Γ_3	Γ_4	α	Modulation Type
0	0	$\pm i0.72(1)$	1	24(1)	Elliptical Helix
0.55	0	$\pm i0.59(1)$	1	16(2)	Elliptical Helix
1.50	0	0	1	36(9)	T-SDW

Table 5.1: Fitted parameters within MagStREXS. The irreducible components $\Gamma_{2,3}$ correspond to SDWs with the moment oscillating parallel/perpendicular to the magnetic wavevector within the *ab*-plane, and Γ_4 being parallel to the *c*-axis. α represents the ratio of the charge and magnetic scattering powers, multiplied by their respective scattering populations.

This is exacerbated at the higher magnetic fields in the SkL phase, which shows a greater ellipticity of ≈ 0.6. This out-of-plane component then vanishes within the IC-II state, revealing that the state is a transverse spin-density wave (T-SDW). The ellipticity of the states requires the moment magnitude to vary in space, which is not the case in a tilted conical or fan-like state [78]. Depending on the superposition and the relative phase-offset between the three degenerate magnetic wavevectors, a lattice of merons/antimerons, skyrmions and phase-separated helices are all candidate phases, and are indistinguishable with diffraction-based techniques. However, our findings show all candidate phases, whose form can be seen later in Figure 5.8, feature an elliptical distortion and a varying moment size.

Notably, the *c*-axis components of the helices are required from the fitting procedure to be out of phase from the in-plane component, meaning these magnetic states have to be chiral and not an oblique SDW, a right-handed helix (RHH) is shown in Figure 5.7 d for clarity. The linear-polarisation of the x-rays leads to ambiguity in sign of the imaginary Γ_3 component, meaning both right-handed textures and left-handed textures give identical signatures in the measured data. However, these two chiralities can be identified by using circularly polarised x-rays. This can be seen in Figure 5.7 e, which shows a simulation of a RHH with both right and left circularly polarised x-rays (dotted lines), and featured a clear

difference in the diffracted intensities. However, the measured data (open circles) show identical behaviour within experimental error, suggesting there are equal volume fractions of left and right-handed elliptical helices, as expected due to the overall centrosymmetry of the crystal system.

Information about the ordering of the magnetic structures can been seen by the reciprocal space scans shown in Figure 5.7 h, which shows the diffracted intensity as a function of the h and l reciprocal space directions. The full-width-half-maximum, $(FWHM)$, varies between the reciprocal space directions. The real-space correlation length, $\xi = \frac{1}{\pi}(FWHM)^{-1}$, for the two directions is $\xi_c = 30(8)$ Å and $\xi_{ab} = 230(30)$ Å. The short correlation length along the crystalline c-axis is over an order of magnitude shorter than the hexagonal plane, and corresponds to roughly one superstructure cell. Similar to the diffuse charge scattering, the magnetic disorder arises due to the irregular stacking of different crystallographic layers.

The real space form of a selection of possible magnetic spin textures can be found in Figure 5.8. Due to the inability[7] to recover phase information from diffraction-based experiments, it is possible to generate a number of two dimensional, multi-q (magnetic texture with more than one diffraction spot, such as skyrmions) spin-textures by superposing a number of single-q textures. The basis spin texture for the IC-I phase and SkL phase is shown in (a), which shows an elliptical helix constructed as $\Gamma_4 + \frac{1}{\sqrt{2}}\Gamma_3$. Superpositions of this same spin-texture with different wavevectors generate two-dimensional spin-textures, which can be written as [304]:

$$\mathbf{m}(\mathbf{r},\mathbf{q}) = \sum_{\nu=1}^{3} \begin{pmatrix} \sin\theta_\nu \sin \mathbf{q}_\nu \cdot \mathbf{r} + \phi_\nu \\ \sin\theta_\nu \sin \mathbf{q}_\nu \cdot \mathbf{r} + \phi_\nu \\ \pm\xi \cos \mathbf{q}_\nu \cdot \mathbf{r} + \phi_\nu \end{pmatrix}, \tag{5.4}$$

[7] Although diffractive magnetic holography and magnetic-contrast phase-retrieval algorithms have been demonstrated [301, 302, 303].

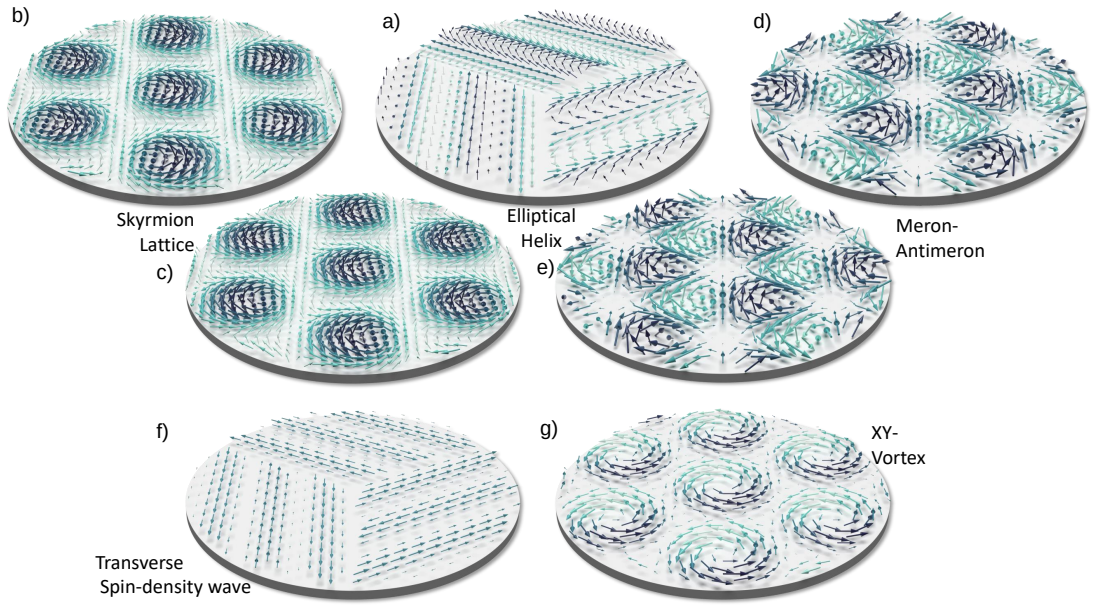

Figure 5.8: a) (top center) the primitive building block of the possible triple-q spin textures (b-e). The following are candidate phases for the IC-I and SkL phases respectively. In a), we have 1-q elliptical helices which may form roughly-equally populated, spatially separated domains of both orientation and chirality. b,c) Elliptical skyrmion spin-textures with different chirality, created by superposing the spin-textures in (a) with no phase shift. d,e) Elliptical Meron-Antimeron lattices with differing chiralities, formed similarly to the skyrmions but differ in terms of a relative phase shift of $\frac{\pi}{2}$ between eacxh single-q strcuture, see text for an in-depth discussion. f,g) Candidate phases for the IC-II region, namely of 1D spin-density-waves and their triple-q superposition state consisting of XY-vortices respectively.

where $\mathbf{q}_\nu$, ϕ_ν and ξ are the wavevector, phase and ellipticity of the νth spiral, respectively, and $\mathbf{r}$ is the position vector. θ_ν is a geometric term to ensure the helices are Bloch-type, such that $\mathbf{m}\cdot\mathbf{q}=0$, and $\phi_\nu=\frac{2}{3}\pi(\nu-1)$. In the following, each wavevector lies along three equivalent directions in the hexagonal plane with $\mathbf{q}_1=(q,0)$, $\mathbf{q}_2=q(-\frac{1}{2},\frac{\sqrt{3}}{2})$ and $\mathbf{q}_3=q(\frac{1}{2},\frac{\sqrt{3}}{2})$. By setting $\phi_{1,2,3}$ to be zero, we generate the lattice of skyrmions in Figure 5.8 b, whose chirality can be reversed as in (c) by changing the sign in the z-component in Eq. 5.4. Similarly, both chiralities of a meron-antimeron lattice can be generated with $\phi_{1,2,3}=\frac{\pi}{2}$ as in (d) and (e). On the other hand, by using superpositions of T-SDW basis (f), one can generate an XY-vortex lattice as shown in (g). Spin-textures (a) to (e) have identical form-factors, are are indistinguishable using diffraction techniques such as REXS.

Whilst in this study we are unable to reveal the true form of the spin-textures, we do unambiguously identify the basis of which multiple-q spin-textures can be built from in all three incommensurate magnetic phases. Furthermore, the diffuse nature of both the magnetic spin-textures and the charge density highlights the importance of the crystallographic superstructure within the material. In particular, the stacking of different layers leads to disorder, as well as local DMI interactions which we shall investigate further in the following section.

5.2.4 Origin of Local Chirality

The crystallographic superstructure in Gd_2PdSi_3 has largely been ignored in the recent experimental and theoretical investigations of the magnetic skyrmions within the material. However, as we have seen in the previous sections, there are a number of implications which the superstructure imposes on the magnetism, not only just increasing the level of disorder due to irregularities in the crystallographic superstructure.

Four distinct arrangements of Pd/Si are allowed through symmetry arguments, and are shown in Figure 5.9 a. Here, the hexagonal lattice of Gd atoms

is sandwiched by a honeycomb lattice of Pd/Si atoms. Layers A,B,C have a pair of Pd atoms near the central Gd, which are distinguished by rotating the location of the Pd pair about the c-axis. Layer D has the pair beyond the nearest Gd neighbours, and other orientations are equivalent by symmetry. A previous density-functional-theory study found the optimal stacking sequence had alternating layers, although double layers were similar in energy which may explain the inherent disorder [291]. Interestingly, despite the overall centrosymmetric crystal structure, the stacking of different Pd-Si layers causes the bonds between the Gd^{3+} ions to exist within non-centrosymmetric environments which gives rise to a local DMI interaction, see Figure. 5.9 a, with a DMI vector perpendicular to the Gd-Gd bond direction.

The orientation of the DMI vector, $\mathbf{D}_{ij}$, between two magnetic ions, i, j, is constrained by the symmetry of the local environment around the centre of the bond. When the magnetic interaction between the two ions is driven by the superexchange mechanism, the orientation of $\mathbf{D}_{ij}$ is defined as [305, 306]:

$$\mathbf{D}_{ij} \propto \mathbf{r}_i \times \mathbf{r}_j, \tag{5.5}$$

where $\mathbf{r}_{i,j}$ is the vector from the relevant magnetic atom to the intermediate atom (Pd in this case) responsible for the superexchange mechanism. The resultant DMI vector for one particular Gd-Gd bond within Gd_2PdSi_3 is shown in Figure 5.9 b. Here, the DMI vector is confined to always point in a direction perpendicular to the bond. As we shall see, the irregular stacking of non-equivalent layers leads to an enlarged unit cell containing 4 (total) Gd atoms. This leads to Gd-Gd bond environments similar to the one shown in Figure 5.9 b, as well as DMI inactive ones where the bonds exist within a centrosymmetric environment that are surrounded by four Si atoms.

The stacking of all possible layer combinations can be seen in Figure 5.10. Here, 12 different combinations are shown which are all equal in crystallographic free energy [291]. Since the stacking of identical layers is higher in energy, they

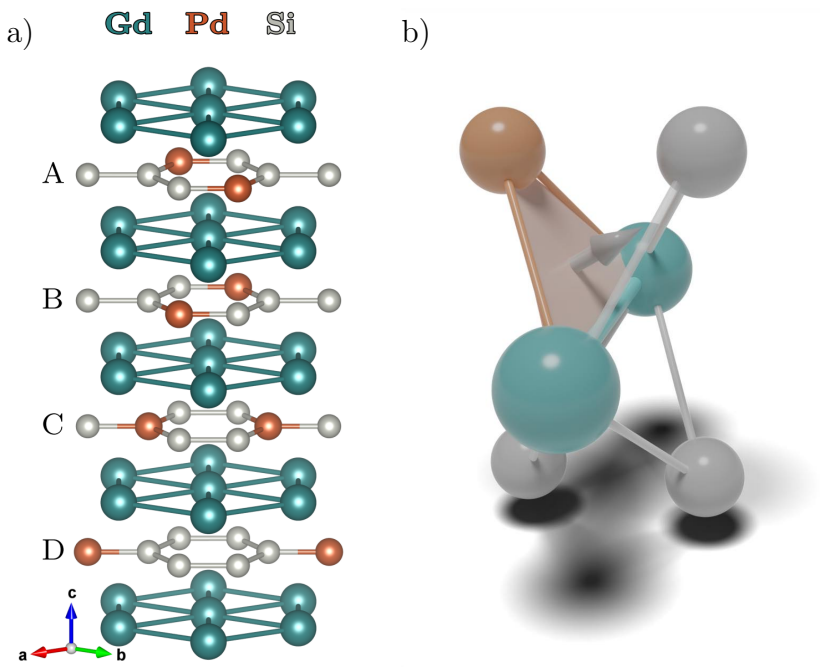

Figure 5.9: a) Crystal structure of Gd_2PdSi_3 with triangular planes of Gd atoms (teal) between a honeycombed mix of Pd/Si (orange/cream) forming a crystalline superstructure that has 8 unit cells stacked along the *c*-direction. Here, only the four distinct layers, A-D, are shown for clarity. b) The stacking of non-equivalent layers leads to a non-centrosymmetric environment at the center of some Gd-Gd bonds, this leads to a DMI vector (white arrow) that is confined to be perpendicular to the Gd-Pd-Gd triangle.

have been omitted. As shown, all 12 layers show a unique structure and a doubling of the unit cell in the a, b hexagonal crystallographic-directions.

The resulting DMI vectors of the layer stacking from Figure 5.10 can be determined using Eq. 5.5, and we show these vectors in Figure 5.11. As can be seen, the orientation of these DMI vectors are constrained to 12 different directions due the symmetry of the enlarged unit cell. Across the unit cell, we find the sum of all DMI vectors results in a vanishing net DMI interaction, as required from the overall centrosymmetry of the unit cell. However, despite the net-zero nature of the DMI, the local interaction between two neighbouring atoms is still present and is currently unaccounted for in most theoretical treatments of the material.

As can be seen, the irregularities of the direction of the DMI leads to non-mutually satisfying interactions across the various pairs of moments which constitute the unit cell, analogous to exchange-frustrated interaction in geometrically non-trivial systems [307, 308]. For example, the natural helicity of the the magnetic textures, that were proven to be chiral in zero-field by the XMCD measurements in the previous section, leads to a reduction/increase in free energy for different bond pairs depending on the relative orientation of the neighbouring moments ($\mathbf{S}_{ij}$) and the DMI vector. This can be seen in the Hamiltonian ($H_{i,j}^{DM}$) of the DMI:

$$H_{i,j}^{DM} = \mathbf{D}_{ij} \cdot (\mathbf{S}_i \times \mathbf{S}_j). \tag{5.6}$$

Here, the DMI vector will have a component lying parallel/anti-parallel to the cross product of the spins, meaning that different Gd atoms within the unit cell will vary in terms of free energy[8]. This variation of free energy across the various sites within the unit cell leads to an interesting situation whose implications can be explained at the mean-field level.

[8]Note, in systems with a non-frustrated DMI interaction, it is known that magnetic helices are stabilised due to competition with the exchange. In this system, it is known that the RKKY interaction drives the formation of these spin-textures.

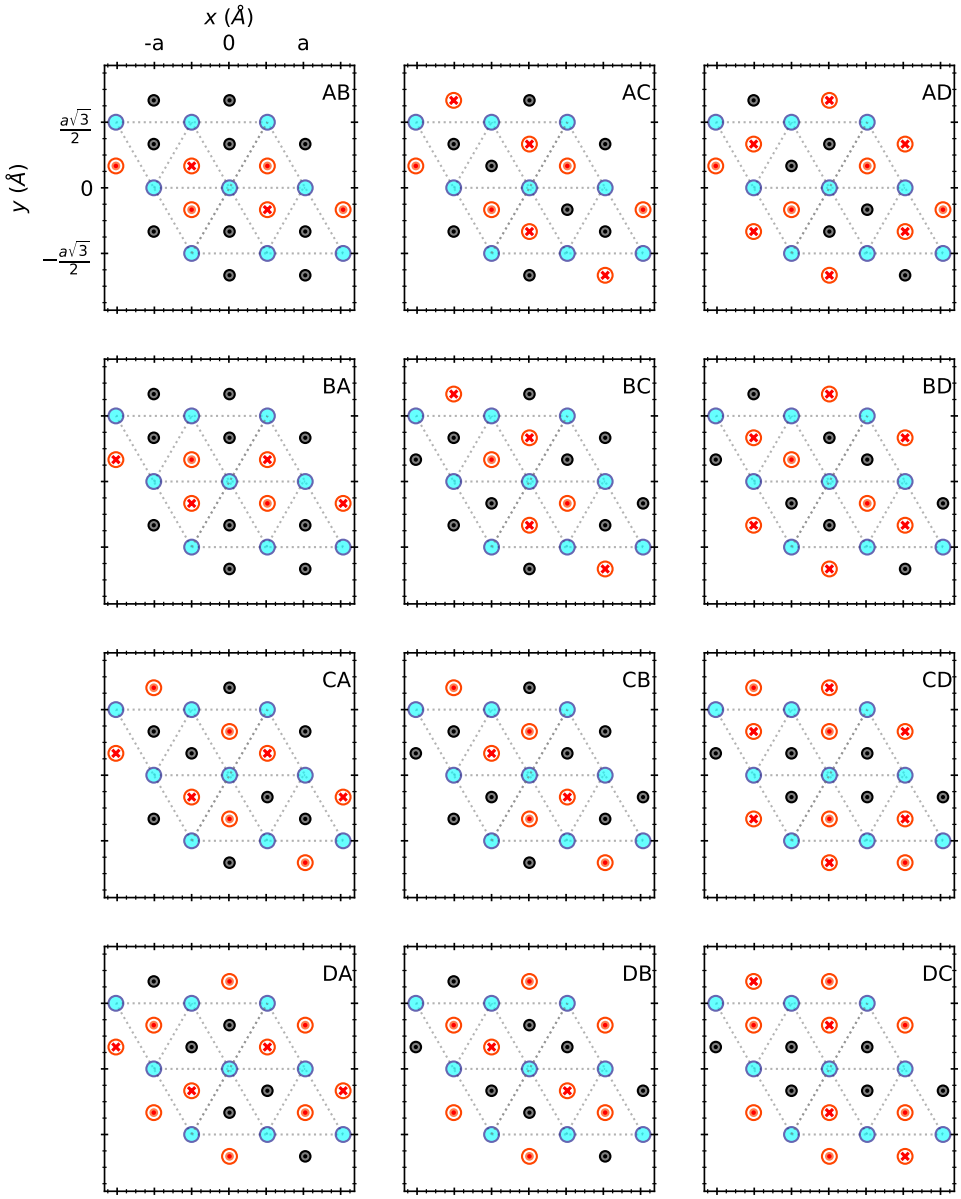

Figure 5.10: Projections of the atoms within enlarged unit cell of all possible stacking pairs, showing the hexagonal plane of Gd atoms at $z = 0$, and both the non-magnetic Pd/Si inter-planar layers at $z = \pm\frac{c}{2}$. When both layers feature Si-Si, the symbol is represented as a black dot. When there is a Pd/Si projection, the symbol is a red cross/dox depending on whether the Pd is located within the bottom/top plane respectively.

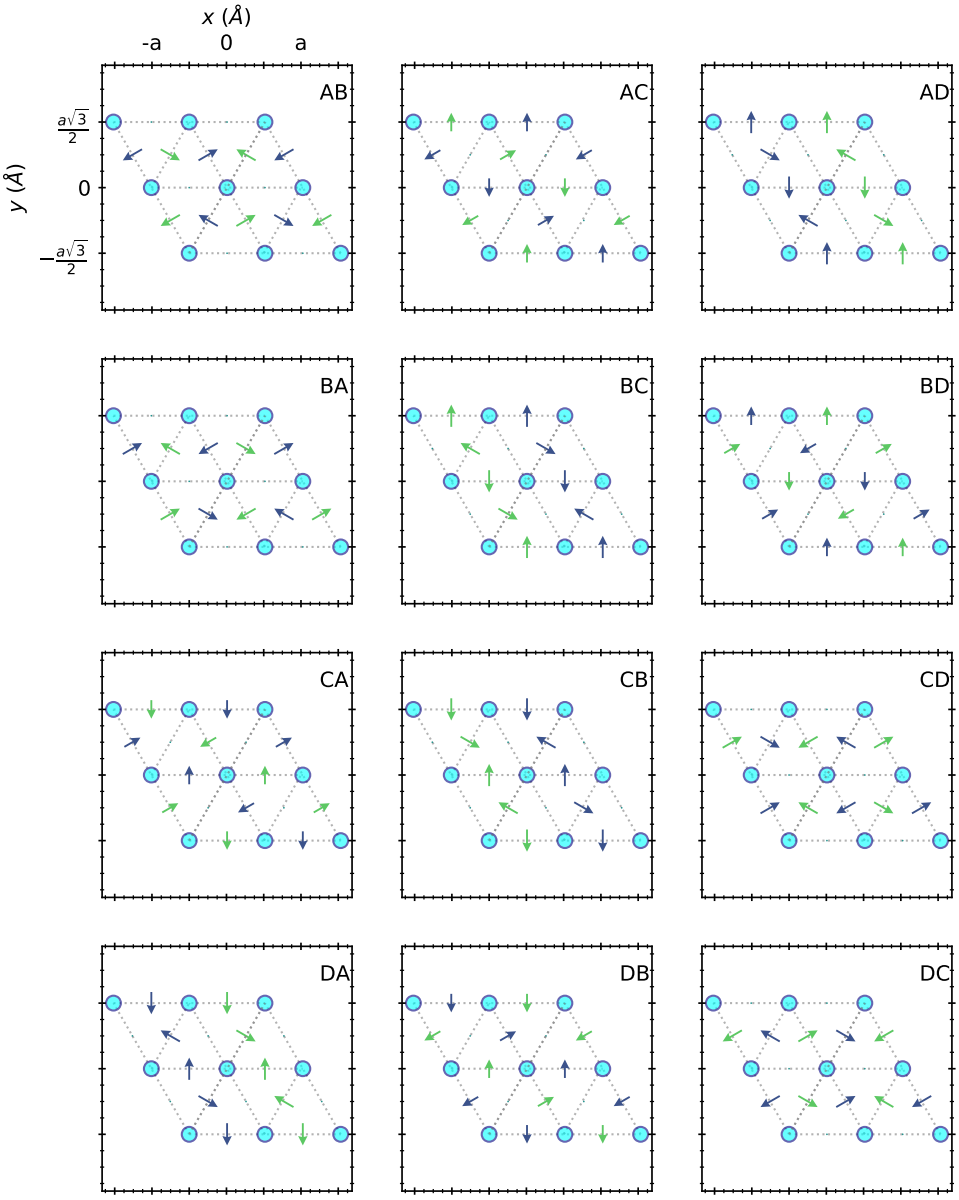

Figure 5.11: Diagram of the Gd atoms within enlarged unit cell of all possible stacking pairs, showing the direction of the local DMI vector between each Gd pair. Some bonds do not feature a DMI vector due to the symmetry of the bond. Green/blue arrows represent the vector canting up/down from the reader.

Following the derivation presented here [309], the i-th site-resolved mean-field spin vector moment $\tilde{\mathbf{m}}_i$, with total-magnitude μ, is temperature dependent with a magnitude:

$$\tilde{\mathbf{m}}_i = \mathcal{L}\left(\frac{\mu}{k_B T}|\tilde{\mathbf{B}}_i^e|\right)\frac{\tilde{\mathbf{B}}_i^e}{|\tilde{\mathbf{B}}_i^e|}, \tag{5.7}$$

where $\mathcal{L}(x)$ is the temperature-dependent (T) Langevin function, and $\tilde{\mathbf{B}}$ is the effective field at site i. As mentioned previously in Chapter 1, the effective field is obtained by taking the variational derivative of the Hamiltonian of the system, $-\delta H/\delta\tilde{\mathbf{m}}_i$, which for the DMI term gives $\mu\tilde{\mathbf{B}}_i^{e,DM} = -\mathbf{D}_{ij} \times \tilde{\mathbf{m}}_j$.

Using Eq. 5.7 together with the knowledge that the discordant DMI vectors lead to a frustration-like effect, a possible origin of the multi-step transition from the paramagnetic state to the T-SDW, IC-II texture at 19.5 K which then further transitions into the elliptical helix texture in zero field at 16.5 K, is that the variation of the site-resolved effective field causes different moments within the unit cell to order at different temperatures. This can be seen by the Langevin function, which scales the magnitude local moment depending on the free energy of the system and the temperature. At temperatures towards T_C, only the sites which are DMI-enhanced will order, which are then followed by the DMI-reduced sites upon cooling which results in a multi-step transition. This effect would also cause the moment magnitude to vary across the cell, as required by the elliptical nature of all of the spin-textures within the material.

5.2.5 Conclusion

In this Chapter we have demonstrated that the simple picture of skyrmions existing within Gd_2PdSi_3 is far more complicated than initially thought. In addition to a number of different incommensurate magnetic phases, we observe a number of effects that are currently unexplained. In particular, the form of the magnetic spin-textures were previously assumed to be composed of helices, which we have shown to be elliptical in nature. This ellipticity leads to interesting effects,

such as the requirement for the moment magnitude to vary in space akin to a spin-density wave. This, coupled with our findings of a step-wise transition in temperature, lead us to investigate alternative mechanisms which may explain the system more accurately.

Here, we have proposed that a site-dependent, local DMI is responsible for our findings, as depending on the particular arrangement of the magnetic moments, the local DMI either reduces/increases the magnetic free energy of the site, naturally leading to magnitude modulations and site-dependent ordering temperatures. Furthermore, depending on the stacking of the crystalline superstructure, different chiralities of magnetism may exist within different layers, meaning when summed along the c-axis no global chirality is present, explaining the lack a magnetic signal within the material when using electron microscopy techniques.

Looking forward, we intend to develop a custom mean-field solver which can implement both a spatially varying DMI interaction as well as the RKKY mechanism to further study this system. Here, we hope to observe that the relative strength between the DMI and exchange interactions to be the main mechanism between the multi-step transition, as well as hopefully observing a breaking of degeneracy between the two-chiralities depending on the particular layer of the crystalline superstructure.

Chapter 6

Unexpected Skyrmion Renucleation

In this Chapter, we present small-angle-neutron-scattering (SANS) results which show that at low temperature, metastable skyrmions within Cu_2OSeO_3 increase in volume fraction during an increasing field scan. We name this effect skyrmion renucleation, as it requires a seeding metastable skyrmion state to occur. Here, we first review why this effect is unexpected within the framework of the current understanding of the literature. Then, we explain how to create metastable skyrmions during a SANS experiment within Cu_2OSeO_3, before showing experimental evidence that renucleation occurs for a variety of temperatures and crystallographic orientations. We end the Chapter with a discussion of possible mechanisms as well future planned works.

6.1 Introduction

In the majority of bulk, single-crystal, skyrmion-containing materials which stabilise their respective incommensurate magnetic phases via the DMI, skyrmions are typically considered to exist within a highly-restricted region of temperatures and magnetic fields. As shown in Figure 6.1 a to d, the existence magnetic skyrmions in a number of materials is confined to a small pocket of phase space,

requiring the application of a moderate magnetic field whilst simultaneously staying within a small window of temperature, typically a few Kelvin below T_C.

The limited extent of the equilibrium skyrmion state presents a challenge in developing spintronic devices, as they impose the condition that the devices need to operate within a narrow temperature range and maintain a remnant field when the device is switched off. However, these concerns can be rectified by rapidly cooling the system within a suitable applied field. This 'freezes' metastable magnetic skyrmions into the system, which have been observed to exist across a greatly extended temperature range in a number of materials including MnSi [313, 314, 315], FeGe [316], $Fe_{0.5}Co_{0.5}Si$ [317, 318], Cu_2OSeO_3 [319, 239, 157], and Co-Zn-Mn alloys[1] [321, 320, 322].

The current understanding of metastable skyrmions is well summarised in a recent Zn-doped Cu_2OSeO_3 study [179, 323], which shows that metastable skyrmions can exist down to 10 K and greater fields than the maximum of the equilibrium skyrmion pocket. We show the region of phase-space where metastable skyrmions exist in Figure 6.2 a. The stability of the metastable magnetic skyrmions can be determined using lifetime measurements, typically by observing a relaxation effect in the magnetic susceptibility [179], or a decay in the scattered SANS intensity [324]. We show a typical relaxation of the magnetic susceptibility from the study in Figure 6.2 b, whose exponential nature allows the extraction of a typical lifetime constant (τ) using an Arrhenius law. This constant is related to the energy barrier of the system (E_B), such that $\tau(T) = \tau_0 \exp[\frac{-E_B}{k_B T}]$. This energy barrier is typically considered to arise from the topological protection of the skyrmions [325], although other effects such as pinning, entropy-limitations and effective anisotropies also contribute [326, 179, 327].

[1] This is particularly exciting in $Co_9Zn_9Mn_2$, where zero-field and room-temperature metastable skyrmions have been observed [320]

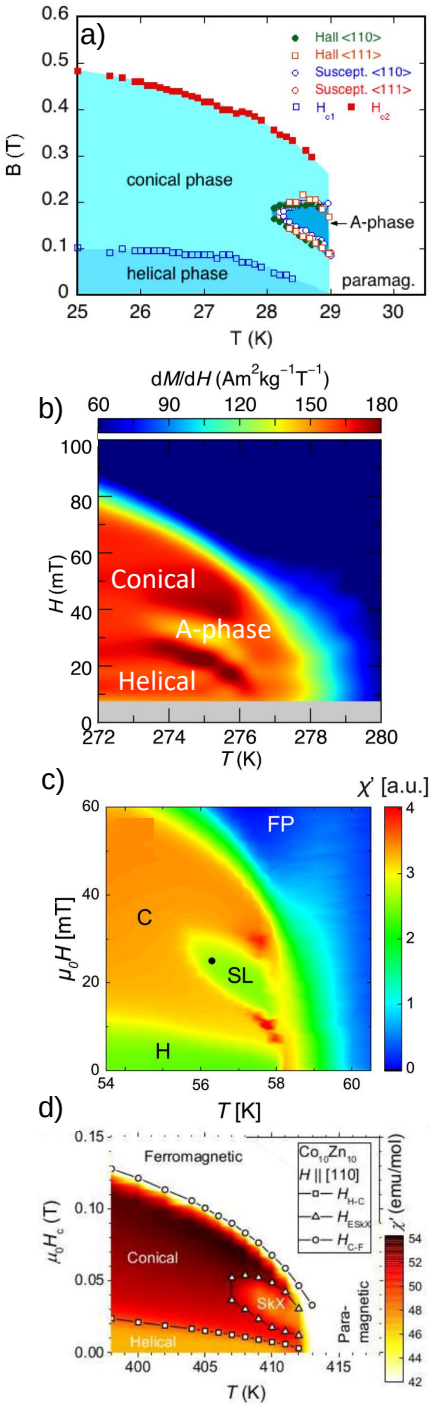

Figure 6.1: Magnetic phase diagrams of MnSi (from [310], transport and magnetometry measurements), FeGe (from [311], magnetometry), Cu_2OSeO_3 (from [312], magnetometry) and $Co_{10}Zn_{10}$ (from [89], magnetometry). Magnetic phases are labelled. A-phase, SkX and SL all refer to the magnetic skyrmion phase.

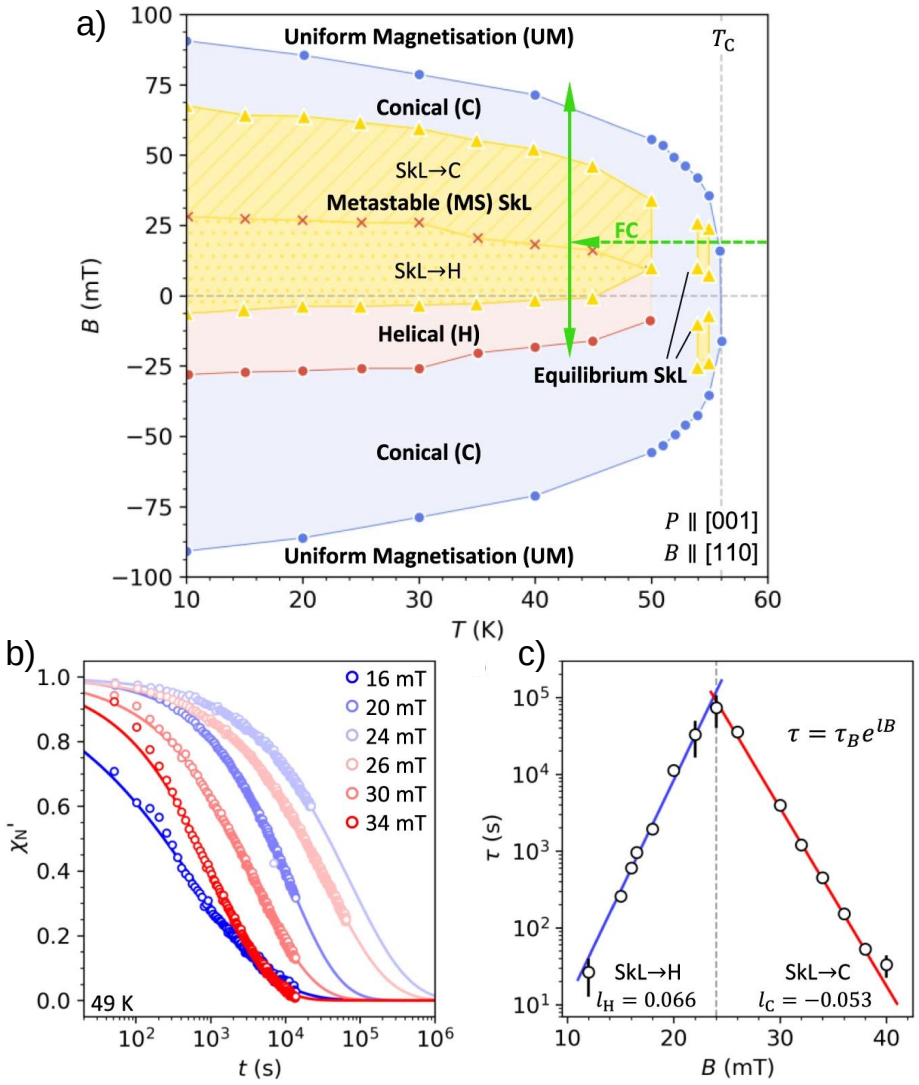

Figure 6.2: a) Supercooled magnetic phase diagram of $(Cu_{0.98}Zn_{0.02})_2OSeO_3$, as determined by measurements of the electric polarisation P along the [0 0 1] crystallographic axis, when the magnetic field is applied along the [1 1 0] axis. The phase diagram was determined by field cooling (FC) at 24 mT, as indicated by the green arrow. The uniform magnetisation (UM, white), conical (C, blue), helical (H, red) and equilibrium skyrmion lattice (SkL, yellow) phases are labelled. b) The normalised real component of the AC susceptibility, χ'_N, measured as a function of time at a range of applied magnetic fields after field cooling the sample at 20 mT from 65 to 49 K, fits are to an Arrenhius law to determine the energy barrier of the system. c) The fitted lifetimes plotted as a function of the applied magnetic field on a logarithmic axis, showing that the lifetime exponentially decreases under the application of a field away from the initial magnetic field. All data taken from [323].

Ultimately, the study [323] concludes that metastable skyrmions exist within a very large region of the overall magnetic phase diagram, and that the energy barrier rapidly decays as one modifies the magnitude of the applied magnetic field away from the initial value. This is shown by the exponential decrease of the skyrmion lifetime shown in Figure 6.2 c. Thus, according to our current understanding, increasing the magnitude of the magnetic field after field cooling should result in a lower population of skyrmions.

In the rest of this Chapter, we show that the low-temperature behaviour of metastable skyrmions is more complex than previously thought. By using SANS together with a super-cooling mount, we are able to rapidly cool the sample from above T_C to 5 K in a matter of seconds, freezing in a large population of metastable skyrmions. We first discuss the differences between the equilibrium and the metastable skyrmion state, before revealing that at low-temperatures, the skyrmion population in fact increases rather then decreasing. We show that this effect is present for a number of crystallographic orientations, and discuss possible mechanisms for such a renucleation.

6.2 Experimental Methods

In order to generate a metastable skyrmion state within pristine Cu_2OSeO_3, rapid field cooling is required as the lifetime of skyrmions at temperatures just under the skyrmion pocket (say $\approx$ 54 K) are of the order of seconds [179]. Therefore, the standard cooling rates of orange cryostats (about 20 K/min) would result in a large amount of skyrmion decay and hinder a thorough investigation of this state. In order to circumvent this issue, we prepared a custom sample mount. As shown in Figure 6.3, a sample of Cu_2OSeO_3 was mounted such that the [1 0 0] direction was normal to the aluminium plate, which was checked using an x-ray Laue camera prior to the experiment using the reference silicon wafer. The sample was mounted in-between two strips of cadmium, whose highly neutron-absorbing properties provide a strong feature to aid with sample alignment. Rapid cooling

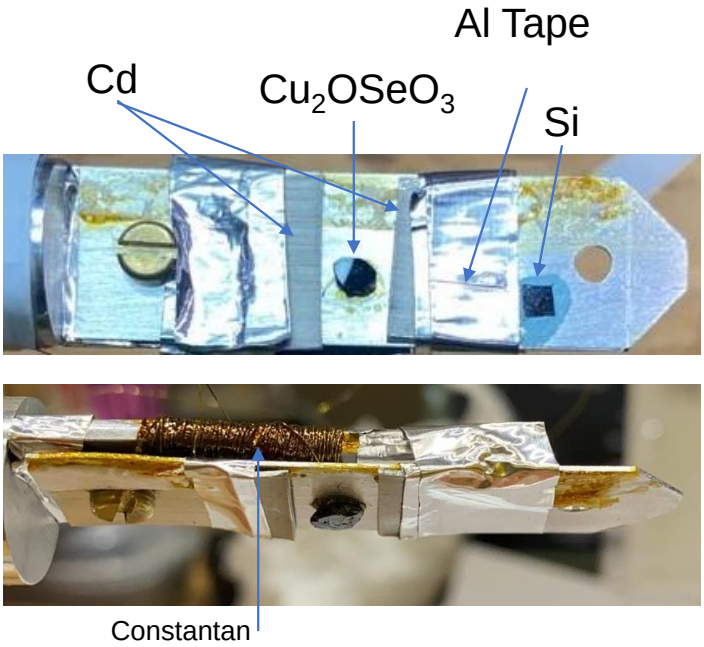

Figure 6.3: Pictures of the sample mount showing the single crystal of Cu_2OSeO_3, silicon wafter and cadmium strips for sample alignment, as well as constantan wire. The constantan wire doesn't block the path of the neutrons, and is able to locally heat the sample.

was achieved by locally heating the entire sample plate. This was achieved by wrapping the prongs on the sample mount with highly resistive constantan wire [328], which locally heats the sample stage, which is surrounded by the cryostat bath. The cryostat is which is kept at the target temperature, typically 5 K. By passing a current through the constantan wire, we are able to locally heat the sample to above T_C from 5 K in a matter of seconds, before turning the current off, which rapidly thermalises the sample with the cryostat to cool back to 5 K, again in a few seconds. This procedure would take more than 10 minutes using a standard cryostat.

We show for completeness the calibration of the heater. The effectiveness of

the heater can be determined by rapidly collecting the SANS patterns[2] from the magnetic state of the sample over the length of an entire current pulse. In the event that the pulse length or pulse current was too low, the sample would fail to reach above T_C, and only a variation of the helical diffraction spot intensity would be noticeable. However, by applying a slight magnetic field to induce skyrmions, we can be sure that we successfully heated above T_C by the presence of metastable skyrmions in the final diffraction pattern, after the heating procedure. A successful calibration run is shown in Figure 6.4 a, which shows the summed intensity from a 0.5 s exposure which was background subtracted with a frame at 60 K. As shown in the initial state in (b), the ZFC procedure leads to two helical domains propagating along the [0 1 0] and [0 0 1] directions[3]. Upon applying a current of 1 A, the helical intensity diminishes, before becoming negligible after 5 s. The heater is switched off at 6 s, at which point there is no appreciable scattering above background as shown in panel c. Due to the helium exchange gas, the temperature of the sample rapidly starts to cool, staying with in the skyrmion pocket (panel d) for only about one second which can be seen in the summed intensities as a large spike of scattered intensity. As expected, a large amount of skyrmions decay as shown by the steep decrease in scattered intensity after $t = 7.5$ s. This is because we have reached temperatures just below the skyrmion pocket, where the skyrmion lifetime is at a minimum. However, this decrease stops once we reach $t = 9$ s, we are now in a regime where the lifetime of the skyrmions has greatly increased [179]. At $t > 14$ s, we find no further increases in intensity, showing us that the system is now in thermal equilibrium with the cryostat bath. As shown in panel (e), we now have a state composed of a mixture between helices and metastable skyrmions, at 5 K, as required. Note that the constant increase in intensity is not from an increase in skyrmion volume population, but an effect of temperature. Namely, as one cools many magnetic

[2]Here, we were able to use such a small exposure time of 0.5 s due to the high neutron flux of D33.

[3]The third domain lies out of the diffraction condition, as the [1 0 0] direction is parallel with the neutron beam.

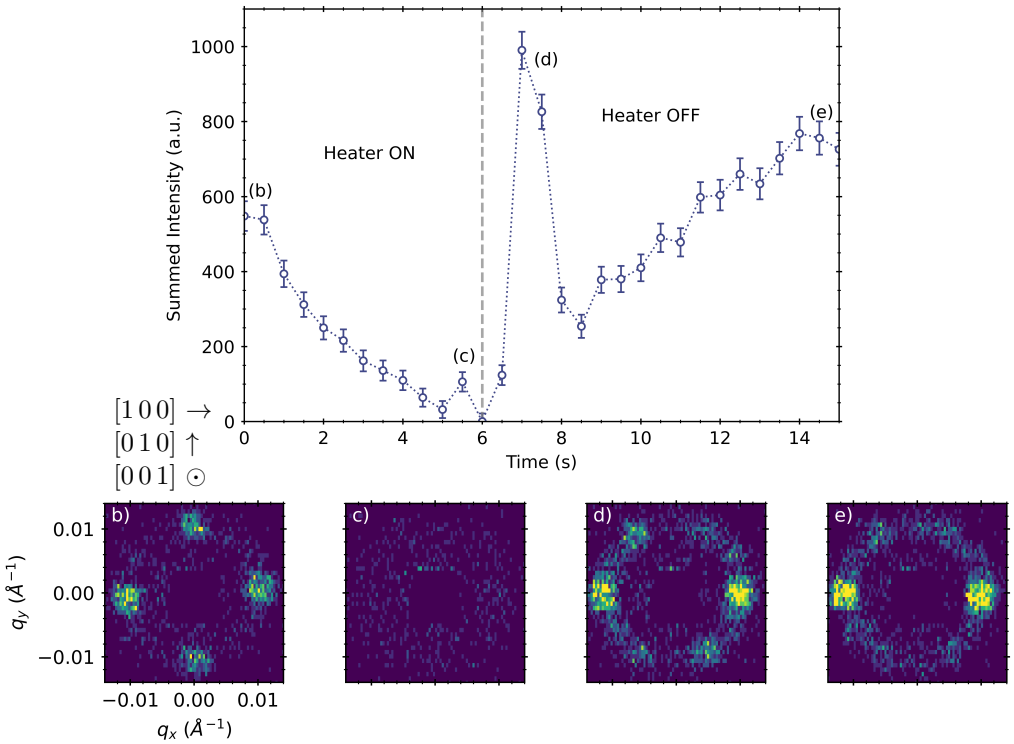

Figure 6.4: Calibration of the flash-heater. a) Summed intensity from an entire sample pattern in a wavevector range between $0.007 \leq q \leq 0.013$ as a function of time. The heater is activated at $t = 0$ s, and turned off at 6 s of heating time. b-e) Single snapshot of the state at different times, see labels in (a).

states, the magnetic state becomes more ordered which results in an increase in scattered intensity at the center of the rocking curve [34].

6.3 Results

6.3.1 Equilibrium Skyrmions V Metastable Skyrmions

SANS not only gives us information about what magnetic state is present, but also the magnetic wavevector, ordering and populations of the different magnetic states within a sample. In the following section, we investigate the metastable skyrmion state within pristine Cu_2OSeO_3 at the D33 beamline, Institut Laue-Langevin. Prior to the beamtime, magnetometry measurements were performed

on a 33.2 mg sample of Cu_2OSeO_3, which was mounted on a quartz rod such that an applied magnetic field would lie along the crystalline [1 1 0] direction. Here, we used the Quantum Design MPMS3 at the R52 ISIS Support Laboratory. A high-resolution phase diagram was mapped by using the MPMS in vibrating sample mode (VSM). Here, the magnetisation of the sample is continuously measured at a high rate whilst slowly increasing the temperature from 54 to 60 K. This would have a density around 40 data points per Kelvin. After reaching the maximum temperature, the sample was zero-field-cooled (ZFC) back to 54 K, before increasing the field to the target value to start the next increasing temperature sweep. By differentiating the data with respect to temperature, sharp magnetic phase boundaries can be seen between the conical, skyrmion lattice, field-polarised and disordered phases can be observed. We show the resultant magnetic phase diagram near T_C in Figure 6.5 a.

An extended magnetic phase diagram for the sample can be found in Figure 6.5 b. Here, phase boundaries are marked by square symbols which were obtained by identifying the peaks in the $\partial M/\partial H$ of a increasing field scan $M(H)$ from 0 to 100 mT, which were taken after ZFC from 60 K. Here, it is important to note that upon rapid, skyrmion-field-cooling (SFC), the metastable skyrmions decay into the helical state at temperatures below 40 K, whereas at higher temperatures the skyrmions decay into the conical state.

In order to visualise and understand the differences between an equilibrium and metastable skyrmion state, micromagnetic simulations were performed using the standard Cu_2OSeO_3 parameters [329]. The clean skyrmion lattice state shown in Figure 6.5 e was generated by using a triple-q initial starting state before relaxation, whilst the disordered state in Figure 6.5 c was relaxed from a skyrmion state with random fluctuations, with a slight reduction in the value of the magnetic field, to encourage the skyrmions to decay into magnetic helices in agreement with the measured magnetic phase diagram. As shown by the simulated SANS scattering patterns in Figure 6.5 d and f, 'metastable' and equilibrium lattices can be distinguished by the presence of diffuse neutron scattering

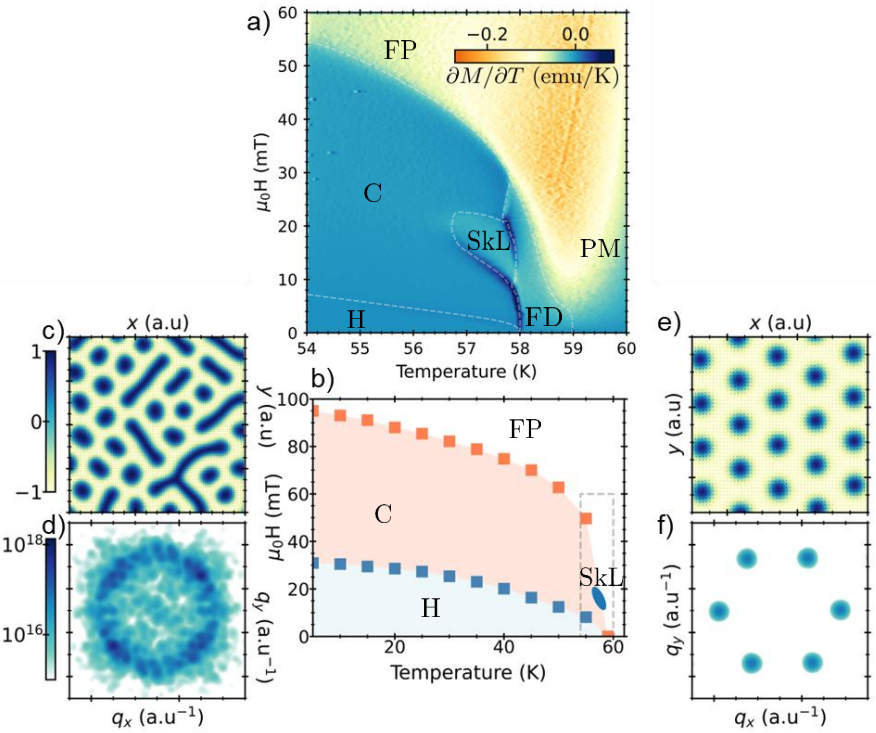

Figure 6.5: Metastable skyrmions in Cu_2OSeO_3, for magnetic field applied along the [1 1 0] direction. a) Magnetic phase diagram near T_C, generated using the temperature gradient of the magnetisation. The equilibrium skyrmion lattice (SkL), helical (H), conical (C), field polarised (FP), fluctuation disordered (FD) and paramagnetic (PM) phases are labelled. b) Extended magnetic phase diagram generated by inflections in the magnetisation as a function of magnetic field. Equilibrium skyrmion pocket represented as blue oval near 60 K. c,e) Micromagnetic simulations of skyrmions within Cu_2OSeO_3 relaxed under clean/disordered initial conditions respectively. d,f) Simulated SANS intensity for the disordered/ordered skyrmion system respectively.

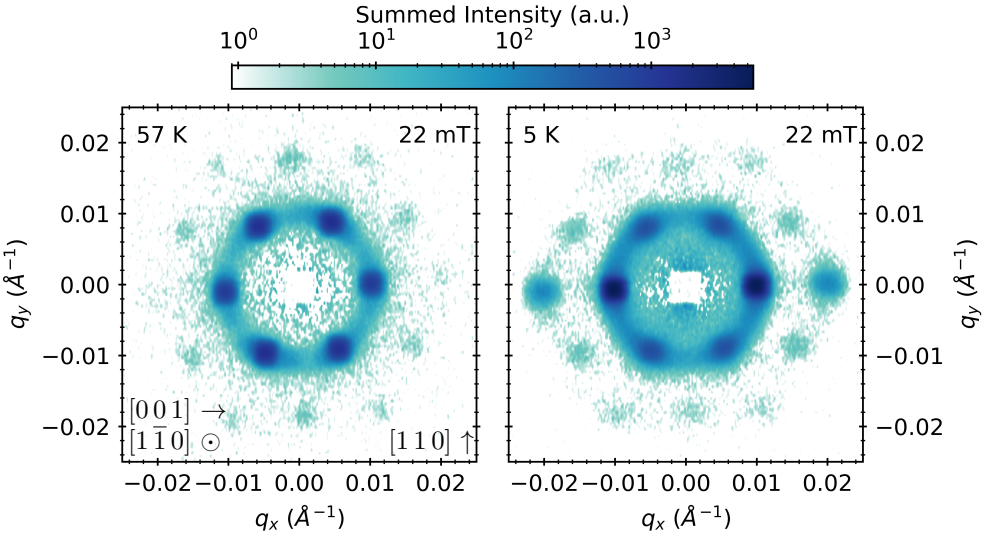

Figure 6.6: SANS patterns made by summing 29 frames of a rocking scan centred about the [1 1 0] direction, rocking scan has a total angular range of 15°, with a 0.5° resolution. The state on the left hand side is from the equilibrium skyrmion pocket at 22 mT and 57 K, whilst the right hand side is after SFC to 5 K.

at low-q, arising due to the disordered nature of the equilibrium state.

As shown in Figure 6.6, clear differences in the rocked SANS patterns can be seen between the equilibrium skyrmion state and the metastable skyrmion state. Whilst a six spot pattern corresponding to the presence of a hexagonal lattice of magnetic skyrmions is present in both cases, we see that whilst the intensities in each of the six spots at 57 K are approximately equal, the horizontal pair of Bragg peaks are dominant in the metastable state. This pair of spots has a wavevector aligned along the [1 0 0][4], so that the helical state and a pair of metastable skyrmion diffraction peaks overlap. This shows us that indeed, the skyrmions have decayed into the helical state upon cooling, as can further be seen by the reduced intensity of the two pairs of skyrmion peaks with $q_y \neq 0$ at 5 K compared with the equilibrium state.

In addition to differences in the intensity distributions, we also see the presence

[4]A different sample orientation was used after calibrating the heater in Figure 6.4.

of a large amount of diffuse scattering at low-q when we compare the metastable skyrmion system to the equilibrium. In both datasets, background measurements were taken in a high-field to minimise the effects of thermal drift. As we saw in Figure 6.5 d, the presence of magnetic disorder leads to this background, as in particular regions of the sample there is a lack of magnetic crystallinity, liberalising the requirement that scattering can only occur at Bragg peaks, allowing diffuse scattering. This signature, together with the intensity, shows us that the equilibrium skyrmions decay into magnetic helicies upon cooling, and form both phase separated regions maintaining translational order but also cause regions of the sample to exhibit highly disordered behaviour, similar to the micromagnetic simulation shown in Figure 6.5 c.

So far, we have shown that we are able to create metastable skyrmions in Cu_2OSeO_3, as well as observing how this state is different to the skyrmions at equilibrium. In the following results sections, we will show what happens to the metastable state as a function of the applied magnetic field.

6.3.2 Field Scans

The field-driven evolution of the metastable skyrmion state is shown in Figure 6.7, after SFC at 22 mT to 5 K. Here, we show the SANS patterns which again are generated by summing every frame within a single rocking curve. At lower magnetic fields (row a), we see the general features of the metastable state. Namely, the presence of diffuse scattering, as well as the horizontal pair of Bragg spots being dominant due to magnetic phase coexistance of skyrmions with the helical state. In addition to first-order peaks, we also see a large number of higher-order peaks within the diffraction pattern, particularly along the horizontal direction. These higher-order peaks give us more information about the detailed form of the spin-texture, although a detailed analysis requires a more thorough study to mitigate the effects of multiple scattering [330].

In the second row, with fields increasing from 55 mT to 85 mT, we observe an overall increase of skyrmion scattered intensity, and the peaks becoming roughly

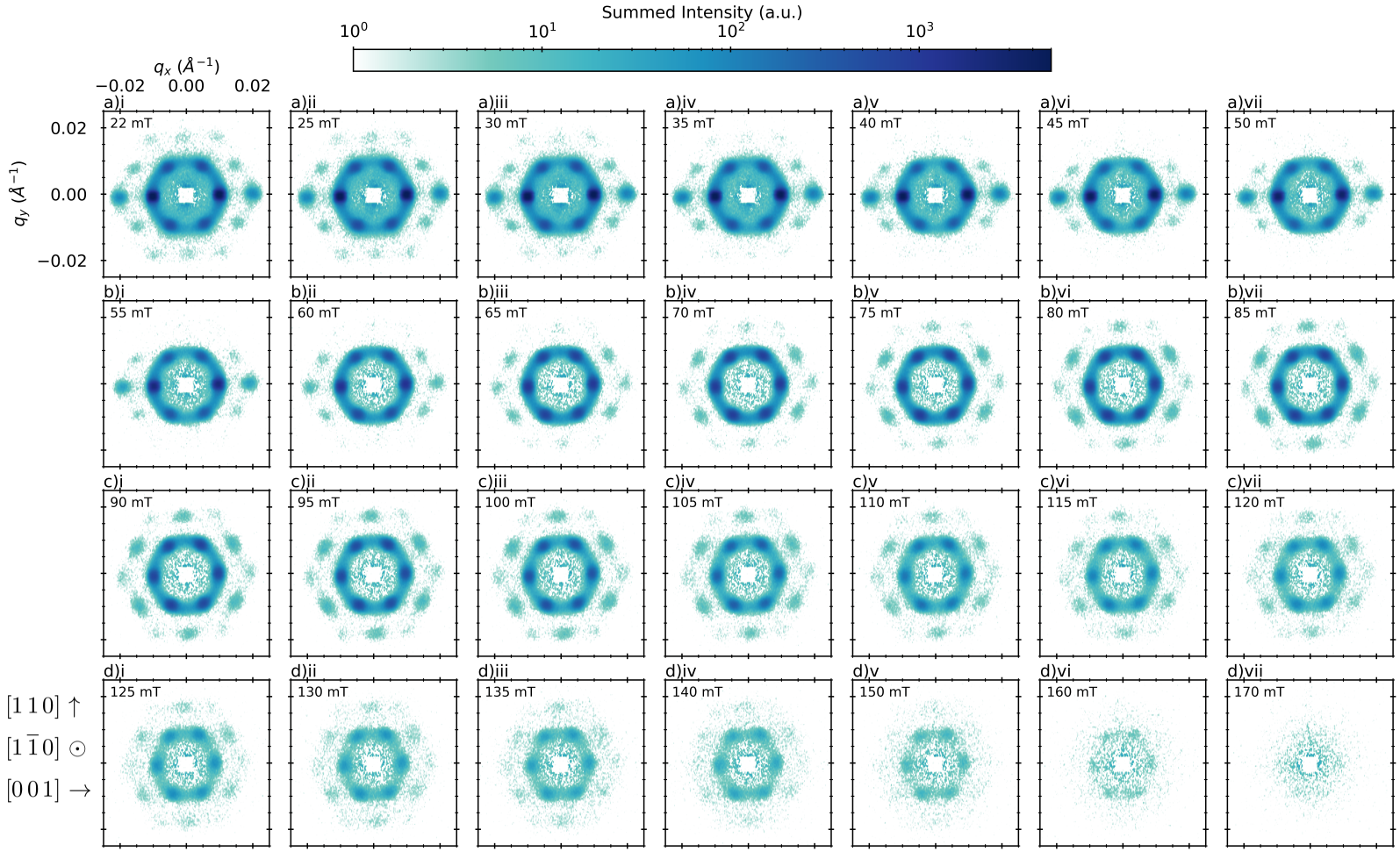

Figure 6.7: Field dependent SANS patterns made by summing 29 frames of a rocking scan centred about the [1 1 0] direction. Taken after SFC at 22 mT to a temperature of 5 K. Magnitude of fields are labelled. Colour-bar and axes are identical for all plots.

equal in magnitude. At the same time, the diffuse scattering reduces. This intensity variation suggests that skyrmions are growing in volume fraction upon increasing the magnetic field, as well as becoming more long-range ordered. Further increases in field, in row c, reverses this trend, showing a decaying skyrmion intensity with further increases field. This is accompanied with a distortion of the hexagonal lattice of skyrmions, as instead of the skyrmion diffraction spots lying on a circle centred about the origin, the skyrmion spots appear to lie on an oval with the major axis lying in the vertical direction. In the final row, we see this trend continue, with the skyrmions further decaying, and becoming further distorted, until no incommensurate magnetism can be seen at 170 mT.

This behaviour can be more quantitatively investigated by fitting 2D Gaussian functions to every peak in the diffraction pattern in a similar manner to those described in the previous SANS experimental Chapters in this thesis. The fitting of Gaussians gives us the benefit that we are able to obtain the intensity, 2D location and the broadening of each peak. We show the fitted results in Figure 6.8, with each pair of spots being plotted separately using the colour-coding shown in the reference image above the figure. The fitted intensities intensities are shown in a, which shows that the two skyrmion peaks (green and orange only) initially decrease in population as expected from previous theory. These peaks fall to roughly half their original intensity at 45 mT. After increasing the field past this minimum, the skyrmions gain population, with around a five times increase in volume fraction at their maximum at 70 mT. Simultaneously to this, we see the helical intensity (blue pair, overlaps with the third skyrmion wavevector), rapidly decaying though this whole process (not shown), and the diffuse scattering at low-q also decrease at the same time as the skyrmions increase in volume fraction.

This rapid increase in skyrmion population can also be seen in the wavevector dependence in panel (c). Here, the initial reduction of each wavevector is thwarted by the onset of the return of skyrmions. This is consistent with the picture that skyrmions are initially decaying, such to increase their separation distance, before becoming more closely packed as the population of skyrmions increases. We note

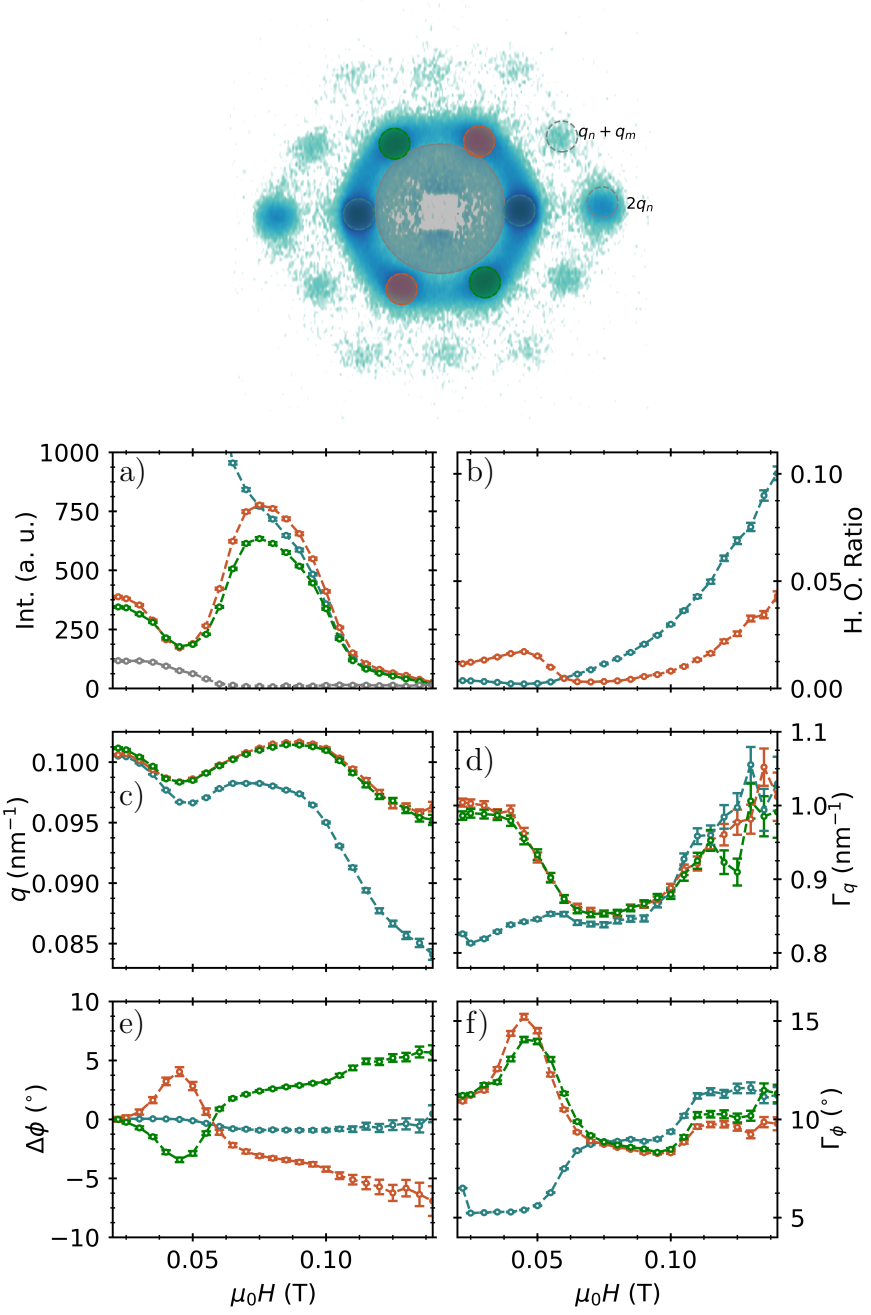

Figure 6.8: Field dependence of the scattered intensity (a), higher-order intensity ratio with $q_n + q_m$ being blue, and $2q_n$ being red (b), wavevector (c), full-width-half-maximum (FWHM) in wavevector (d), deflection in the azimuthal location of the Bragg spots (e) and the FWHM in the azimuthal direction (f). Colours correspond to the pair of spots shown in the reference above. For higher order peaks, the sum of all equivalent wave-vectors is used. The gray trend in (a) Shows the level of diffuse scattering, taken by the sum of the gray circle in reference.

that the wavevector in the horizontal direction (blue), is consistently smaller than the other two pairs, at fields greater that 35 mT, and in fact this difference increases continually with further applications of magnetic field, showing that significant skyrmion-lattice distortion is present. Will will revisit this point later.

Interestingly, the ordering of the wavevector shows also identifiable regimes which also consistently follow the notion that skyrmions start to decay upon increasing the magnetic field, before returning with a greater initial population upon further increases past 45 mT. In panels (d) and (f), the full-width-half-maximum (FWHM) is shown for both the radial (q) and azimuthal (ϕ) directions respectively. In both cases, the helical state has the lowest level of disorder at low-field, and the skyrmion peaks have a high level of initial disorder. This picutre is in agreement that the skyrmions decay into the helical state, leaving behind disordered regions which broaden the skyrmion lattice peaks as well as lead to the low-q diffuse scattering. In the regime where the skyrmions are decaying, we see a slight decrease Γ_q and a strong increase in Γ_ϕ, suggesting that as the skyrmions decay there is a greater level of orientational disorder in the system. Upon reaching the maximum population of skyrmions, the FWHM for all pairs of peaks becomes identical and takes a value far lower than the initial value for the skyrmions, suggesting that this state after skyrmion renucleation is far more ordered than the metastable state at 22 mT.

Upon increasing the field past the greatest population of skyrmions, we again see novel behaviour, this time in the distortion of the skyrmion lattice. The skyrmion lattice distortion is seen in panel (e), which plots the change in the azimuthal location of the diffraction peaks as a function of applied field. Here, we see the horizontal (blue) pair staying in roughly the sample azimuthal location, lying parallel to the crystalline [1 0 0] direction. On the otherhand, the green and orange diffraction spots show rich a field-dependent behaviour. As shown, the the spots initially cant towards the [1 0 0] directions respectively, reaching a maximum deflection at 45 mT, coinciding with the minimum volume fraction of skyrmions. As skyrmions begin to repopulate the system, this canting is reversed

and in fact over shoots, such that these two pairs start canting toward the vertical, [0 1 1] direction. At the largest of fields, we see a large deflection of wavevector direction in (e), very asymmetric wavevector magnitudes in (c), and a clear oval shape to the skyrmion lattice in Figure 6.7. One origin for this lattice distortion may be a geometrical effect, whereby the magnetic field is misaligned with the neutron beam. This would induce a torque effect of the skyrmion lattice, leading to an artifact in the diffraction pattern. However, as shown in Figure 6.9, the centre of the skyrmion peak intensity within the rocking scan appears roughly at 0° for all fields. In order for the torque to cause an equivalent feature to what we see (the wavevector in the q_x direction is roughly equal to $0.8q_y$), an angular offset of nearly 37° would be required, far greater than any torquing we may see in the SANS rocking in Figure 6.9. This tells us that a deformation of the skyrmion lattice is indeed occurring at higher magnetic fields.

As previously mentioned, higher-order peaks in the diffraction pattern reveal more information about the spin-texture. By normalising the higher-order peak intensities to the first-order peak intensities, we are able to track changes in their ratio which avoids issues from multiple scattering, which remain a constant in their contribution to the higher-order peak intensities. We show the field dependence of the higher order peak ratios in Figure 6.8 b. In the $q_n + q_m$ dataset, we see a quadratic trend to the intensity ratios, after applying a field of at least 50 mT. Similarly, we also see quadratic behaviour in the $2q_n$ dataset, this time after 75 mT. At lower fields, there is also non-linear behaviour. In these peaks, the higher order peak from the helical state contributes to the scattered intensity. Here, we explain this low-field behaviour by the helical state deforming under the application of a perpendicular magnetic field, akin to a chiral soliton lattice [331]. This is because the magnetic field induces distortions to the helical spin-texture, whose wavevector is unable to reorient due to being pinned in place by cubic anisotropy. The decrease at 50 mT is due to the helical state decaying at the same time the skyrmions are renucleating. The quadratic behaviour in both sets of higher order peaks is offset from $H = 0$, in strong agreements with

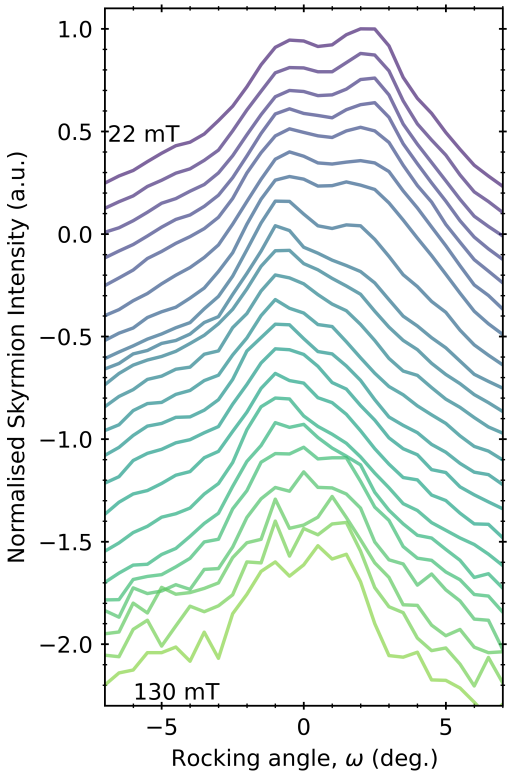

Figure 6.9: Rocking scans of the horizontal pair of magnetic peaks of the metastable skyrmion state at 5 K, normalised to their maximum intensity. Different colours correspond to different external fields, with dark to light being the increasing field direction. The presence of double peak suggest two domains of skyrmions/helicies that are slighly offset from one another, primarily due to demagnetisation effects.

theoretical work [330], which found the the offset to be related to phase of the three wavevectors that constitute the skyrmion lattice in the triple-q model.

To summarise the results of the field-induced behaviour of the metastable state, we have the following:

- Metastable skyrmions at 5 K coexist with helical states, forming a highly disordered state with broad skyrmion peaks and diffuse scatter.
- Small increases in magnetic field reduce the population of skyrmions, increasing their separation and orientational disorder.
- Further increase in magnetic field then cause a remarkable renucleation of skyrmions, greatly increasing the population past the initial value after SFC, and increasing the ordering as shown by a reduction in the FWHMs and the departure of diffuse scattering.
- Even greater increases in field cause the skyrmion lattice to decay, distorting their form as shown by the higher-order-peak ratios, as well as the shape of the lattice, as shown by azimuthal deflection of the peaks.

These observations are at odds with previous assumptions that metastable skyrmion populations decay with an increasing field [179, 326]. In the following results sections, we will explore the temperature and crystallographic-orientation dependence.

6.3.3 Temperature and Crystallographic Dependence

The temperature dependence of skyrmion renucleation is shown in Figure 6.10. Here, the skyrmion intensities were taken by summing an appropriate regions within the summed rocking scans using the GRASP software [332]. Similarly to the previous field scan, the cryostat was set to a particular temperature, before performing the SFC to create a metastable skyrmion state at the cryostat temperatures. As shown, renucleation strongly occurs at 10 K, with slight rises found at 15 and 20 K. At 25 K, we see that the skyrmion population remains constant

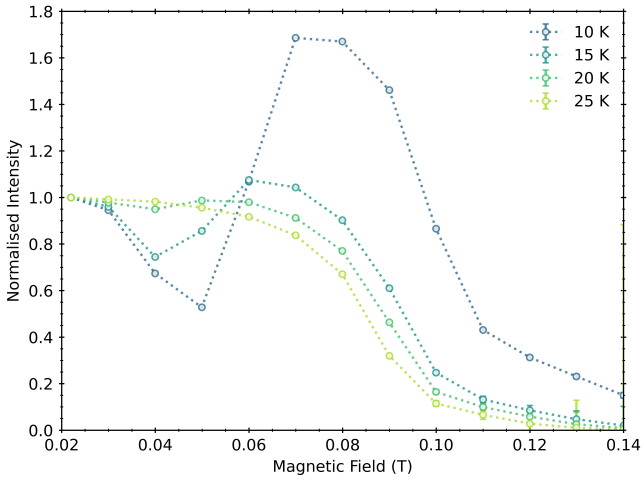

Figure 6.10: Temperature dependence of the renucleation of metastable skyrmions for fields along the [1 1 0]. Intensities are normalised to their initial value, and were obtained by summing suitable regions of interest within the GRASP software [332].

upon minor increases in field, before decaying after 60 mT. This picture at 25 K is more consistent with previous metastable skyrmion studies [179, 326].

The crystallographic-orientation dependence of skyrmion renucleation is shown in Figure 6.11. Here, the skyrmion intensities were again taken by summing an appropriate regions within the summed rocking scans. For all orientations investigated, we see that skyrmion renucleation occurs at 5 K. However, for directions towards the [1 1 1] direction, we see the characteristic dip in intensity (see the [6 6 1] direction for example, close to the [1 1 0]) is not present. Instead, for [1 1 1] the intensity rises straight away to a maximum at 40 mT, before the skyrmion intensity decays. Interestingly, the [1 1 1] direction has the lowest field at which skyrmions decay, despite being a hard axis [183]. This initial increase can also be seen along the [2 2 1] direction, which shows a much greater increase than the [1 1 1], but also doesn't display the characteristic initial dip. At [3 3 1], we reach a cross-over regime, where both an initial increase and the dip of intensities appear to be present, before entering a regime which is similar to the [1 1 0], with [h h 1] ($h > 3$) all showing similar behaviour.

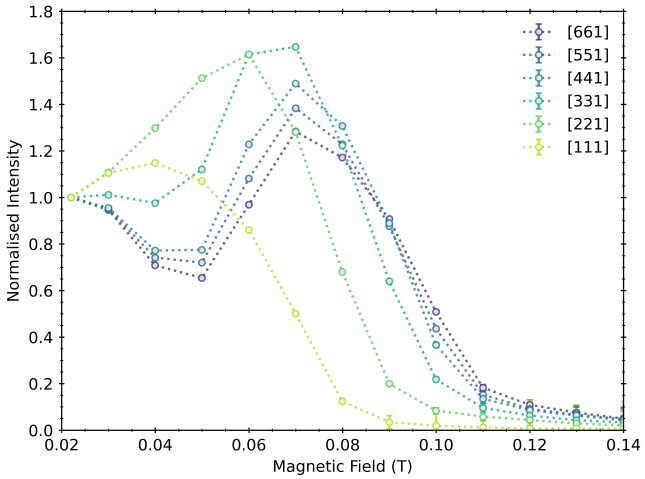

Figure 6.11: Orientation dependence of the renucleation of metastable skymrions at 5 K. Intensities are normalised to their initial value, and were obtained by summing suitable regions of interest within the GRASP software.

6.4 Discussion

As we have shown, metastable skyrmion renucleation is present at temperatures below 15 K and for a wide variety of crystallographic orientations. The exact mechanism behind the renucleation is currently unknown. However, we are able to gain hints of such a mechanism by considering the temperatures and co-exisiting phases.

Since the renucleations only happen at temperatures below 20 K, we can assume that thermal fluctuations do not play a role in stabilising the renucleated skyrmions, unlike the equilibrium phase at 58 K. Furthermore, at these temperatures, the low-temperature-skyrmion (LTS) phase appears only for magnetic fields applied along the [1 0 0]. We note that this entire study was performed away from the $\langle 1\,0\,0 \rangle$ directions, and zero-field-cooled scans displayed trivial magnetic behaviour (specifically, magnetic helices transforming into the conical/field-polarised phase which are not shown.) Therefore, the renucleated skyrmions are intrinsically different from the LTS, as they form along LTS-forbidden directions, and require a seeding, metastable skyrmion state. However, given the tempera-

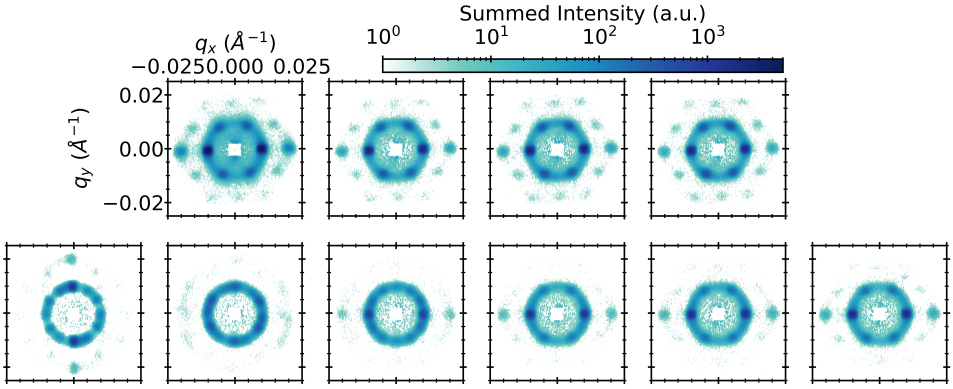

Figure 6.12: Initial metastable skyrmion states after skyrmion-field-cooling. Temperature dependence is in the top row, with temperatures of 10, 15, 20 and 25 K (left to right respectively.) Bottom row shows crystallographic dependence, with the magnetic field applied parallel to [1 1 1], [2 2 1], [3 3 1], [4 4 1], [5 5 1], [6 6 1] (left to right respectively)

tures at which both phases exist, we can assume that changes in crystalline and exchange anisotropies to play a role.

The extent to which these anisotropies play an effect is also unknown. For mechanisms which are highly dependent on the anisotropy, one expects the resultant behaviour to also behave very anisotropically. However, as shown in Figure 6.11, the renucleation phenomenon appears for a number of crystallographic directions. This reduces the reliance on the anisotropic interactions, although there are some notable differences between the crystal directions. For fields near parallel to [1 1 0][5], a magnetic phase coexistance with a helical state with a horizontal propagation vector is present, as well as a significant diffuse scattering at low-q. This is shown in Figure 6.12. On the otherhand, at angles towards the [1 1 1], no helix is is found in the diffraction patterns, although it is probably that 3 domains of helices do exist but do not meet the diffraction condition here. It is also possible, that the phase boundary between the helical state and conical state occurs at lower fields for these directions, meaning the metastable skyrmions

[5]including the [4 4 1], [5 5 1], [6 6 1]

have decayed into the conical state rather than helical state. Further measurements in a field-perpendicular geometry would answer this, or by performing a 3D reciprocal space mapping technique.

Ultimately, the images with both a clear helix and diffuse scattering present are those where the skyrmions initially decay, before renucleating back with much greater intensity, and the other directions lack this initial decay. This may reveal some more information about the role of the disorder. Recently, numerical simulations have shown that skyrmions are seeding from domain-walls between helical states with perpendicular magnetic wavevectors [250]. However, in our ZFC field-scans, we observed no presence of skyrmions, only in systems where a metastable skyrmion lattice was already present. This suggests that skyrmions are able to nucleate off other, already existing skyrmions, more easily than helical domain walls. This argument is further supported by the concomitant decrease in diffuse scattering with skyrmion renucleation in Figure 6.8 a.

In order to understand the nucleations, further work is planned. Here, we intend to do further SANS measurements in a perpendicular geometry in order to measure the role of the conical state during the nucleation procedure. This will allow us to see whether the metastable skyrmions just decay into helices and disorder during the SFC process, as well as look at the orientational dependence too. In order to understand why renucleations happens at all, micromagnetic simulations have been planned in order to show whether skyrmions are able to form at domain walls between skyrmions and the helical state, similar to a previous study just looking domain walls looking at helical textures with orthogonal wavevector [250]. Furthermore, we plan to use a geodesic nudged elastic band (GNEB) approach [333, 334, 335], which will be able to determine the minimum energy transition between a metastable skyrmion state and the renucleated skyrmions.

Finally, we will briefly turn our attention to the high-field (> 100 mT) behaviour during the [1 1 0]-direction field scan, whose data is shown in Figures 6.7 and 6.8. After the renculeation of skyrmions, we see a separate effect of a

skyrmion lattice distortion which gets more distorted with higher fields. The distortion itself is away from a hexagonal packing of skyrmions, breaking the degeneracy of the three magnetic wavevectors. Hexagonal lattice distortions require both a variation in the magnitude of the wavevectors, as well as their azimuthal locations, in agreement with our experimental results. Whilst spontaneous symmetry breaking has been used to describe the distributions in superconducting flux-line lattices [336, 337], here we suggest an alternative mechanism is responsible. As shown in Chapter 3, the anisotropic exchange interaction (AEI) within Cu_2OSeO_3 is both significant and negative in value. This interaction then naturally leads to magnetic helices shortening in wavevector if they are propagating along a $\langle 1\,0\,0 \rangle$ direction, and the $\langle 1\,1\,1 \rangle$ becoming hard axes respectively. Interestingly, the $[1\,1\,1]$ and $[\bar{1}\,1\,1]$ crystal directions are around 57° from the $[1\,0\,0]$ direction. A conventional, triple-q, skyrmion lattice forms with its wavevectors rotated 60° apart. Therefore it is favourable to both reduce the magnitude of the horizontal wavevector, and tilt the remaining two wavectors towards the $[0\,1\,1]$ direction. Both of these effects reduce the energy of the AEI, and the resultant shrinking and rotation describe canonical variables[6] for the distortion of a hexagonal lattice. In order to confirm that it is indeed the AEI that drives this deformation, particle dynamics simulations with novel anisotropic interactions are planned to model the large-scale deformation of an ensemble of skyrmions.

6.5 Conclusions

To conclude, we developed a sample holder in order to rapidly cool a single crystal of Cu_2OSeO_3 and allow the study of metastable skyrmions within the system. After characterising the metastable skyrmions, we discovered the phenomenon that skyrmions grew in volume fraction under the application of an increasing magnetic field, in contrast to our current understanding of metastable skyrmions.

[6] Canonical variables are ones which are linked to the properties of a system in an intrinsic linear combination, meaning any change of the system requires both variable to vary.

We further show this effect is present up to 15 K, and also found for a variety of different crystallographic orientation. The role of disorder, crystallographic orientation, magnetic phase co-existance, energy barriers and lattice distortions are planned to be investigated in follow-up experimental and theoretical investigations.

Chapter 7

Summary and Conclusion

To summarise, we saw in Chapter 1 that the magnetic interactions within certain single-crystal materials are essential for the self-stabilisation of skyrmions, and thus studying these interactions as well as others, leads to new opportunities to stabilise skyrmions in novel materials as well as the possibility for control them.

In Chapter 3, we discussed the importance of anisotropic interactions, such as magnetocrystalline anisotropy (MCA) and the anisotropic exchange interaction (AEI). Particularly, their role in stabilising the low-temperature magnetic states within Cu_2OSeO_3. We developed a methodology to separate out the effects of the two interactions, by looking at the directional dependence of the helical wavevector within a small-angle neutron scattering experiment. We then used this method to measure the AEI as a function of temperature in Zn-subsituted Cu_2OSeO_3, and remarkable saw a transition from having a positive value to negative with decreasing temperature. Our observation unifies why the helical wavevector in Cu_2OSeO_3 always remains along the [1 0 0] directions, as well as confirming that a negative AEI is responsible for forming the tilted conical state within the material. Interestingly, the change of sign corresponds to the overall balance of a large number of magnetic interactions within the unit cell, which form a myriad of individual and effective spin-excitations from a previous theoretical study, and we speculate whether the presence of these excitations is responsible for the large

change in a mean-field, macroscopic material parameter.

In Chapter 4, we investigated how an external electric field could be used within next-generational skyrmionic devices. In particular, we focused on the low-temperature tilted conical phase in Cu_2OSeO_3. By applying an electric field perpendicular to the magnetic field direction, we saw we were able to control the orientation of the tilted conical wavevector. We performed mean-field calculations that were in strong agreement with our experimental observations. Our calculations also provide a recipe for material scientists to engineer future materials to obtain large deflections in the tilted conical wavevector. Furthermore, we performed time-dependent micromagnetic simulations on a toy-system, which shows that our deflection mechanism would be useful for skyrmion transistor-like devices. This is because the tilted conical state could act as a barrier state, which deflects the path of the skyrmion. An electric field could then be used to change the direction of the barrier state, without affecting the stability of the skyrmion.

In Chapter 5, we investigated the spin-textures within the nano-skyrmion compound Gd_2PdSi_3 using resonant elastic x-ray scattering. Here, we were able to identify strong signals in the scattered intensity and the magnetic wavevector dependence as a function of the applied field which correspond to the magnetic phase transitions identified using magnetometry. We performed a full-linear polarisation analysis, which revealed the exact form of the incommensurate spin-textures to be composed of elliptical Bloch-type helices, as well as an omnipresent diffuse charge-scattering background. This charge scattering arises from crystalline stacking-faults in the crystallographic superlattice structure. Our fits show that these helices have to be chiral, but we also found these was no preferred handedness across a macroscopic region of the sample. We show that depending on the crystal-layer stacking, different local Dzyaloshinskii-Moriya interaction (DMI) vectors are present which may break the degeneracy of the helix at particular layers, as well as provide a site-dependent variation in effective field, explaining

a double-step transition upon cooling. We hope that upcoming site-dependent atomic simulations will confirm the DMI plays a significant role in this overall centrosymmetric system.

Finally, in Chapter 6, we revisit Cu_2OSeO_3 and investigated the field-dependent behaviour of metastable magnetic skyrmions. Unexpectedly, we observed a large increase in skyrmion population upon increasing the magnitude of the magnetic field, which is at odds with the current framework of previous studies of metastable skyrmions. This renucleation occurs for a number of crystal-directions, and is only present at low-temperatures. Future micromagnetic and geodesic nudged elastic band theoretical investigations are planned in order to reveal the microscopic mechanism and the relevant magnetic interactions behind this phenomena.

Appendix A

Conical State Ansatz within the Continuum Approximation

Mathematical Coordinate System and Angular Definitions

A.1 Derivation of Free Energy Equation

A.1.1 Mathematical description of a conical state

The conical spin-texture as a function of real-space position, $\mathbf{m}(\mathbf{r})$ is described by:

$$\mathbf{m}(\mathbf{r}) = \begin{pmatrix} m_1 \\ m_2 \\ m_3 \end{pmatrix} = \begin{pmatrix} \sin\theta\cos(\mathbf{q}\cdot\mathbf{r}) \\ \sin\theta\sin(\mathbf{q}\cdot\mathbf{r}) \\ \cos\theta \end{pmatrix} \begin{pmatrix} \hat{\mathbf{e}}_1 \\ \hat{\mathbf{e}}_2 \\ \hat{\mathbf{e}}_3 \end{pmatrix}, \tag{A.1}$$

where θ is the conical angle with $\theta = 0, \frac{\pi}{2}$ forming a field-polarised/helical state respectively. $\mathbf{q}$ is the wavevector of the conical state and contains the information about the wavelength of the conical state as well as specifying the direction the cone would propagate along. Here, $\{\hat{\mathbf{e}}_n\}$ define three mutually orthogonal basis vectors, such that $\mathbf{q} \parallel \hat{\mathbf{e}}_3$.

In our experiment, we observed that at low temperatures and moderate magnetic fields applied along the z-direction, a tilted conical state emerges whose wavevector does not follow the field direction. This tilting corresponded to intensities being recorded at a different azimuthal angle on the detector, ϕ, up towards the $[1\,1\,1]$ direction. In the following analysis, we use spherical polar coordinates to define the direction of the conical wavevector:

$$\begin{pmatrix} \hat{\mathbf{x}} \\ \hat{\mathbf{y}} \\ \hat{\mathbf{z}} \end{pmatrix} = \begin{pmatrix} \sin\phi\cos\chi \\ \sin\phi\sin\chi \\ \cos\phi \end{pmatrix}, \tag{A.2}$$

where the symbol for the polar angle ϕ being chosen due to its similarity for detector azimuthal angle when the equatorial angle $\chi = \frac{\pi}{4}$, *i.e.* it spans the plane normal to the $[1\,\bar{1}\,0]$-direction. This coordinate system is shown schematically in Figure A.1. Since a number of anisotropic energy density terms require the magnetisation along particular directions, it is useful to perform a change of basis into (m_x, m_y, m_z):

$$\begin{pmatrix} m_x \\ m_y \\ m_z \end{pmatrix} = \begin{pmatrix} \cos\chi & \cos\phi\sin\chi & -\sin\phi\sin\chi \\ -\sin\chi & \cos\phi\cos\chi & -\sin\phi\cos\chi \\ 0 & \sin\phi & \cos\phi \end{pmatrix} \begin{pmatrix} m_1 \\ m_2 \\ m_3 \end{pmatrix}. \tag{A.3}$$

Or using the Einstein summation convention:

$$m_i^c = \Lambda_{ij} m_j^e \tag{A.4}$$

where $m_i^{c,e}$ refer to the i^{th} magnetisation component in the cartesian/$\{\hat{\mathbf{e}}_n\}$ basis respectively.

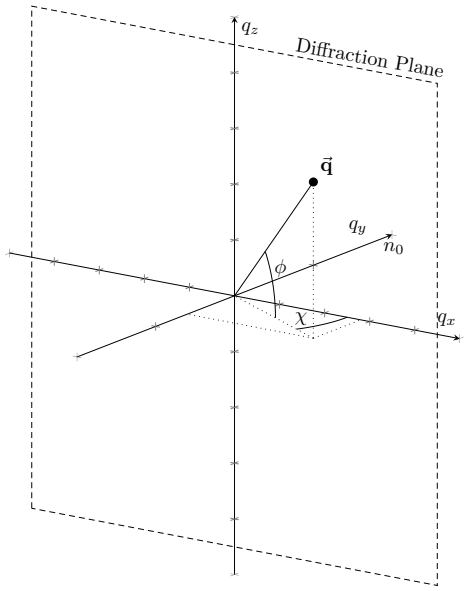

Figure A.1: Coordinate system used for both the experimental and theoretical analysis. Magnetic modulations with a particular wavevector, **q** can be described in polar coordinates using the equatorial, χ, and polar, ϕ, angles. In the SANS experimental results shown in Chapter 4, rotations of the sample (by the angle ω) rotates the diffraction plane about the q_z axis, allowing magnetic modulations which possess a drift in χ to be measured.

A.1.2 Magnetic Free Energy Density

The free energy density expansion for a slowly-varying spin density $\mathbf{m}(\mathbf{r})$ is given by:

$$\begin{aligned} F(\mathbf{r}) &= D\mathbf{m}(\mathbf{r}) \cdot (\nabla \times \mathbf{m}(\mathbf{r})) \\ &+ \frac{1}{2}A[(\nabla m_x)^2 + (\nabla m_y)^2 + (\nabla m_z)^2] \\ &+ \frac{1}{2}\gamma[(\frac{\partial m_x}{\partial x})^2 + (\frac{\partial m_y}{\partial y})^2 + (\frac{\partial m_z}{\partial z})^2] \ , \\ &+ K(m_x^4 + m_y^4 + m_z^4) \\ &- \mu_0 M_s(\mathbf{m}(\mathbf{r}) \cdot \mathbf{H}) - \mathbf{P}(\mathbf{r}) \cdot \mathbf{E} \end{aligned} \tag{A.5}$$

where a description of various energy terms and their constants can be found in the main text. Due to the cyclical nature of the magnetic textures, it's better to evaluate the average free energy density across a whole conical period, $\bar{F}$, where:

$$\bar{F} = \frac{1}{\lambda}\int_0^{\lambda} F(\mathbf{r})\ d^3\mathbf{r}. \tag{A.6}$$

Using this equation, we can determine the free-energy contribution of the various energy terms for different wavevector directions ϕ, χ and conical angles θ. Since both the Dzyaloshinskii Moriya and exchange interactions are isotropic, we do not need to consider them to explain our experimental findings.

Anisotropic Exchange Interaction

The average free energy due to the anisotropic exchange interaction is:

$$\begin{aligned}
\bar{F}_{AEI} &= \frac{1}{2\lambda}\gamma \int_0^{\lambda} [(\frac{\partial m_x}{\partial x})^2 + (\frac{\partial m_y}{\partial y})^2 + (\frac{\partial m_z}{\partial z})^2]\, d^3\mathbf{r} \\
&= \frac{1}{2\lambda}\gamma \int_0^{\lambda} \sum_{i=\{x,y,z\}} (\frac{\partial m_i}{\partial i})^2\, d^3\mathbf{r} \\
&= \frac{1}{2\lambda}\gamma \sum_{i=\{x,y,z\}} \int_0^{\lambda} q_i^2 \Lambda_{i1}^2 \sin^2\theta \sin^2(\mathbf{q}\cdot\mathbf{r}) + q_i^2 \Lambda_{i2} \sin^2\theta \cos(\mathbf{q}\cdot\mathbf{r}) \\
&\qquad\qquad - 2q_i^2 \Lambda_{i1}\Lambda_{i2} \sin(\mathbf{q}\cdot\mathbf{r})\cos(\mathbf{q}\cdot\mathbf{r}) \\
&= \frac{1}{4}\gamma \sum_{i=\{x,y,z\}} (\Lambda_{i1}^2 + \Lambda_{i2}^2) \sin^2\theta q_i^2 \\
&= \frac{1}{4}\gamma q^2 \sin^2\theta (2\sin^2\phi\cos^2\chi\sin^2\chi + \sin^2\phi\cos^2\phi(\cos^4\chi + \sin^4\chi) + \cos^2\phi\sin^2\phi).
\end{aligned}$$

Differentiating with respect to χ we find:

$$\frac{\partial \bar{F}_{AEI}}{\partial \chi} = \frac{1}{2}\gamma q^2 \sin^2\theta \sin^4\phi \sin\chi(\cos\chi + \cos 3\chi). \tag{A.7}$$

Taking a small angle approximation for χ:

$$\frac{\partial \bar{F}_{AEI}}{\partial \chi} \approx \gamma q^2 \chi \sin^2\theta \sin^4\phi, \tag{A.8}$$

we find that the variation of the average free energy due to the AEI is linear with small deviations in χ.

Magnetocrystalline Anisotropy

In a cubic system, the lowest order term which contributes to the magnetic anisotropy is to fourth order. This has the free energy form of:

$$\begin{aligned}
\bar{F}_{MCA} &= \frac{1}{\lambda}\int_0^{\lambda} K(m_x^4 + m_y^4 + m_z^4)\, d^3\mathbf{r} \\
&= \frac{K}{\lambda}\int_0^{\lambda} \sum_{i=x,y,z} m_i^4\, d^3\mathbf{r} \\
&= \frac{K}{\lambda}\int_0^{\lambda} \sum_{i=x,y,z} \Lambda_{i1}^4 m_1^4 + 6\Lambda_{i1}^2\Lambda_{i2}^2 m_1^2 m_2^2 + 6\Lambda_{i1}^2\Lambda_{i3} m_1^2 m_3^2 \\
&\qquad + \Lambda_{i2}^4 m_2^4 + 6\Lambda_{i2}^2\Lambda_{i3}^2 m_2^2 m_3^2 + \Lambda_{i3}^4 m_3^4 + else\ d^3\mathbf{r},
\end{aligned}$$

where *else* contains odd powers of the magnetisation which vanish during the integral. This gives us the result:

$$\begin{aligned}\bar{F}_{MCA} = K \sum_{i=x,y,z} \frac{3}{8} \sin^4\theta(\Lambda_{i1}^4 + 2\Lambda_{i1}^2\Lambda_{i2}^2 + \Lambda_{i2}^4) \\ + 3\cos^2\theta\sin^2\theta(\Lambda_{i1}^2\Lambda_{i3}^2 + \Lambda_{i2}^2\Lambda_{i3}^2) \\ + \cos^4\theta\Lambda_{i3}^4.\end{aligned}$$

Substituting in for a spherical polar coordinate basis yields:

$$\begin{aligned}\bar{F}_{MCA} = \frac{3K}{8}\sin^4\theta(\sin^4\chi + \cos^4\chi + 4\sin^2\chi\cos^2\chi\cos^2\phi + \cos^4\phi(\sin^4\chi + \cos^4\chi) + \sin^4\phi) \\ + 3K\cos^2\theta\sin^2\theta(2\sin^2\phi\sin^2\chi\cos^2\chi + \sin^2\phi\sin^2\phi(\cos^4\chi + \sin^4\chi + 1)) \\ + K\cos^4\theta(\cos^4\phi + \sin^4\phi(\sin^4\chi + \cos^4\chi)).\end{aligned}$$

Differentiating this with respect to χ:

$$\frac{\partial\bar{F}_{MCA}}{\partial\chi} = K\sin^4\phi(\sin\chi(\cos\chi + \cos(3\chi)(6\sin^2\theta\cos^2\theta - \frac{3}{4}\sin^4\theta)) - \sin(4\chi)). \tag{A.9}$$

And finally:

$$\frac{\partial\bar{F}_{MCA}}{\partial\chi} \approx K\sin^4\phi(24\sin^2\theta\cos^2\theta - 3\sin^4\theta - 4\cos^4\theta)\chi. \tag{A.10}$$

Zeeman Energy

The average Zeeman energy is given by:

$$\begin{aligned}\bar{F}_{Zee} &= -\frac{\mu_0 M_s}{\lambda}\int_0^\lambda \mathbf{m}(\mathbf{r})\cdot\mathbf{H}\, d^3\mathbf{r} \\ &= -\frac{\mu_0 M_s H}{\lambda}\int_0^\lambda m_z(\mathbf{r})\, d\mathbf{r} \\ &= -\frac{\mu_0 M_s H}{\lambda}\int_0^\lambda \sin\phi\sin\theta\sin(\mathbf{q}\cdot\mathbf{r}) + \cos\phi\cos\theta\, d\mathbf{r} \\ &= -\mu_0 M_s H\cos\phi\cos\theta,\end{aligned}$$

where we used our experimental geometry of applying a field along the z-direction, and the definition of m_z used in Eq. 3. This equation tells use the intuitive result that the Zeeman energy is minimized if all moments are collinear $\theta = 0$, and point along the magnetic field direction, $\phi = 0$. Note the lack of dependence on the equatorial angle, χ.

EP-Coupling

The average free energy due to an electric polarisation within an applied electric field is:

$$\bar{F}_{EP} = -\int_0^{\lambda} \mathbf{P} \cdot \mathbf{E}\, d^3\mathbf{r}, \tag{A.11}$$

where $P_i = \lambda^c m_j^c m_k^c$, with $\{i,j,k\} = \{x,y,z\}+cycl.$, and λ^c is the electromagnetic coupling constant. Integrating one polarisation component over one wavelength, λ, gives:

$$\begin{aligned}
\int_0^{\lambda} P_i\, d\mathbf{r} &= \lambda^c \int_0^{\lambda} m_j^c m_k^c\, d\mathbf{r} \\
&= \lambda^c \int_0^{\lambda} (\Lambda_{jl} m_l^e)(\Lambda_{kl} m_l^e)\, d\mathbf{r} \\
&= \lambda^c \int_0^{\lambda} \Lambda_{jl}\Lambda_{kl}(m_l^e)^2 + else.\, d\mathbf{r} \\
&= \lambda^c \lambda (\frac{\sin^2\theta}{2}(\Lambda_{j1}\Lambda_{k1} + \Lambda_{j2}\Lambda_{k2}) + \cos^2\theta \Lambda_{kl}\Lambda_{kl}),
\end{aligned}$$

where the $else.$ contains terms which vanish during the integration. Using this result, together with the Λ_{ij} values in (3) we can now determine the free energy due to an E-field along the $[1\,\bar{1}\,0]$:

$$\begin{aligned}
\bar{F}_{EP} &= -E\lambda^c \int_0^{\lambda} (m_y m_z - m_x m_z)\, d^3\mathbf{r} \\
&= -E\lambda^c [\frac{\sin^2\theta}{2}(\Lambda_{z1}(\Lambda_{y1} - \Lambda_{x1}) + \Lambda_{z2}(\Lambda_{y2} - \Lambda_{x2})) \\
&\quad + \Lambda_{z3}\cos^2\theta(\Lambda_{y3} - \Lambda_{x3})] \\
&= -E\lambda^c \sin\phi\cos\phi(\frac{\sin^2\theta}{2}(\cos\chi - \sin\chi) - \cos^2\theta(\cos\chi - \sin\chi)).
\end{aligned}$$

Differentiating with respect to χ gives:

$$\frac{\partial \bar{F}_{EP}}{\partial \chi} = E\lambda^c \sin\phi \cos\phi (\frac{\sin^2\theta}{2} - \cos^2\theta)(\sin\chi + \cos\chi), \tag{A.12}$$

and taking a small angle approximation gives us a linear equation:

$$\frac{\partial \bar{F}_{EP}}{\partial \chi} \approx E\lambda^c \sin\phi \cos\phi (\frac{\sin^2\theta}{2} - \cos^2\theta)(1 + \chi). \tag{A.13}$$

Appendix B

E-field Dependence of the Tilted Conical State

A zero-temperature free energy density expansion for a slowly-varying spin density $\mathbf{m}(\mathbf{r})$ is given by:

$$\begin{aligned} F(\mathbf{r}) &= D\mathbf{m}(\mathbf{r}) \cdot (\nabla \times \mathbf{m}(\mathbf{r})) \\ &+ \frac{1}{2}A[(\nabla m_x)^2 + (\nabla m_y)^2 + (\nabla m_z)^2] \\ &+ \frac{1}{2}\gamma[(\frac{\partial m_x}{\partial x})^2 + (\frac{\partial m_y}{\partial y})^2 + (\frac{\partial m_z}{\partial z})^2] \\ &+ K(m_x^4 + m_y^4 + m_z^4) \\ &- \mu_0 M_s(\mathbf{m}(\mathbf{r}) \cdot \mathbf{H}) - \mathbf{P}(\mathbf{r}) \cdot \mathbf{E}, \end{aligned} \tag{B.1}$$

where D, A is the Dzyaloshinskii-Moriya interaction coefficient and exchange stiffness respectively. The anisotropy constants, K, γ, are for the fourth-order magnetocrystalline anisotropy and anisotropic exchange interactions respectively, and are required take on particular values in order to generate a tilted conical state [156]. $\mathbf{H}$ and $\mathbf{E}$ are the applied magnetic and electric fields respectively, each linearly couple with the reduced magnetization $\mathbf{m}(\mathbf{r})$ and polarization $\mathbf{P}(\mathbf{r})$. We use the same polar coordinate basis to define the conical state wavevector in spherical polar coordinates, where $\mathbf{q} = \mathbf{q}(q, \phi, \chi)$, such that:

$$\mathbf{m}(\mathbf{r})/M_s = \sin\theta(\cos(\mathbf{q} \cdot \mathbf{r})\hat{\mathbf{e}}_1 + \sin(\mathbf{q} \cdot \mathbf{r})\hat{\mathbf{e}}_2) + \cos\theta\hat{\mathbf{e}}_3, \tag{B.2}$$

where θ is the conical angle, and $\{\hat{\mathbf{e}}_n\}$ define three mutually orthogonal basis vectors, such that $\mathbf{q} \parallel \hat{\mathbf{e}}_3$. To match the experimental configuration, we set the equatorial angle ($\chi = 0°$) such that variations in ϕ cause $\mathbf{q}$ to rotate about the $[1\,\bar{1}\,0]$ direction (neutron beam direction), within the plane perpendicular to the neutron beam during the SANS experiment (azimuthal angle on the a SANS experiment detector, see example patterns in Chapters 3,4 and 6). Using $\mathbf{q} = q(\sin\phi\cos\alpha, \sin\phi\sin\alpha, \cos\phi)$, together with an applied electric field along the $[1\,\bar{1}\,0]$ direction, E, inserting this into Eq. B.1, integrating over one conical period to find the average free energy before differentiating with respect to α, we find:

$$\begin{aligned}\frac{\partial \bar{F}}{\partial \alpha} &= \gamma\alpha q^2 \sin^2\theta \sin^4\phi \\ &+ E\lambda^c_{me} \sin\phi\cos\phi(1+\alpha) f(\theta) \\ &+ K\alpha \sin^4\phi g(\theta),\end{aligned} \tag{B.3}$$

where the functions $f(\theta) = \frac{\sin^2\theta}{2} - \cos^2\theta$ and $g(\theta) = 24\sin^2\theta\cos^2\theta - 3\sin^4\theta - 4\cos^4\theta$ are dependent on the conical angle only. As shown, the $(1+\alpha)$ term in Eq. (B.3) causes a non-zero electric field to shift the solutions of the free energy differential to finite values of α. These values can be determined by solving Eq. (4) to obtain $\alpha(E)$, which for small E we find the linear relationship present in the main text:

$$\frac{\partial \alpha}{\partial E} = \frac{\lambda^c_{me}\cos\phi f(\theta)}{\gamma q^2 \sin^2\theta\sin^3\phi + K\sin^4\phi g(\theta)}. \tag{B.4}$$

Furthermore, the magnitude of the gradient allows us to determine the conical angle θ providing the material constants are known. At 5 K, the material parameters of $\gamma = -6.7 \times 10^{-14}$ J m^{-1} [177], $K = -0.6 \times 10^3$ J m^3 [183] and $\lambda^c_{me} = 5.64 \times 10^{-27}$ µC m^{-1} [233] are known, allowing us to use the gradient of the 5 K dataset to determine the conical angle, θ =70.3(2)°.

Appendix C

Extended Results from P09

This appendix provides an extension of the experimental work collected from the P09 found in Chapter 5.

C.1 Field scans

In order to perform the FLPA measurements at appropriate fields, we repeated the field scans from I16 beamtime in order to identifying the phase boundaries. Figure C.1 shows a 3D map of the intensity (height) as a function of both, h, the reciprocal-lattice coordinate and the applied magnetic field, H, in panel (a). As can be seen, and further shown for clarity in panels (b) and (c), a large plateau of intensity between 0.5 and 0.9 T indicates the SkL pahse, as well as a dip in the magnitude of the magnetic wavevector τ. Using these scans, the two phase boundaries between the three magnetic phases were identified and the FLPA measurements were conduced at 0, 0.65 and 1.5 T respectively.

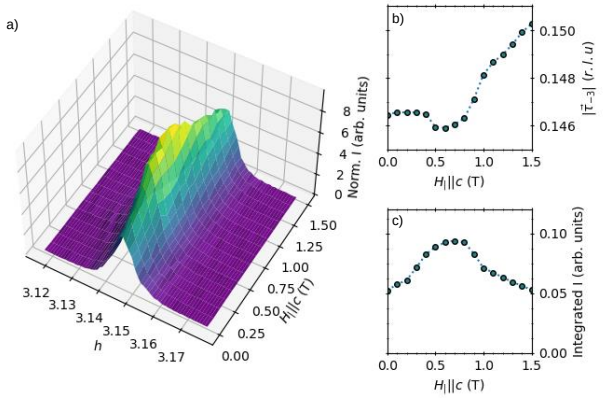

Figure C.1: Extended data from P09. a) 3D intensity map as a function of both magnetic field and recirpocal lattice vector. b, c) Field-dependence of the gaussian-fitted values of the magnitude of the magnetic wavevector (τ) and the intensities repectively

C.2 FLPA Fits Extended

In Chapter 5, we showed that the best fits could be obtained by using an incoherent mixture of the charge and magnetic contributions. In Figure C.2, the FLPA fits for both a coherent (dashed) and incoherent model (solid) are shown in the three magnetic phases. As shown, the incoherent model is clearly superior in fit quality for the IC-I and SkL phases, but both models are degenerate in the IC-II phase. This is because the IC-II phase is a spin-density wave with only one direction magnetic modulation, so the interference between magnetic and charge scattering leads to an identical effect for both an incoherent and coherent model.

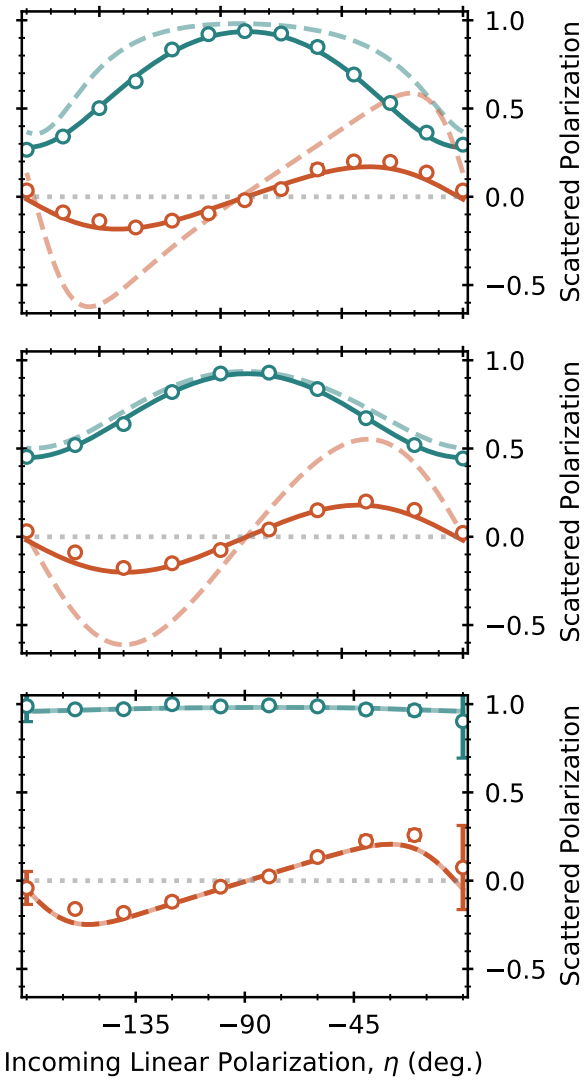

Figure C.2: FLPA data (open circles) with fits from both a model assuming coherent (dashed) and incoherent (solid) charge contributions together with incommensurate magnetism in three dimensions. Top panels shows the Ic-I state, middle is the SkL, and bottom is IC-II taken at fields of 0, 0.65 and 1.5 T respectively. Blue shows the Stokes component, P1, orange shows the P2.

Bibliography

[1] T. Skyrme, A unified field theory of mesons and baryons, Nuclear Physics **31**, 556 – 569 (1961).

[2] J. Perring and T. Skyrme, A model unified field equation, Nuclear Physics **31**, 550 – 555 (1961).

[3] J. K. Perring and T. H. R. Skyrme, The alpha-particle and shell models of the nucleus, Proceedings of the Physical Society. Section A **69**, 600–609 (1956).

[4] G. Zweig, An SU(3) model for strong interaction symmetry and its breaking. Version 2, in *Developments in the Quark Theory of Hadrons. Vol. 1. 1964 - 1978*, edited by D. B. Lichtenberg and S. P. Rosen (1964) pp. 22–101.

[5] M. Gell-Mann, A schematic model of baryons and mesons, Physics Letters **8**, 214–215 (1964).

[6] T. Skyrme, The origins of skyrmions, International Journal of Modern Physics A **03**, 2745–2751 (1988).

[7] C. Naya and P. Sutcliffe, Skyrmions and clustering in light nuclei, Phys. Rev. Lett. **121**, 232002 (2018).

[8] P. Jaikumar, M. Bagchi, and R. Ouyed, High-density skyrmion matter and neutron stars, The Astrophysical Journal **678**, 360 (2008).

[9] C. Adam, C. Naya, J. Sanchez-Guillen, R. Vazquez, and A. Wereszczynski, BPS skyrmions as neutron stars, Physics Letters B **742**, 136–142 (2015).

[10] L. Landau and E. Lifshits, *Statistical Physics*, Addison-Wesley series in advanced physics No. v. 3 (Pergamon Press, 1958).

[11] U. Al Khawaja and H. Stoof, Skyrmions in a ferromagnetic Bose-Einstein condensate, Nature **411**, 918–920 (2001).

[12] R. A. Battye, N. R. Cooper, and P. M. Sutcliffe, Stable skyrmions in two-component Bose-Einstein condensates, Phys. Rev. Lett. **88**, 080401 (2002).

[13] L. S. Leslie, A. Hansen, K. C. Wright, B. M. Deutsch, and N. P. Bigelow, Creation and detection of skyrmions in a Bose-Einstein condensate, Phys. Rev. Lett. **103**, 250401 (2009).

[14] K. Tiurev, T. Ollikainen, P. Kuopanportti, M. Nakahara, D. S. Hall, and M. Möttönen, Three-dimensional skyrmions in spin-2 Bose–Einstein condensates, New Journal of Physics **20**, 055011 (2018).

[15] A. C. Balram, U. Wurstbauer, A. Wójs, A. Pinczuk, and J. K. Jain, Fractionally charged skyrmions in fractional quantum Hall effect, Nature Communications **6**, 8981 (2015).

[16] T. Jolicoeur and B. Pandey, Quantum Hall skyrmions at $\nu = 0, \pm 1$ in monolayer graphene, Phys. Rev. B **100**, 115422 (2019).

[17] E. Mascot, J. Bedow, M. Graham, S. Rachel, and D. K. Morr, Topological superconductivity in skyrmion lattices, npj Quantum Materials **6**, 6 (2021).

[18] M. Garnier, A. Mesaros, and P. Simon, Topological superconductivity with deformable magnetic skyrmions, Communications Physics **2**, 126 (2019).

[19] E. Khalaf, S. Chatterjee, N. Bultinck, M. P. Zaletel, and A. Vishwanath, Charged skyrmions and topological origin of superconductivity in magic-angle graphene, Science Advances **7**, eabf5299 (2021).

[20] D. Foster, C. Kind, P. J. Ackerman, J.-S. B. Tai, M. R. Dennis, and I. I. Smalyukh, Two-dimensional skyrmion bags in liquid crystals and ferromagnets, Nature Physics **15**, 655–659 (2019).

[21] J.-i. Fukuda and S. Žumer, Quasi-two-dimensional skyrmion lattices in a chiral nematic liquid crystal, Nature Communications **2**, 246 (2011).

[22] A. Duzgun and C. Nisoli, Skyrmion spin ice in liquid crystals, Phys. Rev. Lett. **126**, 047801 (2021).

[23] S. Mühlbauer, B. Binz, F. Jonietz, C. Pfleiderer, A. Rosch, A. Neubauer, R. Georgii, and P. Böni, Skyrmion lattice in a chiral magnet, Science **323**, 915–919 (2009).

[24] N. Nagaosa and Y. Tokura, Topological properties and dynamics of magnetic skyrmions, Nature Nanotechnology **8**, 899–911 (2013).

[25] X. Z. Yu, Y. Onose, N. Kanazawa, J. H. Park, J. H. Han, Y. Matsui, N. Nagaosa, and Y. Tokura, Real-space observation of a two-dimensional skyrmion crystal, Nature **465**, 901–904 (2010).

[26] S. Heinze, K. von Bergmann, M. Menzel, J. Brede, A. Kubetzka, R. Wiesendanger, G. Bihlmayer, and S. Blügel, Spontaneous atomic-scale magnetic skyrmion lattice in two dimensions, Nature Physics **7**, 713–718 (2011).

[27] T. Lancaster, Skyrmion review paper, To Be Published (exp. 2019).

[28] E. Khalaf and A. Vishwanath, Baby skyrmions in chern ferromagnets and topological mechanism for spin-polaron formation in twisted bilayer graphene, Nature Communications **13**, 6245 (2022).

[29] P. J. Ackerman, T. Boyle, and I. I. Smalyukh, Squirming motion of baby skyrmions in nematic fluids, Nature Communications **8**, 673 (2017).

[30] B. Piette, B. Schroers, and W. Zakrzewski, Dynamics of baby skyrmions, Nuclear Physics B **439**, 205–235 (1995).

[31] P. C. Hohenberg, Existence of long-range order in one and two dimensions, Phys. Rev. **158**, 383–386 (1967).

[32] N. D. Mermin and H. Wagner, Absence of ferromagnetism or antiferromagnetism in one- or two-dimensional isotropic Heisenberg models, Phys. Rev. Lett. **17**, 1133–1136 (1966).

[33] S. Girvin and K. Yang, *Modern Condensed Matter Physics* (Cambridge University Press, 2019).

[34] S. J. Blundell, *Magnetism in Condensed Matter* (Oxford University Press, Oxford, 2003).

[35] F. J. dos Santos, M. dos Santos Dias, and S. Lounis, Nonreciprocity of spin waves in noncollinear magnets due to the Dzyaloshinskii-Moriya interaction, Phys. Rev. B **102**, 104401 (2020).

[36] B. Odom, D. Hanneke, B. D'Urso, and G. Gabrielse, New measurement of the electron magnetic moment using a one-electron quantum cyclotron, Phys. Rev. Lett. **97**, 030801 (2006).

[37] A. Sommerfeld, Zur feinstruktur der wasserstofflinien. geschichte und gegenwärtiger stand der theorie, Naturwissenschaften **28**, 417–423 (1940).

[38] A. A. Michelson and E. W. Morley, On a method of making the wavelength of sodium light the actual and practical standard of length, American Journal of Science **s3-34**, 427–430 (1887).

[39] H. Kramers, L'interaction entre les atomes magnétogènes dans un cristal paramagnétique, Physica **1**, 182–192 (1934).

[40] C. Zener, Interaction between the *d*-shells in the transition metals. ii. ferromagnetic compounds of manganese with perovskite structure, Phys. Rev. **82**, 403–405 (1951).

[41] D. Cortés-Ortuño, M. Beg, V. Nehruji, L. Breth, R. Pepper, T. Kluyver, G. Downing, T. Hesjedal, P. Hatton, T. Lancaster, R. Hertel, O. Hovorka,

and H. Fangohr, Proposal for a micromagnetic standard problem for materials with Dzyaloshinskii–Moriya interaction, New Journal of Physics **20**, 113015 (2018).

[42] M. A. Ruderman and C. Kittel, Indirect exchange coupling of nuclear magnetic moments by conduction electrons, Phys. Rev. **96**, 99–102 (1954).

[43] T. Kasuya, A Theory of Metallic Ferro- and Antiferromagnetism on Zener's Model, Progress of Theoretical Physics **16**, 45–57 (1956).

[44] K. Yosida, Magnetic properties of Cu-Mn alloys, Phys. Rev. **106**, 893–898 (1957).

[45] J. H. Van Vleck, Note on the interactions between the spins of magnetic ions or nuclei in metals, Rev. Mod. Phys. **34**, 681–686 (1962).

[46] Q.-C. Sun, T. Song, E. Anderson, A. Brunner, J. Förster, T. Shalomayeva, T. Taniguchi, K. Watanabe, J. Gräfe, R. Stöhr, X. Xu, and J. Wrachtrup, Magnetic domains and domain wall pinning in atomically thin $CrBr_3$ revealed by nanoscale imaging, Nature Communications **12**, 1989 (2021).

[47] F. Zheng, F. N. Rybakov, N. S. Kiselev, D. Song, A. Kovács, H. Du, S. Blügel, and R. E. Dunin-Borkowski, Magnetic skyrmion braids, Nature Communications **12**, 5316 (2021).

[48] C. Abert, Micromagnetics and spintronics: models and numerical methods, The European Physical Journal B **92**, 120 (2019).

[49] E. M. de Jager, On the origin of the Korteweg-de Vries equation 10.48550/ArXiV.math/0602661 (2006).

[50] A. Bogdanov and C. Panagopoulos, The emergence of magnetic skyrmions, Physics Today **73**, 44 (2020).

[51] A. N. Bogdanov and D. A. Yablonskii, Thermodynamically stable "vortices" in magnetically ordered crystals. The mixed state of magnets, Soviet Journal of Experimental and Theoretical Physics **68**, 101 (1989).

[52] N. Bogdanov, A, V. Kudinov, M, and A. Yablonskii, D, To the theory of magnetic vortices in easy axis ferromagnets, Phys. Rev. B. Solid State **31**, 1707–1710.

[53] A. Bogdanov and A. Hubert, The properties of isolated magnetic vortices, physica status solidi (b) **186**, 527–543 (1994).

[54] A. Bogdanov and A. Hubert, Thermodynamically stable magnetic vortex states in magnetic crystals, Journal of Magnetism and Magnetic Materials **138**, 255–269 (1994).

[55] A. Bogdanov, New localized solutions of the nonlinear field equations, ZhETF Pisma Redaktsiiu **62**, 231 (1995).

[56] Y. Lin, P. Grundy, and E. Giess, Bubble domains in magnetostatically coupled garnet films, Applied Physics Letters **23**, 485–487 (1973).

[57] M. Slonczewski and A. Malozemoff, Magnetic domain walls in bubble materials, Suppl (1979).

[58] T. Garel and S. Doniach, Phase transitions with spontaneous modulation-the dipolar Ising ferromagnet, Physical Review B **26**, 325 (1982).

[59] S. Takao, A study of magnetization distribution of submicron bubbles in sputtered Ho-Co thin films, Journal of magnetism and magnetic materials **31**, 1009–1010 (1983).

[60] J. Sampaio, V. Cros, S. Rohart, A. Thiaville, and A. Fert, Nucleation, stability and current-induced motion of isolated magnetic skyrmions in nanostructures, Nature Nanotechnology **8**, 839–844 (2013).

[61] B. Dupé, M. Hoffmann, C. Paillard, and S. Heinze, Tailoring magnetic skyrmions in ultra-thin transition metal films, Nature Communications **5**, 4030 (2014).

[62] S. Woo, K. Litzius, B. Krüger, M.-Y. Im, L. Caretta, K. Richter, M. Mann, A. Krone, R. M. Reeve, M. Weigand, P. Agrawal, I. Lemesh, M.-A. Mawass, P. Fischer, M. Kläui, and G. S. D. Beach, Observation of room-temperature magnetic skyrmions and their current-driven dynamics in ultrathin metallic ferromagnets, Nature Materials **15**, 501–506 (2016).

[63] S. Woo, K. Litzius, B. Krüger, M.-Y. Im, L. Caretta, K. Richter, M. Mann, A. Krone, R. M. Reeve, M. Weigand, P. Agrawal, I. Lemesh, M.-A. Mawass, P. Fischer, M. Kläui, and G. S. D. Beach, Observation of room-temperature magnetic skyrmions and their current-driven dynamics in ultrathin metallic ferromagnets, Nature Materials **15**, 501–506 (2016).

[64] R. Wiesendanger, Nanoscale magnetic skyrmions in metallic films and multilayers: a new twist for spintronics, Nature Reviews Materials **1**, 16044 (2016).

[65] S. D. Pollard, J. A. Garlow, J. Yu, Z. Wang, Y. Zhu, and H. Yang, Observation of stable Néel skyrmions in cobalt/palladium multilayers with lorentz transmission electron microscopy, Nature Communications **8**, 14761 (2017).

[66] I. Lemesh, K. Litzius, M. Böttcher, P. Bassirian, N. Kerber, D. Heinze, J. Zázvorka, F. Büttner, L. Caretta, M. Mann, M. Weigand, S. Finizio, J. Raabe, M.-Y. Im, H. Stoll, G. Schütz, B. Dupé, M. Kläui, and G. S. D. Beach, Current-induced skyrmion generation through morphological thermal transitions in chiral ferromagnetic heterostructures, Advanced Materials **30**, 1805461 (2018).

[67] S. Ding, A. Ross, R. Lebrun, S. Becker, K. Lee, I. Boventer, S. Das, Y. Kurokawa, S. Gupta, J. Yang, G. Jakob, and M. Kläui, Interfacial Dzyaloshinskii-Moriya interaction and chiral magnetic textures in a ferrimagnetic insulator, Phys. Rev. B **100**, 100406 (2019).

[68] L. Caretta, E. Rosenberg, F. Büttner, T. Fakhrul, P. Gargiani, M. Valvidares, Z. Chen, P. Reddy, D. A. Muller, C. A. Ross, and G. S. D. Beach,

Interfacial Dzyaloshinskii-Moriya interaction arising from rare-earth orbital magnetism in insulating magnetic oxides, Nature Communications **11**, 1090 (2020).

[69] H. Wang, Y. Dai, Z. Liu, Q. Xie, C. Liu, W. Lin, L. Liu, P. Yang, J. Wang, T. V. Venkatesan, G. M. Chow, H. Tian, Z. Zhang, and J. Chen, Overcoming the limits of the interfacial Dzyaloshinskii–Moriya interaction by antiferromagnetic order in multiferroic heterostructures, Advanced Materials **32**, 1904415 (2020).

[70] L. Powalla, M. T. Birch, K. Litzius, S. Wintz, F. Schulz, M. Weigand, T. Scholz, B. V. Lotsch, K. Kern, G. Schütz, and M. Burghard, Single skyrmion generation via a vertical nanocontact in a 2D magnet-based heterostructure, Nano Letters **22**, 9236–9243 (2022).

[71] W. Jiang, G. Chen, K. Liu, J. Zang, S. G. te Velthuis, and A. Hoffmann, Skyrmions in magnetic multilayers, Physics Reports **704**, 1–49 (2017).

[72] H. A. Dürr, E. Dudzik, S. S. Dhesi, J. B. Goedkoop, G. van der Laan, M. Belakhovsky, C. Mocuta, A. Marty, and Y. Samson, Chiral magnetic domain structures in ultrathin FePd films, Science **284**, 2166–2168 (1999).

[73] K. Zeissler, S. Finizio, K. Shahbazi, J. Massey, F. A. Ma'Mari, D. M. Bracher, A. Kleibert, M. C. Rosamond, E. H. Linfield, T. A. Moore, J. Raabe, G. Burnell, and C. H. Marrows, Discrete Hall resistivity contribution from Néel skyrmions in multilayer nanodiscs, Nature Nanotechnology **13**, 1161–1166 (2018).

[74] T. Okubo, S. Chung, and H. Kawamura, Multiple-q states and the skyrmion lattice of the triangular-lattice heisenberg antiferromagnet under magnetic fields, Physical review letters **108**, 017206 (2012).

[75] S. Heinze, K. Von Bergmann, M. Menzel, J. Brede, A. Kubetzka, R. Wiesendanger, G. Bihlmayer, and S. Blügel, Spontaneous atomic-scale magnetic skyrmion lattice in two dimensions, nature physics **7**, 713–718 (2011).

[76] M. Hirschberger, T. Nakajima, S. Gao, L. Peng, A. Kikkawa, T. Kurumaji, M. Kriener, Y. Yamasaki, H. Sagayama, H. Nakao, K. Ohishi, K. Kakurai, Y. Taguchi, X. Yu, T.-h. Arima, and Y. Tokura, Skyrmion phase and competing magnetic orders on a breathing kagomé lattice, Nature Communications **10**, 5831 (2019).

[77] M. Hirschberger, S. Hayami, and Y. Tokura, Nanometric skyrmion lattice from anisotropic exchange interactions in a centrosymmetric host, New Journal of Physics **23**, 023039 (2021).

[78] T. Kurumaji, T. Nakajima, M. Hirschberger, A. Kikkawa, Y. Yamasaki, H. Sagayama, H. Nakao, Y. Taguchi, T.-h. Arima, and Y. Tokura, Skyrmion lattice with a giant topological Hall effect in a frustrated triangular-lattice magnet, Science **365**, 914–918 (2019).

[79] N. D. Khanh, T. Nakajima, X. Yu, S. Gao, K. Shibata, M. Hirschberger, Y. Yamasaki, H. Sagayama, H. Nakao, L. Peng, K. Nakajima, R. Takagi, T.-h. Arima, Y. Tokura, and S. Seki, Nanometric square skyrmion lattice in a centrosymmetric tetragonal magnet, Nature Nanotechnology **15**, 444–449 (2020).

[80] D. Chakrabartty, S. Jamaluddin, S. K. Manna, and A. K. Nayak, Tunable room temperature magnetic skyrmions in centrosymmetric kagome magnet Mn_4Ga_2Sn, Communications Physics **5**, 189 (2022).

[81] R. Takagi, N. Matsuyama, V. Ukleev, L. Yu, J. S. White, S. Francoual, J. R. L. Mardegan, S. Hayami, H. Saito, K. Kaneko, K. Ohishi, Y. Ōnuki, T.-h. Arima, Y. Tokura, T. Nakajima, and S. Seki, Square and rhombic lattices of magnetic skyrmions in a centrosymmetric binary compound, Nature Communications **13**, 1472 (2022).

[82] J. S. White, A. Butykai, R. Cubitt, D. Honecker, C. D. Dewhurst, L. F. Kiss, V. Tsurkan, and S. Bordács, Direct evidence for cycloidal modulations in the

thermal-fluctuation-stabilized spin spiral and skyrmion states of GaV_4S_8, Phys. Rev. B **97**, 020401 (2018).

[83] T. Kurumaji, T. Nakajima, A. Feoktystov, E. Babcock, Z. Salhi, V. Ukleev, T.-h. Arima, K. Kakurai, and Y. Tokura, Direct observation of cycloidal spin modulation and field-induced transition in Néel-type skyrmion-hosting $VOSe_2O_5$, Journal of the Physical Society of Japan **90**, 024705 (2021).

[84] I. Kézsmárki, S. Bordács, P. Milde, E. Neuber, L. M. Eng, J. S. White, H. M. Rønnow, C. D. Dewhurst, M. Mochizuki, K. Yanai, H. Nakamura, D. Ehlers, V. Tsurkan, and A. Loidl, Néel-type skyrmion lattice with confined orientation in the polar magnetic semiconductor GaV_4S_8, Nature Materials **14**, 1116–1122 (2015).

[85] T. J. Hicken, M. N. Wilson, S. J. R. Holt, R. Khassanov, M. R. Lees, R. Gupta, D. Das, G. Balakrishnan, and T. Lancaster, Magnetism in the Néel skyrmion host GaV_4S_8 under pressure (2022).

[86] K. J. A. Franke, B. M. Huddart, T. J. Hicken, F. Xiao, S. J. Blundell, F. L. Pratt, M. Crisanti, J. A. T. Barker, S. J. Clark, A. c. v. Štefančič, M. C. Hatnean, G. Balakrishnan, and T. Lancaster, Magnetic phases of skyrmion-hosting $GaV_4S_{8-y}S_y$(y=0,2,4,8) probed with muon spectroscopy, Phys. Rev. B **98**, 054428 (2018).

[87] T. J. Hicken, S. J. R. Holt, K. J. A. Franke, Z. Hawkhead, A. Štefančič, M. N. Wilson, M. Gomilšek, B. M. Huddart, S. J. Clark, M. R. Lees, F. L. Pratt, S. J. Blundell, G. Balakrishnan, and T. Lancaster, Magnetism and Néel skyrmion dynamics in $GaV_4S_{8-y}S_y$, Phys. Rev. Res. **2**, 032001 (2020).

[88] X. Z. Yu, N. Kanazawa, Y. Onose, K. Kimoto, W. Z. Zhang, S. Ishiwata, Y. Matsui, and Y. Tokura, Near room-temperature formation of a skyrmion crystal in thin-films of the helimagnet FeGe, Nature Materials **10**, 106–109 (2011).

[89] Y. Tokunaga, X. Z. Yu, J. S. White, H. M. Rønnow, D. Morikawa, Y. Taguchi, and Y. Tokura, A new class of chiral materials hosting magnetic skyrmions beyond room temperature, Nature Communications **6**, 7638 (2015).

[90] S. Seki, X. Z. Yu, S. Ishiwata, and Y. Tokura, Observation of skyrmions in a multiferroic material, Science **336**, 198–201 (2012).

[91] M. Janoschek, M. Garst, A. Bauer, P. Krautscheid, R. Georgii, P. Böni, and C. Pfleiderer, Fluctuation-induced first-order phase transition in Dzyaloshinskii-Moriya helimagnets, Phys. Rev. B **87**, 134407 (2013).

[92] S. Brazovskii, Phase transition of an isotropic system to a nonuniform state - jetp 41, 85 (1975), Soviet Phys JETP. **41** (1996).

[93] S. V. Grigoriev, S. V. Maleyev, E. V. Moskvin, V. A. Dyadkin, P. Fouquet, and H. Eckerlebe, Crossover behavior of critical helix fluctuations in MnSi, Phys. Rev. B **81**, 144413 (2010).

[94] C. Pappas, L. J. Bannenberg, E. Lelièvre-Berna, F. Qian, C. D. Dewhurst, R. M. Dalgliesh, D. L. Schlagel, T. A. Lograsso, and P. Falus, Magnetic fluctuations, precursor phenomena, and phase transition in MnSi under a magnetic field, Phys. Rev. Lett. **119**, 047203 (2017).

[95] C. Pappas, E. Lelièvre-Berna, P. Falus, P. M. Bentley, E. Moskvin, S. Grigoriev, P. Fouquet, and B. Farago, Chiral paramagnetic skyrmion-like phase in MnSi, Phys. Rev. Lett. **102**, 197202 (2009).

[96] C. Pappas, E. Lelièvre-Berna, P. Bentley, P. Falus, P. Fouquet, and B. Farago, Magnetic fluctuations and correlations in MnSi: Evidence for a chiral skyrmion spin liquid phase, Phys. Rev. B **83**, 224405 (2011).

[97] S. Kusaka, K. Yamamoto, T. Komatsubara, and Y. Ishikawa, Ultrasonic study of magnetic phase diagram of MnSi, Solid State Communications **20**, 925–927 (1976).

[98] K. Kadowaki, K. Okuda, and M. Date, Magnetization and magnetoresistance of MnSi, Journal of the Physical Society of Japan **51**, 2433–2438 (1982).

[99] A. A. Leonov, A. N. Bogdanov, and U. K. Roessler, Confinement of skyrmion states in noncentrosymmetric magnets (2010).

[100] X. Zhang, Y. Zhou, K. Mee Song, T.-E. Park, J. Xia, M. Ezawa, X. Liu, W. Zhao, G. Zhao, and S. Woo, Skyrmion-electronics: writing, deleting, reading and processing magnetic skyrmions toward spintronic applications, Journal of Physics: Condensed Matter **32**, 143001 (2020).

[101] R. Tomasello, E. Martinez, R. Zivieri, L. Torres, M. Carpentieri, and G. Finocchio, A strategy for the design of skyrmion racetrack memories, Scientific Reports **4**, 6784 (2014).

[102] A. Fert, N. Reyren, and V. Cros, Magnetic skyrmions: advances in physics and potential applications, Nature Reviews Materials **2**, 17031 (2017).

[103] D. Okuyama, M. Bleuel, J. S. White, Q. Ye, J. Krzywon, G. Nagy, Z. Q. Im, I. Živković, M. Bartkowiak, H. M. Rønnow, S. Hoshino, J. Iwasaki, N. Nagaosa, A. Kikkawa, Y. Taguchi, Y. Tokura, D. Higashi, J. D. Reim, Y. Nambu, and T. J. Sato, Deformation of the moving magnetic skyrmion lattice in MnSi under electric current flow, Communications Physics **2**, 79 (2019).

[104] S. Loth, S. Baumann, C. P. Lutz, D. M. Eigler, and A. J. Heinrich, Bistability in atomic-scale antiferromagnets, Science **335**, 196–199 (2012).

[105] G. Chen, Skyrmion Hall effect, Nature Physics **13**, 112–113 (2017).

[106] W. Jiang, X. Zhang, G. Yu, W. Zhang, X. Wang, M. Benjamin Jungfleisch, J. E. Pearson, X. Cheng, O. Heinonen, K. L. Wang, Y. Zhou, A. Hoffmann, and S. G. E. te Velthuis, Direct observation of the skyrmion Hall effect, Nature Physics **13**, 162–169 (2017).

[107] K. Litzius, I. Lemesh, B. Krüger, P. Bassirian, L. Caretta, K. Richter, F. Büttner, K. Sato, O. A. Tretiakov, J. Förster, R. M. Reeve, M. Weigand, I. Bykova, H. Stoll, G. Schütz, G. S. D. Beach, and M. Kläui, Skyrmion Hall effect revealed by direct time-resolved x-ray microscopy, Nature Physics **13**, 170–175 (2017).

[108] R. Brearton, L. A. Turnbull, J. A. T. Verezhak, G. Balakrishnan, P. D. Hatton, G. van der Laan, and T. Hesjedal, Deriving the skyrmion Hall angle from skyrmion lattice dynamics, Nature Communications **12**, 2723 (2021).

[109] W. Legrand, D. Maccariello, F. Ajejas, S. Collin, A. Vecchiola, K. Bouzehouane, N. Reyren, V. Cros, and A. Fert, Room-temperature stabilization of antiferromagnetic skyrmions in synthetic antiferromagnets, Nature Materials **19**, 34–42 (2020).

[110] R. Juge, N. Sisodia, J. U. Larrañaga, Q. Zhang, V. T. Pham, K. G. Rana, B. Sarpi, N. Mille, S. Stanescu, R. Belkhou, M.-A. Mawass, N. Novakovic-Marinkovic, F. Kronast, M. Weigand, J. Gräfe, S. Wintz, S. Finizio, J. Raabe, L. Aballe, M. Foerster, M. Belmeguenai, L. D. Buda-Prejbeanu, J. Pelloux-Prayer, J. M. Shaw, H. T. Nembach, L. Ranno, G. Gaudin, and O. Boulle, Skyrmions in synthetic antiferromagnets and their nucleation via electrical current and ultra-fast laser illumination, Nature Communications **13**, 4807 (2022).

[111] S. Mallick, S. Panigrahy, G. Pradhan, and S. Rohart, Current-induced nucleation and motion of skyrmions in zero magnetic field, Phys. Rev. Appl. **18**, 064072 (2022).

[112] S. Wang, J. Tang, W. Wang, L. Kong, M. Tian, and H. Du, Electrical detection of magnetic skyrmions, Journal of Low Temperature Physics **197**, 321–336 (2019).

[113] B. Göbel, A. F. Schäffer, J. Berakdar, I. Mertig, and S. S. P. Parkin, Elec-

trical writing, deleting, reading, and moving of magnetic skyrmioniums in a racetrack device, Scientific Reports **9**, 12119 (2019).

[114] J. Spethmann, E. Y. Vedmedenko, R. Wiesendanger, A. Kubetzka, and K. von Bergmann, Zero-field skyrmionic states and in-field edge-skyrmions induced by boundary tuning, Communications Physics **5**, 19 (2022).

[115] Y. Guang, I. Bykova, Y. Liu, G. Yu, E. Goering, M. Weigand, J. Gräfe, S. K. Kim, J. Zhang, H. Zhang, Z. Yan, C. Wan, J. Feng, X. Wang, C. Guo, H. Wei, Y. Peng, Y. Tserkovnyak, X. Han, and G. Schütz, Creating zero-field skyrmions in exchange-biased multilayers through x-ray illumination, Nature Communications **11**, 949 (2020).

[116] D. Li, S. Haldar, and S. Heinze, Strain-driven zero-field near-10 nm skyrmions in two-dimensional van der Waals heterostructures, Nano Letters **22**, 7706–7713 (2022).

[117] L. Peng, K. Karube, Y. Taguchi, N. Nagaosa, Y. Tokura, and X. Yu, Dynamic transition of current-driven single-skyrmion motion in a room-temperature chiral-lattice magnet, Nature Communications **12**, 6797 (2021).

[118] R. Gruber, J. Zázvorka, M. A. Brems, D. R. Rodrigues, T. Dohi, N. Kerber, B. Seng, M. Vafaee, K. Everschor-Sitte, P. Virnau, and M. Kläui, Skyrmion pinning energetics in thin film systems, Nature Communications **13**, 3144 (2022).

[119] C. Hanneken, A. Kubetzka, K. von Bergmann, and R. Wiesendanger, Pinning and movement of individual nanoscale magnetic skyrmions via defects, New Journal of Physics **18**, 055009 (2016).

[120] W. J. Poppelbaum, C. Afuso, and J. W. Esch, Stochastic computing elements and systems, in *Proceedings of the November 14-16, 1967, Fall Joint Computer Conference* (Association for Computing Machinery, New York, NY, USA, 1967) p. 635–644.

[121] B. R. Gaines, Stochastic computing, in *Proceedings of the April 18-20, 1967, Spring Joint Computer Conference* (Association for Computing Machinery, New York, NY, USA, 1967) p. 149–156.

[122] H. Zhang, D. Zhu, W. Kang, Y. Zhang, and W. Zhao, Stochastic computing implemented by skyrmionic logic devices, Phys. Rev. Appl. **13**, 054049 (2020).

[123] A. F. Schäffer, L. Rózsa, J. Berakdar, E. Y. Vedmedenko, and R. Wiesendanger, Stochastic dynamics and pattern formation of geometrically confined skyrmions, Communications Physics **2**, 72 (2019).

[124] D. Pinna, F. Abreu Araujo, J.-V. Kim, V. Cros, D. Querlioz, P. Bessiere, J. Droulez, and J. Grollier, Skyrmion gas manipulation for probabilistic computing, Phys. Rev. Appl. **9**, 064018 (2018).

[125] K. M. Song, J.-S. Jeong, B. Pan, X. Zhang, J. Xia, S. Cha, T.-E. Park, K. Kim, S. Finizio, J. Raabe, J. Chang, Y. Zhou, W. Zhao, W. Kang, H. Ju, and S. Woo, Skyrmion-based artificial synapses for neuromorphic computing, Nature Electronics **3**, 148–155 (2020).

[126] G. Bourianoff, D. Pinna, M. Sitte, and K. Everschor-Sitte, Potential implementation of reservoir computing models based on magnetic skyrmions, AIP Advances **8**, 055602 (2017).

[127] D. Pinna, G. Bourianoff, and K. Everschor-Sitte, Reservoir computing with random skyrmion textures, arXiv: Mesoscale and Nanoscale Physics (2018).

[128] T. Yokouchi, S. Sugimoto, B. Rana, S. Seki, N. Ogawa, Y. Shiomi, S. Kasai, and Y. Otani, Pattern recognition with neuromorphic computing using magnetic field–induced dynamics of skyrmions, Science Advances **8** (2022).

[129] T. Weber, D. M. Fobes, J. Waizner, P. Steffens, G. S. Tucker, M. Böhm, L. Beddrich, C. Franz, H. Gabold, R. Bewley, D. Voneshen, M. Skoulatos,

R. Georgii, G. Ehlers, A. Bauer, C. Pfleiderer, P. Böni, M. Janoschek, and M. Garst, Topological magnon band structure of emergent landau levels in a skyrmion lattice, Science **375**, 1025–1030 (2022).

[130] S. Seki, M. Garst, J. Waizner, R. Takagi, N. D. Khanh, Y. Okamura, K. Kondou, F. Kagawa, Y. Otani, and Y. Tokura, Propagation dynamics of spin excitations along skyrmion strings, Nature Communications **11**, 256 (2020).

[131] D. A. Garanin, R. Jaafar, and E. M. Chudnovsky, Breathing mode of a skyrmion on a lattice, Phys. Rev. B **101**, 014418 (2020).

[132] T. J. Hicken, M. N. Wilson, K. J. A. Franke, B. M. Huddart, Z. Hawkhead, M. Gomilšek, S. J. Clark, F. L. Pratt, A. Štefančič, A. E. Hall, M. Ciomaga Hatnean, G. Balakrishnan, and T. Lancaster, Megahertz dynamics in skyrmion systems probed with muon-spin relaxation, Phys. Rev. B **103**, 024428 (2021).

[133] M. Garst, J. Waizner, and D. Grundler, Collective spin excitations of helices and magnetic skyrmions: review and perspectives of magnonics in non-centrosymmetric magnets, Journal of Physics D: Applied Physics **50**, 293002 (2017).

[134] Y. Onose, Y. Okamura, S. Seki, S. Ishiwata, and Y. Tokura, Observation of magnetic excitations of skyrmion crystal in a helimagnetic insulator Cu_2OSeO_3, Phys. Rev. Lett. **109**, 037603 (2012).

[135] S. Grigoriev, S. Maleyev, A. Okorokov, Y. Chetverikov, and H. Eckerlebe, Field-induced reorientation of helix in MnSi near TC, Journal of Magnetism and Magnetic Materials **310**, 1599–1601 (2007), proceedings of the 17th International Conference on Magnetism.

[136] C. I. Gregory, *Magnetic properties of the Itinerant helimagnets MnSi and FeGe*, Ph.D. thesis, Durham University (1992).

[137] D. Sivia, *Elementary Scattering Theory: For X-ray and Neutron Users* (OUP Oxford, 2011).

[138] V. F. Sears, Appendix. neutron scattering lengths and cross sections, in *Neutron Scattering*, Methods in Experimental Physics, Vol. 23, edited by K. Sköld and D. L. Price (Academic Press, 1986) pp. 521–550.

[139] C. G. Shull, Early development of neutron scattering, Rev. Mod. Phys. **67**, 753–757 (1995).

[140] E. Prince, *International Tables for Crystallography, Volume C: Mathematical, Physical and Chemical Tables*, International Tables for Crystallography (Springer Netherlands, 2004).

[141] G. Squires, *Introduction to the Theory of Thermal Neutron Scattering* (Cambridge University Press, 2012).

[142] M. Born, Quantenmechanik der stoßvorgänge, Zeitschrift für Physik **38**, 803–827 (1926).

[143] J. Trefil and S. McGrayne, *Encyclopedia Britannica* (Encyclopædia Britannica, Inc, 2023).

[144] N. Nagaosa and Y. Tokura, Topological properties and dynamics of magnetic skyrmions, Nature Nanotechnology **8**, 899 (2013), review Article.

[145] C. G. Shull, W. A. Strauser, and E. O. Wollan, Neutron diffraction by paramagnetic and antiferromagnetic substances, Phys. Rev. **83**, 333–345 (1951).

[146] O. Halpern and M. H. Johnson, On the neutron's magnetic moment, Phys. Rev. **57**, 160–160 (1940).

[147] F. De Bergevin and M. Brunel, Observation of magnetic superlattice peaks by x-ray diffraction on an antiferromagnetic NiO crystal, Physics Letters A **39**, 141–142 (1972).

[148] F. Lin, Y. Liu, X. Yu, L. Cheng, A. Singer, O. G. Shpyrko, H. L. Xin, N. Tamura, C. Tian, T.-C. Weng, X.-Q. Yang, Y. S. Meng, D. Nordlund, W. Yang, and M. M. Doeff, Synchrotron x-ray analytical techniques for studying materials electrochemistry in rechargeable batteries, Chemical Reviews **117**, 13123–13186 (2017).

[149] J. P. Hannon, G. T. Trammell, M. Blume, and D. Gibbs, X-ray resonance exchange scattering, Phys. Rev. Lett. **61**, 1245–1248 (1988).

[150] T. A. W. Beale, T. P. A. Hase, T. Iida, K. Endo, P. Steadman, A. R. Marshall, S. S. Dhesi, G. van der Laan, and P. D. Hatton, Rasor: An advanced instrument for soft x-ray reflectivity and diffraction, Review of Scientific Instruments **81**, 073904 (2010).

[151] D. Goldstein, *Polarized Light* (CRC Press, 2011).

[152] M. Born, L. Born, E. Wolf, A. Bhatia, P. Clemmow, D. Gabor, A. Stokes, A. Taylor, P. Wayman, *et al.*, *Principles of Optics: Electromagnetic Theory of Propagation, Interference and Diffraction of Light* (Cambridge University Press, 1999).

[153] R. C. Jones, A new calculus for the treatment of optical systemsi. description and discussion of the calculus, J. Opt. Soc. Am. **31**, 488–493 (1941).

[154] J. P. Hill and D. F. McMorrow, Resonant Exchange Scattering: Polarization Dependence and Correlation Function, Acta Crystallographica Section A **52**, 236–244 (1996).

[155] C. Detlefs, M. Sanchez del Rio, and C. Mazzoli, X-ray polarization: General formalism and polarization analysis, The European Physical Journal Special Topics **208**, 359–371 (2012).

[156] F. Qian, L. J. Bannenberg, H. Wilhelm, G. Chaboussant, L. M. Debeer-Schmitt, M. P. Schmidt, A. Aqeel, T. T. M. Palstra, E. Brück, A. J. E. Lefering, C. Pappas, M. Mostovoy, and A. O. Leonov, New magnetic phase

of the chiral skyrmion material Cu_2OSeO_3, Science Advances **4**, 10.1126/sciadv.aat7323 (2018).

[157] A. Chacon, L. Heinen, M. Halder, A. Bauer, W. Simeth, S. Mühlbauer, H. Berger, M. Garst, A. Rosch, and C. Pfleiderer, Observation of two independent skyrmion phases in a chiral magnetic material, Nature Physics **14**, 936–941 (2018).

[158] M. Oshikawa, Recent developments in low-temperature esr in quantum antiferromagnetic chains, in *EPR in the 21st Century*, edited by A. Kawamori, J. Yamauchi, and H. Ohta (Elsevier Science B.V., Amsterdam, 2002) pp. 15–26.

[159] W. H. Meiklejohn, Exchange anisotropy—a review, Journal of Applied Physics **33**, 1328–1335 (1962).

[160] A. Berkowitz and K. Takano, Exchange anisotropy — a review, Journal of Magnetism and Magnetic Materials **200**, 552–570 (1999).

[161] K. Kumari, A. Kumar, M. Shin, S. Kumar, S. H. Huh, and B. H. Koo, Investigating the magnetocrystalline anisotropy and the exchange bias through interface effects of nanocrystalline FeCo, Journal of the Korean Physical Society **79**, 1180–1189 (2021).

[162] V. Ukleev, O. Utesov, L. Yu, C. Luo, K. Chen, F. Radu, Y. Yamasaki, N. Kanazawa, Y. Tokura, T.-h. Arima, and J. S. White, Signature of anisotropic exchange interaction revealed by vector-field control of the helical order in a FeGe thin plate, Phys. Rev. Res. **3**, 013094 (2021).

[163] S. V. Maleyev, Cubic magnets with dzyaloshinskii-moriya interaction at low temperature, Phys. Rev. B **73**, 174402 (2006).

[164] S. V. Grigoriev, S. V. Maleyev, A. I. Okorokov, Y. O. Chetverikov, R. Georgii, P. Böni, D. Lamago, H. Eckerlebe, and K. Pranzas, Critical fluctuations in MnSi near T_C: A polarized neutron scattering study, Phys. Rev. B **72**, 134420 (2005).

[165] L. Udvardi, L. Szunyogh, K. Palotás, and P. Weinberger, First-principles relativistic study of spin waves in thin magnetic films, Phys. Rev. B **68**, 104436 (2003).

[166] I. Dzyaloshinskii, On the magneto-electrical effect in antiferromagnetics, Zh. Eksp. Teor. Fiz. **37** (1960).

[167] P. Bak and M. H. Jensen, Theory of helical magnetic structures and phase transitions in MnSi and FeGe, Journal of Physics C Solid State Physics **13**, 881–885 (1980).

[168] B. Lebech, J. Bernhard, and T. Freltoft, Magnetic structures of cubic fege studied by small-angle neutron scattering, Journal of Physics: Condensed Matter **1**, 6105 (1989).

[169] J. Rigue, D. Chrischon, A. de Andrade, and M. Carara, A torque magnetometer for thin films applications, Journal of Magnetism and Magnetic Materials **324**, 1561–1564 (2012).

[170] J. Burd, M. Huq, and E. Lee, The determination of magnetic anisotropy constants from torque curves, Journal of Magnetism and Magnetic Materials **5**, 135–141 (1977).

[171] J. S. Kouvel and C. D. Graham, On the determination of magnetocrystalline anisotropy constants from torque measurements, Journal of Applied Physics **28**, 340–343 (1957).

[172] M. Preißinger, K. Karube, D. Ehlers, B. Szigeti, H.-A. Krug von Nidda, J. S. White, V. Ukleev, H. M. Rønnow, Y. Tokunaga, A. Kikkawa, Y. Tokura, Y. Taguchi, and I. Kézsmárki, Vital role of magnetocrystalline anisotropy in cubic chiral skyrmion hosts, npj Quantum Materials **6**, 65 (2021).

[173] V. V. Chirkov, G. G. Gumarov, V. Y. Petukhov, M. M. Bakirov, V. I. Nuzhdin, and V. F. Valeev, FMR investigation of the magnetic anisotropy in films synthesized by Co^+ implantation into Si, Applied Magnetic Resonance **49**, 381–388 (2018).

[174] M. Igarashi, T. Kambe, K. Yoshida, Y. Hosoe, and Y. Sugita, A method of measuring anisotropy field of polycrystalline thin-film media, Journal of Applied Physics **85**, 4720–4722 (1999).

[175] T. Tainosho, J.-i. Inoue, S. Sharmin, M. Takeguchi, E. Kita, and H. Yanagihara, Large negative uniaxial magnetic anisotropy in highly distorted Co-ferrite thin films, Applied Physics Letters **114**, 092408 (2019).

[176] S. Kumar, C. E. Patrick, R. S. Edwards, G. Balakrishnan, M. R. Lees, and J. B. Staunton, Torque magnetometry study of the spin reorientation transition and temperature-dependent magnetocrystalline anisotropy in $NdCo_5$, Journal of Physics: Condensed Matter **32**, 255802 (2020).

[177] S. H. Moody, P. Nielsen, M. N. Wilson, D. A. Venero, A. Štefančič, G. Balakrishnan, and P. D. Hatton, Experimental evidence of a change of exchange anisotropy sign with temperature in Zn-substituted Cu_2OSeO_3, Physical Review Research **3**, 043149 (2021).

[178] A. Štefančič, S. H. Moody, T. J. Hicken, M. T. Birch, G. Balakrishnan, S. A. Barnett, M. Crisanti, J. S. O. Evans, S. J. R. Holt, K. J. A. Franke, P. D. Hatton, B. M. Huddart, M. R. Lees, F. L. Pratt, C. C. Tang, M. N. Wilson, F. Xiao, and T. Lancaster, Origin of skyrmion lattice phase splitting in Zn-substituted Cu_2OSeO_3, Physical Review Materials **2**, 111402(R) (2018).

[179] M. T. Birch, R. Takagi, S. Seki, M. N. Wilson, F. Kagawa, A. Štefančič, G. Balakrishnan, R. Fan, P. Steadman, C. J. Ottley, M. Crisanti, R. Cubitt, T. Lancaster, Y. Tokura, and P. D. Hatton, Increased lifetime of metastable skyrmions by controlled doping, Phys. Rev. B **100**, 014425 (2019).

[180] O. Arnold, J. Bilheux, J. Borreguero, A. Buts, S. Campbell, L. Chapon, M. Doucet, N. Draper, R. Ferraz Leal, M. Gigg, V. Lynch, A. Markvardsen, D. Mikkelson, R. Mikkelson, R. Miller, K. Palmen, P. Parker, G. Passos, T. Perring, P. Peterson, S. Ren, M. Reuter, A. Savici, J. Taylor, R. Taylor, R. Tolchenov, W. Zhou, and J. Zikovsky, Mantid—data analysis and

visualization package for neutron scattering and musr experiments, Nuclear Instruments and Methods in Physics Research Section A: Accelerators, Spectrometers, Detectors and Associated Equipment **764**, 156–166 (2014).

[181] R. M. White, *Quantum Theory of Magnetism* (Springer, Berlin, 1983).

[182] Y. A. Izyumov, Modulated, or long-periodic, magnetic structures of crystals, Soviet Physics Uspekhi **27**, 845–867 (1984).

[183] M. Halder, A. Chacon, A. Bauer, W. Simeth, S. Mühlbauer, H. Berger, L. Heinen, M. Garst, A. Rosch, and C. Pfleiderer, Thermodynamic evidence of a second skyrmion lattice phase and tilted conical phase in Cu_2OSeO_3, Physical Review B **98**, 144429 (2018).

[184] G. S. Tucker, J. S. White, J. Romhányi, D. Szaller, I. Kézsmárki, B. Roessli, U. Stuhr, A. Magrez, F. Groitl, P. Babkevich, P. Huang, I. Živković, and H. M. Rønnow, Spin excitations in the skyrmion host Cu_2OSeO_3, Phys. Rev. B **93**, 054401 (2016).

[185] Y. Luo, G. G. Marcus, B. A. Trump, J. Kindervater, M. B. Stone, J. A. Rodriguez-Rivera, Y. Qiu, T. M. McQueen, O. Tchernyshyov, and C. Broholm, Low-energy magnons in the chiral ferrimagnet Cu_2OSeO_3: A coarse-grained approach, Phys. Rev. B **101**, 144411 (2020).

[186] O. Janson, I. Rousochatzakis, A. A. Tsirlin, M. Belesi, A. A. Leonov, U. K. Rößler, J. van den Brink, and H. Rosner, The quantum nature of skyrmions and half-skyrmions in Cu_2OSeO_3, Nature Communications **5**, 5376 (2014).

[187] D. Astrov, The magnetoelectric effect in antiferromagnets, Sov. Phys. SETP **11** (1960).

[188] S. N. Panja, P. Manuel, and S. Nair, Anisotropy in the magnetization and magnetoelectric response of single crystalline $Mn_4Ta_2O_9$, Phys. Rev. B **103**, 014422 (2021).

[189] V. J. Folen, G. T. Rado, and E. W. Stalder, Anisotropy of the magnetoelectric effect in Cr_2O_3, Phys. Rev. Lett. **6**, 607–608 (1961).

[190] P. Esther Rubavathi, D. Dhayanithi, N. Giridharan, M. Rahul, N. Kalarikkal, and B. Sundarakannan, Origin of magnetic, magnetoelectric effect and the influence of reentrant ferroelectric phase on the structural and multiferroic properties of Dy^{3+}-Fe^{3+} Co-substituted $BaTiO_3$ ceramics, Journal of Magnetism and Magnetic Materials **538**, 168260 (2021).

[191] I. V. Solovyev and T. V. Kolodiazhnyi, Origin of magnetoelectric effect in $Co_4Nb_2O_9$ and $Co_4Ta_2O_9$: The lessons learned from the comparison of first-principles-based theoretical models and experimental data, Phys. Rev. B **94**, 094427 (2016).

[192] A. F. Popkov, M. D. Davydova, K. A. Zvezdin, S. V. Solov'yov, and A. K. Zvezdin, Origin of the giant linear magnetoelectric effect in perovskitelike multiferroic $BiFeO_3$, Phys. Rev. B **93**, 094435 (2016).

[193] G. Yahia, F. Damay, S. Chattopadhyay, V. Balédent, W. Peng, E. Elkaim, M. Whitaker, M. Greenblatt, M.-B. Lepetit, and P. Foury-Leylekian, Recognition of exchange striction as the origin of magnetoelectric coupling in multiferroics, Phys. Rev. B **95**, 184112 (2017).

[194] J.-M. Hu, C.-G. Duan, C.-W. Nan, and L.-Q. Chen, Understanding and designing magnetoelectric heterostructures guided by computation: progresses, remaining questions, and perspectives, npj Computational Materials **3**, 18 (2017).

[195] C. A. F. Vaz, J. Hoffman, Y. Segal, J. W. Reiner, R. D. Grober, Z. Zhang, C. H. Ahn, and F. J. Walker, Origin of the magnetoelectric coupling effect in multiferroic heterostructures, Phys. Rev. Lett. **104**, 127202 (2010).

[196] M. Fiebig, T. Lottermoser, D. Meier, and M. Trassin, The evolution of multiferroics, Nature Reviews Materials **1**, 16046 (2016).

[197] N. A. Spaldin and R. Ramesh, Advances in magnetoelectric multiferroics, Nature Materials **18**, 203–212 (2019).

[198] B. Jana, K. Ghosh, K. Rudrapal, P. Gaur, P. K. Shihabudeen, and A. Roy Chaudhuri, Recent progress in flexible multiferroics, Frontiers in Physics **9**, 10.3389/fphy.2021.822005 (2022).

[199] C.-W. Nan and J.-M. Liu, Multiferroics: a beautiful but challenging multipolar world, National Science Review **6**, 620–620 (2019).

[200] R. d. A. Martins, Joule's 1840 manuscript on the production of heat by voltaic electricity, Notes and Records: the Royal Society Journal of the History of Science **76**, 117–154 (2022).

[201] J.-M. Hu, L.-Q. Chen, and C.-W. Nan, Multiferroic heterostructures integrating ferroelectric and magnetic materials, Advanced materials **28**, 15–39 (2016).

[202] A. Kovács, J. Caron, A. S. Savchenko, N. S. Kiselev, K. Shibata, Z.-A. Li, N. Kanazawa, Y. Tokura, S. Blügel, and R. E. Dunin-Borkowski, Mapping the magnetization fine structure of a lattice of Bloch-type skyrmions in an FeGe thin film, Applied Physics Letters **111**, 192410 (2017).

[203] C. R. MacKinnon, K. Zeissler, S. Finizio, J. Raabe, C. H. Marrows, T. Mercer, P. R. Bissell, and S. Lepadatu, Collective skyrmion motion under the influence of an additional interfacial spin-transfer torque, Scientific Reports **12**, 10786 (2022).

[204] M. T. Birch, D. Cortés-Ortuño, L. A. Turnbull, M. N. Wilson, F. Groß, N. Träger, A. Laurenson, N. Bukin, S. H. Moody, M. Weigand, G. Schütz, H. Popescu, R. Fan, P. Steadman, J. A. T. Verezhak, G. Balakrishnan, J. C. Loudon, A. C. Twitchett-Harrison, O. Hovorka, H. Fangohr, F. Y. Ogrin, J. Gräfe, and P. D. Hatton, Real-space imaging of confined magnetic skyrmion tubes, Nature Communications **11**, 1726 (2020).

[205] T. Yokouchi, F. Kagawa, M. Hirschberger, Y. Otani, N. Nagaosa, and Y. Tokura, Emergent electromagnetic induction in a helical-spin magnet, Nature **586**, 232–236 (2020).

[206] P. Xiong, F. Zhang, X. Zhang, S. Wang, H. Liu, B. Sun, J. Zhang, Y. Sun, R. Ma, Y. Bando, C. Zhou, Z. Liu, T. Sasaki, and G. Wang, Strain engineering of two-dimensional multilayered heterostructures for beyond-lithium-based rechargeable batteries, Nature Communications **11**, 3297 (2020).

[207] S. Paul and S. Heinze, Electric-field driven stability control of skyrmions in an ultrathin transition-metal film, npj Computational Materials **8**, 105 (2022).

[208] P.-J. Hsu, A. Kubetzka, A. Finco, N. Romming, K. von Bergmann, and R. Wiesendanger, Electric-field-driven switching of individual magnetic skyrmions, Nature Nanotechnology **12**, 123–126 (2017).

[209] M. Schott, A. Bernand-Mantel, L. Ranno, S. Pizzini, J. Vogel, H. Bea, C. Baraduc, S. Auffret, G. Gaudin, and D. Givord, The skyrmion switch: Turning magnetic skyrmion off with an electric field, NANO LETTERS **17**, 3006–3012 (2017).

[210] C. Ma, X. Zhang, J. Xia, M. Ezawa, W. Jiang, T. Ono, S. N. Piramanayagam, A. Morisako, Y. Zhou, and X. Liu, Electric field-induced creation and directional motion of domain walls and skyrmion bubbles, NANO LETTERS **19**, 353–361 (2019).

[211] T. Srivastava, M. Schott, R. Juge, V. Křižáková, M. Belmeguenai, Y. Roussigné, A. Bernand-Mantel, L. Ranno, S. Pizzini, S.-M. Chérif, A. Stashkevich, S. Auffret, O. Boulle, G. Gaudin, M. Chshiev, C. Baraduc, and H. Béa, Large-voltage tuning of dzyaloshinskii–moriya interactions: A route toward dynamic control of skyrmion chirality, Nano Letters **18**, 4871–4877 (2018).

[212] P. Upadhyaya, G. Yu, P. K. Amiri, and K. L. Wang, Electric-field guiding of magnetic skyrmions, Phys. Rev. B **92**, 134411 (2015).

[213] H. T. Fook, W. L. Gan, and W. S. Lew, Gateable skyrmion transport via field-induced potential barrier modulation, Scientific Reports **6**, 21099 (2016).

[214] Y. Nakatani, M. Hayashi, S. Kanai, S. Fukami, and H. Ohno, Electric field control of skyrmions in magnetic nanodisks, Applied Physics Letters **108**, 152403 (2016).

[215] J.-M. Hu, T. Yang, and L.-Q. Chen, Strain-mediated voltage-controlled switching of magnetic skyrmions in nanostructures, npj Computational Materials **4**, 62 (2018).

[216] L. Desplat, S. Meyer, J. Bouaziz, P. M. Buhl, S. Lounis, B. Dupe, and P. A. Hervieux, Mechanism for ultrafast electric-field driven skyrmion nucleation, Phys. Rev. B **104**, 10.1103/PhysRevB.104.L060409 (2021).

[217] H. Yang, O. Boulle, V. Cros, A. Fert, and M. Chshiev, Controlling dzyaloshinskii-moriya interaction via chirality dependent atomic-layer stacking, insulator capping and electric field, Scientific Reports **8**, 12356 (2018).

[218] C.-E. Fillion, J. Fischer, R. Kumar, A. Fassatoui, S. Pizzini, L. Ranno, D. Ourdani, M. Belmeguenai, Y. Roussigné, S.-M. Chérif, S. Auffret, I. Joumard, O. Boulle, G. Gaudin, L. Buda-Prejbeanu, C. Baraduc, and H. Béa, Gate-controlled skyrmion and domain wall chirality, Nature Communications **13**, 5257 (2022).

[219] Y. Tikhonov, S. Kondovych, J. Mangeri, M. Pavlenko, L. Baudry, A. Sené, A. Galda, S. Nakhmanson, O. Heinonen, A. Razumnaya, I. Luk'yanchuk, and V. M. Vinokur, Controllable skyrmion chirality in ferroelectrics, Scientific Reports **10**, 8657 (2020).

[220] P. Behera, M. A. May, F. Gómez-Ortiz, S. Susarla, S. Das, C. T. Nelson, L. Caretta, S.-L. Hsu, M. R. McCarter, B. H. Savitzky, E. S. Barnard, A. Raja, Z. Hong, P. García-Fernandez, S. W. Lovesey, G. van der Laan,

P. Ercius, C. Ophus, L. W. Martin, J. Junquera, M. B. Raschke, and R. Ramesh, Electric field control of chirality, Science Advances **8**, eabj8030 (2022).

[221] N. Mathur, F. S. Yasin, M. J. Stolt, T. Nagai, K. Kimoto, H. Du, M. Tian, Y. Tokura, X. Yu, and S. Jin, In-plane magnetic field-driven creation and annihilation of magnetic skyrmion strings in nanostructures, Advanced Functional Materials **31**, 2008521 (2021).

[222] X. Yu, F. Kagawa, S. Seki, M. Kubota, J. Masell, F. S. Yasin, K. Nakajima, M. Nakamura, M. Kawasaki, N. Nagaosa, and Y. Tokura, Real-space observations of 60-nm skyrmion dynamics in an insulating magnet under low heat flow, Nature Communications **12**, 5079 (2021).

[223] X. Yu, K. V. Iakoubovskii, F. S. Yasin, L. Peng, K. Nakajima, S. Schneider, K. Karube, T. Arima, Y. Taguchi, and Y. Tokura, Real-space observations of three-dimensional antiskyrmions and skyrmion strings, Nano Letters **22**, 9358–9364 (2022).

[224] F. S. Yasin, J. Masell, K. Karube, A. Kikkawa, Y. Taguchi, Y. Tokura, and X. Yu, Real space demonstration of electric current-induced isolated skyrmion deformation, Microscopy and Microanalysis **28**, 1724–1725 (2022).

[225] K. Fallon, S. Hughes, K. Zeissler, W. Legrand, F. Ajejas, D. Maccariello, S. McFadzean, W. Smith, D. McGrouther, S. Collin, N. Reyren, V. Cros, C. H. Marrows, and S. McVitie, Controlled individual skyrmion nucleation at artificial defects formed by ion irradiation, Small **16**, 1907450 (2020).

[226] K. Zeissler, S. Finizio, C. Barton, A. J. Huxtable, J. Massey, J. Raabe, A. V. Sadovnikov, S. A. Nikitov, R. Brearton, T. Hesjedal, G. van der Laan, M. C. Rosamond, E. H. Linfield, G. Burnell, and C. H. Marrows, Diameter-independent skyrmion Hall angle observed in chiral magnetic multilayers, Nature Communications **11**, 428 (2020).

[227] K. H. Miller, X. S. Xu., H. Berger, E. S. Knowles, D. J. Arenas, M. W. Meisel, and D. B. Tanner, Magnetodielectric coupling of infrared phonons in single-crystal Cu_2OSeO_3, Phys. Rev. B **82**, 144107 (2010).

[228] J.-W. G. Bos, C. V. Colin, and T. T. M. Palstra, Magnetoelectric coupling in the cubic ferrimagnet Cu_2OSeO_3, Phys. Rev. B **78**, 094416 (2008).

[229] T. Adams, A. Chacon, M. Wagner, A. Bauer, G. Brandl, B. Pedersen, H. Berger, P. Lemmens, and C. Pfleiderer, Long-wavelength helimagnetic order and skyrmion lattice phase in Cu_2OSeO_3, Phys. Rev. Lett. **108**, 237204 (2012).

[230] S. Seki, J.-H. Kim, D. S. Inosov, R. Georgii, B. Keimer, S. Ishiwata, and Y. Tokura, Formation and rotation of skyrmion crystal in the chiral-lattice insulator Cu_2OSeO_3, Phys. Rev. B **85**, 220406 (2012).

[231] S. Seki, S. Ishiwata, and Y. Tokura, Magnetoelectric nature of skyrmions in a chiral magnetic insulator Cu_2OSeO_3, Phys. Rev. B **86**, 060403 (2012).

[232] E. Ruff, P. Lunkenheimer, A. Loidl, H. Berger, and S. Krohns, Magnetoelectric effects in the skyrmion host material Cu_2OSeO_3, Scientific reports **5**, 15025 (2015).

[233] M. Mochizuki and S. Seki, Dynamical magnetoelectric phenomena of multiferroic skyrmions, Journal of Physics: Condensed Matter **27**, 503001 (2015).

[234] H. Murakawa, Y. Onose, S. Miyahara, N. Furukawa, and Y. Tokura, Comprehensive study of the ferroelectricity induced by the spin-dependent d-p hybridization mechanism in $Ba_2XGe_2O_7$ (X = Mn, Co, and Cu), Phys. Rev. B **85**, 174106 (2012).

[235] T.-h. Arima, Ferroelectricity induced by proper-screw type magnetic order, Journal of the Physical Society of Japan **76**, 073702 (2007).

[236] C. Jia, S. Onoda, N. Nagaosa, and J. H. Han, Bond electronic polarization induced by spin, Phys. Rev. B **74**, 224444 (2006).

[237] C. Jia, S. Onoda, N. Nagaosa, and J. H. Han, Microscopic theory of spin-polarization coupling in multiferroic transition metal oxides, Phys. Rev. B **76**, 144424 (2007).

[238] J. S. White, K. Prša, P. Huang, A. A. Omrani, I. Živković, M. Bartkowiak, H. Berger, A. Magrez, J. L. Gavilano, G. Nagy, J. Zang, and H. M. Rønnow, Electric-field-induced skyrmion distortion and giant lattice rotation in the magnetoelectric insulator Cu_2OSeO_3, Phys. Rev. Lett. **113**, 107203 (2014).

[239] Y. Okamura, F. Kagawa, S. Seki, and Y. Tokura, Transition to and from the skyrmion lattice phase by electric fields in a magnetoelectric compound, Nature Communications **7**, 12669 (2016).

[240] M. N. Wilson, M. Crisanti, C. Barker, A. Štefančič, J. S. White, M. T. Birch, G. Balakrishnan, R. Cubitt, and P. D. Hatton, Measuring the formation energy barrier of skyrmions in zinc-substituted Cu_2OSeO_3, Phys. Rev. B **99**, 174421 (2019).

[241] J. S. White, I. Levatić, A. A. Omrani, N. Egetenmeyer, K. Prša, I. Živković, J. L. Gavilano, J. Kohlbrecher, M. Bartkowiak, H. Berger, and H. M. Rønnow, Electric field control of the skyrmion lattice in Cu_2OSeO_3, Journal of Physics: Condensed Matter **24**, 432201 (2012).

[242] X. Wan, Y. Hu, and B. Wang, First and second order rotational transitions of skyrmion crystal in multiferroic Cu_2OSeO_3 under electric field, Applied Physics Letters **116**, 182403 (2020).

[243] P. Huang, M. Cantoni, A. Magrez, F. Carbone, and H. M. Rønnow, Electric field writing and erasing of skyrmions in magnetoelectric cu2oseo3 with an ultralow energy barrier, Nanoscale **14**, 16655–16660 (2022).

[244] J. S. White, I. Živković, A. J. Kruchkov, M. Bartkowiak, A. Magrez, and H. M. Rønnow, Electric-field-driven topological phase switching and skyrmion-lattice metastability in magnetoelectric Cu_2OSeO_3, Physical Review Applied **10**, 014021 (2018).

[245] P. Huang, M. Cantoni, A. Kruchkov, J. Rajeswari, A. Magrez, F. Carbone, and H. M. Rønnow, In situ electric field skyrmion creation in magnetoelectric Cu_2OSeO_3, Nano Letters **18**, 5167–5171 (2018).

[246] Y. Okamura, Y. Yamasaki, D. Morikawa, T. Honda, V. Ukleev, H. Nakao, Y. Murakami, K. Shibata, F. Kagawa, S. Seki, T. Arima, and Y. Tokura, Directional electric-field induced transformation from skyrmion lattice to distinct helices in multiferroic Cu_2OSeO_3, Phys. Rev. B **95**, 184411 (2017).

[247] M. Bartkowiak, J. S. White, H. M. Rønnow, and K. Prša, Note: Versatile sample stick for neutron scattering experiments in high electric fields, Review of Scientific Instruments **85**, 026112 (2014).

[248] T. Nagase, Y.-G. So, H. Yasui, T. Ishida, H. K. Yoshida, Y. Tanaka, K. Saitoh, N. Ikarashi, Y. Kawaguchi, M. Kuwahara, and M. Nagao, Observation of domain wall bimerons in chiral magnets, Nature Communications **12**, 3490 (2021).

[249] A. O. Leonov and A. N. Bogdanov, Crossover of skyrmion and helical modulations in noncentrosymmetric ferromagnets, New Journal of Physics **20**, 043017 (2018).

[250] A. O. Leonov and C. Pappas, Topological boundaries between helical domains as a nucleation source of skyrmions in the bulk cubic helimagnet Cu_2OSeO_3, Phys. Rev. Research **4**, 043137 (2022).

[251] J. S. White, I. Levatić, A. A. Omrani, N. Egetenmeyer, K. Prša, I. Živković, J. L. Gavilano, J. Kohlbrecher, M. Bartkowiak, H. Berger, and H. M. Rønnow, Electric field control of the skyrmion lattice in Cu_2OSeO_3, Journal of Physics: Condensed Matter **24**, 432201 (2012).

[252] J. S. White, K. Prša, P. Huang, A. A. Omrani, I. Živković, M. Bartkowiak, H. Berger, A. Magrez, J. L. Gavilano, G. Nagy, J. Zang, and H. M. Rønnow, Electric-field-induced skyrmion distortion and giant lattice rotation in the

magnetoelectric insulator Cu_2OSeO_3, Physical Review Letters **113**, 107203 (2014).

[253] A. Kruchkov, J. White, M. Bartkowiak, I. Zivkovic, A. Magrez, and H. Ronnow, Direct electric field control of the skyrmion phase in a magnetoelectric insulator, Scientific Reports **8**, 10466 (2018).

[254] M. N. Wilson, M. Crisanti, C. Barker, A. Štefančič, J. S. White, M. T. Birch, G. Balakrishnan, R. Cubitt, and P. D. Hatton, Measuring the formation energy barrier of skyrmions in zinc-substituted Cu_2OSeO_3, Physical Review B **99**, 174421 (2019).

[255] Z. Hou, Y. Wang, X. Lan, S. Li, X. Wan, F. Meng, Y. Hu, Z. Fan, C. Feng, M. Qin, M. Zeng, X. Zhang, X. Liu, X. Fu, G. Yu, G. Zhou, Y. Zhou, W. Zhao, X. Gao, and J.-m. Liu, Controlled switching of the number of skyrmions in a magnetic nanodot by electric fields, Advanced Materials **34**, 2107908 (2022).

[256] X. Yu, D. Morikawa, Y. Tokunaga, M. Kubota, T. Kurumaji, H. Oike, M. Nakamura, F. Kagawa, Y. Taguchi, T.-h. Arima, M. Kawasaki, and Y. Tokura, Current-induced nucleation and annihilation of magnetic skyrmions at room temperature in a chiral magnet, Advanced Materials **29**, 1606178 (2017).

[257] Z. Hou, Q. Zhang, X. Zhang, G. Xu, J. Xia, B. Ding, H. Li, S. Zhang, N. M. Batra, P. M. F. J. Costa, E. Liu, G. Wu, M. Ezawa, X. Liu, Y. Zhou, X. Zhang, and W. Wang, Current-induced helicity reversal of a single skyrmionic bubble chain in a nanostructured frustrated magnet, Advanced Materials **32**, 1904815 (2020).

[258] M. Mochizuki and S. Seki, Magnetoelectric resonances and predicted microwave diode effect of the skyrmion crystal in a multiferroic chiral-lattice magnet, Physical Review B **87**, 134403 (2013).

[259] Y.-H. Liu, Y.-Q. Li, and J. H. Han, Skyrmion dynamics in multiferroic insulators, Physical Review B **87**, 100402 (2013).

[260] J. Bardeen and W. H. Brattain, The transistor, a semi-conductor triode, Phys. Rev. **74**, 230–231 (1948).

[261] M. Beg, M. Lang, and H. Fangohr, Ubermag: Towards more effective micromagnetic workflows, IEEE Transactions on Magnetics **58**, 1–5 (2022).

[262] M. Donahue and D. Porter, *OOMMF User's Guide, Version 1.0* (Interagency Report NISTIR 6376, National Institute of Standards and Technology, Gaithersburg, MD, 1999).

[263] S. L. Zhang, W. W. Wang, D. M. Burn, H. Peng, H. Berger, A. Bauer, C. Pfleiderer, G. van der Laan, and T. Hesjedal, Manipulation of skyrmion motion by magnetic field gradients, Nature Communications **9**, 2115 (2018).

[264] A. O. Leonov and M. Mostovoy, Edge states and skyrmion dynamics in nanostripes of frustrated magnets, Nature Communications **8**, 14394 (2017).

[265] S.-Z. Lin, C. Reichhardt, C. D. Batista, and A. Saxena, Particle model for skyrmions in metallic chiral magnets: Dynamics, pinning, and creep, Physical Review B **87**, 214419 (2013).

[266] S. L. Zhang, W. W. Wang, D. M. Burn, H. Peng, H. Berger, A. Bauer, C. Pfleiderer, G. van der Laan, and T. Hesjedal, Manipulation of skyrmion motion by magnetic field gradients, Nature Communications **9**, 2115 (2018).

[267] J. Iwasaki, M. Mochizuki, and N. Nagaosa, Current-induced skyrmion dynamics in constricted geometries, Nature Nanotechnology **8**, 742–747 (2013).

[268] D. Cortés-Ortuño, W. Wang, M. Beg, R. A. Pepper, M.-A. Bisotti, R. Carey, M. Vousden, T. Kluyver, O. Hovorka, and H. Fangohr, Thermal stability and topological protection of skyrmions in nanotracks, Scientific Reports **7**, 4060–4060 (2017).

[269] J. Zázvorka, F. Jakobs, D. Heinze, N. Keil, S. Kromin, S. Jaiswal, K. Litzius, G. Jakob, P. Virnau, D. Pinna, K. Everschor-Sitte, L. Rózsa, A. Donges, U. Nowak, and M. Kläui, Thermal skyrmion diffusion used in a reshuffler device, Nature Nanotechnology **14**, 658–661 (2019).

[270] H. Zhang, D. Zhu, W. Kang, Y. Zhang, and W. Zhao, Stochastic computing implemented by skyrmionic logic devices, Physical Review Applied **13**, 054049 (2020).

[271] D. Pinna, G. Bourianoff, and K. Everschor-Sitte, Reservoir computing with random skyrmion textures, Physical Review Applied **14**, 054020 (2020).

[272] A. O. Leonov and C. Pappas, Skyrmion clusters and conical droplets in bulk helimagnets with cubic anisotropy, Physical Review B **99**, 144410 (2019).

[273] R. Brearton, G. van der Laan, and T. Hesjedal, Magnetic skyrmion interactions in the micromagnetic framework, Physical Review B **101**, 134422 (2020).

[274] P. Kotsandis, J. Yakinthos, and E. Gamariseale, Magnetic-properties of the ternary rare-earth silicides Pr_2PdSi_3, Nd_2PdSi_3, Gd_2PdSi_3, Tb_2PdSi_3, Dy_2PdSi_3, Ho_2PdSi_3, Er_2PdSi_3, Tm_2PdSi_3 and Y_2PdSi_3, Journal of Magnetism and Magnetic Materials **87**, 199–204 (1990).

[275] K. Mukherjee, T. Basu, K. K. Iyer, and E. V. Sampathkumaran, $4f$ hybridization effect on the magnetism of Nd_2PdSi_3, Phys. Rev. B **84**, 184415 (2011).

[276] R. Mallik, E. V. Sampathkumaran, M. Strecker, and G. Wortmann, Observation of a minimum in the temperature-dependent electrical resistance above the magnetic-ordering temperature in Gd_2PdSi_3, Europhysics Letters **41**, 315 (1998).

[277] R. Mallik, E. Sampathkumaran, P. Paulose, H. Sugawara, and H. Sato, Magnetic anomalies in Gd_2PdSi_3, Physica B: Condensed Matter **259-261**, 892–893 (1999).

[278] S. Saha, H. Sugawara, T. Matsuda, Y. Aoki, H. Sato, and E. Sampathkumaran, Resistivity minimum and anisotropy in $(Ce, Gd)_2PdSi_3$, Physica B: Condensed Matter **281-282**, 116–117 (2000).

[279] S. Zhang, D. M. Burn, N. Jaouen, J.-Y. Chauleau, A. A. Haghighirad, Y. Liu, W. Wang, G. van der Laan, and T. Hesjedal, Robust perpendicular skyrmions and their surface confinement, Nano Letters **20**, 1428–1432 (2020).

[280] S. Majumdar, E. V. Sampathkumaran, D. Eckert, A. Handstein, K.-H. Müller, S. R. Saha, H. Sugawara, and H. Sato, Magnetic relaxation behaviour in Gd_2PdSi_3 alloys, Journal of Physics: Condensed Matter **11**, L329 (1999).

[281] S. R. Saha, H. Sugawara, T. D. Matsuda, H. Sato, R. Mallik, and E. V. Sampathkumaran, Magnetic anisotropy, first-order-like metamagnetic transitions, and large negative magnetoresistance in single-crystal Gd_2PdSi_3, Phys. Rev. B **60**, 12162–12165 (1999).

[282] R. Rawat and I. Das, Magnetocaloric and magnetoresistance studies of $GdPd_2Si_3$, Journal of Physics: Condensed Matter **13**, L57 (2001).

[283] Z. J. Mo, J. Shen, X. Q. Gao, Y. Liu, C. C. Tang, J. F. Wu, F. X. Hu, J. R. Sun, and B. G. Shen, Magnetic properties and magnetocaloric effect in the R_2PdSi_3 compounds, Journal of Alloys and Compounds **626**, 145–149 (2015).

[284] M. Hirschberger, L. Spitz, T. Nomoto, T. Kurumaji, S. Gao, J. Masell, T. Nakajima, A. Kikkawa, Y. Yamasaki, H. Sagayama, H. Nakao, Y. Taguchi, R. Arita, T.-h. Arima, and Y. Tokura, Topological Nernst effect of the two-dimensional skyrmion lattice, Phys. Rev. Lett. **125**, 076602 (2020).

[285] A. Neubauer, C. Pfleiderer, B. Binz, A. Rosch, R. Ritz, P. G. Niklowitz,

and P. Böni, Topological Hall effect in the a phase of MnSi, Phys. Rev. Lett. **102**, 186602 (2009).

[286] N. Matsuyama, T. Nomura, S. Imajo, T. Nomoto, R. Arita, K. Sudo, M. Kimata, N. D. Khanh, R. Takagi, Y. Tokura, S. Seki, K. Kindo, and Y. Kohama, Quantum oscillations in a centrosymmetric skyrmion-hosting magnet $GdRu_2Si_2$ (2022).

[287] D. S. Inosov, D. V. Evtushinsky, A. Koitzsch, V. B. Zabolotnyy, S. V. Borisenko, A. A. Kordyuk, M. Frontzek, M. Loewenhaupt, W. Löser, I. Mazilu, H. Bitterlich, G. Behr, J.-U. Hoffmann, R. Follath, and B. Büchner, Electronic structure and nesting-driven enhancement of the RKKY interaction at the magnetic ordering propagation vector in Gd_2PdSi_3 and Tb_2PdSi_3, Phys. Rev. Lett. **102**, 046401 (2009).

[288] J. A. M. Paddison, B. K. Rai, A. F. May, S. Calder, M. B. Stone, M. D. Frontzek, and A. D. Christianson, Magnetic interactions of the centrosymmetric skyrmion material Gd_2PdSi_3, Phys. Rev. Lett. **129**, 137202 (2022).

[289] T. Nomoto, T. Koretsune, and R. Arita, Formation mechanism of the helical q structure in Gd-based skyrmion materials, Phys. Rev. Lett. **125**, 117204 (2020).

[290] J. Bouaziz, E. Mendive-Tapia, S. Blügel, and J. B. Staunton, Fermi-surface origin of skyrmion lattices in centrosymmetric rare-earth intermetallics, Phys. Rev. Lett. **128**, 157206 (2022).

[291] F. Tang, M. Frontzek, J. Dshemuchadse, T. Leisegang, M. Zschornak, R. Mietrach, J.-U. Hoffmann, W. Löser, S. Gemming, D. C. Meyer, and M. Loewenhaupt, Crystallographic superstructure in R_2PdSi_3 compounds, Phys. Rev. B **84**, 104105 (2011).

[292] S. Spachmann, A. Elghandour, M. Frontzek, W. Löser, and R. Klingeler, Magnetoelastic coupling and phases in the skyrmion lattice magnet

Gd_2PdSi_3 discovered by high-resolution dilatometry, Phys. Rev. B **103**, 184424 (2021).

[293] T. Inami, N. Terada, H. Kitazawa, and O. Sakai, Resonant magnetic x-ray diffraction study on the triangular lattice antiferromagnet $GdPd_2Al_3$, Journal of the Physical Society of Japan **78**, 084713 (2009).

[294] T. Matsumura, Y. Ozono, S. Nakamura, N. Kabeya, and A. Ochiai, Helical ordering of spin trimers in a distorted kagome lattice of $Gd_3Ru_4Al_{12}$ studied by resonant x-ray diffraction, Journal of the Physical Society of Japan **88**, 023704 (2019).

[295] J. Strempfer, S. Francoual, D. Reuther, D. K. Shukla, A. Skaugen, H. Schulte-Schrepping, T. Kracht, and H. Franz, Resonant scattering and diffraction beamline P09 at PETRA III, Journal of Synchrotron Radiation **20**, 541–549 (2013).

[296] M. Blume and D. Gibbs, Polarization dependence of magnetic x-ray scattering, Phys. Rev. B **37**, 1779–1789 (1988).

[297] J. P. Hannon, G. T. Trammell, M. Blume, and D. Gibbs, X-ray resonance exchange scattering, Phys. Rev. Lett. **62**, 2644–2644 (1989).

[298] P. J. Bereciartua, J. Rodríguez-Carvajal, and S. Francoual, *MagStREXS*: crystallographic software for magnetic structure determination through resonant X-ray magnetic diffraction data, Acta Crystallographica Section A **77**, C177 (2021).

[299] L. Spitz, T. Nomoto, S. Kitou, H. Nakao, A. Kikkawa, S. Francoual, Y. Taguchi, R. Arita, Y. Tokura, T.-h. Arima, and M. Hirschberger, Entropy-assisted, long-period stacking of honeycomb layers in an AlB_2-type silicide, Journal of the American Chemical Society **144**, 16866–16871 (2022).

[300] S. H. Moody, M. N. Wilson, M. T. Birch, M. Gomilšek, S. P. Collins, A. Štefančič, G. Balakrishnan, and P. D. Hatton, Charge density waves and coplanar magnetism in Gd_2PdSi_3 (2020).

[301] S. Roy, D. Parks, K. A. Seu, R. Su, J. J. Turner, W. Chao, E. H. Anderson, S. Cabrini, and S. D. Kevan, Lensless x-ray imaging in reflection geometry, Nature Photonics **5**, 243–245 (2011).

[302] H. Popescu, F. Fortuna, R. Delaunay, N. Jaouen, C. Spezzani, and M. Sacchi, Soft x-ray lensless imaging in reflection mode, Photonics **8**, 10.3390/photonics8120569 (2021).

[303] Y. Yokoyama, Y. Yamasaki, M. Okada, and M. Mizumaki, Phase retrieval algorithm based on total variation regularization for ferromagnetic domain patterns, Journal of the Physical Society of Japan **91**, 034701 (2022).

[304] S. Hayami, T. Okubo, and Y. Motome, Phase shift in skyrmion crystals, Nature Communications **12**, 6927 (2021).

[305] F. Keffer, Moriya interaction and the problem of the spin arrangements in $\beta - \mathrm{MnS}$, Phys. Rev. **126**, 896–900 (1962).

[306] S.-W. Cheong and M. Mostovoy, Multiferroics: a magnetic twist for ferroelectricity, Nature Materials **6**, 13–20 (2007).

[307] G. H. Wannier, Antiferromagnetism. the triangular Ising net, Phys. Rev. **79**, 357–364 (1950).

[308] L. Balents, Spin liquids in frustrated magnets, Nature **464**, 199–208 (2010).

[309] O. Hovorka and T. J. Sluckin, A computational mean-field model of interacting non-collinear classical spins (2020).

[310] R. Georgii and T. Weber, The helical magnet MnSi: Skyrmions and magnons, Quantum Beam Science **3**, 10.3390/qubs3010004 (2019).

[311] J. D. Bocarsly, R. F. Need, R. Seshadri, and S. D. Wilson, Magnetoentropic signatures of skyrmionic phase behavior in FeGe, Phys. Rev. B **97**, 100404 (2018).

[312] K. J. A. Franke, P. R. Dean, M. C. Hatnean, M. T. Birch, D. D. Khalyavin, P. Manuel, T. Lancaster, G. Balakrishnan, and P. D. Hatton, Investigating the magnetic ground state of the skyrmion host material Cu_2OSeO_3 using long-wavelength neutron diffraction, AIP Advances **9**, 125228 (2019).

[313] H. Oike, A. Kikkawa, N. Kanazawa, Y. Taguchi, M. Kawasaki, Y. Tokura, and F. Kagawa, Interplay between topological and thermodynamic stability in a metastable magnetic skyrmion lattice, Nature Physics **12**, 62–66 (2016).

[314] T. Nakajima, H. Oike, A. Kikkawa, E. P. Gilbert, N. Booth, K. Kakurai, Y. Taguchi, Y. Tokura, F. Kagawa, and T. Arima, Skyrmion lattice structural transition in MnSi, Science Advances **3**, e1602562 (2017).

[315] F. Kagawa, H. Oike, W. Koshibae, A. Kikkawa, Y. Okamura, Y. Taguchi, N. Nagaosa, and Y. Tokura, Current-induced viscoelastic topological unwinding of metastable skyrmion strings, Nature Communications **8**, 1332 (2017).

[316] M. T. Littlehales, L. A. Turnbull, M. N. Wilson, M. T. Birch, H. Popescu, N. Jaouen, J. A. T. Verezhak, G. Balakrishnan, and P. D. Hatton, Enhanced skyrmion metastability under applied strain in FeGe, Phys. Rev. B **106**, 214434 (2022).

[317] W. Münzer, A. Neubauer, T. Adams, S. Mühlbauer, C. Franz, F. Jonietz, R. Georgii, P. Böni, B. Pedersen, M. Schmidt, A. Rosch, and C. Pfleiderer, Skyrmion lattice in the doped semiconductor $Fe_{1-x}Co_xSi$, Physical Review B **81**, 041203 (2010).

[318] P. Milde, D. Köhler, J. Seidel, L. M. Eng, A. Bauer, A. Chacon, J. Kindervater, S. Mühlbauer, C. Pfleiderer, S. Buhrandt, C. Schütte, and A. Rosch,

Unwinding of a skyrmion lattice by magnetic monopoles, Science **340**, 1076–1080 (2013).

[319] L. J. Bannenberg, H. Wilhelm, R. Cubitt, A. Labh, M. P. Schmidt, E. Lelièvre-Berna, C. Pappas, M. Mostovoy, and A. O. Leonov, Multiple low-temperature skyrmionic states in a bulk chiral magnet, npj Quantum Materials **4**, 11 (2019).

[320] K. Karube, J. S. White, D. Morikawa, M. Bartkowiak, A. Kikkawa, Y. Tokunaga, T. Arima, H. M. Rønnow, Y. Tokura, and Y. Taguchi, Skyrmion formation in a bulk chiral magnet at zero magnetic field and above room temperature, Phys. Rev. Mater. **1**, 074405 (2017).

[321] K. Karube, J. S. White, N. Reynolds, J. L. Gavilano, H. Oike, A. Kikkawa, F. Kagawa, Y. Tokunaga, H. M. Rønnow, Y. Tokura, and Y. Taguchi, Robust metastable skyrmions and their triangular–square lattice structural transition in a high-temperature chiral magnet, Nature Materials **15**, 1237–1242 (2016).

[322] D. Morikawa, X. Yu, K. Karube, Y. Tokunaga, Y. Taguchi, T.-h. Arima, and Y. Tokura, Deformation of topologically-protected supercooled skyrmions in a thin plate of chiral magnet $Co_8Zn_8Mn_4$, Nano Letters **17**, 1637–1641 (2017).

[323] M. T. Birch, D. Cortés-Ortuño, N. D. Khanh, S. Seki, A. Štefančič, G. Balakrishnan, Y. Tokura, and P. D. Hatton, Topological defect-mediated skyrmion annihilation in three dimensions, Communications Physics **4**, 175 (2021).

[324] M. Crisanti, M. T. Birch, M. N. Wilson, S. H. Moody, A. Štefančič, B. M. Huddart, S. Cabeza, G. Balakrishnan, P. D. Hatton, and R. Cubitt, Position-dependent stability and lifetime of the skyrmion state in nickel-substituted Cu_2OSeO_3, Phys. Rev. B **102**, 224407 (2020).

[325] S.-G. Je, H.-S. Han, S. K. Kim, S. A. Montoya, W. Chao, I.-S. Hong, E. E. Fullerton, K.-S. Lee, K.-J. Lee, M.-Y. Im, and J.-I. Hong, Direct demonstration of topological stability of magnetic skyrmions via topology manipulation, ACS Nano **14**, 3251–3258 (2020).

[326] J. Wild, T. N. G. Meier, S. Pöllath, M. Kronseder, A. Bauer, A. Chacon, M. Halder, M. Schowalter, A. Rosenauer, J. Zweck, J. Müller, A. Rosch, C. Pfleiderer, and C. H. Back, Entropy-limited topological protection of skyrmions, Science Advances **3**, e1701704 (2017).

[327] R. Yanes, O. Chubykalo-Fesenko, H. Kachkachi, D. A. Garanin, R. Evans, and R. W. Chantrell, Effective anisotropies and energy barriers of magnetic nanoparticles with Néel surface anisotropy, Phys. Rev. B **76**, 064416 (2007).

[328] M. Laughton and D. Warne, *Electrical Engineer's Reference Book* (Elsevier Science, 2002).

[329] S. Zhang, G. van der Laan, J. Müller, L. Heinen, M. Garst, A. Bauer, H. Berger, C. Pfleiderer, and T. Hesjedal, Reciprocal space tomography of 3D skyrmion lattice order in a chiral magnet, Proceedings of the National Academy of Sciences **115**, 6386–6391 (2018).

[330] T. Adams, S. Mühlbauer, C. Pfleiderer, F. Jonietz, A. Bauer, A. Neubauer, R. Georgii, P. Böni, U. Keiderling, K. Everschor, M. Garst, and A. Rosch, Long-range crystalline nature of the skyrmion lattice in MnSi, Phys. Rev. Lett. **107**, 217206 (2011).

[331] Y. Togawa, T. Koyama, K. Takayanagi, S. Mori, Y. Kousaka, J. Akimitsu, S. Nishihara, K. Inoue, A. S. Ovchinnikov, and J. Kishine, Chiral magnetic soliton lattice on a chiral helimagnet, Phys. Rev. Lett. **108**, 107202 (2012).

[332] S. R. Kline, Reduction and analysis of SANS and USANS data using IGOR Pro, Journal of Applied Crystallography **39**, 895–900 (2006).

[333] P. F. Bessarab, V. M. Uzdin, and H. Jónsson, Method for finding mechanism and activation energy of magnetic transitions, applied to skyrmion and antivortex annihilation, Computer Physics Communications **196**, 335–347 (2015).

[334] F. Muckel, S. von Malottki, C. Holl, B. Pestka, M. Pratzer, P. F. Bessarab, S. Heinze, and M. Morgenstern, Experimental identification of two distinct skyrmion collapse mechanisms, Nature Physics **17**, 395–402 (2021).

[335] D. Cortés-Ortuño, W. Wang, M. Beg, R. A. Pepper, M.-A. Bisotti, R. Carey, M. Vousden, T. Kluyver, O. Hovorka, and H. Fangohr, Thermal stability and topological protection of skyrmions in nanotracks, Scientific Reports **7**, 4060 (2017).

[336] A. D. Huxley, M.-A. Measson, K. Izawa, C. D. Dewhurst, R. Cubitt, B. Grenier, H. Sugawara, J. Flouquet, Y. Matsuda, and H. Sato, Flux-line lattice distortion in $PrOs_4Sb_{12}$, Phys. Rev. Lett. **93**, 187005 (2004).

[337] K.-U. Neumann, F. Kusmartsev, H.-J. Lauter, O. Schärpf, T. J. Smith, and K. R. A. Ziebeck, Experimental observation of lattice distortions due to a flux line lattice in niobium, The European Physical Journal B - Condensed Matter and Complex Systems **1**, 5–9 (1998).